APPLIED COMPUTATIONAL ELECTROMAGNETICS SOCIETY JOURNAL

NOVEMBER 2019 REVIEWERS: REGULAR PAPERS

Marinko Barukcic
Mehmet Belen
Fangyuan Chen
Manohar Deshpande
Joseph Diener
Pasquale Dottorato
Ozgur Ergul
Andrey Grigoryev
Amir Hajiaboli
Mourad Ibrahim
Tianqi Jiao
Fatih Kaburcuk
Ashutosh Kedar
Rakhesh Kshetrimayum
Ali Lalbakhsh
Yue Li
Neng-Wu Liu
Hend Malhat
Riyadh Mansoor
Naobumi Michishita
Mohammad Neshati
Elangovan P.
Karthikkeyan P.
Andrew Peterson
Mohammd Pourbagher

MuhibUr Rahman
Zbynek Raida
C.J. Reddy
Vince Rodriguez
Tayyab Shabbir
Yan Shi
Hari Singh
Javad Soleiman Meiguni
Abhay Srivastava
Sellakkutti Suganthi
Yi Sui
Yuvaraja T.
Yogesh Thakare
Xuezhe Tian
Hossein Torkaman
Christopher Trueman
Krushna Kanth V.
Qi Wu
Run Xiong
Huanhuan Yang
Traianos Yioultsis
John Young
Huapeng Zhao
Theodoros Zygiridis

THE APPLIED COMPUTATIONAL ELECTROMAGNETICS SOCIETY JOURNAL

TABLE OF CONTENTS – REGULAR PAPERS

FDTD Modeling of Coils for Wireless Charging Applications

Santosh Pokhrel [1], Gregory Moss [2], and Jamesina J. Simpson [1]

[1] Department of Electrical Engineering
University of Utah, Salt Lake City, UT, 84112, USA
santoshpokhrel1991@gmail.com, jamesina.simpson@utah.edu

[2] Remcom, State College, PA, 16801, USA
gregory.moss@remcom.com

Abstract ─ Wireless power transfer using inductive/ resonant coupling is studied using the finite-difference time-domain (FDTD) method. Three-dimensional FDTD models are used to simulate the source and load loops as well as frequency-dependent magnetized ferrite shields. A series of tests are run to determine the required distance between the coils and the domain edges, the PML thickness, and convergence level. The FDTD-calculated coil parameters (self-inductance and quality factor) are then validated against measurement results. The efficiency of the inductive link is studied without ferrite shields and then with two ferrite slabs added. It is observed that adding ferrite slabs improves the efficiency by ~40%.

Index Terms ─ Coils, FDTD, flux coupling, magnetized ferrite, simulation and wireless charging.

I. INTRODUCTION

Interest in wireless power transfer has been growing due to its utility and convenience when applied to numerous applications [1], including charging of laptops to mobile phones, medical implants [2], near field communication (NFC) antennas [3], and electric vehicles [4]. Generally, low frequencies (kHz and MHz frequencies) are used for wireless charging applications due to safety issues [5]. For instance, according to the Qi wireless charging standard [6], wireless charging of mobile phones is performed in the lower kHz band (110 kHz – 205 kHz). Wireless charging for biological telemetry [7] is performed in the lower MHz frequency band.

To transmit power wirelessly between transmitter and receiver coils, non-radiative techniques [2], [8]-[11] are typically used, such as inductive coupling [10] and magnetic resonant coupling [11]. As shown in Fig. 1, a source coil (loop) connected to an AC power source generates magnetic flux. When a load loop is brought into the vicinity of the source loop, an electromotive force is induced in the load coil which eventually drives current through it. The performance of the coupling is dependent on its power transfer efficiency (PTE) and power transmission distance. The PTE can be improved by shielding the coils with magnetized ferrite slabs. Another possibility is to use metamaterials [12].
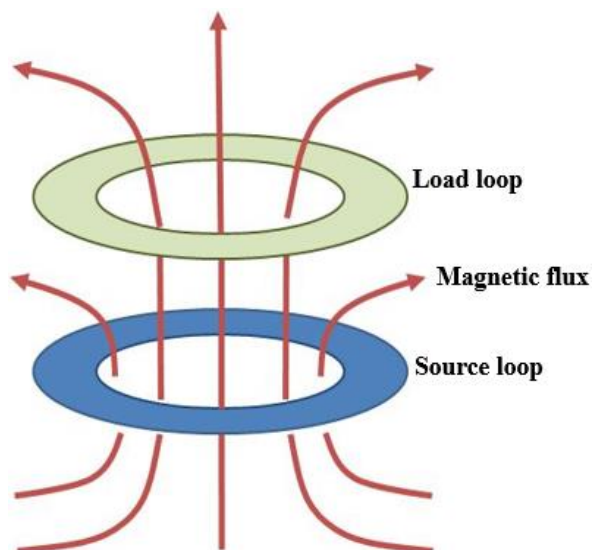
Fig. 1. Magnetic flux coupling between a source and load loop.

Various commercial electromagnetic (EM) solvers exist that may be used to simulate coils. For example, the frequency domain solver [13], [14] provided by ANSYS may be used, as well as the magnetostatic domain solver [15] provided by Computer Simulation Technology (CST). Further, the finite-difference time-domain (FDTD) has been used to model RF coils for different applications, such as magnetic resonant imaging (MRI) [16], biomedical telemetry system [17], open vertical field magnetic resonance guided focused ultrasound system [18], nuclear magnetic resonance (NMR) [19], inductive power transfer system [20] etc. Similarly, using the FEKO electromagnetics software, the Method

of Moments (MOM) has been applied to wireless power transfer via magnetic resonance coupling [21].

An advantage of FDTD for this application is that it can be used to simulate anisotropic and frequency-dependent materials such as magnetized ferrite and magnetized plasma in a relatively easier manner (e.g., [22]). In this paper, XFdtd [23] is used to simulate wireless charging coil designs with magnetized ferrite shields.

There are a number of challenges when simulating low frequency wireless charging coils using the FDTD method. First, the dimensions of the coils are extremely small, on the order of millimeters. As a result, a large number of grid cells (high resolution mesh) are required to correctly resolve the coil geometry. This is especially important because the fundamental coil parameters (inductance and AC resistance) are extremely sensitive to the coil dimensions, therefore a high degree of spatial accuracy is required. Second, the rate of convergence can be extremely slow for low frequency problems. Third, thick absorbing boundary conditions (such as a perfectly matched layer (PML)) [24] are needed to effectively absorb low frequency waves, which have long wavelengths compared to the dimensions of the grid cells.

We note that an inductive power system using two-step scaled frequency FDTD methods has been recently reported [20]. However, the effect of the magnetized ferrite on the important coil parameters such as self-inductance, quality factor, mutual inductance, coupling coefficient and efficiency was not quantified. Therefore, the contribution of this paper includes: (1) comparing simulation results with measurements; and (2) using the FDTD method to perform a complete 3-D simulation of two coils while including magnetized ferrite shields. In particular, the effect of the magnetized ferrite on the important coil parameters is computed. These simulation results provide additional insight into designing wireless charging coil systems.

This paper is organized as follows: In Section II, an equivalent circuit model of the coil system is provided. Section III elaborates on the challenges of using FDTD for this application. Information is also provided for setting up effective simulations. In addition, FDTD-calculated results are validated against measurements. Section IV provides details on magnetized ferrite and the results including it in the FDTD simulations. Finally, Section V discusses strategies for boosting the magnetic flux coupling between coils.

II. EQUIVALENT CIRCUIT MODEL

The fundamental structure for wireless power transfer consists of two coils: a transmitter (driver) coil connected to an AC excitation and a receiver (load) coil (as shown in Figs. 1 and 2). An equivalent circuit is shown in Fig. 3.

The two coils may be represented by a two-port network with the transmitter coil attached to Port-1 and the receiver coil attached to Port-2. The two-port network results in a 2×2 S-parameter matrix, which are evaluated at the nodes during the simulation. The measured S-parameters are obtained from the terminals (see Fig. 2). In the measurements, the S-parameters are obtained from the vector network analyzer (VNA). The S-parameters are then converted into impedances (Z). The self-inductances (L_1 and L_2) of the transmitter coil and the receiver coil, respectively are determined by dividing the imaginary part of Z_{11} and Z_{22}, respectively, by the angular frequency. The real part of Z_{11} yields the parasitic resistance of the coil. R_1 and R_2 are the parasitic resistances of the two coils. The mutual inductance (M) is determined by dividing the imaginary component of Z_{12} or Z_{21} by the angular frequency. Two capacitors (C_1 and C_2) may be connected in series to represent the resonant circuit at the desired frequency.
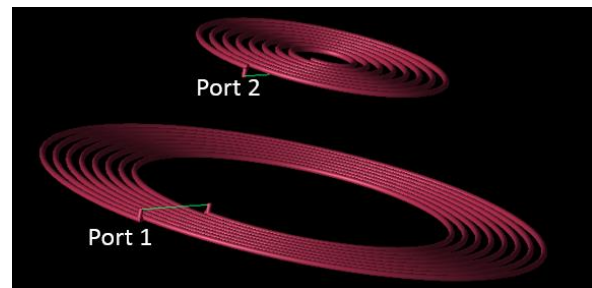
Fig. 2. Inductive link (driver coil and load coil) modeled in XFdtd. The bigger coil at bottom is the transmitter coil, and the smaller one at the top is the receiver coil. The green line in the driver coil represents the resistive voltage connection between two terminals. Similarly, the green line in the load coil represents the resistive load connection between two terminals.
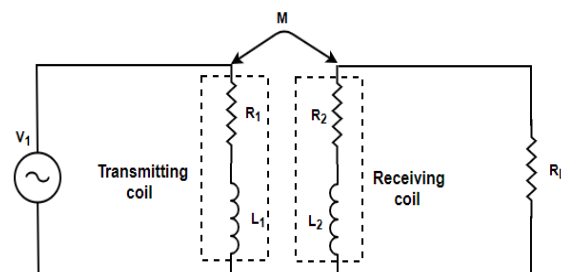
Fig. 3. Circuit model of the two port network representing the two coils.

Q1 is the intrinsic quality factor of the transmitting coil, Q2 is the intrinsic quality factor of the receiving coil, and Q2L is the loaded quality factor of the receiving coil. The quality factors are determined using equations (1) – (3):

$$Q_1 = \frac{\omega L_1}{R_1}, \tag{1}$$

$$Q_2 = \frac{\omega L_2}{R_2}, \tag{2}$$

$$Q_{2L} = \frac{\omega L_2}{R_2 + R_L}. \tag{3}$$

K_{12} is the coupling coefficient representing the magnetic flux coupling between the two coils (the transmitter and receiver coils). Its value depends on the mutual inductance between the coils, and the self-inductance of the individual coils, as shown in (4). Numerically, its value ranges from 0 to 1. A value of zero indicates that little or no coupling is achieved, and a value of one indicates that perfect coupling is achieved. Practically, it is impossible to achieve perfect coupling:

$$K_{12} = \frac{M}{\sqrt{L_1 . L_2}}. \tag{4}$$

The power transfer efficiency (PTE) of the link determines how much total power has been coupled to the receiver. Its value gives the final figure of merit of the system. The PTE depends on the magnetic flux coupling between the coils, the quality factors of both coils, and the resistance of the load and receiver coils. The expression for the PTE is given by (5):

$$PTE = \frac{K_{12}^2 Q_1 Q_{2L}}{1 + K_{12}^2 Q_1 Q_{2L}} \cdot \frac{R_L}{R_L + R_2}. \tag{5}$$

Equations (1-5) are used in the upcoming sections analyze the system.

III. VALIDATION

A. Simulation details

The simulation examples provided here are for the kHz range, however, an analogous procedure may be followed for higher frequencies. An example circular coil is modeled with a diameter of 67 mm, 10 turns, 1 mm spacing between turns, and a 0.8 mm wire diameter. The two ends of the coil are connected via a copper wire with a resistive voltage source having an internal resistance of 50 ohms. A Gaussian source time-waveform is used to excite a range of frequencies from DC to 260 kHz. A conductivity of 5.95×10^7 S/m is used for the copper.

The models employ conformal meshing, [25] which helps to resolve the complex geometry and small gap efficiently. The spatial grid resolution is 0.4 mm. At this resolution, two to three cells are used to resolve the traces of the conductor and one to two cells are used to resolve the gap between the turns of the coil. Additional simulations demonstrated that doubling the number of cells used to model the wire and gap (i.e., doubling the grid resolution) does not change the results significantly (for both cases, the results compare well with theory and measurements as shown in Section III B). We note that advanced computational techniques have been developed to more accurately and efficiently model thin wires in FDTD models (e.g., [26]-[27]). However,

XFdtd, which was used in the simulations does not provide this modeling capability in its software.

By default, XFdtd uses a tenth of a wavelength free space padding between the object and the grid boundaries. However, at the low frequencies of interest here, a one-tenth wavelength padding would increase the simulation size by around 500,000 grid cells on each direction. By running a series of tests and comparing against measurements, it is found that the simulation domain may be twice the largest dimension of the coil. As a result, a grid with $335 \times 335 \times 40$ cells in the x-, y-, and z-directions, respectively, is used to model the coil.

The small grid cell dimensions relative to the wavelength at low frequencies also influences the implementation and performance of absorbing boundary conditions. A convolutional PML (CPML) [28] is implemented along all of the edges of the grid. In Fig. 4, the relative error (reflection error) caused by the PML is compared for different PML thicknesses (10 cells, 15 cells and 20 cells). A 20-cell thick PML (black plot in Fig. 2) has less than 1% error. Appendix A summarizes the PML parameters that are used in the simulation. It may be possible to tweak these parameters to improve the PML absorption. Additionally, using an even thicker PML than 20 cells is expected to further reduce the error. However, a thicker PML requires more grid cells and thus increases the memory and computational time of the simulation. Therefore, if thicker PMLs are employed, a level of error must be chosen that makes a suitable trade-off between numerical accuracy and the simulation time.

A time step set to the Courant limit [29] is used. The complete simulation is run on eight graphics processing units (GPUs).

As for many commercial solvers, before simulation begins, an acceptable level of a numerical convergence must be chosen (as time-stepping progresses). For example, the electric or magnetic field components between two successive time-step iterations should not change by a value of more than 0.01 or 20 dB, i.e., $|x_n - x_{n-1}| < 0.01$, where x is an electric or magnetic field component at one position within the grid. It is desirable to have the convergence level as low as possible to yield higher accuracy. Higher accuracy (low convergence level) is obtained by running longer simulations with a smaller threshold of electric or magnetic field variations between time steps (such as 0.001 or even smaller). This ensures that the (pulsed) source decays fully to zero. Otherwise, undesirable frequency components (out of the band) will appear in the spectrum. However, there is a sluggish rate of convergence (global order of accuracy) at low frequencies in the numerical EM solution. Figure 5 plots frequency vs. the imaginary part of coil impedance for different convergence levels.
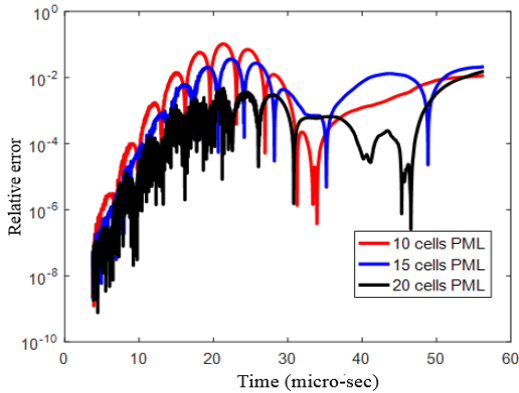
Fig. 4. Relative error (reflection error) for different PML thicknesses.
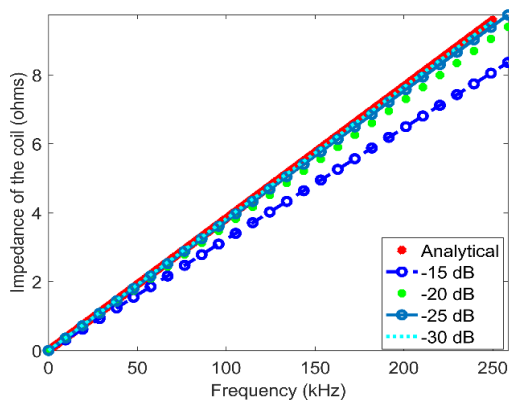
Fig. 5. Comparison of different levels of convergence with analytical impedance (imaginary part) of the coil as simplified by Wheeler approximation.

Table 1 lists the simulation time and error level corresponding to each convergence level (compared to the analytical result). From Table 1, a convergence level of -25 dB yields an error of less than 2%. The numerical solution converges to an analytical solution with an error around 0.3% for a convergence of -30 dB. Using a better convergence level than -30 dB will minimize the error, however the simulation time increases significantly. The simulation time nearly doubles when changing from a convergence level of -25 dB to -30 dB.

Table 1: Comparison of simulation time with different convergence level

Level of Convergence (in dB)	Time of Simulation (in Hours)	Error (at 156 kHz)
-15	0.55	17.28%
-20	1.1	5.44%
-25	1.46	1.8%
-30	2.85	0.3%

All of the remaining simulations are performed at a convergence level of -30 dB.

B. Comparison

The self-inductance of the coil depends on the diameter of the wire, number of turns, spacing between the turns, inner diameter, outer diameter of coil, and permeability of the core [30]. The quality factor of the coil depends on its self-inductance and parasitic resistance (see (1)-(3)).

The self-inductance of the transmitter and receiver coils are calculated via FDTD and compared with both measurement results (as given in [31]) and approximate analytical values as calculated by the Wheeler expression for planar spiral coils [13]. Figure 6 shows the laboratory transmitter and receiver coils used in the measurements. The coil measurements were performed in [31] using a vector network analyzer (VNA). The dimensions of the two coils are tabulated in Table 2.
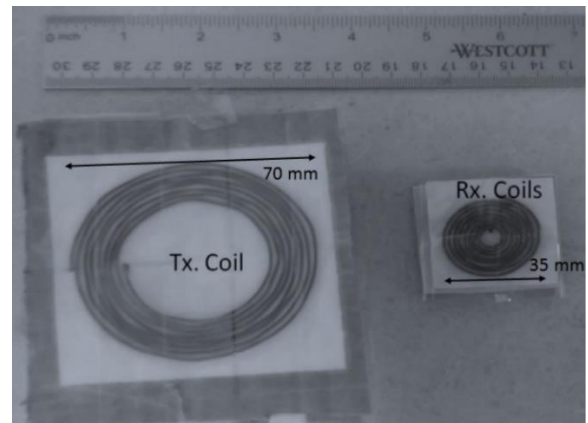
Fig. 6. Coil used for measurement in lab (figure courtesy of [31]). The left coil is the transmitter coil and the right coil is the receiver coil.

Table 2: Dimension for both transmitter and receiver coils

Coil	Diameter (mm)	Number of Turns	Wire Radius (mm)	Gap (mm)
Transmitter	70	8	0.4059	1
Receiver	35	8	0.4059	1

The FDTD grid is run at a resolution of 0.4 mm and at the Courant time-stepping limit. A resistive voltage source with an internal resistance of 50 ohms is modeled on a single electric field component.

Table 3 compares the inductance of both the transmitter and receiver coils. The FDTD simulated inductance values are very close to the measured and analytical values. The error in both cases is less than 2%.

Table 4 compares the simulated and measured quality factor. The simulated quality factor is evaluated using (1) and (2). The quality factor is very sensitive to the coil's inductance and parasitic resistance. There is no standard way to analytically determine the parasitic resistance of the coil [32] (unlike Wheeler's method for calculating self-inductance), so Table 4 does not include analytical results.

Table 3: Comparison of self-inductance of the coil at 5 MHz

	Self-Inductance (μH) of Transmitter Coil	Self-Inductance (μH) of Receiver Coil
Analytical (Wheeler Approximation)	5.088	1.097
Measurement	5	1
FDTD Simulation	5.0038	1.01

Table 4: Comparison of quality factor of the coil at 5 MHz

Methods	Transmitter Coil	Receiver Coil
Measurement	150.00	70.00
FDTD Simulation	256.02	157.07

The measured and simulated results in Table 4 are not in good agreement. A likely reason for the discrepancy is that the FDTD simulation does not account for some physical resistances present in the measured circuit, specifically the stray resistance of the VNA cables/clippers. As a sanity check, the same coils are modeled in another electromagnetic solver (CST) and quality factors of 304 and 176 are obtained for the transmitting and receiving coils, respectively. These values are also too high compared with the measurements result. We conclude that the simulations are missing the physical resistances caused by the VNA cables / clippers during the measurement.

To emulate the parasitic resistances of the physical coils, an external resistance of 0.43 ohms and 0.24 ohms are added in series with the transmitter and receiver coils, respectively. These external resistances are obtained by calculating what additional resistances in the FDTD simulation would lead to quality factors that more closely match the measured quality factors of the coils (these values are shown in Table 5). Note that the inaccuracy in the quality factors caused by the missing external resistances in the measurement do not influence the magnetic flux generated by the coil or the effect of the ferrite shields on the inductance and coupling coefficient, which will be studied next.

Table 5: Comparison of the adjusted Q of the coils at 5 MHz

Methods	Transmitter Coil	Receiver Coil
Measurement	150	70
FDTD Simulation	150.57	71.7

IV. EFFECT OF MAGNETIZED FERRITE

Ferrite is an anisotropic, dispersive and gyrotropic magnetic material [33] with a magnetic permeability characterized by (6) [34]:

$$\mu = \mu_o \begin{bmatrix} 1 + \chi_m(\omega) & -jk(\omega) & 0 \\ j\,k\,(\omega) & 1 + \chi_m(\omega) & 0 \\ 0 & 0 & 1 \end{bmatrix}, \qquad (6)$$

where the susceptibilities are given by (7) and (8).

$$\chi_m(\omega) = \frac{(\omega_o + j\omega\alpha)\omega_m}{(\omega_o + j\omega\alpha)^2 - \omega^2}, \qquad (7)$$

$$k(\omega) = \frac{-\omega\omega_m}{(\omega_o + j\omega\alpha)^2 - \omega^2}, \qquad (8)$$

$$\omega_o = \gamma_m H_o, \qquad (9)$$

$$\omega_m = \gamma_m 4\pi M_o. \qquad (10)$$

Note: α, γ_m, H_o and $4\pi M_o$ refer to the damping constant, gyromagnetic ratio, static biasing field and static magnetization, respectively, of a ferrite. Usually, ferrite materials are represented by the empirical formula $XO \cdot Fe_2O_3$ where 'X' can be any divalent metal (such as cobalt, manganese, nickel, zinc) [34].

The FDTD implementation of a magnetized ferrite involves special updates for the tangential magnetic field components (H_x and H_y). The stability of the update equations depends on the damping constant (α). Note that the FDTD calculation of EM propagation in ferrite materials has been successfully validated against exact solutions in the past (e.g., [35], [36]).

The presence of a ferrite alters the intensity of the magnetic field. It acts as a magnetic shield and boosts the inductance of the coil, thereby improving the magnetic flux coupling between the links. Therefore, adding a ferrite shield can help to increase the PTE of a wireless power transfer system. Parameters extracted from a datasheet for the magnetized ferrite used in the following simulations and measurements are shown in Table 6. This data is from the datasheet for the ferrite plate RP series from Laird Smart Technology. The magnetic loss tangent ($\tan\delta$), which is defined as the ratio of imaginary permeability to real permeability, is 0.04 for the ferrite material specified in Table 6.

The simulation case of Section III is now modeled with two ferrite slabs added (behind each coil). The dimensions of the ferrite slabs (length and width) are slightly larger than the dimensions of the coils. The ferrite slab that is used near the transmitter coil is 80 mm × 80 mm × 5 mm, whereas the ferrite slab that

is used near the receiver coil is $40\ mm \times 40$ mm $\times$ 5 mm. The slabs are finely meshed in the lengthwise directions at the spatial resolution used for the coils (0.4 mm). The thickness of the slabs are resolved using 0.8 mm resolution.

Table 6: Datasheet specification of magnetized ferrite (RP Series) as provided by Laird

Property	Value
Real permeability	250
Imaginary permeability	10
Flux density	390 mT
Field strength	1200 A/m
Resistivity	10^7 ohm-cm

Figure 7 shows the magnetic flux when no ferrite shields are used. The magnetic flux extends away from the transmitter coil on both sides. On the other hand, Fig. 8 shows how the magnetic flux is confined to the space between the two coils after the magnetized ferrite shields (represented by the red lines) have been added. Depending upon the application at hand, a ferrite shield may be added next to the transmitter coil (as for a biological telemetry system) or added next to both coils (as for wireless charging of mobile phones). Note that a minimum distance (~ mm) should be maintained between the coil traces and the ferrite to avoid an electrical contact between them [10].
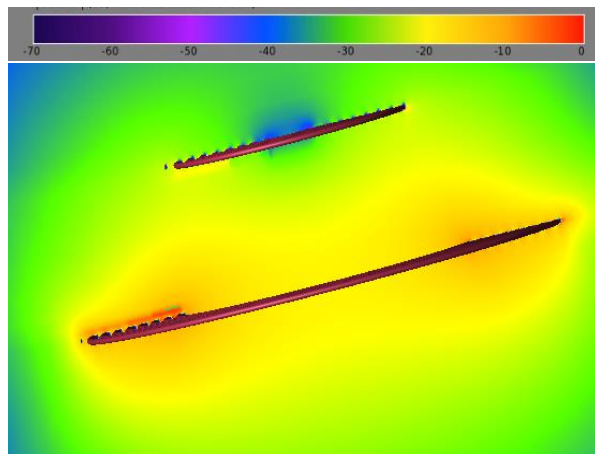
Fig. 7. Magnetic field over a 2-D cross-sectional slice through the center of the coils for the case without the ferrite slabs. The coils (driver and load) are separated by a distance of 20 mm. The colorbar represents the value of the absolute magnetic field using a dB scale.

Comparing Figs. 7 and 8, it is observed that the self-inductance of the coil improves after adding the ferrite slabs as current finds additional dispersive and resistive paths along which to flow. The addition of the ferrite slabs also increases the effective parasitic resistance of the coil. It is difficult to quantify how ferrite, a frequency dependent gyrotropic medium, changes the parasitic components.

Figure 9 compares the FDTD-calculated quality factor of the receiver coil with and without magnetized ferrite. The quality factor is seen to decrease by around 30%. This is due to the parasitic components (especially resistance) changing after the ferrite slabs are added next to the coils.
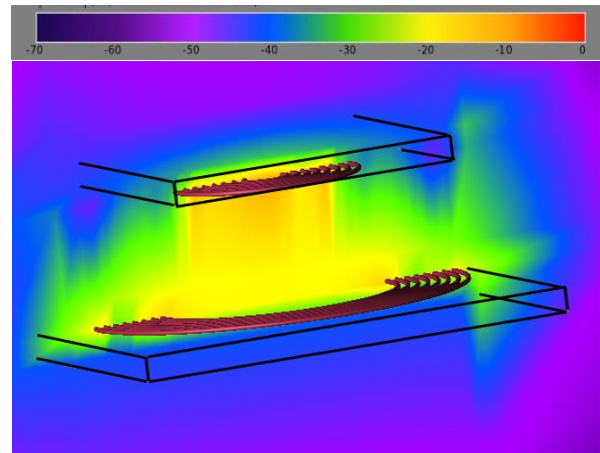
Fig. 8. Magnetic field confined between the coils after adding two ferrite slabs of thickness 5 mm. The black boxes outline the two ferrite slabs. The colorbar represents the value of the absolute magnetic field using a dB scale.
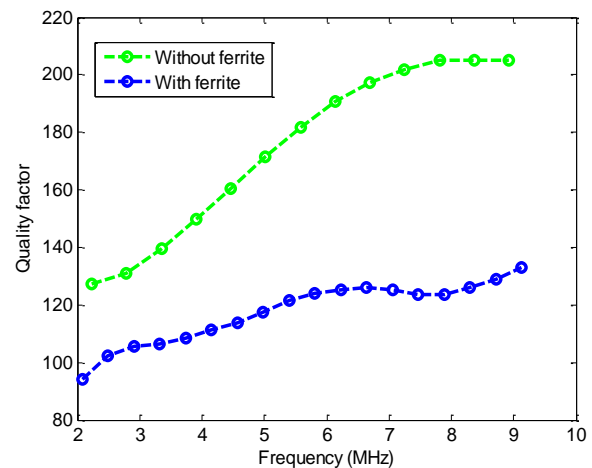
Fig. 9. Comparison of the quality factor of the receiver coil before and after the ferrite slabs are added.

As can be seen in (5), the PTE is directly proportional to $K_{12}^2 Q_1 Q_{2L}$. According to Fig. 10, the K_{12}^2 increases by ~60% when the ferrite slabs are included. This is because the mutual inductance increases when the flux on one side of the coil is shielded.

Figure 11 shows that the mutual inductance almost doubles with the addition of the ferrite shields. At 5 MHz, it increased from $0.275\ uH$ to $0.55\ uH$. Although the quality factor decreases when ferrite is added (as shown in Fig. 9), the PTE improves slightly with the ferrite shields because the K_{12}^2 term (which depends on mutual inductance) changes more dramatically than the quality factor (which depends on self-inductance).

As shown in Fig. 12, the PTE at 5 MHz is improved by ~40% because of the ferrite shields. The improvement would likely be less when a ferrite shield is used only on one side of one coil, rather than on the sides of both coils as shown in Fig. 8.
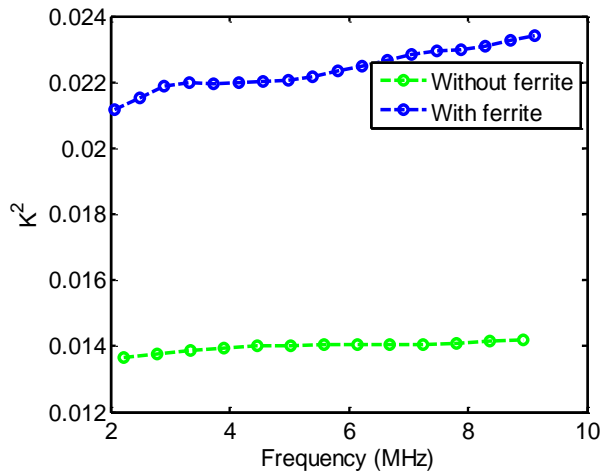
Fig. 10. Comparison of K_{12}^2 for the receiver coil before and after the ferrite slabs are added. The Y-axis is expressed in decimal (not in percentage).
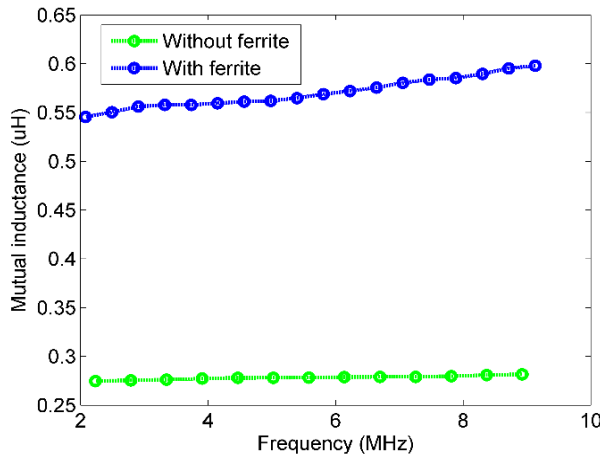
Fig. 11. Comparison of the mutual inductance before and after the ferrite slabs are added.
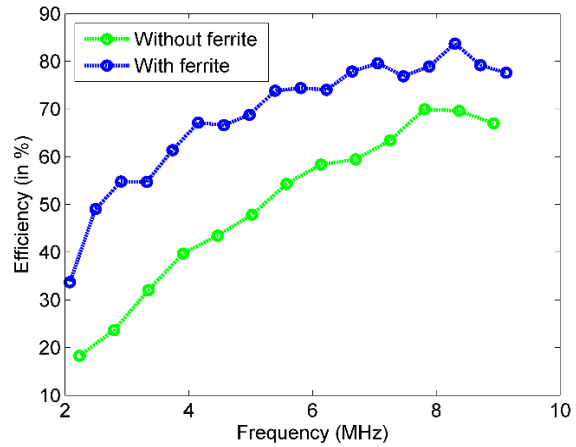
Fig. 12. Comparison of the PTE before and after the ferrite slabs are added.

V. TECHNIQUES FOR IMPROVING PTE

The parasitic components (especially resistance) are the major impediment to achieving a high PTE. The AC parasitic resistance in the coil is caused primarily by eddy current loss and proximity effect. The former effect is caused by changing magnetic field in the conductor, and the latter effect is the phenomena of current crowding in the conductor when AC current is passed through the coils with multiple nearby conductors. These effects may be minimized by using Litz wire. Litz wire has many insulated thin strands, which can considerably reduce the skin effect and proximity effect. However, modeling many thin strands of Litz wire in place of one thicker copper wire would greatly increase the computational requirements (memory and simulation time).

Additionally, the magnetic field enhancement is dependent on the dimensions of the ferrite slab and its placement. The larger the piece of ferrite, the more the flux is shielded. However, using a larger piece of ferrite takes up more space and this can be a concern for industrial applications. Then, an optimal distance between the coil and ferrite slab must be determined for real applications. Ideally, there would be no separation between the coils and ferrite slabs, but this is infeasible because any electrical contact between them should be avoided [10].

Finally, multiple coils (instead of just two coils) may be used to further boost the flux coupling [7], [37]. Instead of direct coupling between a driver and load, the driver can couple the flux to a transmitter, the transmitter to a receiver, and then finally the receiver to a load. The transmitter and receiver should resonate at the same frequency for maximum flux coupling.

VI. CONCLUSION

Wireless power transfer was modeled using the FDTD method. First, two spiral inductive coils were modeled with open boundaries. The simulated values were validated against measurement results. Then the effect of adding magnetized ferrite slabs was studied. It was found that the quality factor of the coils slightly decreased with the addition of the ferrite slabs. However, there was an appreciable boost in mutual inductance and flux coupling between the coils after the ferrite slabs were added. As a result, the PTE improved by ~40%. For the coil dimensions given in Table 1, a maximum PTE of 85% was achieved for a two coil system separated by 20 mm.

A two-coil design is efficient for wireless power transmission for biological implants. A three-coil system [7] or multiple coils may be used to further enhance the efficiency of the coil system. There are additional constraints for biomedical applications such as electromagnetic safety standards, biocompatible, longevity requirements [38], [39] etc.

FDTD is an effective method for modeling coil geometries and magnetized ferrite slabs. Due to the required small spatial resolution of the grid to resolve the coil geometry and spacing, and because of the ferrite specifications, the numerical time step may be very small in order to maintain stability. However, the computation may be distributed onto a supercomputing cluster in a straight-forward manner and use parallel I/O such as hierarchical data format (HDF) [40] for efficient processing.

APPENDIX

The PML parameters that are used in the simulations are listed below. Note that the parameters are scaled tensor parameters, and they carry the same meaning as used in [29]. The x, y and z subscripts refer to the spatial coordinate axes:

$$a_x^{max} = 0, a_y^{max} = 0, a_z^{max} = 0,$$
$$\kappa_x^{max} = 1, \kappa_y^{max} = 1, \kappa_z^{max} = 1,$$
$$m = 4, ma = 2.$$

These PML parameters are equivalent to UPML. The XFdtd software uses UPML parameters by default.

ACKNOWLEDGEMENT

REFERENCES

[1] K. Wu, D. Choudhury, and H. Matsumoto, "Wireless power transmission, technology, and applications," *Proc. IEEE*, vol. 101, no. 6, pp. 1271-1275, 2013.

[2] R. Bashirullah, "Wireless implants," *IEEE Microw. Mag.*, vol. 11, no. 7, pp. S14-S23, 2010.

[3] K. Finkenzeller, *RFID Handbook: Fundamentals and Applications in Contactless Smart Cards, Radio Frequency Identification and Near-Field Communication*. John Wiley & Sons, 2010.

[4] F. Musavi and W. Eberle, "Overview of wireless power transfer technologies for electric vehicle battery charging," *IET Power Electron.*, vol. 7, no. 1, pp. 60-66, 2014.

[5] O. P. Gandhi, "Electromagnetic fields: Human safety issues," *Annu. Rev. Biomed. Eng.*, vol. 4, no. 1, pp. 211-234, 2002.

[6] G. Kiruthiga, M. Y. Jayant, and A. Sharmila, "Wireless charging for low power applications using Qi standard," in *Communication and Signal Processing (ICCSP), 2016 International Conference on*, pp. 1180-1184, 2016.

[7] A. K. RamRakhyani and G. Lazzi, "On the design of efficient multi-coil telemetry system for biomedical implants," *IEEE Trans. Biomed. Circuits Syst.*, vol. 7, no. 1, pp. 11-23, 2013.

[8] S. Y. R. Hui, W. Zhong, and C. K. Lee, "A critical review of recent progress in mid-range wireless power transfer," *IEEE Trans. Power Electron.*, vol. 29, no. 9, pp. 4500-4511, 2014.

[9] J. D. Joannopoulos, A. Karalis, and M. Soljacic, "Wireless non-radiative energy transfer," June 2010.

[10] G. Vigneau, M. Cheikh, R. Benbouhout, and A. Takacs, "Design and modeling of PCB coils for inductive power charging," *Wirel. Power Transf.*, vol. 2, no. 2, pp. 143-152, 2015.

[11] A. Kurs, A. Karalis, R. Moffatt, J. D. Joannopoulos, P. Fisher, and M. Soljačić, "Wireless power transfer via strongly coupled magnetic resonances," *Science*, vol. 317, no. 5834, pp. 83-86, 2007.

[12] J. Chen and H. Tan, "Metamaterial for wireless power transfer system at 13.56 MHz with coil misalignment," in *Microwave, Antenna, Propagation, and EMC Technologies (MAPE), 2017 7th IEEE International Symposium on*, pp. 313-317, 2017.

[13] A. C. Polycarpou, "Introduction to the finite element method in electromagnetics," *Synth. Lect. Comput. Electromagn.*, vol. 1, no. 1, pp. 1-126, 2005.

[14] Q. Yu and T. W. Holmes, "A study on stray capacitance modeling of inductors by using the finite element method," *IEEE Trans. Electromagn. Compat.*, vol. 43, no. 1, pp. 88-93, 2001.

[15] M. Studio, "Cst-computer simulation technology," *Bad. Nuheimer. Str.*, vol. 19, p. 64289, 2008.

[16] D. M. Sullivan and J. Nadobny, "FDTD simulation of RF coils for MRI," in *Antennas and Propagation Society International Symposium, 2009, APSURSI'09,*

IEEE, 2009, pp. 1-4.

[17] S. Schmidt and G. Lazzi, "Use of the FDTD thin-strut formalism for biomedical telemetry coil designs," *IEEE Trans. Microw. Theory Tech.*, vol. 52, no. 8, pp. 1952-1956, 2004.

[18] X. Xin, D. Wang, J. Han, Y. Feng, Q. Feng, and W. Chen, "Numerical optimization of intra-operative RF coil for open vertical-field MRgFUS using hybrid MoM/FDTD method," in *Biomedical Imaging: From Nano to Macro, 2011 IEEE International Symposium on*, 2011, pp. 750-753.

[19] M. Gupta and P. Agarwal, "To model magnetic field of RF planar coil for portable NMR applications," in *Inventive Computing and Informatics (ICICI), International Conference on*, 2017, pp. 490-494.

[20] M. Zang, M. Clemens, C. Cimala, J. Streckert, and B. Schmuelling, "Simulation of inductive power transfer systems exposing a human body with two-step scaled-frequency FDTD methods," *IEEE Trans. Magn.*, vol. 53, no. 6, pp. 1-4, June 2017.

[21] X. Shi, C. Qi, M. Qu, S. Ye, and G. Wang, "Effects of coil locations on wireless power transfer via magnetic resonance coupling," *Appl. Comput. Electromagn. Soc. J.*, vol. 31, no. 3, pp. 270-278, 2016.

[22] S. Pokhrel, V. Shankar, and J. J. Simpson, "3-D FDTD modeling of electromagnetic wave propagation in magnetized plasma requiring singular updates to the current density equation," *IEEE Trans. Antennas Propag.*, vol. 66, no. 9, pp. 4772-4781, 2018.

[23] R. XFDTD, *Electromagnetic Solver Based on the Finite Difference Time Domain Method*. Remcom Inc., 2005.

[24] J.-P. Bérenger, "Perfectly matched layer (PML) for computational electromagnetics," *Synth. Lect. Comput. Electromagn.*, vol. 2, no. 1, pp. 1-117, 2007.

[25] G. Waldschmidt and A. Taflove, "Three-dimensional CAD-based mesh generator for the Dey-Mittra conformal FDTD algorithm," *IEEE Trans. Antennas Propag.*, vol. 52, no. 7, pp. 1658-1664, 2004.

[26] R. M. Makinen, J. S. Juntunen, and M. A. Kivikoski, "An improved thin-wire model for FDTD," *IEEE Trans. Microw. Theory Tech.*, vol. 50, no. 5, pp. 1245-1255, 2002.

[27] M. Douglas, M. Okoniewski, and M. A. Stuchly, "Accurate modeling of thin wires in the FDTD method," in *IEEE Antennas and Propagation Society International Symposium. 1998 Digest. Antennas: Gateways to the Global Network. Held in conjunction with: USNC/URSI National Radio Science Meeting (Cat. No. 98CH36)*, 1998, vol. 2,

pp. 1246-1249.

[28] J. A. Roden and S. D. Gedney, "Convolution PML (CPML): An efficient FDTD implementation of the CFS–PML for arbitrary media," *Microw. Opt. Technol. Lett.*, vol. 27, no. 5, pp. 334-339, 2000.

[29] A. Taflove, S. C. Hagness, and M. Piket-May, "Computational electromagnetics: The finite-difference time-domain method," in *The Electrical Engineering Handbook*, Elsevier Inc., 2005.

[30] S. S. Mohan, M. del Mar Hershenson, S. P. Boyd, and T. H. Lee, "Simple accurate expressions for planar spiral inductances," *IEEE J. Solid-State Circuits*, vol. 34, no. 10, pp. 1419-1424, 1999.

[31] M. Machnoor, E. S. G. Rodríguez, P. Kosta, J. Stang, and G. Lazzi, "Analysis and design of a 3-coil wireless power transmission system for biomedical applications," *IEEE Trans. Antennas Propag.*, 2018.

[32] C. Peters and Y. Manoli, "Inductance calculation of planar multi-layer and multi-wire coils: An analytical approach," *Sens. Actuators Phys.*, vol. 145, pp. 394-404, 2008.

[33] B. Lax and K. J. Button, "Microwave ferrites and ferrimagnetics," 1962.

[34] K. S. Kunz and R. J. Luebbers, *The Finite Difference Time Domain Method for Electromagnetics*, CRC press, 1993.

[35] F. Hunsberger, R. Luebbers, and K. Kunz, "Finite-difference time-domain analysis of gyrotropic media. I. Magnetized plasma," *IEEE Trans. Antennas Propag.*, vol. 40, no. 12, pp. 1489-1495, 1992.

[36] F. P. Hunsberger, Jr., "Extension of the finite-difference time-domain method to gyrotropic media," 1991.

[37] J. Zhang, X. Yuan, C. Wang, and Y. He, "Comparative analysis of two-coil and three-coil structures for wireless power transfer," *IEEE Trans. Power Electron.*, vol. 32, no. 1, pp. 341-352, 2017.

[38] IEEE Standards Coordinating Committee 28, *IEEE Standard for Safety Levels with Respect to Human Exposure to Radio Frequency Electromagnetic Fields, 3kHz to 300 GHz*, Institute of Electrical and Electonics Engineers, Incorporated, 1992.

[39] P. Kosta, *et al.*, "Electromagnetic safety assessment of a cortical implant for vision restoration," *IEEE J. Electromagn. RF Microw. Med. Biol.*, vol. 2, no. 1, pp. 56-63, 2018.

[40] S. Pokhrel, M. Rodriquez, A. Samimi, G. Heber, and J. Simpson, "Parallel I/O for 3-D global FDTD earth-ionosphere waveguide models at resolutions on the order of~ 1 km and higher using HDF5," *IEEE Trans. Antennas Propag.*, 2018.

Application of Barycentric Subdivision Method for Singularity Integration in Method of Moments

Chunwang Xiang [1], Xunwang Dang [2], Maokun Li [1*], Fan Yang [1], and Shenheng Xu [1]

[1] Department of Electronic Engineering
Tsinghua University, Beijing 100084, China
State Key Laboratory on Microwave and Digital Communications
Beijing National Research Center for Information Science and Technology (BNRist)
maokunli@tsinghua.edu.cn

[2] Science and Technology on Electromagnetic
Scattering Laboratory, Beijing 100854, China

Abstract ─ Method of moments (MoM) is an essential tool to model electromagnetic wave interactions with three-dimensional targets. Numerical integration is a key technique in MoM. Due to the singular nature of Green's function, MoM requires special treatment in the calculation of singular integration, which is usually time-consuming. In this study, the barycentric subdivision method is investigated to compute numerical integration in three-dimensional surface integral equations. This method allows a uniform treatment for both singular and non-singular integrals. Numerical examples show that this method could reach the same level of accuracy as the singularity extraction method for RWG basis functions, and the computational time of setting up the matrix can be reduced by half.

Index Terms ─ Barycentric subdivision method, method of moments (MoM), Rao-Wilton-Glisson (RWG) basis, singular integration, singularity extraction method.

I. INTRODUCTION

Rao-Wilton-Glisson (RWG) basis [1] has been widely used in Method of Moments (MoM) for modeling electromagnetic wave interactions with 3D targets. While setting up the matrix equation of MoM, we usually use numerical integration to evaluate the source integrals and field integrals, both of which contain the Green's function. Because of the singular nature of the Green's function, the integrals need to be treated carefully when the domain of the source integral overlaps with the one of the field integrals. The commonly used techniques include singularity extraction [1, 2], Duffy coordinate transformation [3-5], polar co-ordinate transformation, and etc.

The singularity extraction method was proposed by Wilton et al. [1]. This method evaluates the non-singular part of the integral by numerical quadrature and the singular part by analytical formula [2]. Khayat and Wilton proposed a simple and efficient numerical procedure, which uses singularity cancellation scheme [6]. Khayat et al. further optimized this method for the integration scheme [7]. Vipiana and Wilton presented a purely numerical procedure to evaluate strongly near-singular integrals in the gradient of Helmholtz-type potentials for observation points at small distances from the source domain [8]. Popovic [9], Geng and Tong [10, 11] also applied potential integral method to computing singular integrals based on bilinear surface modeling. Wang, Nie et al., used the singularity transferring method to calculate the integral with 1/R singularity in its integrand and remove the small area, which makes zero contribution to the numerical integration [12]. Hua and Xu reduced the order of singularity and avoided the coincidences between the source and field points [13]. Wu et al. extracted the strong singularity of Magnetic Field Integral Equation (MFIE) and used the integral domain transform to eliminate the residual mild singularity [14]. Vipiana and Wilton presented a simple and efficient numerical procedure for evaluating singular and near-singular source vector potential integrals involving junction basis functions based on a double transformation, which could cancel singularities [22]. Jarvenpaa presented recursive formulas by which they can extract any number of terms from the singular kernel and generalize the singularity extraction technique for surface and volume integral equation with high-order basis functions [23]. These methods can compute the singular integral with good accuracy. However, we have to carefully separate the singular and non-singular integral so that they can be treated differently. Also, compared with non-singular integrals, the singular integrals are more expensive to compute. It can become

a bottleneck in computing time for method of moments.

The Duffy coordinate transform method was proposed by M. G. Duffy [3]. This is a simple transformation that facilitates the evaluation of integrals with singular integrands at a vertex. Zhao, Nie et al. used domain decomposition and Duffy coordinate transformation to remove the singularity in the integrand [4]. Botha presented a new family of systematically constructed near-singularity cancellation transformations, which yields quadrature rules for integrating near-singular kernels over triangular surfaces based on Duffy transformation [5]. Zhang and Sun constructed a general variable transformation based on the idea of diminishing the difference of the orders of magnitude, which can remove the near singularity efficiently by eliminating the rapid variations of the integrand in nearly singular integrals and improve the accuracy of numerical results [23]. Duffy transformation eliminates the singularity in the integral through coordinate transformation and evaluates the integral numerically. But the non-singular and singular integrations are still treated separately. Besides, the errors of the numerical quadrature would increase for triangles with small aspect ratios. Because Duffy transformation requires coordinate transform and computation of quadrature points, fast evaluation of the singular integrals is still a challenge.

In this work, we studied the barycentric subdivision method, which is also known as the nine-point numerical integration, for computing integrals in MoM. It was originally applied to image rendering in computer science [15]. Makarov introduced the method into RWG-MoM [16], and he stated in his works that this technique was not very accurate. Hence, this method has not been widely used. Xiang et al. also studied this method in 2017 [21]. In this method, the singular integrals are evaluated in the same fashion as the non-singular ones, which allows a uniform treatment of the numerical integrals. Therefore, the time of setting up the MoM matrix equation can be reduced. Numerical examples showed that the accuracy is still in remained in the results.

Compared with [16], more details of the barycentric method are studied in this paper, especially its numerical accuracy, which is compared with one of the singularity extraction schemes. The accuracy is important in the application of the scheme for solving electromagnetic problems. Based on both derivation and numerical examples, we found that the accuracy of this scheme is comparable to the singularity extraction scheme. A more detailed convergence analysis of the numerical accuracy of this scheme is presented. It is proved that the integral will converge when the triangle gets smaller, similar as other integration schemes. This scheme is only applied to EIFE in [16], we also investigated its applicability for MFIE, PMCHWT and FEM-BI formulations. It seems to work as well.

This paper is organized as follows: Section II describes the formulation. In Section III, numerical examples are given to show the efficiency and accuracy of this method. In Section IV, a convergence analysis is carried out. Section V summarizes this work.

II. FORMULATION

A. Electric field integral equation (EFIE) for PEC targets

The electric field on the surface of a perfect electric conductor (PEC) target satisfies the following integral equation [17, 18]:

$$\hat{n} \times \bar{\bar{L}}(\bar{J}) = \hat{n} \times E^{inc}(r), r \in S_0, \tag{1}$$

where,

$$\bar{\bar{L}}(\bar{J}) = jk_0 \oiint_{s_0} \bar{J}(r')G(r,r')dS' + \frac{j}{k_0}\iint_{s_0}\nabla'\cdot\bar{J}(r')\nabla G(r,r')dS', \tag{2}$$

where $G(\mathbf{r},\mathbf{r'})$ denotes the Green's function in free space, $\bar{J}$ denotes the scaled electric current density on the surface of the target. Discretizing $\bar{J}$ by RWG basis and applying the Galerkin's method, we can setup a matrix of MoM with elements as [18]:

$$Z_{mn} = jk_0 \oiint_{s_0} f_m(r)\cdot\left[\oiint_{s_0} f_n(r')G(r,r')dS'\right]dS$$

$$-\frac{j}{k_0}\oiint_{s_0}\nabla\cdot f_m(r)\left[\oiint_{s_0}\nabla'\cdot f_n(r')G(r,r')dS'\right]dS, \tag{3}$$

where Z_{mn} represents the electric field generated by the n-th basis function and tested by the m-th basis function. $f_m(\mathbf{r})$ and $f_n(\mathbf{r})$ represent the RWG basis functions, which can be written as,

$$f_m(r) = \begin{cases} \dfrac{l_n}{2A_m^+}\rho_m^+(r), r \text{ in } T_m^+ \\ \dfrac{l_n}{2A_m^-}\rho_m^-(r), r \text{ in } T_m^-, \\ \\ 0, \quad otherwise \end{cases} \tag{4}$$

where $T_m^\pm$ denote the two triangles associated with the m-th edge, $A_m^\pm$ are the areas of triangles $T_m^\pm$, and $\rho_m^\pm$ are the vectors defined in Fig. 1, other symbols are the same as those in [1].

The integral in (3) then becomes,

$$Z_{mn} = jk_0\frac{l_m}{2A_m^+}\iint_{T_m^+}(r-r_i)\cdot\tilde{A}[r,f_n(r')]dS$$

$$+jk_0\frac{l_m}{2A_m^-}\iint_{T_m^-}(r_j-r)\cdot\tilde{A}[r,f_n(r')]dS$$

$$-\frac{jl_m}{k_0A_m^+}\iint_{T_m^+}\tilde{\Phi}[r,f_n(r')]dS + \frac{jl_m}{k_0A_m^-}\iint_{T_m^-}\tilde{\Phi}[r,f_n(r')]dS. \tag{5}$$

In this method, we can use one-point quadrature for the field integral. The barycenter of the m-th triangle elements is chosen as the testing point. The matrix element Z_{mn} can then be written as:

$$Z_{mn} = jk_0 \frac{l_m}{2}(r_m^{c+} - r_i) \cdot \tilde{A}[r_m^{c+}, f_n(r')]$$

$$+ jk_0 \frac{l_m}{2}(r_j - r_m^{c-}) \cdot \tilde{A}[r_m^{c-}, f_n(r')]$$

$$- \frac{jl_m}{k_0} \tilde{\Phi}\left[r_m^{c+}, f_n(r')\right] + \frac{jl_m}{k_0} \tilde{\Phi}\left[r_m^{c-}, f_n(r')\right]. \qquad (6)$$
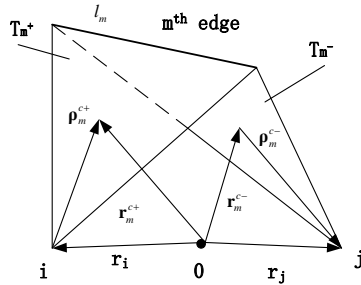
Fig. 1. RWG basis function defined on the *m-th* edge.

Here $\mathbf{r}_m^{c\pm}$ is the barycenter of triangle in the *m-th* basis function, $\tilde{A}$ and $\tilde{\Phi}$ represent the source integrals, which can be written as:

$$\tilde{A}[r, f_n(r')] = \frac{1}{4\pi} \frac{l_n}{2A_n^+} \iint_{T_n^+} (r' - r_i) \frac{e^{-jk_0 R}}{R} dS'$$

$$+ \frac{1}{4\pi} \frac{l_n}{2A_n^-} \iint_{T_n^-} (r_j' - r') \frac{e^{-jk_0 R}}{R} dS', \qquad (7)$$

$$\tilde{\Phi}[r, f_n(r')] = \frac{1}{4\pi} \frac{l_n}{A_n^+} \iint_{T_n^+} \frac{e^{-jk_0 R}}{R} dS' - \frac{1}{4\pi} \frac{l_n}{A_n^-} \iint_{T_n^-} \frac{e^{-jk_0 R}}{R} dS', (8)$$

where $R = |\mathbf{r} - \mathbf{r}'|$. The source integration in the *n-th* patch can be calculated by the barycentric subdivision method.

B. Magnetic field integral equation (MFIE) for PEC targets

The magnetic field on the surface of a perfect electric conductor (PEC) target satisfies the following integral equation [17, 18]:

$$\frac{1}{2}\bar{J} + \hat{n} \times \bar{\bar{K}}(\bar{J}) = \hat{n} \times H^{inc}(r), r \in S_0, \qquad (9)$$

where $\bar{\bar{K}}(\bar{J}) = \oiint_{S_0} \bar{J}(\mathbf{r}') \times \nabla G(\mathbf{r}, \mathbf{r}') dS'$. Using the same method as EFIE, we can get the impedance matrix elements for MFIE as:

$$Z_{mn} = \frac{1}{2}\oiint_{S_0} f_m(r) \cdot f_n(r') dS$$

$$+ \oiint_{S_0} f_m(r) \cdot \left[\hat{n} \times \oiint_{S_0} f_n(r') \times \nabla G(r,r') dS'\right] dS, \qquad (10)$$

here, $\nabla G(\mathbf{r}, \mathbf{r}') = (-jk_0 - \frac{1}{R}) \frac{e^{-jk_0 R}}{4\pi R^2} \mathbf{R}$.

Now the source integral for the singular point is extracted for separate analysis. We defined the $\mathbf{H}_i(r)$ as:

$$H_i(r) = \oiint_{S_0} f_n(r') \times \nabla G(r,r') dS'$$

$$= -\frac{1}{2A_n} \oiint_{S_0} (-jk_0 - \frac{1}{R}) \frac{e^{-jk_0 R}}{4\pi R^2} R \times \rho_i' dS'. \qquad (11)$$
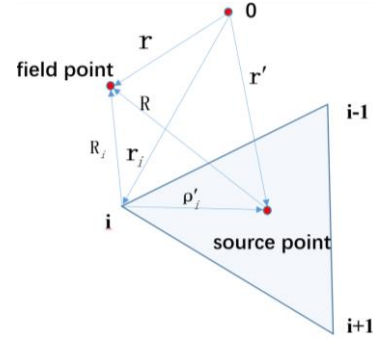
Fig. 2. The related vector and scalar location relationship between the field point and the source point coordination.

Figure 2 depicts the geometric relationship between the vector and the scalar, which are involved in the formula; substituting $\mathbf{R} = \mathbf{R}_i - \boldsymbol{\rho}_i'$ into (12), which will take the cross product out of the integral. Equation (12) can be written as:

$$H_i(r) = \frac{1}{2A_n} R_i \times \oiint_{s_0} (jk_0 + \frac{1}{R}) \frac{e^{-jk_0 R}}{4\pi R^2} \rho_i' dS'. \qquad (12)$$

The integral of impedance matrix element, which is related to the *m-th* and *n-th* edges, can be written as:

$$Z_{mn} = I_0(m^+, n) + I_0(m^-, n)$$

$$+ \frac{l_m}{2A_m^+} \iint_{T_m^+} (r - r_i) \cdot \tilde{V}[r, f_n(r')] dS$$

$$+ \frac{l_m}{2A_m^-} \iint_{T_m^-} (r_j - r) \cdot \tilde{V}[r, f_n(r')] dS, \qquad (13)$$

where,

$$I_0(m^+, n) = \begin{cases} \frac{l_m l_n}{8A_n^+}(r_m^{c+} - r_i) \cdot (r_n^{c+} - r_i'), r_m^{c+} \in T_n^+ \\ \frac{l_m l_n}{8A_n^-}(r_m^{c+} - r_i) \cdot (r_j' - r_n^{c-}), r_m^{c+} \in T_n^- \\ 0, \qquad\qquad otherwise \end{cases} \quad (14)$$

$$I_0(m^-, n) = \begin{cases} \frac{l_m l_n}{8A_n^+}(r_j - r_m^{c-}) \cdot (r_n^{c+} - r_i'), r_m^{c-} \in T_n^+ \\ \frac{l_m l_n}{8A_n^-}(r_j - r_m^{c-}) \cdot (r_j' - r_n^{c-}), r_m^{c-} \in T_n^- \\ 0, \qquad\qquad otherwise \end{cases} \quad (15)$$

$$\tilde{V}[r, f_n(r')] = \frac{l_n}{2A_n^+} \hat{n}_m \times (r - r_i') \times \iint_{T_n^+} (r' - r_i')(jk_0 + \frac{1}{R}) \frac{e^{-jkR}}{4\pi R^2} dS'$$

$$+ \frac{l_n}{2A_n^-} \hat{n}_m \times (r - r_j') \times \iint_{T_n^-} (r_j' - r')(jk_0 + \frac{1}{R}) \frac{e^{-jkR}}{4\pi R^2} dS', (16)$$

here, $\hat{n}_m$ is the outer normal on the patch of the *m-th* edge.

After using the one-point quadrature for the field integral about *r*, the matrix element $\mathbf{Z}_{mn}$ can be written as:

$$Z_{mn} = I_0(m^+, n) + I_0(m^-, n)$$

$$+ \frac{l_m l_n}{16\pi A_n^+}(r_m^{c+} - r_i) \cdot \hat{n}_m \times (r_m^{c+} - r_i') \times \iint_{T_n^+}(r' - r_i')\tilde{G}(R)dS'$$

$$+ \frac{l_m l_n}{16\pi A_n^+}(r_m^{c+} - r_i) \cdot \hat{n}_m \times (r_m^{c+} - r_j') \times \iint_{T_n^-}(r_j' - r')\tilde{G}(R)dS'$$

$$+ \frac{l_m l_n}{16\pi A_n^-}(r_j - r_m^{c-}) \cdot \hat{n}_m \times (r_m^{c-} - r_i') \times \iint_{T_n^+}(r' - r_i')\tilde{G}(R)dS'$$

$$+ \frac{l_m l_n}{16\pi A_n^-}(r_j - r_m^{c-}) \cdot \hat{n}_m \times (r_m^{c-} - r_j') \times \iint_{T_n^-}(r_j' - r')\tilde{G}(R)dS', \quad (17)$$

where, $\tilde{G}(R) = (jk_0 + \frac{1}{R})\frac{e^{-jk_0R}}{R^2}$.

The remaining source integrals about r' in the above equations can be calculated with the following nine-point integration method.

C. Barycentric subdivision method for numerical integration

We can apply the barycentric subdivision method (the nine-point quadrature) to the source integral in (6) and (17). Each edge of a triangle is equally partitioned into three parts to construct small triangles as shown in Fig. 3, and the small circle "○" in the figure represents the barycenter of the triangle element.
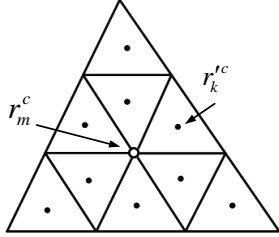
Fig. 3. Nine-point subdivision of a triangle element, where the small circle "○" denotes the barycenter of the triangle element, "." denotes the barycenter of the sub-triangle elements.

Each triangle is divided into nine equal-sized sub-triangles as shown in Fig. 3. The source integral of the patch can then be approximated by the nine sub-triangles with the same weights. Since these nine triangles have the same area, the integral can be written as:

$$\iint_{T_n} G(r, r')dS' = \frac{A_n}{9}\sum_{k=1}^{9} G(r, r_k'^c). \quad (18)$$

By using similar process, the integral in MFIE can be written as:

$$\iint_{T_n}(r' - r_i)\tilde{G}(r, r')dS' = \frac{A_n}{9}\sum_{k=1}^{9}(r_k'^c - r_i)\tilde{G}(r, r_k'^c), \quad (19)$$

where $\mathbf{r}_k'^c$ denotes the quadrature points shown as Fig. 3. The quadrature point of the field integral resides on the barycenter of the patch (triangle), so the quadrature point of the field integral will not coincide with the one of the source integral. Therefore, the value of the integrand will not become singular.

III. NUMERICAL EXAMPLES

A. Computation of radar cross section (RCS)

Case 1: We consider the plane wave scattering of a PEC sphere with radius of $1m$. We use the Mie series result as benchmark. The incident plane wave has frequency of 300 MHz, $\varphi^{inc} = 0°$, $\theta^{inc} = 90°$, and vertical polarization. The surface current is computed using the nine-point numerical integration method. The bistatic RCS with VV polarization (vertical polarization excitation and vertical polarization reception) is computed with EFIE and MFIE respectively when the observation angle at $\varphi = 0°$ and $\theta \in [0°, 180°]$. In the computation, the current on the sphere is partitioned into 4527 unknowns.

(a)   (b)
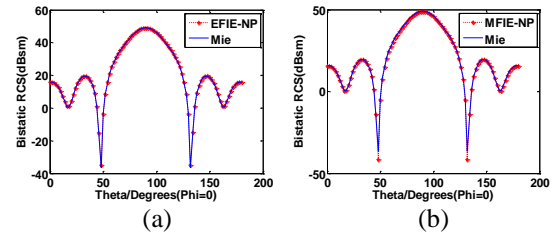
Fig. 4. The calculation on bistatic RCS: (a) Bistatic RCS for PEC sphere solved by EFIE, and (b) bistatic RCS for PEC sphere solved by MFIE.

From Fig. 4 (a) and Fig. 4 (b), we can see that the numerical results have a good agreement with the Mie series results [17, 18, 20]. We can also see that the proposed method works not only for the EFIE equation but also for the MFIE equation.

Case 2: In order to further validate the efficiency of this method to other integral equation and structures, a dielectric sphere and a dielectric cube are computed with PMCHWT and FEM-BI equation, respectively.

(a)   (b)
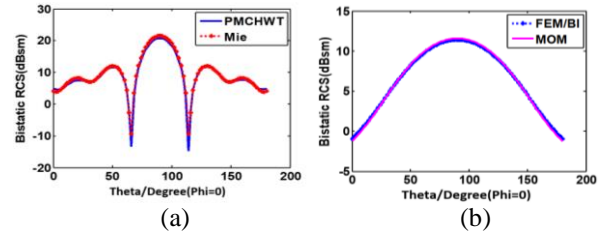
Fig. 5. Bistatic RCS: (a) Dielectric sphere solved by PMCHWT, and (b) dielectric cube solved by FEM-BI.

The dielectric sphere has $\varepsilon_r = 2.5$, radius $= 1m$, the number of unknowns after discretization is 6875. The dielectric cube has $\varepsilon_r = 2.5$, side length $= 1m$, the number of unknowns is 4440. The incident plane wave has the

same parameters as Case 1.

From Fig. 5 (a) and Fig. 5 (b), we can see that the numerical results agree well with the Mie series results.

From the above two examples, we can see that this method can be applied to various integration equation and complex structures.

B. Matrix setup time

Using the parameters of Case 1, a comparison of matrix setup time between the nine-point numerical integration and the singularity extraction method is shown in Table 1.

Table 1: Comparison of matrix setup time

Unknowns	Matrix Setup Time (seconds)	
	Nine-Point Numerical Integration	*Singularity Extraction*
1197	10s	17s
4527	2m 20s	4m 26s
6993	5m 45s	10m 34s
18297	46m 30s	88m 12s
50886	367m 20s	700m 40s

In Table 1, the previous four models are computed on a PC with Intel(R) Core(M) i5-4690K, CPU@3.5GHz/64, RAM 32G, and the last example is a server with Intel(R) Xeon(R) E7-8857v2@3.0GHz, 4 cores, RAM 1.5T.

From Table 1, we can see that the barycentric subdivision method can save nearly half of the setup time compared with the singularity extraction method.

IV. CONVERGENCE ANALYSIS

A. Theory on the barycentric subdivision method

In this section, we will study the convergence of numerical integration using the barycentric subdivision method.
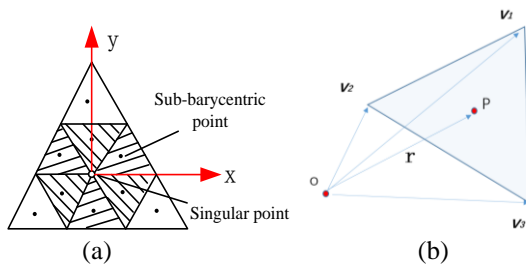
Fig. 6. Six sub-triangles around the singular point in a triangle element and vector in a sub-triangle: (a) The six small sub-triangles (the shaded area) around the singular point (barycenter of triangle), and (b) the vector for three vertices and quadrature point in a sub-triangle.

The source integral becomes singular when its integration domain overlaps with the field integral. In this case, the source integrals over 6 small triangles around the barycenter "∘" in Fig. 6 (a) will have singularity at one of their corners, i.e., the barycenter "∘" of the triangle.

We can analyze these singular integrals based on the Duffy transform. It transforms from the original barycenter coordinate system (ξ_1, ξ_2, ξ_3) to a new coordinate (u, v), as shown Fig. 6 (b) below (Here $\mathbf{v}_1$ is the vector of the singular point "∘" when the field point O is overlapped with $\mathbf{v}_1$):

$$r = \xi_1 v_1 + \xi_2 v_2 + \xi_3 v_3$$
$$= u v_1 + v(1-u)v_2 + (1-v)(1-u)v_3, \qquad (20)$$

here $\mathbf{v}_1$ is the vector of the singular point, $\xi_3 = 1 - \xi_1 - \xi_2$, then the singular integral for one sub-triangle can be transformed into:

$$I = \int_S \frac{e^{-jk_0 R}}{R} dS = A\int_S \frac{e^{-jk_0|r-v_1|}}{|r-v_1|} d\xi_1 d\xi_2$$

$$= A\int_0^1 \int_0^1 \frac{e^{-jk_0(1-u)|vv_2+(1-v)v_3-v_1|}}{|vv_2+(1-v)v_3-v_1|} dvdu, \qquad (21)$$

where A denotes the area of one sub-triangle S. The integral on S is then converted to a 2-fold integral of u and v, respectively. Now we can define the function $a(v)$:

$$a(v) = k_0 |vv_2 + (1-v)v_3 - v_1|$$
$$= k_0 |v(v_2 - v_3) + (v_3 - v_1)|. \qquad (22)$$

From (22), we can see $a(v)$ is linear with the size of triangle, As the mesh of the target becomes denser, $a(v)$ will be smaller, so the analytical expression I_D of integral I for v is:

$$I_D = A\int_0^1 \frac{dv}{a(v)} \frac{1-e^{-ja(v)}}{ja(v)} \approx Ak_0 \int_0^1 \frac{dv}{a(v)}(1+o(a)) = Ak_0 / a(\zeta), (23)$$

where $a(\zeta)$ is derived from the mean value theorem for definite integrals [19].

Since the Duffy transformation can eliminate the singularity when the field point overlaps with the singular point as shown in Fig. 6 (a), we can try to eliminate the singularity when the field point at the sub-barycentric point, and further compare these two integral value. The quadrature for the above integral on each sub-triangle samples the domain of integration at $(\xi_1, \xi_2) = (1/3, 1/3)$, namely $(u,v) = (1/3, 1/2)$ in the new coordinate, substituting the $u = 1/3$, $v = 1/2$ into (21), the numerical integration on the sub-barycentric point is:

$$I_c \approx Ak_0 / a(1/2). \qquad (24)$$

The numerical difference between I_D (based on Duffy transform at the singular point) and I_c (based on Duffy transform at the sub-barycentric point) is:

$$I_D - I_c \approx Ak_0 [1/a(\zeta) - 1/a(1/2)]. \qquad (25)$$

This difference is only related to the area A. When the area A of triangle tends to zero, the numerical difference $I_D - I_c$ will converge to zero as well. This can ensure that the error is only related to the mesh density,

and convergence of the integral has a good agreement with the traditional Duffy method.

B. Convergence analysis based on numerical experiments

To verify the convergence of the barycentric subdivision method, we compute the bistatic RCS for a PEC sphere with EFIE and MFIE, respectively.

We compute the RCS with the nine-point method and traditional singularity extraction method (S-E) respectively. These two methods are compared with Mie series results respectively. The results are shown in Fig. 7.
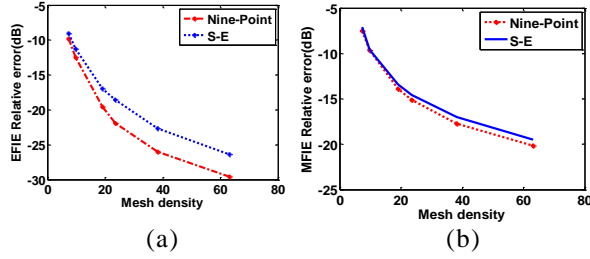
Fig. 7. Comparison of relative error in RCS: (a) EFIE, and (b) MFIE.

The relative error is defined as,

$$error = 10\log(\|RCS_{\_cal} - RCS_{\_mie}\| / \|RCS_{\_mie}\|), \qquad (26)$$

and the mesh density is defined as,

$$\text{mesh density} = \sqrt{\frac{N}{S}} \cdot \lambda, \qquad (27)$$

where N denotes the numbers of unknowns, S denotes the surface area of the sphere, and λ denotes the wave length of the incident wave. From Fig. 7, we can observe that the error decreases as the mesh density increases.

C. Computation of integrals of 1/R

To check the convergence, we also study the singular integration on a triangle as the below:

$$I = \oiint_{S_m} \left[\oiint_{S_n} (1/R) dS' \right] dS, \qquad (28)$$

where R denotes the distance between the source and field point.

In Fig. 8, the size of the area zooms step by step, and the side length L declines by half every time. The value of integration for (28) is shown in Table 2.

It can be seen from Table 2 that the results of the nine-point method agree well with those of the analytical method. Besides, the two methods diverge at the same time when the area of the triangle becomes too small due to the limited machine precision. In summary, this illustrates that our method is applicable to the cases where the mesh size is small enough.
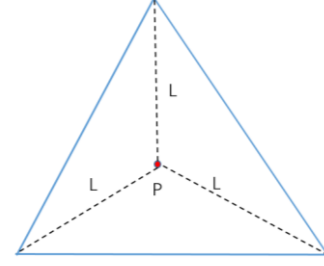
Fig. 8. The area of the triangle changes with L.

Table 2: Comparison of integral value

The Size of Area (L)	The Value of Integral for 1/R	
	The Nine-Point	Analytical
1	4.218747139	5.132335663
0.5	0.527344286	0.641542614
0.25	6.59E-02	8.02E-02
0.125	8.24E-03	1.00E-02
0.125/2	1.03E-03	1.25E-03
0.125/2/2	1.29E-04	1.57E-04
0.125/2/2/2	1.61E-05	1.96E-05
0.125/2/2/2/2	2.01E-06	2.45E-06
0.125/2/2/2/2/2	2.51E-07	3.06E-07
0.5/2/2/2/2/2/2/2/1000	2.17E-16	2.64E-16
0.5/2/2/2/2/2/2/2/1000/2	NaN	NaN
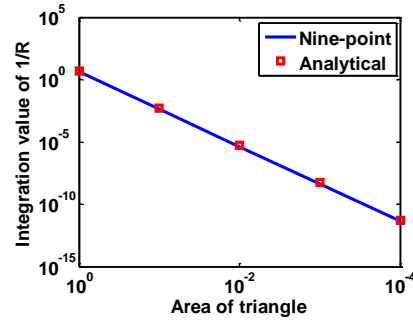
Fig. 9. Convergence for 1/R

The above integral is computed by both the nine-point integration and the analytical method [1], respectively. Figure 9 shows the values of I with respect to mesh density using the two methods. They agree well with each other.

V. CONCLUSION

In this study, we investigated the barycentric subdivision method. We studied the numerical convergence of this method for singular integration by both theoretical analysis and numerical examples. We observe that this method converges at the same level of accuracy as other method such as the singularity extraction. This method avoids the complex treatment of

singular integrals and allows an uniform procedure for both singular and non-singular integrations in method of moments. Numerical examples show that this method can reduce the matrix setup time by half. We hope this study could help us to further understand this method and extend its applications in solving 3D scattering problems using method of moments.

ACKNOWLEDGMENT

REFERENCES

[1] S. M. Rao, D. R. Wilton, and A. W. Glisson, "Electromagnetic scattering by surfaces of arbitrary shape," *IEEE Trans. Antennas and Propagation*, vol. 30, no. 3, pp. 409-418, 1982.

[2] D. R. Wilton, S. M. Rao, A. W. Glisson, D. H. Schaubert, O. M. Al-Bundak, and C. M. Butler, "Potential integrals for uniform and linear source distributions on polygonal and polyhedral domains," *IEEE Trans. Antennas and Propagation*, vol. 32, no. 3, pp. 276-281, 1984.

[3] M. G. Duffy, "Quadrature over a pyramid or cube of integrands with a singularity at a vertex," *SIAM J Numer-Anal*, vol. 19, no. 6, pp. 1260-1262, 1982.

[4] Y. W. Zhao, Z. P. Nie, J. H. Xu, and S. B. Wu, "Accurate and efficient calculation of singular integrals in Galerkin method with RWG basis functions," *ACTA Electronica Sinica*, vol. 33, no. 6, pp. 1019-1023, 2005.

[5] M. M. Botha, "A family of augmented Duffy transformations for near-singularity cancellation quadrature," *IEEE Trans. Antennas and Propagation*, vol. 61, no. 6, pp. 3123-3134, 2013.

[6] M. A. Khayat and D. R. Wilton, "Numerical evaluation of singular and near-singular potential integrals," *IEEE Trans. Antennas and Propagation*, vol. 53, no. 10, pp. 3180-3190, 2005.

[7] M. A. Khayat, D. R Wilton, and P. W. Fink, "An improved transformation and optimized sampling scheme for the numerical evaluation of singular and near-singular potentials," *IEEE Antennas and Wireless Propagation Letters*, vol. 7, pp. 377-380, 2008.

[8] F. Vipiana, D. R. Wilton, et al., "Numerical evaluation via singularity cancellation schemes of near-singular integrals involving the gradient of Helmholtz-type potentials," *IEEE Trans. Antennas and Propagation*, vol. 61, no. 3, pp. 1255-1265, 2013.

[9] B. D. Popovic and B. M. Kolundzija, *Analysis of Metallic Antennas and Scatters*, The Institution of Electrical Engineers, London, pp. 58, 1988.

[10] F. Z. Geng and C. M. Tong, "An efficient method of singular integrals in hybrid basis MoM solutions," *Journal of Air Force Engineering University (N.S.E.)*, vol. 7, no. 3, pp. 65-68, 2006.

[11] C. W. Xiang, C. M. Tong, et al., "Modeling method of reduced dimension for complex targets and application in electromagnetic scattering analysis," *Chinese Journal of Radio Science*, vol. 20, no. 2, pp. 189-192, 2005.

[12] H. G. Wang, Z. P. Nie, et al., "Singularity analysis of the integral equation for three dimension vector fields scattering," *ACTA Electronica Sinica*, vol. 27, no. 12, pp. 68-71, 1999.

[13] Y. H. Hua, J. P. Xu, et al., "Integration singularity reduction by the locally continuous functions used in moment method with EFIE," *Journal of Electronics and Information Technology*, vol. 25, no. 10, pp. 1436-1440, 2003.

[14] J. H. Wu, X. Y. Cao, H. B. Yuan, and J. Gao, "Effective method to solve magnetic field integral equation with method of moment," *Chinese Journal of Radio Science*, vol. 28, no. 5, pp. 974-978, 2013.

[15] Y. Kamen and L. Shirman, "Triangle rendering using adaptive subdivision," *IEEE Computer Graphics and Application*, pp. 95-103, Mar.-Apr. 1998.

[16] S. N. Makarov, *Antenna and EM Modeling with Matlab*, NY: Wiley-Interscience, New York, pp. 128, 2002.

[17] W. C. Chew, E. Michielssen, J. M. Song, and J. M. Jin, *Fast and Efficient Algorithms in Computational Electromagnetics*, MA: ArtechHouse, Boston, 2001.

[18] J. M. Jin, *Theory and Computation of Electromagnetic Fields*, John Wiley & Sons, Inc, Hoboken, New Jersey, USA, 2010.

[19] A. Ben-Israel and R. Gilbert, *Computer-Supported Calculus*, pp. 224-278, Springer-Verlag Wien, 2002.

[20] X. Q. Sheng, J. M. Jin, J. M. Song, C. C. Lu, and W. C. Chew, "On the formulation of hybrid finite-element and boundary-integral methods for 3-D scattering," *IEEE Trans. Antennas and Propagation*, vol. 46, no. 3, pp. 303-311, 1998.

[21] C. W. Xiang, X. W. Dang, M. K. Li, F. Yang and S. H. Xu, "The application of Barycentric subdivision method for numerical integration in method of moments," *2018 IEEE International Conference on Computational Electromagnetics (ICCEM)*, Chengdu, pp. 1-3, 2018.

[22] F. Vipiana and D. R. Wilton, "Optimized numerical evaluation of singular and near-singular potential integrals involving junction basis functions," *IEEE Trans. Antennas and Propagation*, vol. 59, no. 1, pp. 162-171, 2011.

[23] S. Jarvenpaa, M. Taskinen, and P. Y. Oijala, "Singularity extraction technique for integral equation methods with higher order basis functions on plane triangles and tetrahedral," *Int. J. Numer. Meth. Eng.*, vol. 58, pp. 1149-1165, Aug. 2003.

Chunwang Xiang received the B.S. degree from Air Force Engineering University, Xi'an, China, in 2002. He is now a Ph.D. student at Tsinghua University, Beijing, China. His current research interests include finite element method (FEM), time-domain finite element method (FETD), finite element boundary integral method (FE-BI),and design on Radar antenna and etc.

Shenheng Xu received the B.S. and M.S. degrees in 2001 and 2004, respectively, from the Southeast University, Nanjing, China, and the Ph.D. degree in Electrical Engineering in 2009 from the University of California, Los Angeles (UCLA), CA, USA. From 2000 to 2004, he was a Research Assistant with the State Key Laboratory of Millimeter Waves, Southeast University, Nanjing, China. From 2004 to 2011, he was a Graduate Student Researcher and later a Postdoctoral Researcher with the Antenna Research, Analysis, and Measurement Laboratory, UCLA. In 2012, he joined the Department of Electronic Engineering, Tsinghua University, Beijing, China, as an Associate Professor. His research interests include novel designs of high-gain antennas for advanced applications, artificial electromagnetic structures, and electromagnetic and antenna theories.

Xunwang Dang received the B.S. degree from Tsinghua University, Beijing, China, in 2013, and the Ph.D. degree from the same university in 2018. His current research interests include reduced basis method (RBM), equivalent principle algorithm (EPA), fast algorithms in the method of moments, deep learning techniques in electromagnetics etc.

Maokun Li received his B.S. degree in Electronic Engineering from Tsinghua University, Beijing, China, in 2002, and the M.S. and Ph.D. degrees in Electrical Engineering from University of Illinois at Urbana-Champaign in 2004 and 2007, respectively. After graduation, he joined Schlumberger-Doll Research as a Post-doc Research Scientist, and later as a Senior Research Scientist. In June 2014, he joined the Department of Electronic Engineering in Tsinghua University as an Associate Professor. His research interests include fast algorithms in computational electromagnetics and electromagnetic inverse problems.

Fan Yang received the B .S. and M.S. degrees in Electronic Engineering from Tsinghua University, Beijing, China, in 1997 and 1999, respectively, and the Ph.D. degree in Electrical Engineering from the University of California, Los Angeles (UCLA), Los Angeles, CA, USA, in 2002. From 2002 to 2004, he was a Postdoctoral Research Engineer and Instructor with the Electrical Engineering Department, UCLA. In 2004, he joined the Electrical Engineering Department, The University of Mississippi as an Associate Professor in 2009. In 2011, he joined the Electronic Engineering Department, Tsinghua University as a Professor, and has served as the Director of the Microwave and Antenna Institute since then. He has authored or coauthored more than 300 journal articles and conference papers, 6 book chapters, and 5 books. His research interests include antennas, surface electromagnetics, computational electromagnetics, and applied electromagnetic systems.

Yang served as an Associate Editor for the IEEE Transactions on Antennas and Propagation (2010-2013) and an Associate Editor-in-Chief for Applied Computational Electromagnetics Society Journal (2008-2014). He was the Technical Program Committee Chair of 2014 IEEE International Symposium on Antennas and Propagation and USNC-URSI Radio Science Meeting. He is an ACES Fellow and IEEE Fellow, as well as an IEEE APS Distinguished Lecturer for 2018-2020.

Propagating and Scattering of the Electromagnetic Vortex Generated by a Spiral Parabolic Antenna

B. H. Yin, Z. He, and R. S. Chen

Department of Communication Engineering
Nanjing University of Science and Technology, Nanjing, 210094, China
eerschen@mail.njust.edu.cn

Abstract ─ A modified octree grouping scheme of the multilevel fast multipole algorithm (MLFMA) is proposed to analyze the electromagnetic (EM) scattering from the electrically large target, which is illuminated by a spiral parabolic antenna. The spiral parabolic antenna is used to generate the electromagnetic vortex of a specific mode number by adjusting the height of split. The proposed method builds two octree groups and decouples the interaction between the antenna and the target, so as to save the computational resource and improve the computational efficiency. Using this scheme, the numerical example with double metal spheres illuminated by the electromagnetic vortex reveals some special phenomena due to the spiral phase distribution, while the example with a scaled-down airplane at long operating range demonstrates that the electromagnetic vortex tends to be plane wave locally with the increase of propagation distance.

Index Terms ─ Electromagnetic vortex, incorporate modeling, MLFMA, octree grouping, orbital angular momentum, spiral parabolic antenna.

I. INTRODUCTION

Orbital angular momentum (OAM) has been found in the laser of the Laguerre-Gaussian mode for a few decades [1]. The electromagnetic wave carrying orbital angular momentum is also called the electromagnetic vortex or the vortex electromagnetic beam. The orbital angular momentum number carried by the electromagnetic vortex is defined as the topological charge or the mode number l. A large quantity of research has been conducted in optics so far, such as the micro-particle operation [2], the optical communication [3], the rotating objects detection [4], etc. The investigation of OAM in the radio domain falls behind optics. In 2007, Thidé proposed a generation method of the vortex electromagnetic beam in the low-frequency radio domain [5]. Since then, a series of explorations on the OAM-based communication and detection have springed up like mushrooms. Tamburini and Thidé conducted a series of wireless communication experiments on the

electromagnetic vortex, which validate the feasibility of the multiplexing scheme using orbital angular momentum [6-8]. However, some scholars put forward their doubts and considered that the OAM-based multiplexing scheme is essentially a particular case of the Multiple-input-Multiple-output (MIMO) system [9-10]. After some debates, the research team of Thidé acknowledged that their proposed scheme could be equivalent to the MIMO system in the case of a limited receiving aperture [11]. Guo proposed a new radar imaging scheme utilizing the electromagnetic vortex [12], and the researchers of his university did much work on the imaging model and the imaging method later on [13-15], but there are also controversies about the resolution performance of their schemes [16]. Fonseca designed a Fresnel-like reflector antenna to generate high-order orbital angular momentum states in the radio band [17]. Guan designed a new type of metasurface to generate the vortex beam of two different modes simultaneously [18]. For the scattering problem, there are only a few open literatures conducting the simulation on the OAM-based scattering of macro targets in the low-frequency radio domain [19-21], and all of these simulations are based on the ideal and analytical source model.

In this paper, we propose a modified octree grouping scheme of MLFMA [22-23] based on the method of momentum (MoM) [24-25] to conduct the approximate incorporate modeling of an electrically large scattering target and a spiral parabolic antenna efficiently. This full wave EM simulation uses a practical OAM antenna as the radiation source and takes the operating range and antenna coupling into account. Thus, it can simulate the reality as far as possible. The algorithm starts with dividing the computational region into two parts, namely radiation and scattering regions. Firstly, the induced current on the antenna (radiation region) is computed with the excitation source; secondly, the necessary radiation field is calculated as the incident field for the target (scattering region) with the induced current on the antenna, and finally the scattered field of the target (scattering region) is obtained with the

multilevel fast multipole algorithm. It should be noted that there are two octree groups built just close to the surfaces of the antenna and the target respectively, which avoids the unnecessary octree grouping of the whole solution domain in the situation of a long operating range. The simulations in this paper reveal some special scattering phenomena caused by the spiral phase distribution of the electromagnetic vortex. The near-field characteristic of the electromagnetic vortex is demonstrated by considering the effect of the operating range. We also provide further verifications and explanations for the corresponding consequences.

This paper is organized as follows. Section II describes the spatial phase distribution of the electromagnetic vortex generated by a spiral parabolic antenna with different parameter settings. Section III illustrates the modified octree grouping scheme and provides the numerical example of double metal spheres with different mode numbers. Section IV provides the numerical example of a scaled-down airplane which is illuminated by a spiral parabolic antenna at long operating ranges and some consequence analyses. Finally, further discussions and conclusions are drawn in Section V.

II. PROPAGATION OF THE ELECTROMAGNETIC VORTEX GENERATED BY A SPIRAL PARABOLIC ANTENNA

Take the spiral parabolic antenna in [6] as the example to research on the spatial phase distribution of the vortex electromagnetic beam by practical antennas. This type of OAM antennas has the advantages such as high gain, small divergence angle, high mode purity, and fits for the situation of a long operating range between the antenna and the target. Figure 1 shows the antenna model used in the following simulations. The electromagnetic vortices of different mode numbers can be achieved by means of adjusting the height of the split. Figure 2 reveals the phase distribution of the mode 1 and the mode 2 in different propagation distances through the full wave simulation. The observation planes used for sampling are perpendicular to the propagation axis Z and they are centered with the axis Z.

It can be seen that the electromagnetic vortices of nonzero modes tend to be that of the mode 0 from the beam center with the increase of the propagation distance, and the higher the mode is , the more obvious the degradation is. This is difficult to be observed with the ideal and analytical model of the electromagnetic vortex. Figure 3 shows that the spiral phase distribution can recover gradually with the expansion of the aperture.
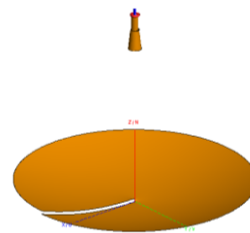
Fig. 1. The model of the spiral parabolic antenna used in numerical simulations. (The horn can be replaced by the ideal Gaussian feed source).
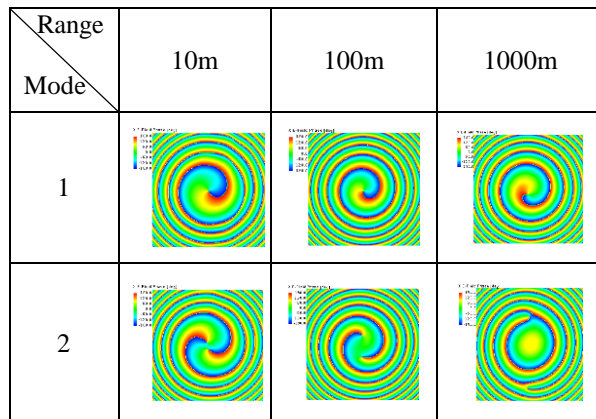
Fig. 2. The phase distribution of the electromagnetic vortex on an observation plane in different propagation distances. (The size of observation plane is 3m*3m, 10m*10m, 30m*30m from left to right; the operating frequency is 10GHz; the aperture of the parabolic antenna is 36λ, the focus length is 25λ.)
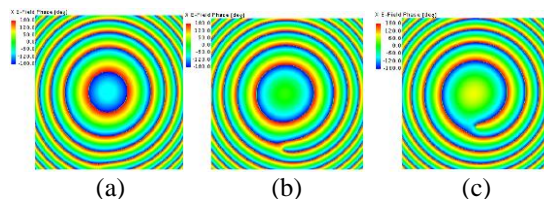
Fig. 3. The phase distribution of the mode 1 at 100km with different antenna apertures. (The aperture of the antenna is 36λ, 50λ, 80λ from (a) to (c); the size of the observation plane is 300m*300m, other parameters are same with those in Fig. 2).

As we know, the radiation pattern of the OAM beam with a nonzero mode is doughnut-like and the direction of the maximum radiation is not along the propagation axis. The phase variation along the direction of the maximum radiation is more significant. Just take the mode 1 in Fig. 2 as an example. Figure 4 (a) and Fig. 5 illustrate that the phase gradient can still be maintained along the direction of the maximum

radiation. However, this phase gradient is meaningless because the scope of the observation area is too large for common applications on radar. If the observation circle has a fixed size and it is centered with the propagation axis, the similar consequence can be obtained as Fig. 2, which is illustrated in Fig. 4 (b) and Fig. 6. The full wave simulations above show that the electromagnetic vortex by a spiral parabolic antenna has the characteristic of the near field.

(a)   (b)
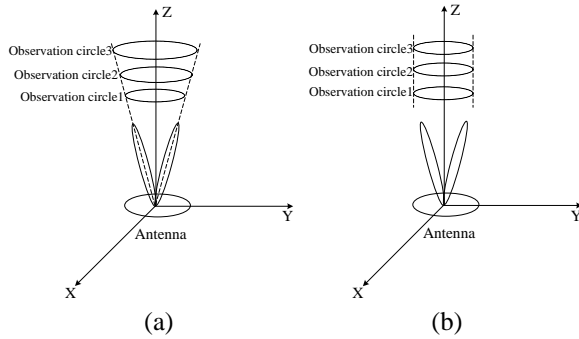
Fig. 4. Two phase sampling schemes.
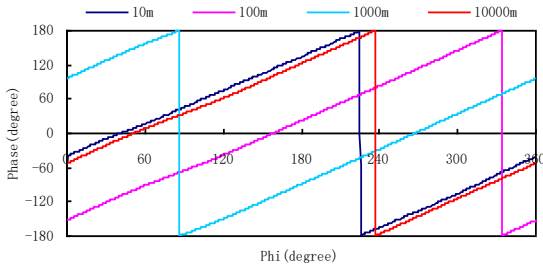
Fig. 5. The phase variation along the dynamic-sized circles which are placed along the direction of the maximum radiation.
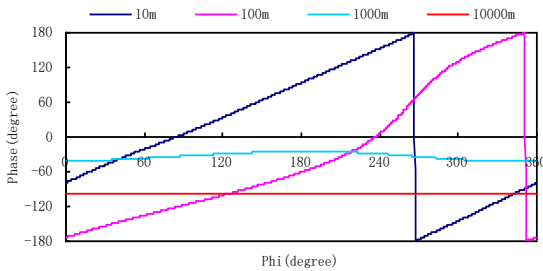
Fig. 6. The phase variation along the fix-sized circles which are placed around the propagation axis.

III. A MODIFIED OCTREE GROUPING SCHEME FOR SOLVING THE EM SCATTERING OF THE ELECTROMAGNETIC VORTEX

For analyzing the long-distance scattering problem with the method of momentum efficiently, a modified octree grouping scheme of the MLFMA is proposed and illustrated in Fig. 7. The proposed scheme divides the original incorporate solving process into three steps: the first step is to compute the induced current on the antenna with the excitation source. The induced current for a spiral parabolic antenna is computed with the electric field integrated equation (EFIE) because of the open structure:

$$\mathbf{E}_a^i(\mathbf{r})\,|_{\tan} = j\omega\mu\int\left[\mathbf{J}_a(\mathbf{r}') + \frac{1}{k^2}\nabla(\nabla'\cdot\mathbf{J}_a(\mathbf{r}'))\right]G(\mathbf{r},\mathbf{r}')d\mathbf{S}_a'\,|_{\tan}.$$

(1)

Where $\mathbf{E}_a^i$ and $\mathbf{J}_a$ denote the incident electric field and the induced current on the antenna respectively, $\mathbf{r}$ and $\mathbf{r}'$ are the observation point and the source point respectively, G is the scalar Green's function.
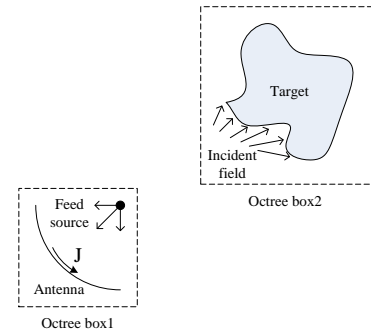
Fig. 7. The illustration of the modified octree grouping scheme for solving the electromagnetic scattering of the electromagnetic vortex generated by practical antennas.

The second step is to compute necessary radiation field (according to the location of the target) as the incident field for the target according to this induced current:

$$\mathbf{E}_t^i(\mathbf{r}) = \mathbf{E}_a^r(\mathbf{r}) = j\omega\mu\int\left[\mathbf{J}_a(\mathbf{r}') + \frac{1}{k^2}\nabla(\nabla'\cdot\mathbf{J}_a(\mathbf{r}'))\right]G(\mathbf{r},\mathbf{r}')d\mathbf{S}_a',$$

(2)

$$\mathbf{H}_t^i(\mathbf{r}) = \mathbf{H}_a^r(\mathbf{r}) = \int\mathbf{J}_a(\mathbf{r}')\times\nabla G(\mathbf{r},\mathbf{r}')d\mathbf{S}_a'.$$ (3)

Where $\mathbf{E}_a^r$ and $\mathbf{H}_a^r$ denote the radiation electric field and the radiation magnetic field of the antenna respectively, while $\mathbf{E}_t^i$ and $\mathbf{H}_t^i$ denote the incident electric field and the incident magnetic field of the target respectively

The third step is to compute the scattered field of the target by the corresponding incident field. The induced current of a close structure is computed with the combined field integrated equation (CFIE):

$$\alpha\mathbf{E}_t^i(\mathbf{r}) + (1-\alpha)\eta\mathbf{H}_t^i(\mathbf{r})\,|_{\tan} = \alpha\, j\omega\mu\int\left[\mathbf{J}_t(\mathbf{r}') + \frac{1}{k^2}\nabla(\nabla'\cdot\mathbf{J}_t(\mathbf{r}'))\right]G(\mathbf{r},\mathbf{r}')d\mathbf{S}_t'$$
$$+ (1-\alpha)\eta\int\mathbf{J}_t(\mathbf{r}')\times\nabla G(\mathbf{r},\mathbf{r}')d\mathbf{S}_t'\,|_{\tan}.$$

(4)

Where $\mathbf{J}_t$ denotes the induced current on the target, ω is the angular frequency, μ is the permeability, η is the wave impedance, and α is the combination coefficient of the CFIE from 0 to 1.

The purpose of this process is to decouple the interaction between the antenna and the target because it is weak enough to be neglected for a long operating range. The decomposition of the original incorporate solving process makes the octree group is only built close to the surfaces of the antenna and the target respectively. It avoids the unnecessary octree grouping of the whole solution domain for the incorporate modeling and the accompanying calculation cost in the situation of a long operating range. To avoid the ambiguous definition of the OAM-based RCS, we use the scattered field in the far field as the evaluation index.
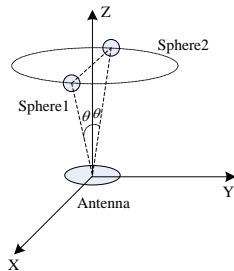
Fig. 8. Two metal spheres placed on a circle surrounding the Z-axis with an azimuthal difference of 180°. (The solving frequency is 30GHz, the height of the spheres is 300λ and their radius is 2.5λ, they are aligned with a pitch angle of 5° in the XOZ plane; the aperture of the parabolic antenna is 10λ and the focus length is 15λ.)

To validate the feasibility of this approximation scheme, the bistatic scattered field of two metal spheres in the far field is shown in Fig. 8 and Fig. 9. It can be seen that well agreements between the proposed approximation method and the original incorporate modeling method by the commercial software FEKO 7.0 are achieved. The differences among the scattered field amplitudes of three modes are caused by the maximum gain of the corresponding mode as well as its direction. Drawing the curves in one chart, some special phenomena can be observed, which are shown in Fig. 10.

The variation trends of the scattered field with the pitch angle are same for the mode 0 and the mode 2, while the mode 1 is opposite. The monostatic scattered field also has the same phenomenon, as shown in Fig. 11. A similar consequence had been found by the

system experiment in [19]. This phenomenon can be explained with the distributions of the spiral phase and the target: the two metal spheres are placed on a circle surrounding the Z-axis with an azimuthal difference of 180°, thus the phase difference between the incident fields of two spheres is 0° for the mode 0, 180° for the mode 1, and 360° for the mode 2 approximately. Therefore, if the scattered field for the mode 0 and the mode 2 stacks in same phase at some angles, then it is opposite for the mode 1 at these angles.

To validate this inference, we conduct another simulation furthermore, which is illustrated in Fig. 12. This time, the two metal spheres are aligned at the same height with an azimuthal difference of 90°. It can be predicted from the inference above that the scattered field of the mode 0 and the mode 2 should have the opposite variation trend, while the mode 1 falls in between, which is proved in Fig. 13.

(a)

(b)

(c)
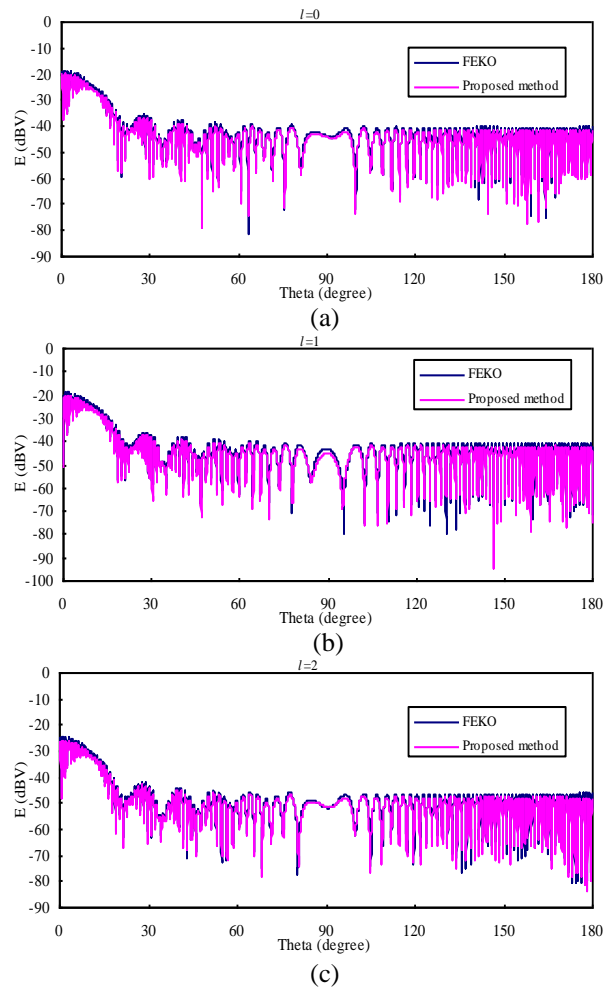
Fig. 9. The scattered electric field intensity in the far field (Phi=0°) for the proposed method and the original method: (a) $l=0$, (b) $l=1$, and (c) $l=2$.
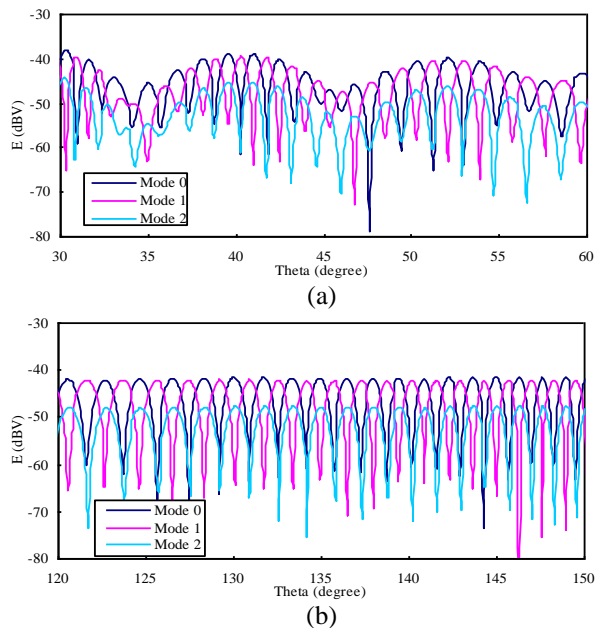
Fig. 10. The bistatic scattered field in the far field (Phi=0˚) for different mode numbers. (a) The observed pitch angle is from 30˚ to 60˚. (b) The observed pitch angle is from 120˚ to 150˚.
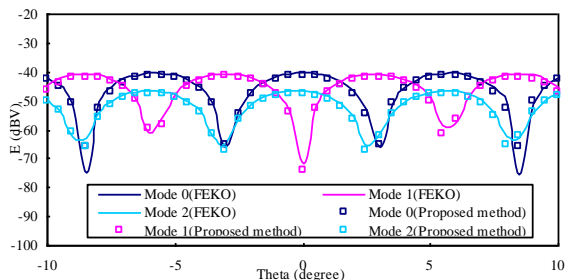
Fig. 11. The monostatic scattered field in the far field (Phi=0˚) for different mode numbers.
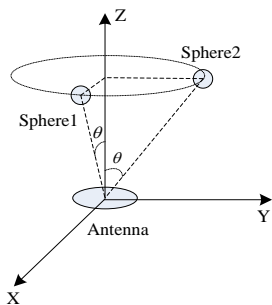
Fig. 12. Two metal spheres are placed on a circle surrounding the Z-axis with an azimuthal difference of 90˚. (Other parameters are same with those in Fig. 8).
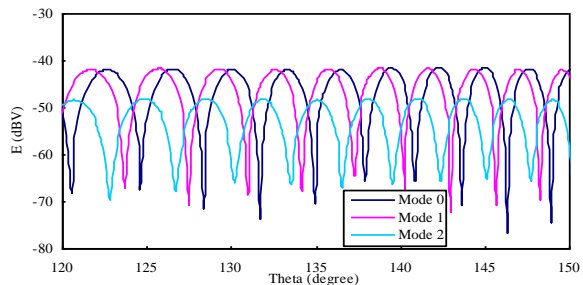
Fig. 13. The bistatic scattered field in the far field (Phi=0˚) for different mode numbers.

IV. SCATTERING OF THE ELECTROMAGNETIC VORTEX BY ELECTRICALLY LARGE TARGETS AT LONG OPERATING RANGES

To demonstrate the effect of the operating range on the scattering of the electromagnetic vortex, the bistatic scattered field of a plane model with a scaling of 0.1 compared with the real size is computed. The solving setting is illustrated in Fig. 14 and the consequences are given in Fig. 15. In this simulation, we point the direction of the maximum radiation to the nose to avoid the hollow area and the mode degradation. Meanwhile, the mode 10 in Fig. 15 is generated by a modified spiral parabolic antenna proposed in [17] to ensure its purity.
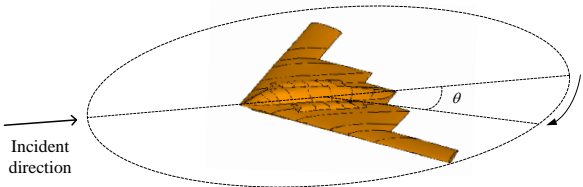
Fig. 14. The bistatic scattering computation of a scaled-down plane model.

It can be seen from Fig. 15 that with the increase of the operating range, the variation trends of the scattered field tend to be the same as the mode 0, and the lower the mode is, the more obvious this phenomenon is. It also can be explained by the phase distribution in the far field.

As shown in Fig. 16, when the target is placed along the direction of the maximum radiation, the azimuthal variation for the target becomes smaller and smaller with the increase of the distance. It means the phase gradient of the incident field is unapparent and the incident field can be approximated to the plane wave locally just as the mode 0. Therefore, there is a pair of contradictions for the practical OAM-based radar application because of this special beam structure:

the null region of the vortex electromagnetic beam can't be used for the detection, while the direction of the annular beam can't reflect the phase gradient of the electromagnetic vortex for a size-limited target. These lead to the limited usage of the OAM in the radar realm, which is eager to be solved in the future research.
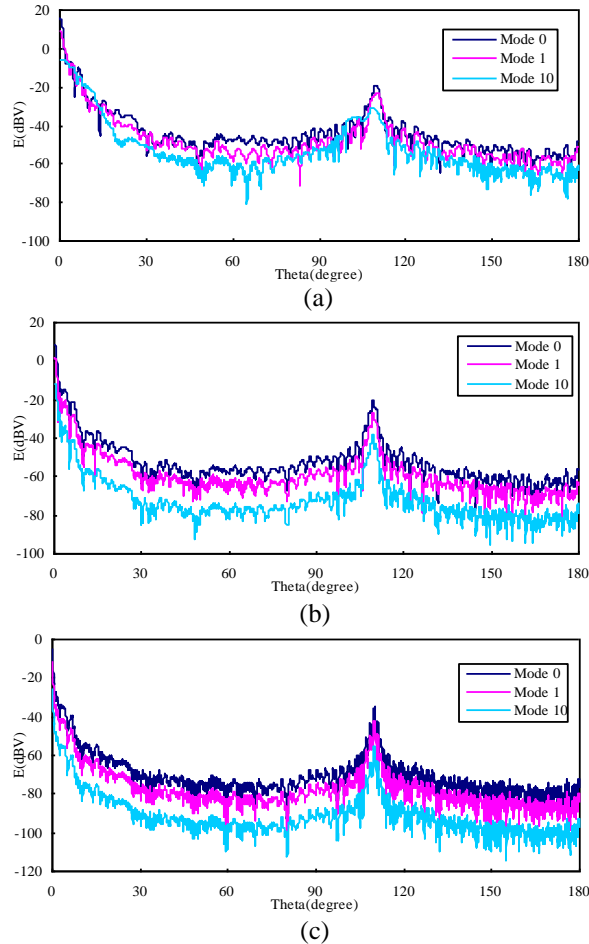
Fig. 15. The bistatic scattered field in the far field of the plane model; (a), (b) and (c) are corresponding to the operating range of 10m, 100m and 1000m respectively.
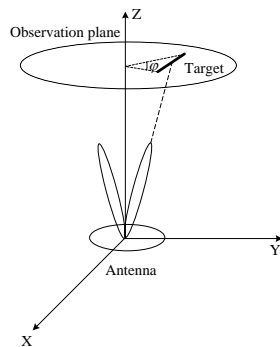
Fig. 16. The positional relationship between the antenna and the target in the far field.

V. CONCLUSION

To summarize, the approximate incorporate modeling of an electrically large scattering target and a practical antenna is conducted in this paper. The octree grouping scheme is modified to solve the EM scattering problem based on the electromagnetic vortex. The phase distributions of the field near the propagation axis in different propagation distances are simulated, which prove the degradation characteristic for the vortex electromagnetic beam generated by a spiral parabolic antenna. The numerical simulation of an airplane model and a spiral parabolic antenna reveals a pair of contradictions for the OAM-based radar application. However, during its effective operating range, the scattered field may show a regular difference compared to the plane wave for some particular structures. This research demonstrates the significant effect of the operating range for the OAM-based radar application in the real world. The following work includes narrowing the divergence angle of the electromagnetic vortex, generating the electromagnetic vortex with very high modes, and exploring some suitable applications during appropriate operating ranges.

REFERENCES

[1] L. Allen, M. W. Beijersbergen, R. J. C. Spreeuw, *et al.*, "Orbital angular momentum of light and transformation of Laguerre Gaussian laser modes," *Physical Review A*, vol. 45, no. 11, pp. 8185-8189, 1992.

[2] M. Yang, Y. Wu, K. F. Ren, and X. Sheng, "Computation of radiation pressure force exerted on arbitrary shaped homogeneous particles by high-order Bessel vortex beams using MLFMA," *Optics Express*, vol. 24, no. 24, p. 27979, 2016.

[3] M. Krenn, J. Handsteiner, M. Fink, *et al.*, "Twisted light transmission over 143 kilometers," *Proceedings of the National Academy of Sciences*, 2016.

[4] M. P. J. Lavery, F. C. Speirits, S. M. Barnett, *et al.*, "Detection of a spinning object using light's orbital angular momentum," *Science*, vol. 341, no. 6145, pp. 537-540, 2013.

[5] B. Thidé, H. Then, J. SjÖHolm, *et al.*, "Utilization of photon orbital angular momentum in the low-frequency radio domain," *Physical Review Letters*, vol. 99, no. 8, p. 087701, 2007.

[6] F. Tamburini, E. Mari, A. S Ponselli, *et al.*,

"Encoding many channels in the same frequency through radio vorticity: first experimental test," *New Journal of Physics*, vol. 14, no. 11, pp. 78001-78004, 2011.

[7] F. Tamburini, E. Mari, B. Thidé, *et al*., "Experimental verification of photon angular momentum and vorticity with radio techniques," *Applied Physics Letters*, vol. 99, no. 20, p. 204102, 2011.

[8] F. Tamburini, B. Thidé, V. Boaga, *et al*., "Experimental demonstration of free-space information transfer using phase modulated orbital angular momentum radio," *Physics*, 2013.

[9] O. Edfors and A. J. Johansson, "Is orbital angular Momentum (OAM) Based Radio Communication an unexploited area," *IEEE Transactions on Antennas and Propagation*, vol. 60, no. 2, pp. 1126-1131, 2012.

[10] M. Tamagnone, C. Craeye, and J. Perruisseau-Carrier, "Comment on 'encoding many channels on the same frequency through radio vorticity: First experimental test'," *New Journal of Physics*, vol. 14, no. 11, p. 118001, 2012.

[11] M. Oldoni, F. Spinello, E. Mari, *et al*., "Space-division demultiplexing in orbital-angular-momentum based MIMO radio systems," *IEEE Transactions on Antennas and Propagation*, vol. 63, no. 10, pp. 1-1, 2015.

[12] G. R. Guo, W. D. Hu, and X. Y Du, "Electromagnetic vortex based radar target imaging," (in Chinese) *Journal of National University of Defense Technolology*, vol. 35, no. 6, pp. 71-76, Dec. 2013.

[13] K. Liu, Y. Q. Cheng, Z. C. Yang, *et al*., "Orbital-angular-momentum-based electromagnetic vortex imaging," *IEEE Antennas and Wireless Propagation Letters*, vol. 14, pp. 711-714, 2015.

[14] T. Z. Yuan, H. Q. Wang, Y. L. Qin, *et al*., "Electromagnetic vortex imaging using uniform concentric circular arrays," *IEEE Antennas and Wireless Propagation Letters*, vol. 15, pp. 1-1, 2015.

[15] K. Liu, Y. Q. Cheng, Y. Gao, *et al*., "Super-resolution radar imaging based on experimental OAM beams," *Applied Physics Letters*, vol. 110, no. 16, p. 164102, 2017.

[16] B. Tang, K. Y. Guo, J. P. Wang, *et al*., "Resolution performance of the orbital-angular-momentum-based imaging radar," *IEEE Antennas and Wireless Propagation Letters*, vol. 16, pp. 2975-2978, 2017.

[17] N. J. G. Fonseca, L. Coulomb, and J. C. Angevain, "A Fresnel-like reflector antenna design for high-order orbital angular momentum states," *IEEE European Conference on Antennas & Propagation*, 2015.

[18] L. Guan, Z. He, D. Z. Ding, Y. F. Yu, W. Zhang and R. S. Chen, "Polarization-controlled shared-aperture metasurface for generating the vortex beam with different modes," *IEEE Transactions on Antennas and Propagation*, vol. 66, no. 12, pp. 7455-7459, Dec. 2018.

[19] C. Zhang, D. Chen, and X. Jiang, "RCS diversity of electromagnetic wave carrying orbital angular momentum," *Scientific Reports*, vol. 7, no. 1, p. 15412, 2017.

[20] M. P. Yu, Y. P. Han, and Z. W. Cui, "Scattering of non-diffracting vortex electromagnetic wave by typical targets," *Progress In Electromagnetics Research Letters*, vol. 70, pp. 139-146, 2017.

[21] K. Liu, Y. Gao, X. Li, *et al*., "Target scattering characteristics for OAM-based radar," Aip Advances, vol. 8, no. 2, p. 025002, 2018.

[22] Z. He, H. H. Zhang, and R. S. Chen, "Parallel marching-on-in-degree solver of time-domain combined field integral equation for bodies of revolution accelerated by MLACA," *IEEE Transactions on Antennas and Propagation*, vol. 63, no. 8, pp. 3705-3710, Aug. 2015.

[23] J. H. Gu, Z. H. Fan, D. Z. Ding, and R. S. Chen, "A low frequency EFIE-MLFMA solver based on approximate diagonalization of the green's function," *IEEE Transactions on Antennas and Propagation*, vol. 65, no. 12, pp. 7150-7156, Dec. 2017.

[24] Z. He, J. H. Gu, W. Sha, and R. S. Chen, "An efficient volumetric method of moments for modeling plasmonic thin-film solar cells with periodic structures," *Optics Express*, vol. 26, no. 19, pp. 25037-25046, Nov. 2018.

[25] K. C. Wang, Z. He, D. Z. Ding, and R. S. Chen, "Uncertainty scattering analysis of 3-D objects with varying shape based on method of moments," *IEEE Transactions on Antennas and Propagation*, vol. 67, no. 4, pp. 2835-2840, Apr. 2019.

Bihuan Yin was born in Jiangsu, China. He received the B.Sc. degree in Communication Engineering from the School of Electrical Engineering and Optical Technique, Nanjing University of Science and Technology, Nanjing, China, in 2014, where he is currently working towards the Ph.D. degree.

His research interests include computational electromagnetics, radar imaging, and orbital angular momentum.

Zi He was born in Hebei, China. She received the B.Sc. and Ph.D. degrees in Electronic Information Engineering from the School of Electrical Engineering and Optical Technique, Nanjing University of Science and Technology, Nanjing, China, in 2011 and 2016, respectively. She has worked as a visiting scholar in the University of Illinois at Urbana and Champaign (UIUC) from September 2015 to September 2016. She works as a postdoctor at the Science and Technology on Electromagnetic Scattering Laboratory, BIEF.

Since 2016, she has been an Assistant Professor with the Department of Communication Engineering, Nanjing University of Science and Technology. Her research interests include antenna, RF-integrated circuits, and computational electromagnetics.

Rushan Chen was born in Jiangsu, China. He received the B.Sc. and M.Sc. degrees from the Department of Radio Engineering, Southeast University, China, in 1987 and 1990, respectively, and the Ph.D. degree from the Department of Electronic Engineering, City University of Hong Kong, in 2001.

He joined the Department of Electrical Engineering, Nanjing University of Science and Technology (NJUST), China, where he became a Teaching Assistant in 1990 and a Lecturer in 1992. Since September 1996, he has been a Visiting Scholar with the Department of Electronic Engineering, City University of Hong Kong, first as Research Associate, then as a Senior Research Associate in July 1997, a Research Fellow in April 1998, and a Senior Research Fellow in 1999. From June to September 1999, he was also a Visiting Scholar at Montreal University, Canada. In September 1999, he was promoted to Full Professor and Associate Director of the Microwave and Communication Research Center in NJUST, and in 2007, he was appointed as the Head of the Department of Communication Engineering, NJUST. He was appointed as the Dean in the School of Communication and Information Engineering, Nanjing Post and Communications University in 2009. And in 2011 he was appointed as Vice Dean of the School of Electrical Engineering and Optical Technique, NJUST. Currently, he is a principal investigator of more than 10 national projects. His research interests mainly include computational electromagnetics, microwave integrated circuit and nonlinear theory, smart antenna in communications and radar engineering, microwave material and measurement, RF-integrated circuits, etc. He has authored or coauthored more than 260 papers, including over 180 papers in international journals.

Fan-Type AMC Surface for Broadband Low-RCS Applications

Xueyan Song [1], Lei Chen [2], Zehong Yan [2], and Yanyan Li [3]

[1] School of Electronic Engineering
Xi'an University of Posts & Telecommunications, Xi'an, 710121, China
xysong6597@126.com

[2] National Key Laboratory of Antennas and Microwave Technology
Xidian University, Xi'an, 710071, China
leichen@mail.xidian.edu.cn, zhyan@mail.xidian.edu.cn

[3] National Key Laboratory of Science and Technology on Aerospace Intelligent Control
Beijing, 100854, China
liyanyan0418@126.com

Abstract ─ An artificial magnetic conductor (AMC) surface is proposed in this paper to reduce radar cross section (RCS) by more than 10 dB in a broad frequency band. The proposed AMC structure consists of two different units - seven hexagonal circles and Jerusalem cross loaded with four L-type branches, contributing to a wide phase difference ($180°\pm37°$) frequency band. To obtain a low RCS value, the two proposed units are arranged in fan-type for the AMC surface. The simulated results show that the RCS can be reduced by more than 10 dB in a broad frequency band from 12.2 to 27 GHz (75.5%). The proposed AMC structure combined by 20×20-unit cells is fabricated and measured in anechoic chamber. Measured results in the band below 18 GHz of the fabricated prototype agree well with the simulated ones, which validates that the proposed AMC surface may be utilized on low-RCS platforms.

Index Terms─ AMC, broadband, RCS reduction.

I. INTRODUCTION

With the rapid development of stealth and anti-stealth technology, materials for radar cross section (RCS) reduction in wide band have been paid more attention. To reduce RCS, there have been several techniques, such as metamaterial absorbers [1-2], Salisbury screen [3], electromagnetic band gap (EBG) [4-5], etc. Nevertheless, with the structures proposed above, the RCS can only be reduced in narrow frequency bands.

AMCs attract much attention because of their phase characteristics. With in-phase reflection property, AMC can be utilized to obtain low-profile antennas [6-7] and to enhance gain of antennas [8]. Moreover, AMCs play an important role in low-RCS designs. To obtain low-RCS characteristic in broad band, many RCS suppressing metasurfaces [9-15] have been proposed, among which, design of checkerboard configuration combined by AMC structures [10-15] has gradually been a more popular and effective method. In the beginning, a planar chessboard arranged by AMC and PEC is proposed by Paquay in 2007 [10]. With that configuration, the energy can be scattered in other directions after it reaches the surface and a cancellation of energy in boresight direction can be obtained. That is because, the metallic cells can reflect incident waves with a $180°$ change of phase, and AMC units can bring in no phase change at the operation frequency. By arrangement of the two units, destructive interference is produced, and a null can be achieved in normal direction. However, the bandwidth for RCS reduction is limited by the narrow in-phase reflection bandwidth of AMC. To obtain a wider bandwidth for RCS reduction, surfaces arranged by AMC unit cells with different dimensions [11-12] or different structures [13-16] have been presented, resulting in broad phase difference ($180°\pm37°$) bands. In [11], a novel polarization-insensitive metasurface which consists of four inter-twined subarrays, is investigated for ultra-broadband RCS reduction. The unit is a disc-shaped metallic patch with a concentric metallic ring patch. Consists of carefully arranged units with spatially varied dimension, the surface can achieve more than 10 dB RCS reduction in the band from 7 to 12 GHz. In addition, Pei Yao designed a miniaturized chessboard-like AMC reflecting screen [12], which is arranged by two different square AMC unit cells. The in-band RCS reduction is obtained in the band ranging from 13.4 to 20.5 GHz, and the out-of-band RCS reduction is achieved by cancellation between the approximately PEC and AMC in the band of 20.5-26.9 GHz. The measured results

show that the proposed surface can achieve 10 dB RCS reduction in the band from 13.5 to 28.1 GHz (70.2%). Additionally, an AMC structure, consisting of two different types of AMCs, is proposed for ultra-thin and broadband radar absorbing material design in [13]. The measured results show that, the screen achieved a wide phase difference band from 13.25 to 24.2 GHz, in which the RCS is reduced by 10 dB except for some frequency shift. Moreover, a hexagonal checkerboard and a square checkerboard are designed and compared with each other in [14] for wideband RCS reduction. They are composed of two kinds of AMC units utilizing square- and circular- shaped patches and realize over 60% frequency bandwidth for 10 dB RCS reduction. In [15], an AMC surface, combined by two different AMC unit cells, is designed as the ground of a low scattering microstrip antenna. The RCS is reduced by 10 dB in a wide band from 6 to 13.4 GHz and the maximum RCS reduction is 17 dB at 10 GHz. It can be seen that most of the array arrangements of AMC or PEC unit cells in the above references are chessboard. To obtain larger RCS reduction values, a fan type arrangement of AMC unit cells is employed in this paper as proposed in [16] to enhance the cancellation effect by increase the common boundaries of the two units. The low-RCS screen is combined by square loop and square patch units. However, the simulated results show that the bandwidth in [16] remains to be improved.
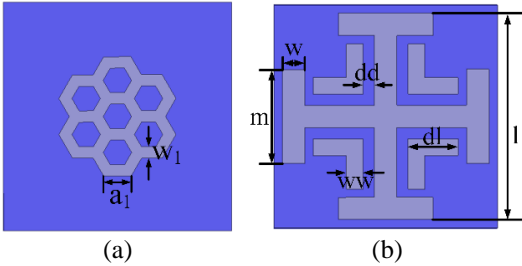
Fig. 1. Unit cells designs for: (a) AMC1 and (b) AMC2.

Based on the previous research in paper [17], an AMC surface for broadband RCS reduction is proposed in this paper to achieve a wider low-RCS bandwidth and a larger RCS reduction value simultaneously. With two new-style AMC unit cells, phase difference $(180°±37°)$ of the reflective waves is produced in a broad frequency range, which can contribute to a wide band for 10 dB RCS reduction. To further decrease the RCS value, the fan type arrangement of AMC unit cells is adopted in this paper. A broad band from 12.2 GHz to 27 GHz (75.5%) of 10 dB RCS reduction is obtained. Moreover, the designed AMC surface is fabricated and measured in anechoic chamber. A good agreement between the simulated and measured results shows that the presented AMC surface can be employed for broadband low-RCS applications.

II. DESIGN AND ANALYSIS OF AMC SURFACE

A. Design principle of broadband AMC surface

From [17, 18], when plan waves radiate normally on the AMC surface, the total energy reflected from the surface equals the total of the reflected energy from all AMC blocks. Assume that the reflection magnitude of all the AMC blocks is equal to A, which keeps no change with frequency. Hence, based on the concept of standard array theory [9, 10], the total reflected field is,

$$E_r = 2Ae^{j\bullet\varphi_1} + 2Ae^{j\bullet\varphi_2} = 2Ae^{j\bullet\varphi_1}(1+e^{j\bullet(\varphi_2-\varphi_1)}), \quad (1)$$

where, A is the reflection magnitude of the AMC blocks; φ_1 and φ_2 is the reflection phase of AMC1 and AMC2, respectively. It can be seen from (1) that, when $\varphi_2 - \varphi_1 = \pm180°$, the total reflected field is zero. In other words, the reflected energy from the two AMCs can be totally canceled out. However, the reflection phase is a variable which changes with frequency. In general, compared with PEC surface with the equal size, the reflection which can be reduced by more than 10 dB in boresight direction is set as a criterion [17] and it can be express as the following inequality:

$$|E_r|^2 / |E_{pec}|^2 \leq -10dB, \quad (2)$$

where, E_{pec} represents the total reflection field of PEC surface of the same dimension. From the inequality (2) above, it can be calculated the effective reflection phase difference of the presented AMC surface, which is:

$$143° \leq |\varphi_2 - \varphi_1| \leq 217°. \quad (3)$$

Consequently, the phase difference ranging from $143°$ to $217°$ is considered to be effective for subsequent analysis.

B. Design and analysis of AMC surface

To obtain a wide enough phase difference frequency band, the $0°$ phase reflection frequency of one unit should be as close to the $180°$ phase reflection frequency of the other unit as possible. A great many kinds of AMC units have been designed to constitute AMC surfaces, such as square patches, circle patches, Jerusalem Crosses, rings, etc. [11-16]. After an extensive analysis of their frequency behaviors, hexagon rings and Jerusalem Cross in Fig. 1 are designed as the two AMC units. Since it has a first-mode resonant frequency two times that of other ring types with the exception of the square spiral element and its second resonance is approximately three times that of the fundamental one, the hexagonal ring has superior bandwidth characteristic [19]. Therefore, to obtain a broad in-phase reflection bandwidth, the AMC unit cell1 is made up of seven hexagons, which can generate a $0°$ reflection phase at the center frequency of the required operating band and contribute to a gentler phase curve than a unit combined by one single hexagon. The AMC unit cell2 is a Jerusalem Cross loaded with

four L-type branches. The Jerusalem Cross is used to product a $180°$ reflection phase at the center frequency, and the four L-type branches are loaded to make the reflection phase curves located at the two sides of the $180°$ phase reflection frequency smoother. The two kinds of metal units are etched on a 2-mm-thickness F4B (ε_r=2.65, tanδ=0.002) substrate, which is loaded with metallic ground plane to achieve total reflection. To obtain a wide bandwidth in the band higher than 12 GHz (λ_L=25 mm), the unit dimension of the proposed AMC should be in the range from $0.1\lambda_L$ to $0.2\lambda_L$ (2.5 mm~5 mm). In consideration of the complexity of the unit design, the AMC unit dimension is chosen as 4 mm. The optimized parameters of the two AMC units are listed in Table 1.

Table 1: Optimized parameters of the two AMC units

Parameters	Values	Parameters	Values
a1	0.48 mm	w	0.4 mm
w1	0.2 mm	dd	0.2 mm
l	3.7 mm	dl	0.9 mm
m	1.69 mm	ww	0.3 mm

The reflection phase properties of the two AMC unit are calculated by ANSYS HFSS, which utilizes a unit cell with Floquet-port excitation and master/slave boundaries. As can be obtained in Fig. 2 (a), the AMC unit cell1 demonstrates a $0°$ phase reflection value at 20 GHz. In addition, near the location of the $0°$ reflection phase frequency point of AMC unit cell1, the AMC unit cell2 depicts a $180°$ reflection phase at 19 GHz, which contributes to a broad reflection phase difference frequency band. As shown in Fig. 2 (b) is the reflection phase difference curve between the two AMCs. It illustrates that a reflection phase difference $(180°\pm37°)$ frequency band ranging from 11.6 GHz to 28.1 GHz for normal incidence can be obtained. Consequently, with the two novel types of AMC units, a wide band of 83.1% for 10 dB RCS reduction can be expected compared with the phase difference bandwidth results achieved in [11-15].

Of all the parameters, parameters a_1, l, and dd have a great impact on the reflection phase property of the two AMC units, as can be seen in Figs. 3 (a-c). The values of a_1 and l determine the center frequency of the two AMC unit cells. To make the phase difference in high frequency band be lower than $217°$ on the basis of wide phase different bandwidth, the values of a_1 is chosen as 0.48 mm. For the compromise of wide phase different bandwidth and the phase difference in low frequency band, which should be lower than $217°$, the value of l is decided to be 3.7 mm. In addition, from Fig. 3 (c), it can be obtained that the parameter dd makes an effect on the reflection phase beside the $180°$ phase reflection frequency of AMC unit cell2, which finally determines

the phase difference between the two AMC units.

(a) Reflection phases

(b) Reflection phase difference
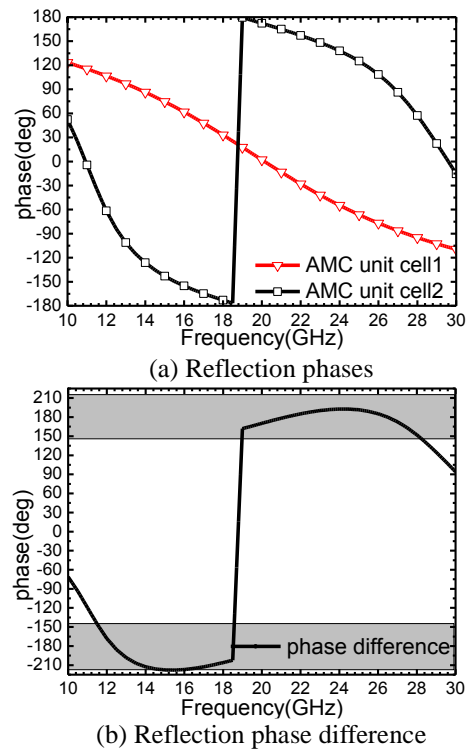
Fig. 2. (a) Reflection phases for both AMCs, and (b) reflection phase difference between two AMCs versus frequency.

Once the dimensions of the two units are fixed, the AMC configuration can be designed. To further decrease the RCS value, the AMC surface is made up of the two units by fan-type arrangement, as shown in Fig. 4. While, an array with an infinite dimension cannot be fabricated in applications. Thus, an array combined by finite number of units need to be designed. If the number of units is too small, the frequency band will move to high frequency and there will be poor property of the phase cancellation between two type of units, which makes it difficult to reduce RCS in the required band. In addition, too large number of AMC units will cause the grating lobes to converge in the edge direction [10], which go also against the RCS reduction. According to the research on AMC structure in [14] and [15], an array arranged by 20×20 units are enough to valid the simulated results in an infinite environment and to be utilized to reduce RCS. Therefore, an AMC surface, the dimensions of which is 80×80 mm^2, is arranged by 20×20-unit cells in this paper. With fan-type arrangement, the number of interfaces between different units can be increased, which helps the energy be scattered more effectively in non-specular directions [16, 17]. Therefore, the proposed AMC array can obtain a larger value for RCS reduction.

(a) Impact of a1 on AMC unit cell1

(b) Impact of l on AMC unit cell2

(c) Impact of dd on AMC unit cell2
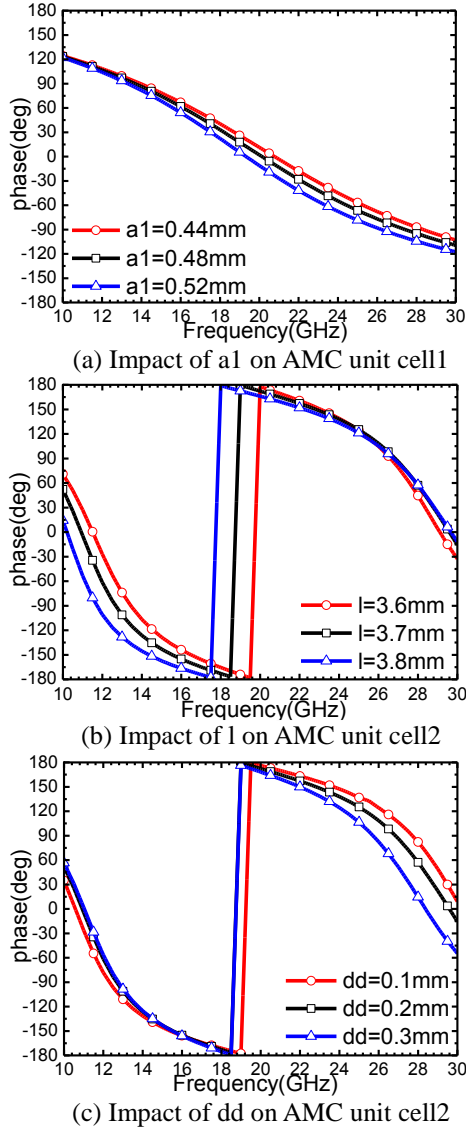
Fig. 3. (a) Impact of a_1 on the reflection phase of AMC unit cell1, and impact of (b) l, and (c) dd on the reflection phase of AMC unit cell2.
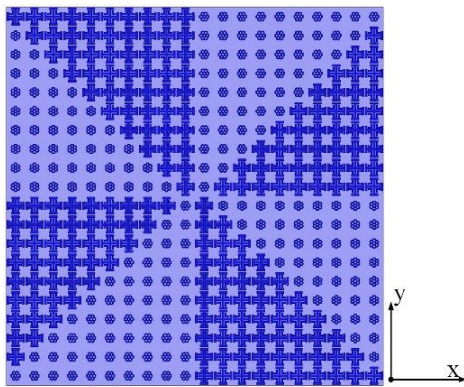
Fig. 4. Top view of the AMC surface configuration.

III. EXPERIMENT AND SIMULATION RESULTS AND DISCUSSION

A. Simulated results

To evaluate the RCS reduction bandwidth of the proposed AMC surface, the monostatic RCS of the AMC surface and PEC surface with equal size for normal incidence is simulated, and Fig. 5 (a) shows the co- and cross-polarized RCS under normal incidence for both x and y polarizations. To calculate the value of RCS reduction, the RCS values are normalized with respect to the PEC surface, as demonstrated in Fig. 5 (b). It can be obtained from the simulated RCS reduction curve, a broad 10 dB RCS reduction frequency band ranging from 12.2 GHz to 27 GHz (75.5%) for x-polarization and from 12.2 GHz to 27.2 GHz (76.1%) for y-polarization is achieved. And the maximum co-polarized RCS reduction, which is more than 30 dB, is obtained at 23 GHz. The simulated RCS reduction band agrees well with the phase difference frequency band (11.6-28.1 GHz) of the two unit cells discussed in the previous section.

(a) Monostatic RCS of PEC and AMC
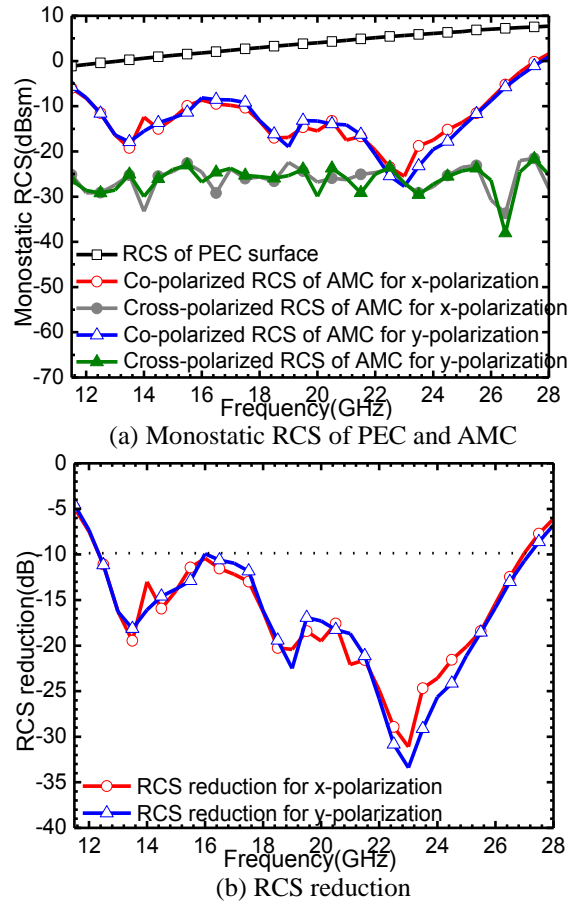
(b) RCS reduction

Fig. 5. Simulated monostatic RCS of the proposed AMC surface and PEC surface with the equal size and the simulated RCS reduction of the proposed AMC structure under normal x- and y-polarized incident waves.

Moreover, Fig. 6 depicts the normalized bistatic RCS of the proposed AMC surface at 20 GHz (which is close to the center frequency point of the RCS reduction band). It shows that it can be achieved about more than 20 dB RCS reduction at 20 GHz by the proposed AMC surface for x polarization in all incident angles. In addition, Fig. 7 demonstrates the simulated 3-D normalized bistatic RCS for x polarization of the proposed AMC surface and PEC surface with the same dimension at 20 GHz. Compared with the bistatic RCS of PEC surface, the designed AMC surface achieves low RCS in boresight direction and reflects the scattering energy in other directions.
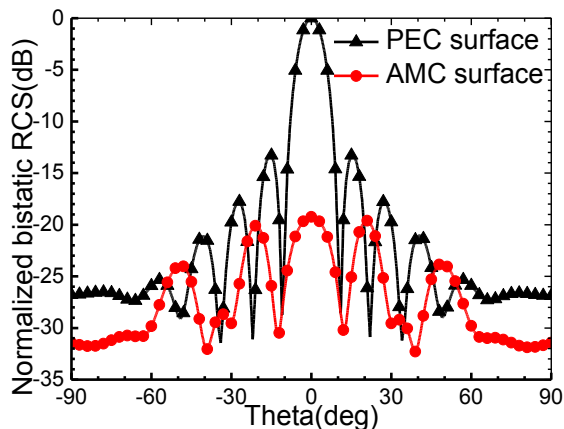
Fig. 6. Simulated 2-D normalized bistatic RCS of the proposed AMC surface and PEC surface for x polarization under normal incidence at 20 GHz.

B. Fabrication and measured results

To validate the simulated RCS property, the proposed AMC surface with dimensions of $80 \times 80 mm^2$ is fabricated, as shown in Fig. 8 (a), and is measured by the compact antenna test range method in anechoic chamber, as depicted in Fig. 8 (b). Owing to the limit of test factor, the monostatic RCS of the fabrication is measured in the band below 18 GHz.

From the simulated results in Fig. 5, it can be obtained that the co-polarized RCS for y polarization is similar to that for x polarization owing to the approximate rotational symmetry of the AMC structure. Therefore, the co-polarized RCS of the AMC surface for x polarization is measured only. Figure 9 (a) illustrates the measured monostatic RCS of the proposed AMC surface and PEC surface (a replacement by an aluminum sheet) with the same dimension under normal incidence for x polarization. By normalizing with respect to the equal size PEC surface, Fig. 9 (b) demonstrates the measured RCS reduction of the fabricated AMC surface. It can be obtained from the measured results that the RCS

reduction frequency band below 18 GHz ranges from 13.16 to 18 GHz. Compared with the simulated frequency band (12.2-18 GHz), there is a good agreement between the simulated and measured results except for a little frequency shifting, which is caused by fabricated and measured errors and the limited size of the fabricated AMC surface.

(a) PEC surface

(b) AMC surface for x polarization
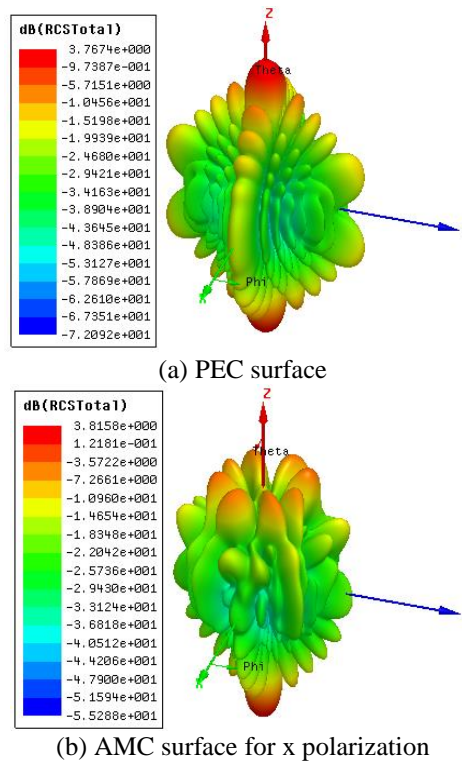
Fig. 7. Simulated 3-D normalized bistatic RCS of the proposed AMC surface and PEC surface for x polarization under normal incidence at 20 GHz.

(a)   (b)
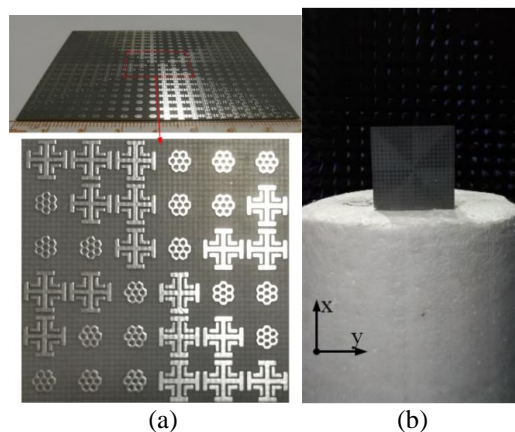
Fig. 8. Photograph of fabricated fan-type AMC surface and its measured environment.

(a) Monostatic RCS
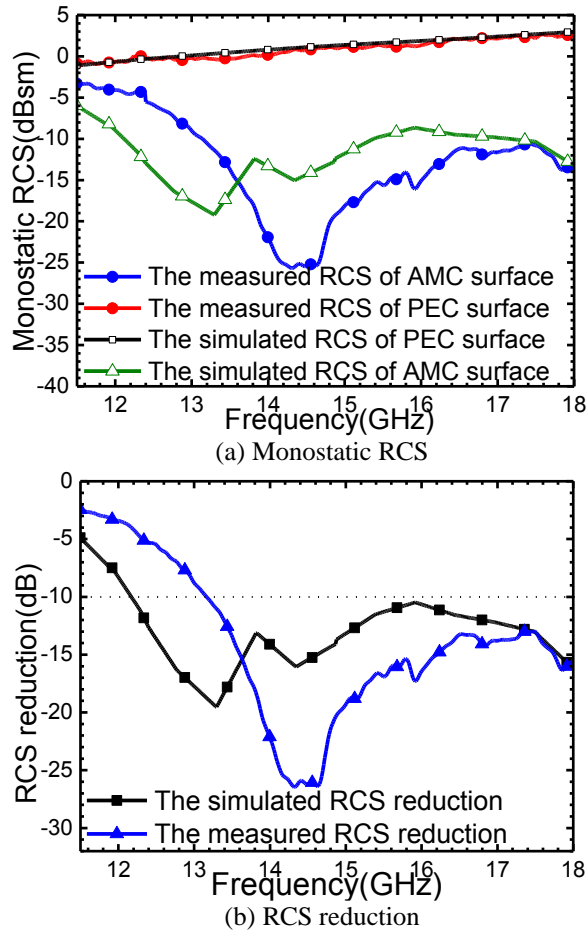
(b) RCS reduction

Fig. 9. Simulated and measured co-polarized: (a) monostatic RCS of the proposed AMC surface and PEC surface with the equal size, and (b) RCS reduction of the proposed AMC surface under normal incidence for x polarization.

Table 2: Comparison on the simulated and measured performances with previously proposed AMC surface

Ref.	Phase Difference BW (GHz)	Simulated 10 dB RCS Reduction BW (GHz)	Measured 10 dB RCS Reduction BW (GHz)
[11]	--	7-12 (52.8%)	7-12 (52.8%)
[12]	12.1-20.5 (51.5%)	13.4-26.9 (67%)	13.5-28.1 (70.2%)
[13]	13.25-24.2 (58.5%)	13.25-24.2 (58.5%)	--
[14]	--	3.76-7.51 (67%)	4.1-7.59 (60%)
[15]	6-14 (80%)	6-13.4 (76%)	6-12 (66.7%)
Our work	**11.6-28.1 (83.1%)**	**12.2-27.2 (76.1%)**	**13.16- …**

Table 2 depicts the comparison performances of the designed AMC structure to the previously proposed AMC surface. From the compared results, it can be demonstrated that the fan-type AMC configuration presented in this paper can achieve wider phase difference frequency band and broader bandwidth for 10 dB RCS reduction.

IV. CONCLUSION

A novel AMC surface is investigated to achieve RCS reduction in a wide band. The configuration is combined by two kinds of unit cells - hexagon rings and Jerusalem crosses. With these two novel units, a reflection phase difference ($180°\pm37°$) band from 11.6 GHz to 28.1 GHz for normal incidence can be obtained. Furthermore, with a fan type arrangement by the two units, the proposed AMC surface demonstrates a broad 10 dB RCS reduction frequency band ranging from 12.2 GHz to 27 GHz (75.5%) for x-polarization and from 12.2 GHz to 27.2 GHz (76.1%) for y-polarization. Then, the proposed AMC surface with dimensions of 80×80 mm^2 is fabricated and measured by the compact antenna test range method in anechoic chamber. The agreement between the measured and simulated results in the band below 18 GHz verifies that the proposed AMC configuration can be utilized in low-RCS platforms.

REFERENCES

[1] Y. Ishii, T. Masaki, N. Michishita, H. Morishita, and H. Hada, "RCS reduction characteristics of thin wave absorbers composed of flat and curved metasurfaces," *2016 International Symposium on Antennas and Propagation (ISAP)*, pp. 192-193, 2016.

[2] Z. X. Zhang and J. C. Zhang, "RCS reduction for patch antenna based on metamaterial absorber," *2016 Progress in Electromagnetic Research Symposium (PIERS)*, pp. 364-368, 2016.

[3] K. L. Ford and B. Chambers, "Tunable single layer phase modulated radar absorber," *in 2001 Eleventh International Conference on Antennas and Propagation*, vol. 2, pp. 588-592, 2001.

[4] Y. Q. Li, H. Zhang, Y.-Q. Fu, and N. C. Yuan, "RCS reduction of ridged waveguide slot antenna array using EBG radar absorbing material," *IEEE Antennas Wireless Propag. Lett.*, vol. 7, pp. 473-476, 2008.

[5] H. K. Jang, J. H. Shin, and C. G. Kim, "Low RCS patch array antenna with electromagnetic bandgap using a conducting polymer," *2010 International Conference on Electromagnetics in Advanced Applications*, pp. 140-143, 2010.

[6] D. Feng, H. Zhai, L. Xi, S. Yang, K. Zhang, and D. Yang, "A broadband low-profile circular-polarized antenna on an AMC reflector," *IEEE Antennas Wireless Propag. Lett.*, vol. 16, pp. 2840-2843, 2017.

[7] H. Zhai, K. Zhang, S. Yang, and D. Feng, "A low-profile dual-band dual-polarized antenna with an AMC surface for WLAN applications," *IEEE Antennas Wireless Propag. Lett.*, vol. 16, pp. 2692-2695, 2017.

[8] M. A. Belen, F. Güneş, P. Mahouti, and A. Belen, "UWB gain enhancement of horn antennas using miniaturized frequency selective surface," *ACES Journal*, vol. 33, no. 9, pp. 997-1002, 2018.

[9] Y. Zhao, X. Y. Cao, J. Gao, X. Yao, T. Liu, W. Q. Li, and S. J. Li, "Broadband low-RCS metasurface and its application on antenna," *IEEE Trans. Antennas Propag.*, vol. 64, no. 7, pp. 2954-2962, 2016.

[10] M. Paquay, J. C. Iriarte, and I. Ederra, "Thin AMC structure for radar cross section reduction," *IEEE Trans. Antennas Propag.*, vol. 55, no. 12, pp. 3630-3638, 2007.

[11] Y. C. Song, J. Ding, C. J. Guo, Y. H. Ren, and J. K. Zhang, "Ultra-broadband backscatter radar cross section reduction based on polarization-insensitive metasurface," *IEEE Antennas Wireless Propag. Lett.*, vol. 15, pp. 329-332, 2016.

[12] P. Yao, B. Z. Zhang, and J. P. Duan, "A broadband artificial magnetic conductor reflecting screen and application in microstrip antenna for radar cross-section reduction," *IEEE Antennas Wireless Propag. Lett.*, vol. 17, no. 3, pp. 869-872, 2018.

[13] Y. Zhang, R. Mittra, B. Z. Wang, and N. T. Huang, "AMCs for ultra-thin and broadband RAM design," *Electronics Lett.*, vol. 45, no. 10, pp. 484-485, 2009.

[14] W. G. Chen, C. A. Balanis and C. R. Birtcher, "Checkerboard EBG surfaces for wideband radar cross section reduction," *IEEE Trans. Antennas Propag.*, vol. 63, no. 6, pp. 2636-2645, 2015.

[15] C. Zhang, J. Gao, X. Y. Gao, L. Xu, and J. F. Han, "Low scattering microstrip antenna array using coding artificial magnetic conductor ground," *IEEE Antennas Wireless Propag. Lett.*, vol. 17, no. 5, pp. 869-872, 2018.

[16] Y. Zhang, R. Mittra, and B. Z. Wang, "Novel design for low-RCS screens using a combination of dual-AMC," *2009 IEEE Antennas and Propagation Society International Symposium*, pp. 1-4, 2009.

[17] X. Y. Song, Z. H. Yan, and T. L. Zhang, "Broadband AMC surface for radar cross section reduction," *The 10th International Conference on Microwave and Millimeter Wave Technology*, Chengdu, China, 2018.

[18] Y. Zhao, X. Y. Cao, J. Gao, X. Yao, and X. Liu, "A low-RCS and high-gain slot antenna using broadband metasurface," *IEEE Antennas Wireless Propag. Lett.*, vol. 15, pp. 290-293, 2016.

[19] B. A. Munk, *Frequency Selective Surfaces: Theory and Design*, New York, John Wiley & Sons, 2000.

Xueyan Song was born in Henan Province, China, 1989. She received the B. E. degree in Electronic and Information Engineering from Xidian University, Xi'an, China, in 2012. She received the Ph.D. degree in Electromagnetic Fields and Microwave Technology from Xidian University, Xi'an, China, in 2018.

She joined the School of Electronic Engineering, Xi'an University of Posts and Telecommunications in 2018. Her research interests include artificial magnetic conductors, low RCS antennas, low-profile antennas, frequency selective surfaces, and reflector antennas.

Lei Chen was born in Shaanxi Province, China, 1982. She received the Ph.D. degrees in Electromagnetic Fields and Microwave Technology from Xidian University, Xi'an, China, in 2010.

She is an Associate Professor at Xidian University. Her research interests include retrodirective array, reflectarray and smart antenna.

Zehong Yan was born in Hubei Province, China, 1964. He received the B.E. degree in Antenna and Microwave from Xidian University, Xi'an, China, in 1984. He received the Ph.D. degree in Electromagnetic Fields and Microwave Technology from Northwestern Polytechnical University, Xi'an, China, in 1996.

He joined the School of Electronic Engineering, Xidian University in 1987 and was promoted to Associate Professor and Professor in 1996 and 2000, respectively, where he is currently a doctoral supervisor with the School of Electronic Engineering. His research interests include communication antennas, satellite tracking antennas, and microwave devices.

Yanyan Li was born in Shanxi Province, China, 1988. She received the B.E. degree in Electronic Information Science and Technology from Xinzhou Teachers University, Xinzhou, China, in 2012. She received the Ph.D. degree in Electromagnetic Fields and Microwave Technology from Xidian University, Xi'an, China, in 2017.

Her research interests include computational electromagnetics, Radar target characteristics and phased array antennas.

Full and Independent Manipulation of Co- and Cross-polarized Waves with Metasurface

Jianxun Su [1], Jiayi Liu [1], Zengrui Li [1], and Lamar Y. Yang [2]

[1] School of Information and Communication Engineering
Communication University of China, Beijing, 100024, China
zrli@cuc.edu.cn

[2] Department of Electrical and Computer Engineering
University of Nebraska-Lincoln, NE, 68182, USA

Abstract ─ A novel metasurface based on the amplitude-phase manipulation and beamforming is proposed for the control of co- and cross-polarized wave simultaneously and independently. The metasurface consists of two polarization conversion elements (PCEs) and their mirrors: the two PCEs are used to control the co-polarized waves with the co-polarized field component of equal amplitude and opposite phase, and the mirrors of them that are intent to control the cross-polarized waves. Full manipulation of the amplitude and phase for both co- and cross-polarized components of the reflected waves is realized by adjusting the geometric parameters of two PCEs. Compared with the traditional co-polarized phase-only manipulation, freedom degree of manipulation is increased from 1 to 4, which greatly increases the ability of manipulating electromagnetic waves. The arrangement of PCEs is obtained based on the planar array theory to achieve the desired co-polarized and cross-polarized scattering patterns. The theoretical analysis, simulation and experiment results are in good agreement and verify the proposed mechanism.

Index Terms ─ Co-polarized, cross-polarized, metasurface, manipulation.

I. INTRODUCTION

As a very important breakthrough, metamaterials have powerful abilities to manipulate electromagnetic waves because they can be designed to have arbitrary permittivity and permeability. By tailoring the geometry or materials of the components, many special phenomena have been demonstrated, such as subwavelength imaging [1], beam rotation [2], invisibility cloaks [3, 4], and so on. Therefore, the use of ultra-thin design to effectively manipulate the propagation of electromagnetic waves attracted more and more research efforts. In recent years, the two-dimensional metamaterials which are called metasurfaces have subwavelength characteristics in the direction of wave propagation and greatly simplify the

requirements of fabrication while maintaining powerful functionality of controlling the propagation properties of electromagnetic waves [5, 6]. By introducing abrupt phase discontinuities on the surface of the metal or dielectric structure, metasurfaces can realize extraordinary light manipulations, for example, light bending [7, 8], vortex beam generation [9], focusing [10, 11], wave plates [12, 13], holograms [14, 15], and microstrip filter [16]. Benefiting from small profile and flexible phase control, metasurfaces become very attractive and replace the traditional polarization controller for miniaturization devices. In the past few years, a variety of designs have been proposed to achieve effective polarization alteration from visible light to microwaves [17, 18]. Anisotropic structures such as T-shaped, C-shaped and L-shaped structures and the split ring are widely used to adjust the phase difference of two orthogonal electric field components [19, 20]. In addition to radar scattering cross section reduction, a new type of polarization conversion metasurface was put forward [21]. Theoretical and numerical of investigation of the chiral slab exhibiting polarization rotation is presented in detail [22].

Full control of both the magnitude and phase of transmission and reflection respectively are important issue for free manipulation of electromagnetic wave propagation. Recently, many efforts have been made to manipulate the electromagnetic waves by using metamaterials and metasurfaces. However, most of them mainly adjust the phase of the co-polarized component of the reflected waves, namely single-degree-of-freedom manipulation. For example, a method by designing the reflection-phase distributions of the anisotropic metasurface with Jerusalem Cross structures along the x and y directions has been proposed [23], the x- and y-polarized incident waves can be manipulated independently to realize multi-beam reflections. The proposed method provides an extensive approach to manipulate the reflected beams and their polarizations independently. Otherwise, methods to tailor the reflection

and scattering of THz waves in an anomalous manner by using coding metamaterials have been presented [24-26]. The THz coding metamaterials realized by using two structures formed without and with, respectively, a metallic ring resonator on top of a metal ground plane in [24] are proposed. The anisotropic coding metasurfaces which use square-shaped and dumbbell-shaped metallic structures in [25] are proposed. A general coding unit based on a Minkowski closed-loop particle in [26] are proposed. The proposed structures have strong abilities to control THz waves by designing specific coding sequences of the phase of the co-polarized component of the reflected waves. These works reveal new methodology arising from coding metamaterials in effective manipulation of THz wave propagation and may offer widespread applications. In addition to effective medium parameters, the programmable metamaterials have recently been proposed as an alternative approach to manipulate the electromagnetic waves. The element integrated with one PIN diode is designed for two reflection-type elements with a 180° phase difference [27], and thus a binary coded phase is realized for a single polarization. Based on this idea, various functionalities, such as steering, bending, focusing and random electromagnetic waves scattering, can be simply implemented by digitally encoding metasurfaces with the corresponding coding sequences.

In this paper, we propose two metasurfaces based on a novel physical mechanism which can realize the beamforming and multi-degree-of-freedom manipulation of electromagnetic waves. We designed three different kinds of PCEs. By changing their geometric parameters, we can get the relationship between the amplitude and phase of the co-polarized and cross-polarized components of the reflected waves for different PCEs. By combining the proposed PCEs and their mirrors on the metasurface, we can realize the control of the amplitude and phase of the co- and cross-polarized components of the reflected waves, namely four-degree-of-freedom manipulation of electromagnetic waves. In this work, the state of the polarization mode and the power density distribution of the beams of the reflected waves can be manipulated flexibly and simultaneously. One of the metasurfaces is fabricated and measured to further prove the feasibility of our novel physical mechanism. The analysis, simulation and measurement results demonstrate that the proposed metasurface can realize beamforming and manipulate electromagnetic waves in four-degree-of-freedom, which may have potential applications in satellite communications, millimeter wave image system, radar system and so on.

II. THEORY AND PCE DESIGN

A. Theory

The design of coding sequences is based on the planar array theory. As shown in Fig. 1, "1" and "0" coding particles are distributed in a chessboard configuration. The lengths of each coding particle along x- and y-axis are marked by d_x and d_y, respectively. The planar array has N_x rows along the x axis and N_y columns along the y axis, $N_x = md_x$, $N_y = nd_y$.
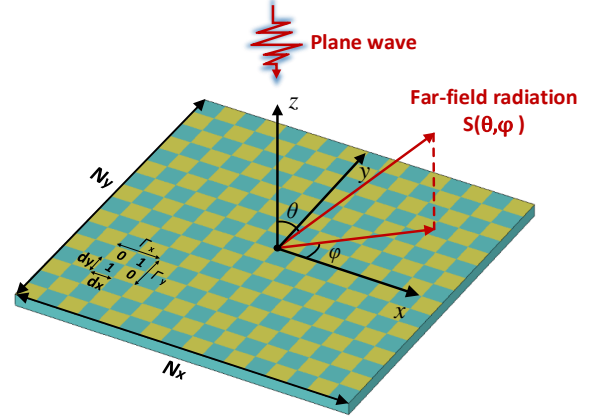
Fig. 1. The schematic for the rectangular grid coding plane array.

The formula for calculating the far-field pattern of the metasurface under the normal illumination of plane wave is expressed below:

$$S(\theta,\varphi) = \sum_{m=1}^{M}\sum_{n=1}^{N} R_{mn} \exp\{ jk\sin\theta[(m-\frac{1}{2})d_x\cos\varphi + (n-\frac{1}{2})d_y\sin\varphi]\},$$

(1)

where R_{mn} is the reflection coefficient of the (m, n)-th coding particle is defined by:

$$R_{mn} = A_{mn}e^{j\psi_{mn}} = \begin{cases} Ae^{j\psi_0} & \text{For coding particle "0",} \\ Ae^{j(\psi_0+\pi)} & \text{For coding particle "1".} \end{cases}$$

(2)

For the 1-bit coding metasurface, the reflection amplitudes of coding particles "0" and "1" are unity and the phase difference between them are 0 and π, respectively. Since the absolute value of reflection phase Ψ_0 is a constant and can be moved out of the summation, it is assumed to be zero. The double summation in (1) can be separated as:

$$S(\theta,\varphi) = \sum_{m=1}^{M} \exp\{ j[(m-\frac{1}{2})kd_x\sin\theta\cos\varphi + m\pi]\}$$
$$\cdot \sum_{n=1}^{N} \exp\{ j[(n-\frac{1}{2})kd_x\sin\theta\sin\varphi + n\pi]\}.$$

(3)

From (3) we can obtain the far field scattering of the reflected waves.

Next, the derivation of the abnormal reflection angle is introduced [25]. When the angles θ and φ satisfying the following conditions, the first diffraction order of the reflected beam becomes:

$$\varphi = \pm \arctan(\frac{d_x}{d_y}) \text{ and } \varphi = \pi \pm \arctan(\frac{d_x}{d_y}), \quad (4)$$

$$\theta = \arcsin(\frac{\pi}{k} \cdot \sqrt{\frac{1}{d_x^2} + \frac{1}{d_y^2}}) \cdot \quad (5)$$

Considering $\Gamma_x = 2d_x$, $\Gamma_y = 2d_y$, $k = 2\pi/\lambda$, (5) can be written as:

$$\theta = \arcsin(\lambda \cdot \sqrt{\frac{1}{\Gamma_x^2} + \frac{1}{\Gamma_y^2}}) \cdot \quad (6)$$

The anomalous reflection direction of the normally incident is given by (4) and (6). They are not only applicable to the coding metasurface encoded with 1-bit but also valid for higher bits. If the metasurface is encoded with periodic coding sequences along one direction (x- or y-direction), the elevation angle θ defined in equation can be simplified as below:

$$\theta = \arcsin(\frac{\lambda}{\Gamma}), \quad (7)$$

where λ and Γ represent the free-space wavelength and the physical length of one period of the coding sequence (that is the minimum length of gradient phase). So the anomalously deflected angles along the x- and y-directions can be independently calculated by (7).

B. PCE design

Electromagnetic waves controlled by PCEs are flexible and independent, and distinct functionalities can be realized via the combination of different elements and different arrangement. In order to ensure that the PCE is insensitive to the polarization of the impinging wave, the geometric structure is symmetrical with respect to 45° diagonal. For the sake of analysis, u- and v-axes are introduced here along 45° direction with respect to x- and y-directions. For the different power density distribution of the co- and cross-polarized components of the reflected waves, three types of PCEs have been presented, the structures of them are depicted in Fig. 2, and all of them are symmetrical along u- and v-axes. The PCEs are printed on the surface of PTFE woven glass (Model: F4B-2) substrate with a thickness of 2.93 mm and a dielectric constant $\varepsilon_r = 2.65$ (loss tangent tan δ = 0.001). As shown in Figs. 2 (a)-(c), PCE_1 is composed of a structure combined with a square ring and a cut wire, PCE_2 is a double-head arrow structure and PCE_3 is composed of a symmetric spilt ring and a cut wire. The geometric parameters of the structures are illustrated in Fig. 2. By changing the parameter values of the structures, two PCEs with equal amplitude and opposite phase in both co- and cross-polarized components at a certain frequency and their mirrors are selected. By designing coding sequences and forming a metasurface, the multi-degree-of-freedom manipulation of electromagnetic waves can be realized. The far-field scattering patterns are presented to demonstrate the characteristics of the encoded metasurface.
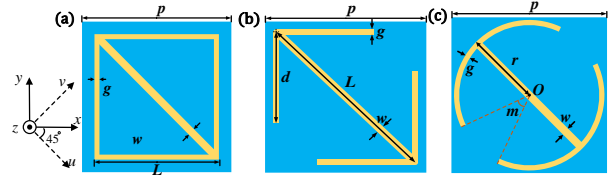
Fig. 2. The front view of the three PCEs: (a) PCE_1, p=6mm, g=0.2mm, w=0.3mm, L is a variable, (b) PCE_2, p=6mm, g=0.2mm, w=0.3mm, L is a variable, d=k*L (k=0.5), and (c) PCE_3, p=6mm, g=0.2mm, w=0.3mm, r=2.65mm, m is a variable.
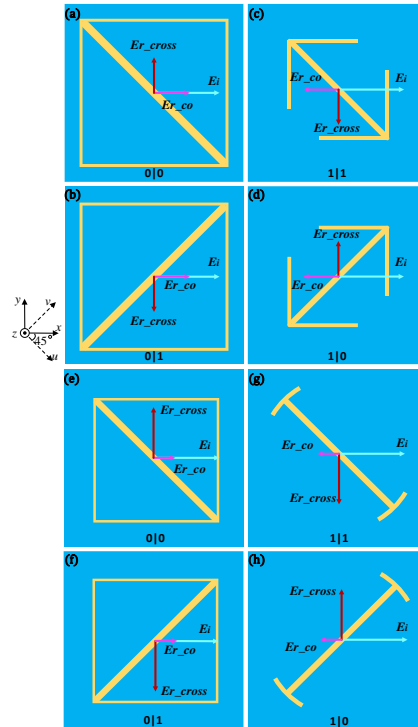
Fig. 3. The designed PCEs for the coding metasurfaces. The first group: (a) PCE_{1-1}, (b) the mirror of PCE_{1-1}, (c) PCE_{2-1}, and (d) the mirror of PCE_{2-1}. The second group: (e) PCE_{1-2}, (f) the mirror of PCE_{1-2}, (g) PCE_{3-1}, and (h) the mirror of PCE_{3-1}.

We use the 1-bit case to demonstrate the control of functionalities via the coding metasurface with PCEs. For the different power density distribution of the co- and cross-polarized components of the reflected waves, two groups of PCEs are picked out. The first group satisfies that both the co- and cross-polarized components of the reflected waves account for 50% of power density at 20.7 GHz. As shown in Figs. 3 (a)-(d), it consists of four PCEs: PCE_1 with L=5.1 mm which is marked as PCE_{1-1}, PCE_2 with L=3.15 mm which is marked as PCE_{2-1} and their mirrors. The numerical simulation results of the reflected amplitude and phase obtained by CST indicate that PCE_{1-1} and PCE_{2-1} have equal

amplitude and nearly 180° phase difference in both co- and cross-polarized components of the reflected waves at 20.7 GHz under the normal x-polarized incident waves as shown in Fig. 4. For PCE$_{1-1}$, the amplitude and phase of co-polarized reflected waves are 0.71 and 453.3°, the amplitude and phase of cross-polarized reflected waves are 0.70 and -543.6°. For PCE$_{2-1}$, the amplitude and phase of co-polarized reflected waves are 0.71 and -273.2°, and the amplitude and phase of cross-polarized reflected waves are 0.70 and -363.1°.
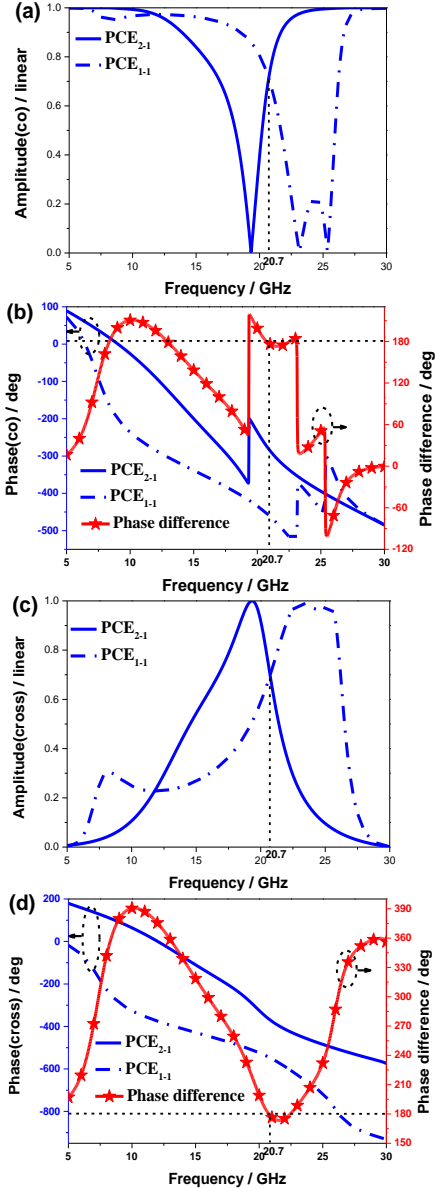
Fig. 4. The co- and cross-polarized reflection coefficients for PCE$_{1-1}$ and PCE$_{2-1}$ under normal x-polarized incident waves: (a) amplitude and (b) phase of co-polarized reflection coefficient, (c) amplitude and (d) phase of cross-polarized reflection coefficient.

Besides, the co-polarized components of the reflected waves of the PCE and their mirrors are equal in amplitude and phase, while the cross-polarized components of reflected waves are equal in amplitude but opposite in phase. The combination of the four PCEs can realize the control of co- and cross-polarized.
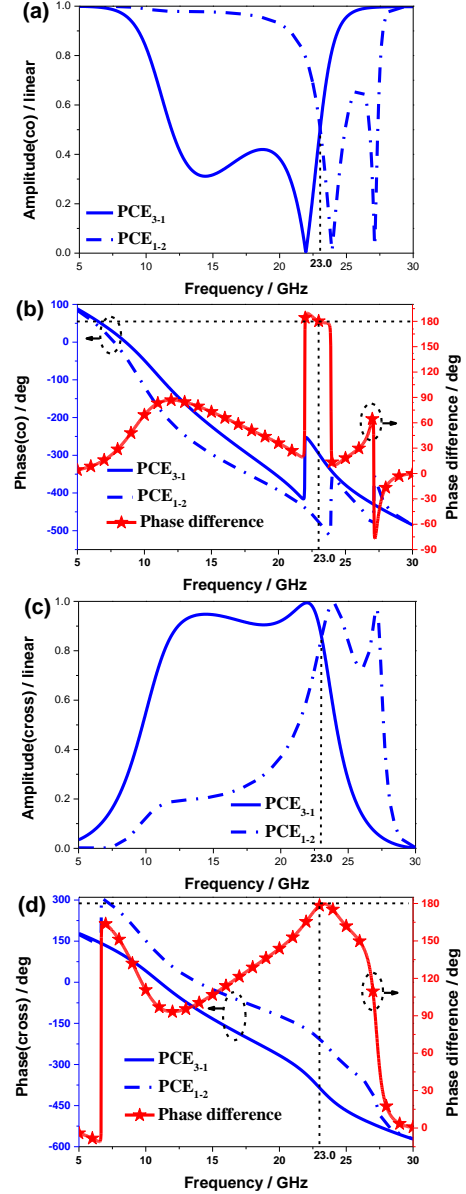
Fig. 5. The co- and cross-polarized reflection coefficients for PCE$_{1-2}$ and PCE$_{3-1}$ under normal x-polarized incident waves: (a) amplitude and (b) phase of co-polarized reflection coefficient, (c) amplitude and (d) phase of cross-polarized reflection coefficient.

The second group satisfies that the co-polarized component of the reflected waves accounts for 25% of power density at 23.0 GHz and the cross-polarized

component accounts for 75%. As shown in Figs. 3 (e)-(h), it consists of four elements: PCE$_1$ with L=4.15 mm which is marked as PCE$_{1-2}$, PCE$_3$ with m=151° which is marked as PCE$_{3-1}$ and their mirrors. The numerical simulation results of the reflected amplitude and phase indicate that PCE$_{1-2}$ and PCE$_{3-1}$ have equal amplitude and nearly 180° phase difference in both co- and cross-polarized components of the reflected waves at 23.0 GHz under the normal x-polarized incident waves as shown in Fig. 5. For PCE$_{1-2}$, the amplitude and phase of co-polarized reflected waves are 0.51 and -476.9°, and the amplitude and phase of cross-polarized reflected waves are 0.85 and -207.7°. For PCE$_{3-1}$, the amplitude and phase of co-polarized reflected waves are 0.50 and -297.0°. The amplitude and phase of cross-polarized reflected waves are 0.86 and -386.3°.

III. DESIGN, SIMULATION, AND MEASUREMENT OF METASURFACES

A. Design and simulation of metasurfaces

The elements mentioned above (Fig. 3) are defined as '0|0' '1|0' '0|1' '1|1' coding particles, where the binary codes before and after the symbol (|) represent the digital states of co- and cross-polarized components of reflected waves, respectively. The selection and arrangement of PCEs on the metasurface requires two steps. For example, we use PCE$_{1-1}$ and PCE$_{2-1}$ and their mirrors to design a metasurface. The first step is to determine the coding table for the co-polarized component. Because PCE$_{1-1}$ and the mirror of PCE$_{2-1}$ have equal amplitude and opposite phase in co-polarized component of the reflected waves at 20.7 GHz under the normal x-polarized incident waves, they are used to design the desired co-polarized scattering pattern based on array theory [28]. Secondly, the coding table for the desired cross-polarized scattering pattern is also determined based on planar array theory. If it has the same code with co-polarized component at the same location, the PCE at that location doesn't change, however, the PCE should be changed to its mirror. The process for the arrangement of PCEs on the metasurface is shown in the Fig. 6.

In order to further analyze the coding metamaterials quantitatively, we first use PCE$_{1-1}$, PCE$_{2-1}$ and their mirrors to encode a metasurface MS$_1$. MS$_1$ is formed by repeating a 2D code matrix m$_1$ with a simple coding sequence of '010101…' along x-axis for the digital states of co-polarized component of reflected waves as well as '010101…' alternates with '101010…' along y-axis for the digital states of cross-polarized component:

$$m_1 = \begin{bmatrix} 0|1 & 1|0 \\ 0|0 & 1|1 \end{bmatrix}.$$

The lattice as shown in Fig. 7 (a) generated by a subarray of the same basic PCEs with a size of 5×5, is used to minimize the unwanted coupling effect resulting from adjacent elements with different geometries. The final encoded metasurface MS$_1$ that contains 6×6 lattices (Fig. 7 (a)) is designed to illustrate the novel physical mechanism. We apply the open boundary condition and plane wave excitation in CST Microwave Studio to simulate the whole encoded metasurface MS$_1$. Figures 8 (a)-(c) shows the total, co-polarized and cross-polarized 3D far-field scattering patterns of MS$_1$ under the normal x-polarized incident waves at 20.7 GHz. The co-polarized component of reflected waves is equally split into two symmetrically oriented beams in the x-z plane at the same angle with respect to z-axis as shown in Fig. 8 (b). And the cross-polarized component of reflected waves is equally split into four symmetrically oriented beams in the φ=45° and 135° planes at the same angle with respect to the z-axis as shown in Fig. 8 (c). In theory, if the co- and cross-polarized components of the reflected waves account for 50% of power density respectively, the power density of each of four beams of cross-polarized component should be decreased by 3.01 dBm^2 compared to each of two beams of co-polarized component. In the result of our simulation, the power density of each of four beams of cross-polarized component is 7.30 dBm^2 while each of two beams of co-polarized component is 10.80 dBm^2, and the difference between them is 3.50 dBm^2, basically consistent with the theoretical value. Besides, the anomalous reflection angle can be calculated by (5) and (6) theoretically. For the main two beams of co-polarized of reflected waves, θ is 13.96°. And for the main four beams of cross-polarized component of reflected waves, θ is 19.95°. The simulated results demonstrate that the main lobe of co-polarized component in the x-z plane deviates from the z-axis to 13.5°, and the main lobe of cross-component in the φ=45° and 135° planes deviates from the z-axis to 19.3°. So the simulation result of the anomalous reflection angle agrees well with the analytical predictions. The 2D far-field scattering pattern in the x-z plane for co-polarized component is shown in Fig. 9 (a), and the patterns in the φ=45°and 135° planes for cross-polarized component are shown in Figs. 9 (b)-(c). We consider that the small disturbance observed in the scattered electric field is attributed to the true reflection phase difference of the adjacent lattice coupling, which is not exactly 180° at 20.7 GHz. However, if we increase the size of the lattice, this effect can be suppressed.

Based on the designed method of MS$_1$, we further propose coding metasurface MS$_2$ as shown in Fig. 7 (b) which consists of PCE$_{1-2}$, PCE$_{3-1}$ and their mirrors. The coding sequences of MS$_2$ are '101010' alternates with '010101…' along x-axis for the digital states of co-polarized component and a random matrix [25] for the digital states of cross-polarized component of reflected waves. The coding matrix is written as:

$$m_2 = \begin{bmatrix} 0|1 & 1|1 & 0|0 & 1|1 & 0|0 & 1|0 & 0|1 & 1|1 \\ 1|1 & 0|1 & 1|1 & 0|1 & 1|0 & 0|0 & 1|1 & 0|0 \\ 0|0 & 1|0 & 0|1 & 1|1 & 0|0 & 1|1 & 0|0 & 1|1 \\ 1|1 & 0|1 & 1|1 & 0|0 & 1|1 & 0|1 & 1|1 & 0|0 \\ 0|1 & 1|1 & 0|1 & 1|1 & 0|1 & 1|0 & 0|1 & 1|1 \\ 1|0 & 0|0 & 1|0 & 0|0 & 1|0 & 0|0 & 1|0 & 0|0 \\ 0|0 & 1|1 & 0|1 & 1|1 & 0|1 & 1|0 & 0|0 & 1|1 \\ 1|1 & 0|0 & 1|1 & 0|0 & 1|0 & 0|1 & 1|0 & 0|1 \end{bmatrix}.$$
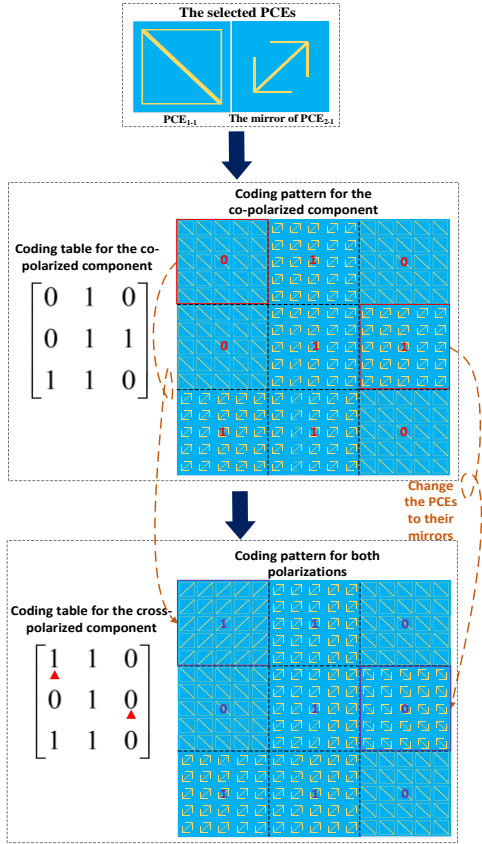
Fig. 6. The process for the arrangement of PCEs on the metasurface.

The basic PCEs of MS$_2$ are PCE$_{1-2}$, PCE$_{3-1}$ and their mirrors. MS$_2$ satisfies that the co-polarized component of the reflected waves accounts for 25% of power density at 23.0 GHz and the cross-polarized component accounts for 75%. Figures 8 (d)-(f) shows the total, co-polarized and cross-polarized 3D far-field scattering patterns of MS$_2$ under the normal x-polarized incident waves at 23.0 GHz. The co-polarized component of reflected waves which accounts for 25% of power density is equally split into four symmetrically oriented beams in the φ=45° and 135° planes at the same angle with respect to the z-axis as shown in Fig. 8 (e). And the cross-polarized component of reflected waves is randomly scattered into many directions and results in a diffusion pattern in the upper half- space which is shown in Fig. 8 (f).
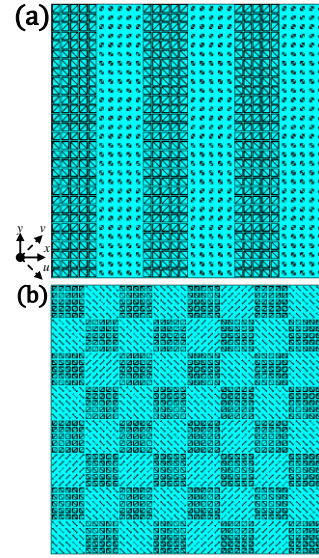
Fig. 7. Coding patterns of two 1-bit metasurfaces: (a) Pattern of MS$_1$ that contains 6×6 lattices with a size of 5×5, and (b) pattern of MS$_2$ that contains 8×8 lattices with a size of 5×5.
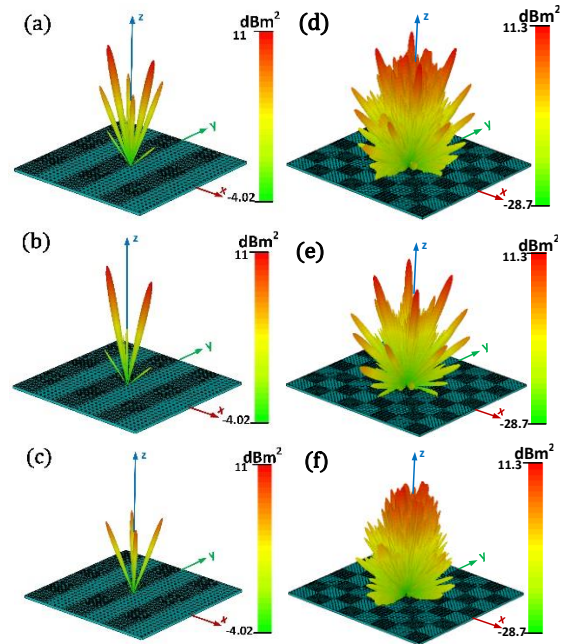
Fig. 8. Simulated 3D far-field scattering patterns for two metasurfaces under the normal x-polarized incident waves: (a)-(c) The total, co-polarized and cross-polarized 3D far-field scattering patterns of MS$_1$ at 20.7 GHz, and (d)-(f) the total, co-polarized and cross-polarized 3D far-field scattering patterns of MS$_2$ at 23.0 GHz.
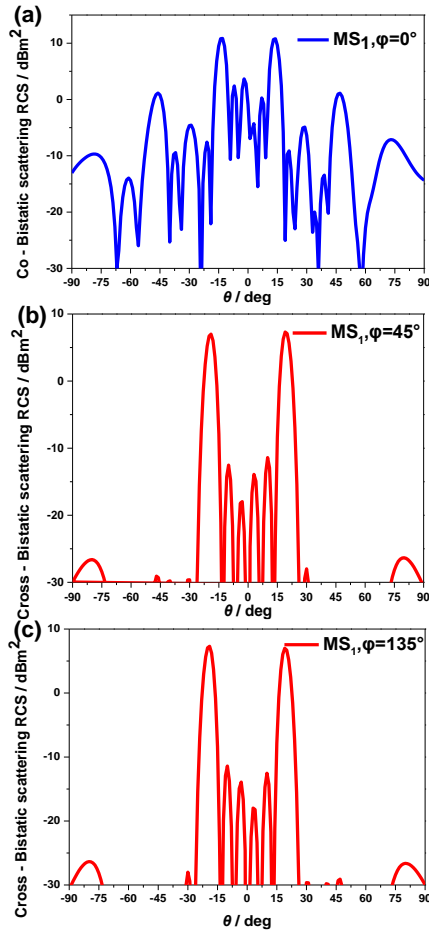
Fig. 9. Simulated 2D far-field scattering patterns for MS_1 under the normal x-polarized incident waves at 20.7 GHz: (a) The co-polarized 2D far-field scattering patterns of MS_1 in the x-z plane, and (b)-(c) the cross-polarized 2D far-field scattering patterns of MS_1 in $\varphi=45°$ and $135°$ plane.

B. Measurement of the metasurface

To further verify the design, a sample (300 mm x 300 mm) of the metasurface is fabricated, as depicted in Fig. 10 (a), which is an extension of MS_1. The sample is manufactured by LPKF ProtoLaser using printed circuit board (PCB) technology. The dielectric substrate is F4B-2 substrate with a thickness of 2.93 mm and a dielectric constant $\varepsilon_r = 2.65$ (loss tangent $\tan \delta = 0.001$). The metal patches and ground are 0.035 mm-thick copper layers. For bistatic measurement setup shown in Fig. 10 (b), transmit antenna is fixed while receive antenna moves along an arc track to detect the reflection fields at scattering angle θ from 6° to 90°. Because the two antennas are very close to each other in the range of -6° to 6°, the bistatic measurement setup is similar to a monostatic measurement setup. Therefore, accurate measurement results cannot be obtained at these locations. Measurement results of bistatic RCS along the

principal (XoZ) plane for the metasurface are presented in Fig. 11, which is the co-polarized 2D far-field scattering pattern of the sample under the normal x-polarized incident waves at 20.7 GHz. It shows that the measured results agree well with the simulations especially the main lobes and verifies that the proposed metasurface can realize the beamforming and multi-degree-of-freedom manipulation of electromagnetic waves. And we consider that the small perturbations observed in the scattered electric field are caused by the true reflection phase difference of the coupling of adjacent lattices.
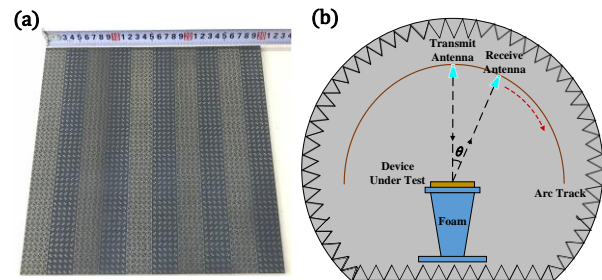
Fig. 10. Photographs of the fabricated sample and schematics of the experimental setup: (a) a sample which is an extension of MS_1, and (b) measurement setup for bistatic RCS.
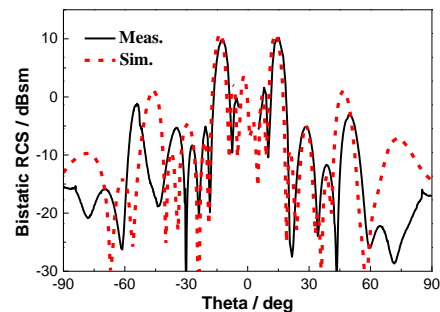
Fig. 11. The measured co-polarized bistatic RCS of the sample under the normal x-polarized incident waves at 20.7 GHz.

IV. CONCLUSION

We have proposed two anisotropic metasurfaces based on a novel mechanism to control the co- and cross-polarized waves full and independently, thus the beamforming and the multi-degree-of-freedom manipulation of electromagnetic waves have been realized. The metasurface, which can increase the freedom degree of manipulation from 1 to 4 compared with co-polarized phase-only manipulation, is composed of two types of PCEs and their mirrors. The full-wave simulated results verify that the scattering pattern of co- and cross-polarized waves can be manipulated independently and simultaneously, such as beamforming,

scattering angles and polarization states. To validate the proposed design, one typical metasurface has been fabricated and measured. Our experiment results show very good agreement with the corresponding simulation in terms of bistatic RCS pattern. In addition, the flexibility in manipulating the electromagnetic waves can be provided by selecting more kinds of combinations of PCEs and diversifying the arrangement of them on metasurfaces. The proposed metasurface shows the advantage of easy fabrication, compactness, and also provides a good choice for manipulating the reflected beams and their polarizations independently, which makes it promising in the broad applications such as electromagnetic cloaking, subwavelength imaging, beam rotation, etc.

ACKNOWLEDGMENT

REFERENCES

[1] J. B. Pendry, "Negative refractive makes a perfect lens," *Phys. Rev. Lett.*, vol. 85, pp. 3966-3969, 2000.

[2] H. Chen, B. Hou, S. Chen, X. Ao, W. Wen, and C. T. Chan, "Design and experimental realization of a broadband transformation media field rotator at microwave frequencies," *Phys. Rev. Lett.*, vol. 102, p. 183903, 2009.

[3] J. B. Pendry, D. Schurig, and D. R. Smith, "Controlling electromagnetic fields," *Science*, vol. 312, pp. 1780-1782, 2006.

[4] D. Schurig, J. J. Mock, B. J. Justice, et al., "Metamaterial electromagnetic cloak at microwave frequencies," *Science*, vol. 314, pp. 977-980, 2006.

[5] S. Y. Luo, Y. S. Li, Y. F. Xia, and L. Zhang, "A low mutual coupling antenna array with gain enhancement using metamaterial loading and neutralization line structure," *Appl. Comput. Electromagn. Soc. J.*, vol. 34, pp. 411-418, 2019.

[6] K. Yu, Y. S. Li, and X. G. Liu, "Mutual coupling reduction of a MIMO antenna array using 3-D novel meta-material structures," *Appl. Comput. Electromagn. Soc. J.*, vol. 33, 2018.

[7] N. Yu, P. Genevet, M. A. Kats, et al., "Light propagation with phase discontinuities reflection and refraction," *Science*, vol. 334, pp. 333-337, 2011.

[8] X. Ni, N. K. Emani, A. V. Kildishev, et al., "Broadband light bending with plasmonic nano-antennas," *Science*, vol. 335, p. 427, 2012.

[9] L. Huang, X. Chen, H. Mühlenbernd, et al., "Dispersionless phase discontinuities for controlling light propagation," *Nano Lett.*, vol. 12, pp. 5750-5755, 2012.

[10] F. Aieta, P. Genevet, M. A. Kats, et al., "Aberration-free ultrathin flat lenses and axicons at telecom wavelengths based on plasmonic meta-surfaces," *Nano Lett.*, vol. 12, pp. 4932-4936, 2012.

[11] A. Pors, M. G. Nielsen, R. L. Eriksen, et al., "Broadband focusing flat mirrors based on plasmonic gradient metasurfaces," *Nano Lett.*, vol. 13, pp. 829-834, 2013.

[12] Y. Yang, W. Wang, P. Moitra, et al., "Dielectric meta-reflectarray for broadband linear polarization conversion and optical vortex generation," *Nano Lett.*, vol. 14, pp. 1394-1399, 2014.

[13] N. Yu, F. Aieta, P. Genevet, et al., "A broadband, background-free quarter-wave plate based on plasmonic metasurfaces," *Nano Lett.*, vol. 12, pp. 6328-6333, 2012.

[14] X. Ni, A. V. Kildishev, and V. M. Shalaev, "Metasurface holograms for visible light," *Nat. Commun.*, vol. 4, 2013.

[15] L. Huang, X. Chen, H. Mühlenbernd, et al., "Three-dimensional optical holography using a plasmonic metasurface," *Nat. Commun.*, vol. 4, pp. 2808, 2013.

[16] M. A. Abaga Abessolo, Y. Diallo, A. Jaoujal, A. E. I. Moussaoui, and N. Aknin, "Stop-band filter using a new metamaterial complementary split triangle resonators (CSTRs)," *Appl. Comput. Electromagn. Soc. J.*, vol. 28, pp. 353-358, 2013.

[17] F. Ding, Z. Wang, S. He, et al., "Broadband high-efficiency half-wave plate: A super-cell based plasmonic metasurface approach," *ACS Nano.*, vol. 9, pp. 4111-4119, 2015.

[18] A. Shaltout, J. Liu, V. M. Shalaev, et al., "Optically active metasurface with non-chiral plasmonic nano-antennas," *Nano Lett.*, vol. 14, pp. 4426-4431, 2014.

[19] S. C. Jiang, X. Xiong, Y. S. Hu, et al., "High-efficiency generation of circularly polarized light via symmetry-induced anomalous reflection," *Phys. Rev. B.*, vol. 91, 2015.

[20] S. C. Jiang, X. Xiong, Y. S. Hu, et al., "Controlling the polarization state of light with a dispersion-free metastructure," *Phys. Rev. X.*, vol. 4, 2014.

[21] J. X. Su, C. Y. Kong, Z. R. Li, X. J. Yuan, and Y. Q. Yang, "Ultra-wideband and polarization-insensitive RCS reduction of microstrip antenna using polarization conversion metasurface," *Appl. Comput. Electromagn. Soc. J.*, vol. 32, pp. 524-530, 2017.

[22] I. Comez, M. Kraaslan, F. Dincer, F. Karadag, and C. Sabah, "Systematic analysis on the optical

properties of chiral metamaterial slab for micro-wave polarization control," *Appl. Comput. Electromagn. Soc. J.*, vol. 30, pp. 478-487, 2015.

[23] F. M. Hui, Q. L. Yan, and L. Kang, "Multi-beam reflections with flexible control of polarizations by using anisotropic metasurfaces," *Sci. Rep.*, vol. 6, 2016.

[24] L. Liang, M. Qi, J. Yang, et al., "Anomalous terahertz reflection and scattering by flexible and conformal coding metamaterials," *Adv. Opt. Mater.*, vol. 3, pp. 1374-1380, 2015.

[25] S. Liu, T. J. Cui, Q. Xu, et al., "Anisotropic coding metamaterials and their powerful manipulation of differently polarized terahertz waves," *Light Sci. Appl.*, vol. 5, 2016.

[26] L. H. Gao, Q. Cheng, J. Yang, et al., "Broadband diffusion of terahertz waves by multi-bit coding metasurfaces," *Light Sci. Appl.*, vol. 4, 2015.

[27] H. Yang, X. Cao, Y. Fan, et al., "A programmable metasurface with dynamic polarization, scattering and focusing control," *Sci. Rep.*, vol. 6, 2016.

[28] C. A. Balanis, *Antenna Theory: Analysis and Design*. 3rd Edition, Wiley, New York, 2005.

Jiayi Liu received the B. Eng. degree in Communication Engineering from the Communication University of China in 2017. She is currently pursuing the M.S. degree at Communication University of China.

Her research interests include metamaterial, corner reflector and electromagnetic wave manipulation.

Jianxun Su received the B.S. degree in Electronic Information Engineering from Taiyuan University of Technology, Taiyuan, China, in 2006; the M.S. degree and the Ph.D. degree in Electromagnetic Field and Microwave Technology from the Communication University of China and Beijing Institute of Technology, Beijing, China, in 2008 and 2011, respectively.

From 2012 to 2014, he was with China Electronics Technology Group Corporation (CETC), where he engaged in phased-array system research. He is currently working as associate researcher at School of Information Engineering, Communication University of China and also with the Science and Technology on Electromagnetic Scattering Laboratory. His special research interests include integral equation method, metamaterial, phased-array antenna, radar target characteristics.

Zengrui Li received the B.S. degree in Communication and Information System from Beijing Jiaotong University, Beijing, China, in 1984; the M.S. degree in Electrical Engineering from Beijing Broadcast Institute, Beijing, China, in 1987; and the Ph.D. degree in Electrical Engineering from Beijing Jiaotong University, Beijing, China, in 2009.

He is currently a Professor with the Communication University of China, Beijing, China. He studied at Yokohama National University, Yokohama, Japan, from 2004 to 2005. His research interests include the areas of finite-difference time-domain (FDTD) methods, electromagnetic scattering, metamaterials and antennas. Li is a Senior Member of the Chinese Institute of Electronics.

Yaoqing Lamar Yang (S'02-M'09-SM'09) received his B.S. degree from the Northern Jiaotong University, China, in 1983, and his M.S. degree from the Beijing Broadcast Institute, China, in 1986, both in Electrical Engineering. He received his Ph.D. degree in the area of Wireless Communications and Networks from the University of Texas (UT) at Austin in 2006. He is now an Associate Professor in the Department of Computer and Electronics Engineering, University of Nebraska-Lincoln (UNL).

His current research interests lie in wireless communications and networks with emphasis on radio channel characterizations, cognitive radio networks, and statistical signal processing. Yang is a senior member of IEEE.

An Effective Iterative Algorithm to Correct the Probe Positioning Errors in a Non-Redundant Plane-Rectangular Near-Field to Far-Field Transformation

F. D'Agostino, F. Ferrara, C. Gennarelli, R. Guerriero, and M. Migliozzi

Department of Industrial Engineering
University of Salerno, via Giovanni Paolo II, 132-84084, Fisciano, Italy
cgennarelli@unisa.it

Abstract ─ An algorithm for the effective compensation of known positioning errors, affecting the samples acquired by the probe in a non-redundant plane-rectangular (PR) near-field to far-field (NFFF) transformation, is presented and fully assessed by experimental tests. This transformation adopts a non-conventional PR scan, named planar wide-mesh scan (PWMS), characterized by meshes widening more and more as their distance from the measurement plane center increases, and uses a non-redundant sampling representation of the probe voltage. Such a representation is obtained by considering the antenna as contained in an oblate spheroid, to precisely determine the input NF data for the traditional PR NFFF transformation from the PWMS samples. These samples are unavailable in presence of positioning errors, but, as it will be shown, can be effectively retrieved from the errors affected ones by applying an iterative procedure.

Index Terms ─ Antenna measurements, non-conventional plane-rectangular scanning, non-redundant sampling representations, plane-rectangular near-field to far-field transformation, positioning errors compensation.

I. INTRODUCTION

In recent years, the near-field to far-field (NFFF) transformation techniques [1-5] have become extensively employed and well-assessed tools to precisely predict the far field radiated by an electrically large antenna from measurements performed in its NF region. As a matter of fact, the accurate measurement of the antenna radiated electromagnetic (EM) fields can be done only in a controlled environment, such as an anechoic chamber, where the propagation condition in free-space is very well approximated, by significantly reducing the field reflected from its walls, as well as the EM interferences from external sources. However, for an antenna under test (AUT) having large sizes as compared to the wavelength, it is practically impossible to fulfill the FF distance requirements in an anechoic chamber, so that only NF measurements can be carried out. Accordingly, the use of NFFF transformation techniques becomes mandatory to evaluate the radiated far field. Among

these techniques, that adopting the plane-rectangular (PR) scan [6, 7] is undoubtedly the most simple one from the analytical and computational viewpoint. In fact, from the fast Fourier transform (FFT) of the complex voltages measured by the probe in two its orientations in a suitable lattice of the PR scanning surface, it is possible to determine the plane waves spectrum of the AUT field and then the radiated far field [6, 7]. This scan, as all the planar ones [5], is suitable to very directive AUTs, radiating pencil beam patterns, as e.g., those recently proposed in [8, 9], since, due to the truncation of the scanning area, a good FF reconstruction is obtained only in the angular region specified by the limits of this last and the AUT edges. As well-known, in the classical PR scanning, the spacings between two adjacent points of the lattice are constant and bounded by $\lambda/2$, λ being the wavelength. Accordingly, these spacings are determined only by the operating frequency of the AUT and are independent of its dimension and geometry. On the contrary, the knowledge of the geometric characteristics and sizes of the antenna is suitably taken into account in the non-redundant (NR) PR transformations [10, 11] employing a novel planar scan, named planar wide-mesh scan (PWMS), characterized by rectangular meshes which widen more and more as their distance from the measurement plane center grows. These NFFFs transformations have been developed by applying the NR sampling representations of the EM fields [12, 13] to the voltage revealed by the probe and modeling a volumetric AUT with a sphere and a quasi-planar one with a surface formed by joining together two circular bowls with the same aperture (double bowl) or with an oblate spheroid. The related two-dimensional optimal sampling interpolation (OSI) expansions allow an efficient and very precise reconstruction of the massive input NF data for the traditional PR NFFF [7] from the NR ones gathered using the PWMS. A drastic savings in the measurement time, as compared to that needed by the classical PR scan, is so achieved and this result is very important, since the acquisition time is today by far greater than the computing one to execute the NFFF transformation.

It must be pointed out that, as a result of a not accurate control of the probe and AUT positioners, as well as of their finite resolution, a precise acquisition of the NF data at the points set by the NR sampling representation it is not always possible. In any case, the use of laser interferometric techniques makes possible to exactly determine the real locations of the acquired NF data. Hence, it becomes of key importance to have at one's disposal an efficient and stable method for the precise recovery of the NF data required to execute the classical PR NFFF transformation from the probe positioning errors affected ones acquired by using the PWMS. In this framework, an algorithm, adopting the conjugate gradient iteration technique and taking advantage from the fast Fourier transform for not equispaced data [14], has been utilized in [15] and [16] to compensate known positioning errors affecting the NF data necessary for the classical NFFF transformations with PR and spherical scans, respectively. By following the Yen's approach [17], an interpolation technique, that allows the correction of small position errors corrupting the NF data in the traditional PR NFFF transformation, has been proposed in [18]. In any case, these techniques are not suited to the NFFF transformations with PWMS [10, 11], where the massive PR NF data are recovered by interpolating the acquired NR ones, so that a different approach has to be applied. As underlined in [19], the direct reconstruction of the PR NF data from the positioning errors affected and, as consequence, irregularly spaced (non-uniform) samples is inopportune. A more convenient and viable approach is the retrieving of the regularly spaced (uniform) PWMS samples from the collected non-uniform ones and after that the accurate reconstruction of the PR NF data via an effective OSI algorithm [19]. To reach this objective, an iterative algorithm has been exploited for recovering the uniform samples from the not evenly distributed ones in PR [19], cylindrical or spherical lattices [20]. However, the existence of a one-to-one correspondence between every uniform sampling point and the closest non-uniform one is needed for its convergence. To overcome this shortcoming, a different approach, using the singular value decomposition (SVD) technique, has been afterward proposed and properly employed in the NR NFFF transformations with cylindrical [21], plane-polar [22], and bi-polar [23] scans from positioning errors affected NF data. Such an approach allows one to take advantage from the redundancy of data to improve the algorithm stability with respect to random errors affecting them, but requires that the retrieving of the uniform samples can be split in two separate one-dimensional problems. If this is not the case, a very large computational effort is needed due to the remarkable increase in the involved matrices dimensions. Both approaches have been compared through numerical simulations and experimentally assessed in [24] with reference to a NR spherical NFFF

transformation, while their effectiveness in the NR NFFF transformations with cylindrical and plane-polar scannings has been experimentally assessed in [25] and [26, 27], respectively. Finally, the efficacy of the SVD-based approach, to retrieve the uniform (positioning errors free) samples from the positioning errors affected samples, in the NR NFFF transformation with PWMS employing an oblate spheroid as antenna modeling, has been proven through numerical simulations in [28] and via experimental tests in [29].

The aim of this paper is to suitably exploit the iterative algorithm to correct known positioning errors affecting the collected NF samples in the NFFF transformation with PWMS based on the oblate spheroidal model of the AUT (see Fig. 1) and to provide the experimental validation of the developed procedure.
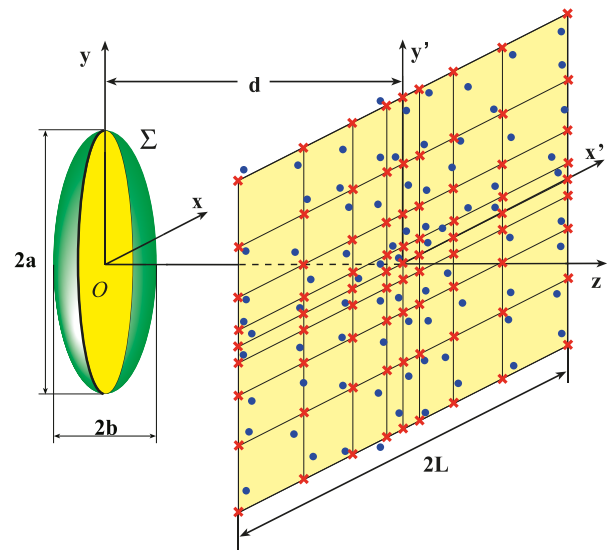
Fig. 1. PWMS scanning. Red crosses: uniform samples. Blue dots: non-uniform samples.

II. NON-REDUNDANT REPRESENTATION ON A PLANE FROM PWMS SAMPLES

An efficient NR representation of the voltage, detected by an electrically small probe on a plane d away from a quasi-planar AUT through a PWMS NF measurement system, and the corresponding OSI expansion are briefly recalled in this section for reader's convenience. In the following, two Cartesian coordinate systems are introduced to tackle this issue. The former (x, y, z) is used to denote a generic observation point and has its origin O at the center of the AUT aperture, while the latter (x', y', z'), having its z' axis coincident with the z one and the origin O' in correspondence of the scanning plane center at distance d from O (Fig. 1), is adopted to specify a point P belonging to the plane. A spherical reference system (r, ϑ, φ) with the origin again at O is also introduced. Because the voltage measured by a probe,

whose dimensions are small with respect to the wavelength, has about the same spatial bandwidth of the EM field radiated by the AUT [30], the NR sampling representations [12] can be exploited to get the requested representation using a minimum number of samples. According to these representations, the AUT must be first of all modeled by an appropriate convex rotational surface $\sum$, enclosing it and fitting well its shape. In fact, the minimum number of samples needed to represent the voltage on any rotational surface containing the AUT is proportional to the area of $\sum$. Afterward, a suitable parameterization $\underline{r} = \underline{r}(\tau)$ must be adopted to describe any curve Γ lying on the plane and an appropriate phase factor $e^{-j\psi(\tau)}$ has to be singled out from the voltage V detected by the probe (V_y) and by the rotated probe (V_x), thus obtaining the so called "reduced voltage":

$$\tilde{V}(\tau) = V(\tau)e^{j\psi(\tau)}, \qquad (1)$$

which is a function spatially almost bandlimited to W_τ [12]. This means that the error made when approximating it by a function bandlimited to $\chi'W_\tau$ can be made negligible [12] by properly choosing the enlargement bandwidth factor $\chi' > 1$. Since the PWMS, as all the planar scans, is well suited for AUTs characterized by a quasi-planar geometry, a double bowl or an oblate spheroid can be chosen as modeling surface $\sum$. The choice between which of the two models is more convenient to adopt falls on that minimizing the area of the surface $\sum$. Anyhow, the oblate spheroidal model gives rise to a simpler NR representation, conversely, the double bowl one is more flexible, allowing a better fitting of antennas characterized by a non-symmetrical profile with respect to the plane identified by their maximum transverse dimension. In the following, an oblate spheroid, with major and minor semi-axes a and b, is chosen as surface $\sum$. In such a case, the expressions of the bandwidth W_τ, parameter τ, and function ψ for a meridian curve Γ, as the x' (or y') axis, are [10-12]:

$$W_\tau = \frac{4a}{\lambda}E\left(\frac{\pi}{2}\Big|\varepsilon^2\right), \qquad \tau = \frac{\pi E\left(\sin^{-1}u\,|\varepsilon^2\right)}{2E\left(\pi/2\,|\varepsilon^2\right)}, \qquad (2)$$

$$\psi = \frac{2\pi a}{\lambda}\left[v\sqrt{\frac{v^2-1}{v^2-\varepsilon^2}} - E\left(\cos^{-1}\sqrt{\frac{1-\varepsilon^2}{v^2-\varepsilon^2}}\Big|\varepsilon^2\right)\right], \qquad (3)$$

where $\varepsilon = f/a$ is the eccentricity of the spheroid, $2f$ is its focal distance, $E(\cdot\,|\,\cdot)$ is the second kind elliptic integral, and $u = (r_1 - r_2)/2f$, $v = (r_1 + r_2)/2a$ are the elliptic coordinates, $r_{1,2}$ being the distances from the observation point P to the foci.

It must be underlined that, to allow the factorization of the two-dimensional OSI reconstruction algorithm into one-dimensional interpolations along lines, it is indispensable that the same parameterization $x' = x'(\xi)$ or $y' = y'(\eta)$, with the optimal parameters ξ and η defined by (2), has to be employed for describing all lines parallel to the x' or y' axis, respectively [10, 11]. As a consequence, the samples spacing for all lines parallel to

the x' (or y') axis coincides with that corresponding to the x' (or y') axis. Accordingly, the PWMS lattice has rectangular meshes, which widen more and more as their distance from the center of the measurement plane increases (see Fig. 1). Regarding the phase function ψ, it depends only on the distances $r_{1,2}$, i.e., it is the same which would be used when interpolating along the radial line passing through P and, accordingly, it can be evaluated [10, 11] by applying (3).

In light of these results, the voltage V can be accurately determined at any point $P(x', y')$ via the following two-dimensional OSI expansion [8, 9]:

$$V(\xi(x'),\eta(y')) = e^{-j\psi(x',y')}\sum_{m=m_0-p+1}^{m_0+p}\left\{G(\eta,\eta_m,\bar{\eta},N,N'')\cdot\right.$$

$$\left.\sum_{n=n_0-q+1}^{n_0+q}\tilde{V}(\xi_n,\eta_m)\,G(\xi,\xi_n,\overline{\xi},N,N'')\right\}, \qquad (4)$$

wherein $m_0 = \text{Int}(\eta/\Delta\eta)$, $n_0 = \text{Int}(\xi/\Delta\xi)$, $2q\times 2p$ is the number of the considered reduced voltage samples $\tilde{V}(\xi_n,\eta_m) = V(\xi_n,\eta_m)e^{j\psi(x'_n,\,y'_m)}$ closest to P:

$$\eta_m = m\Delta\eta = 2\pi m/(2N''+1), \quad \xi_n = n\Delta\xi = n\Delta\eta, \quad (5)$$

$$N'' = \text{Int}(\chi N')+1, \quad N' = \text{Int}(\chi'W_\tau)+1, \qquad (6)$$

$$N = N''-N', \quad \bar{\eta} = p\Delta\eta, \quad \overline{\xi} = q\Delta\xi. \qquad (7)$$

$\text{Int}(\alpha)$ staying for the greatest integer less than or equal to α and $\chi > 1$ being an oversampling factor needed for the control of the truncation error [12, 13]. Moreover:

$$G(\alpha,\alpha_i,\bar{\alpha},L,L'') = \Omega_L(\alpha-\alpha_i,\bar{\alpha})\,D_{L''}(\alpha-\alpha_i), \quad (8)$$

is the interpolation function of the OSI expansion, where $\Omega_L(\bullet,\bullet)$ and $D_{L''}(\bullet)$ are the Tschebyscheff and Dirichlet sampling functions [12].

The two-dimensional OSI expansion (4) can be suitably exploited to accurately recover V_x and V_y at the points needed by the standard PR NFFF transformation [7]. The corresponding probe compensated formulas in the adopted reference frame when the used probe is an open-ended rectangular waveguide, fed by the TE_{10} mode and characterized as described in [31], are shown in [32].

III. RETRIEVING OF THE UNIFORM SAMPLES

In the following, the collected PWMS samples are assumed as affected by known positioning errors, so that they are irregularly spaced on the plane. It is also supposed that there exists a bijection associating each of the $M = M_x \times M_y$ uniform sampling points to the closest non-uniform one. As explicitly emphasized in the Introduction, the iterative procedure can be suitably applied in these hypotheses. According to such an approach, by exploiting the OSI formula (4), the reduced voltage value in correspondence of each non-uniform sampling point (δ_k, σ_j) is expressed as function of the unknown ones

at the closest uniform sampling points (ξ_n, η_m), thus obtaining the linear system:

$$\tilde{V}(\delta_k, \sigma_j) = \sum_{m=m_0-p+1}^{m_0+p} \left\{ G(\sigma_j, \eta_m, \bar{\eta}, N, N'') \cdot \right.$$
$$\left. \sum_{n=n_0-q+1}^{n_0+q} \tilde{V}(\xi_n, \eta_m)\ G(\delta_k, \xi_n, \bar{\bar{\xi}}, N, N'') \right\} \quad,$$
$$k = 1,\dots,M_x\ ;\quad j = 1,\dots,M_y\ , \qquad (9)$$

that, in matrix form, becomes $\underline{\underline{C}}\ \underline{X} = \underline{B}$, wherein $\underline{\underline{C}}$ is a $M \times M$ sized sparse matrix, whose elements are linked to the interpolating functions of the OSI expansion (4), $\underline{X}$ the unknown uniform samples vector, and $\underline{B}$ the known non-uniform samples one. As emphasized in the Introduction, it is not convenient to solve this system via the SVD method, due to the large dimensions of the matrix $\underline{\underline{C}}$. Conversely, its solution can be efficiently achieved by applying an iterative procedure, whose derivation is shown below. As first step, the matrix $\underline{\underline{C}}$ is subdivided into its diagonal and non-diagonal parts $\underline{\underline{C}}_D$ and $\underline{\underline{\Delta}}$, respectively. After that, both sides of the system $\underline{\underline{C}}\ \underline{X} = \underline{B}$ are multiplied by $\underline{\underline{C}}_D^{-1}$, thus obtaining:

$$\underline{X} + \underline{\underline{C}}_D^{-1}\underline{\underline{\Delta}}\ \underline{X} = \underline{\underline{C}}_D^{-1}\underline{B}\,. \qquad (10)$$

By rearranging the terms of this last relation, the following iterative scheme is finally attained:

$$\underline{X}^{(\mu)} = \underline{\underline{C}}_D^{-1}\underline{B} - \underline{\underline{C}}_D^{-1}\underline{\underline{\Delta}}\underline{X}^{(\mu-1)} = \underline{X}^{(0)} - \underline{\underline{C}}_D^{-1}\underline{\underline{\Delta}}\underline{X}^{(\mu-1)}\,, \ (11)$$

with $\underline{X}^{(\mu)}$ being the uniform samples vector attained at the μth iteration. To assure the convergence of the iterative scheme (11), it is necessary but not sufficient, as underlined in [19], that the magnitude of each element of the main diagonal of the matrix $\underline{\underline{C}}$ be non-zero and greater than the magnitudes of those belonging to the same column or row. It is easy to recognize that these conditions are certainly fulfilled, in the assumed hypothesis of existence of a bijection associating the uniform sampling points to the closest non-uniform ones. In explicit form, relation (11) becomes:

$$\tilde{V}^{(\mu)}(\xi_n, \eta_m) = \frac{1}{G(\sigma_m, \eta_m, \bar{\eta}, N, N'')\, G(\delta_n, \xi_n, \bar{\bar{\xi}}, N, N'')} \cdot$$
$$\left\{ \tilde{V}(\delta_n, \sigma_m) - \sum_{\substack{i=i_0-p+1 \\ (i \neq m)}}^{i_0+p} \sum_{\substack{s=s_0-q+1 \\ \wedge\ (s \neq n)}}^{s_0+q} G(\sigma_m, \eta_i, \bar{\eta}, N, N'') \cdot \right.$$
$$\left. G(\delta_n, \xi_s, \bar{\bar{\xi}}, N, N'')\tilde{V}^{(\mu-1)}(\xi_s, \eta_i) \right\}, \qquad (12)$$

wherein:

$$i_0 = \begin{cases} m & \text{if } \sigma_m \geq \eta_m \\ m-1 & \text{if } \sigma_m < \eta_m \end{cases},\quad s_0 = \begin{cases} n & \text{if } \delta_n \geq \xi_n \\ n-1 & \text{if } \delta_n < \xi_n \end{cases}. \ (13)$$

IV. EXPERIMENTAL TESTING

Some results of experimental proofs assessing the validity of the developed iterative algorithm to effectively compensate even severe positioning errors, affecting the collected NF samples in the NR PR NFFF transformation with PWMS based on the oblate spheroidal AUT model, are shown below. The proofs have been performed by means of the flexible NF measurement system available in the anechoic chamber of the Antenna Characterization Laboratory of the University of Salerno. This NF acquisition system is equipped with a vertical linear positioner and several rotators, so that, by properly arranging these elements, it is possible to collect the NF data as they would be acquired in a cylindrical, spherical, plane-polar, bi-polar, and PR scanning NF facility. Moreover, by means of continuous and synchronized movements of the probe and AUT positioning systems, it is also possible to perform the helicoidal, as well as the planar and spherical spiral scannings. The acquisition of the classical PR NF data and of the PWMS ones is carried out by using the same arrangement allowing the plane-polar scanning. In such an arrangement, the probe is mounted on the linear vertical positioner and the AUT on a rotator with its rotation axis normal to the vertical positioner. This rotator is anchored to an L-shaped bracket, placed on a horizontal slide, so that the scanning plane distance can be suitably modified. Another rotator is placed between the positioner and the probe, to allow that the probe axes remain parallel to the AUT ones, as requested in the PWMS and in the classical PR scanning. The walls of the anechoic chamber, $8\text{m} \times 5\text{m} \times 4\text{m}$ sized, are coated with pyramidal absorbers, guaranteeing a reflectivity smaller than -40 dB in the X band. An Anritsu vector network analyzer is used to perform the magnitude and phase measurements of the voltage acquired by an open-ended WR90 rectangular waveguide, employed as probe. The AUT considered in the reported experimental results is a dual pyramidal horn antenna with vertical polarization, operating at 10 GHz. The horn apertures ($8.9\text{cm} \times 6.8\text{cm}$ sized) are located on the plane $z = 0$ and the distance between their centers is 26.5 cm. An oblate spheroid with $a = 18.3$ cm and $b = 6.3$ cm has been chosen to model this antenna. To assess the efficacy of the proposed iterative approach, the PWMS samples have been gathered in a circle of radius 110 cm, lying on the plane at $z = 16.5$ cm, in such a way that their positions are intentionally affected by severe errors. In particular, the shifts in the x' and y' directions between the positions of the error affected PWMS samples and those of the corresponding error free ones are random variables with uniform distribution in $(-\Delta\eta/3, \Delta\eta/3)$.

In Figs. 2 and 3, the magnitude and phase of the voltage V_x, directly measured along the scanning plane line $y' = 0$ cm, are compared with those recovered via the iterative scheme from the PWMS positioning errors

affected samples, while Figs. 4 and 5 show the analogous comparisons relevant to the line $y' = 3.6$ cm. For completeness, in Fig. 6, it is shown the reconstruction of the magnitudes of V_x and V_y along the line $y' = 10.0$ cm. As can be clearly observed, despite the considerable and pessimistic enforced positioning errors, very good reconstructions result, save for small discrepancies arising in the zones characterized by a very small voltage level, wherein the recovered voltages patterns appear smoother and more regular. This behaviour is imputable to the peculiar feature of the OSI function of cutting away the noise sources harmonics which exceed the spatial bandwidth of the AUT. It must be stressed that these reconstructions have been obtained by using 10 iterations, enough to ensure the convergence of the algorithm with very low errors [24].

The efficacy of the presented approach for the correction of the positioning errors is confirmed by the comparison (see Figs. 7 and 8) of the E-plane and H-plane FF patterns recovered from the 2601 positioning errors affected PWMS data through the iterative scheme with those, assumed as references, got from the 11025 PR NF data directly collected at 0.45λ spacing on the square of side 140cm, inscribed in the scanning circle. For sake of comparison, the related FF patterns got without using the iterative scheme are shown in Figs. 9 and 10. As can be observed, these last recoveries appear severely deteriorated, thus further confirming the efficacy of the proposed procedure. This efficacy is even more evident by comparing the very low errors in the reconstructed magnitudes shown in Figs. 7 and 8 with the significantly larger ones clearly visible in Figs. 9 and 10.
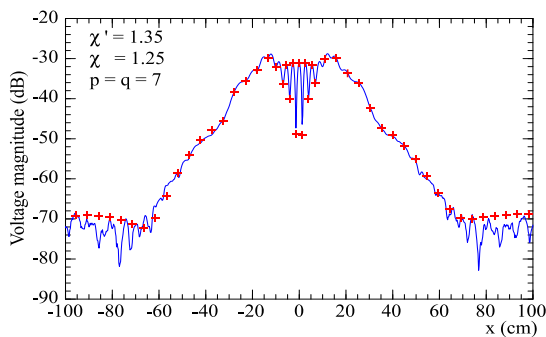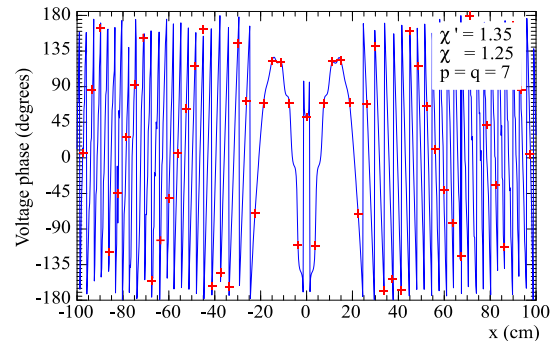
Fig. 3. Phase of V_x along the line $y' = 0$ cm. Solid line: measured. Crosses: recovered from the positioning errors affected PWMS measurements.
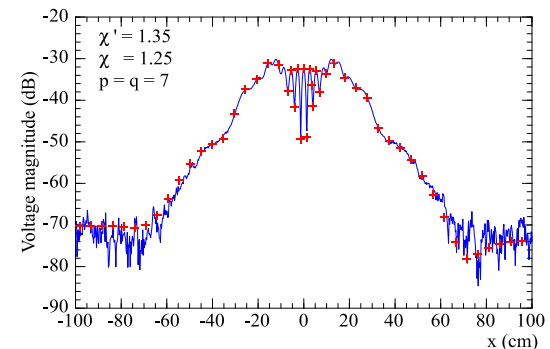
Fig. 4. Magnitude of V_x along the line $y' = 3.6$ cm. Solid line: measured. Crosses: recovered from the positioning errors affected PWMS measurements.

Fig. 5. Phase of V_x along the line $y' = 3.6$ cm. Solid line: measured. Crosses: recovered from the positioning errors affected PWMS measurements.
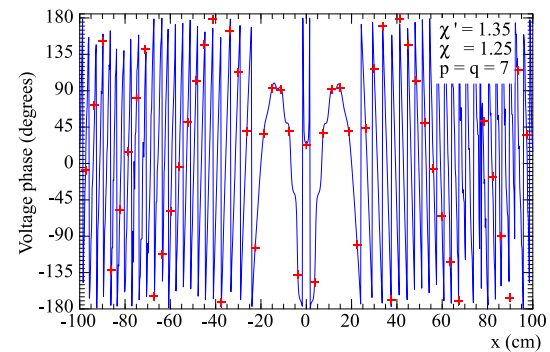
Fig. 2. Magnitude of V_x along the line $y' = 0$ cm. Solid line: measured. Crosses: recovered from the positioning errors affected PWMS measurements.
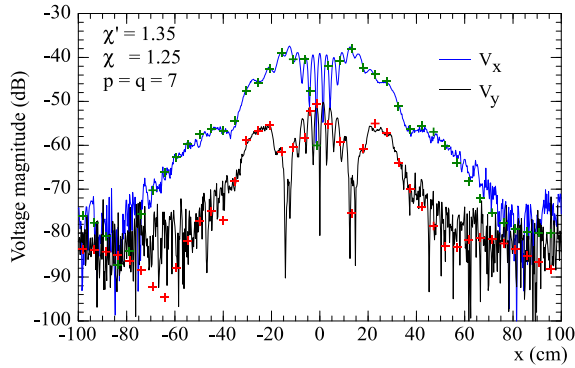
Fig. 6. Magnitudes of V_x and V_y along the line $y' = 10.0$ cm. Solid lines: measured. Crosses: recovered from the positioning errors affected PWMS measurements.
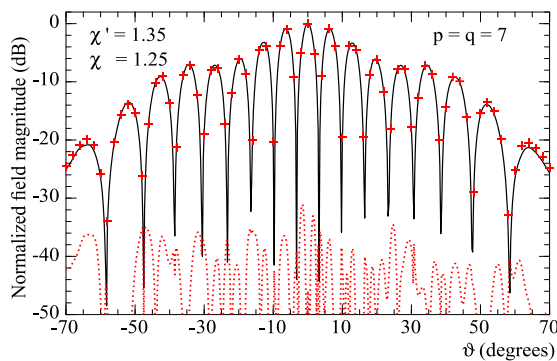
Fig. 7. E-plane pattern. Solid line: reference. Crosses: attained from the positioning errors affected PWMS samples applying the iterative scheme. Dashes: reconstruction error.
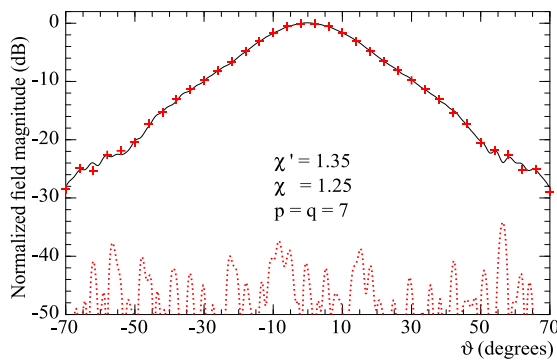
Fig. 8. H-plane pattern. Solid line: reference. Crosses: attained from the positioning errors affected PWMS samples applying the iterative scheme. Dashes: reconstruction error.

The interested reader can find in [33] a further set of laboratory results, which assess the efficacy of the proposed procedure for correcting known positioning errors and relevant to a different AUT.

V. CONCLUSION

An effective algorithm that allows the accurate compensation of known positioning errors affecting the acquired NF samples in the NFFF transformation with PWMS, using the oblate spheroidal modeling of the AUT, has been presented and experimentally assessed. Such an algorithm relies on an iterative procedure, which allows the accurate retrieving of the voltage samples at the points prescribed by the NR sampling representation from the gathered, positioning errors affected, PWMS samples. Once the positioning errors free PWMS samples have been determined, the massive NF data necessary for the classical PR NFFF transformation are accurately evaluated via an efficient OSI formula. The very accurate NF and FF reconstructions attained when such an algorithm is applied even to correct large positioning errors, as compared to the remarkably worsened FF reconstructions achieved when it is not used, assess its efficacy.
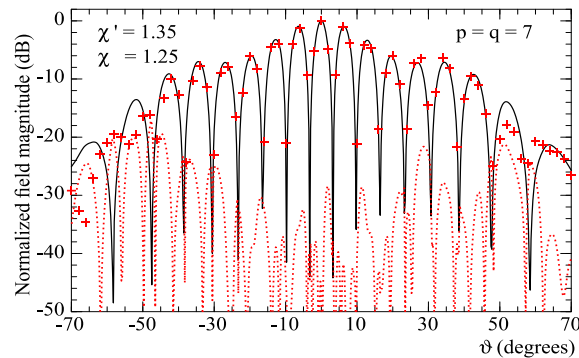
Fig. 9. E-plane pattern. Solid line: reference. Crosses: attained from the positioning errors affected PWMS samples without applying the iterative scheme. Dashes: reconstruction error.
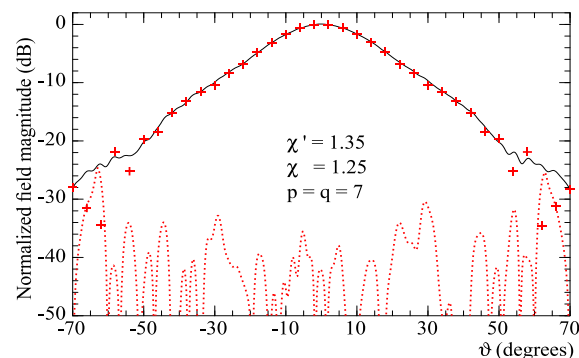
Fig. 10. H-plane pattern. Solid line: reference. Crosses: attained from the positioning errors affected PWMS samples without applying the iterative scheme. Dashes: reconstruction error.

REFERENCES

[1] A. D. Yaghjian, "An overview of near-field antenna measurements," *IEEE Trans. Antennas Prop.*, vol. AP-34, pp. 30-45, Jan. 1986.

[2] E. S. Gillespie, "Special issue on near-field scanning techniques," *IEEE Trans. Antennas Prop.*, vol. 36, pp. 727-901, June 1988.

[3] M. H. Francis and R. W. Wittmann, *Near-Field Scanning Measurements: Theory and Practice*, in *Modern Antenna Handbook*, C.A. Balanis, Ed., John Wiley & Sons, Hoboken, NJ, USA, pp. 929-976, 2008.

[4] M. H. Francis, *IEEE Recommended Practice for Near-Field Antenna Measurements*, IEEE Standard 1720-2012, 2012.

[5] F. Ferrara, C. Gennarelli, and R. Guerriero, *Near-Field Antenna Measurement Techniques*, in *Handbook of Antenna Technologies*, Z. N. Chen, D. Liu, H. Nakano, X. Qing, and T. Zwick, Eds., Springer, Singapore, pp. 2107-2163, 2016.

[6] D. T. Paris, W. M. Leach Jr., and E. B. Joy, "Basic theory of probe-compensated near-field measurements," *IEEE Trans. Antennas Prop.*, vol. AP-26, pp. 373-379, May 1978.

[7] E. B. Joy, W. M. Leach, Jr., G. P. RodrigueZ, and D. T. Paris, "Application of probe-compensated near-field measurements," *IEEE Trans. Antennas Prop.*, vol. AP-26, pp. 379-389, May 1978.

[8] A. Lalbakhsh, M. U. Afzal, and K. P. Esselle, "Multi-objective particle swarm optimization to design a time-delay equalizer metasurface for an electromagnetic band-gap resonator antenna," *IEEE Antennas Wireless Prop. Lett.*, vol. 16, pp. 912-915, 2017.

[9] A. Lalbakhsh, M. U. Afzal, K. P. Esselle, and S. L. Smith, "Wideband near-field correction of a Fabry-Perot resonator antenna," *IEEE Trans. Antennas Prop.*, vol. 67, pp. 1975-1980, Mar. 2019.

[10] F. Ferrara, C. Gennarelli, R. Guerriero, G. Riccio, and C. Savarese, "An efficient near-field to far-field transformation using the planar wide-mesh scanning," *Jour. Electromagn. Waves Appl.*, vol. 21, no. 3, pp. 341-357, 2007.

[11] F. D'Agostino, I. De Colibus, F. Ferrara, C. Gennarelli, R. Guerriero, and M. Migliozzi, "Far-field pattern reconstruction from near-field data collected via a nonconventional plane-rectangular scanning: Experimental testing," *Int. Jour. Antennas Prop.*, vol. 2014, ID 763687, 9 pages, 2014.

[12] O. M. Bucci, C. Gennarelli, and C. Savarese, "Representation of electromagnetic fields over arbitrary surfaces by a finite and nonredundant number of samples," *IEEE Trans. Antennas Prop.*, vol. 46, pp. 351-359, Mar. 1998.

[13] O. M. Bucci and C. Gennarelli, "Application of non-redundant sampling representations of electromagnetic fields to NF-FF transformation techniques," *Int.*

Jour. Antennas Prop., vol. 2012, ID 319856, 14 pages, 2012.

[14] A. Dutt and V. Rohklin, "Fast Fourier transforms for nonequispaced data," *Proc. SIAM Jour. Scie. Comput.*, vol. 14, pp. 1369-1393, Nov. 1993.

[15] R. C. Wittmann, B .K. Alpert, and M. H. Francis, "Near-field antenna measurements using nonideal measurement locations," *IEEE Trans. Antennas Prop.*, vol. 46, pp. 716-722, May 1998.

[16] R. C. Wittmann, B. K. Alpert, and M. H. Francis, "Near-field, spherical-scanning antenna measurements with nonideal probe locations," *IEEE Trans. Antennas Prop.*, vol. 52, pp. 2184-2186, Aug. 2004.

[17] J. L. Yen, "On nonuniform sampling of bandwidth-limited signals," *IRE Trans. Circuit Theory*, vol. CT-3, pp. 251-257, Dec. 1956.

[18] V. Dehghanian, M. Okhovvat, and M. Hakkak, "A new interpolation technique for the reconstruction of uniformly spaced samples from non-uniformly spaced ones in plane-rectangular near-field antenna measurements," *Prog. Electromagn. Res.*, vol. 72, pp. 47-59, 2007.

[19] O. M. Bucci, C. Gennarelli, and C. Savarese, "Interpolation of electromagnetic radiated fields over a plane from nonuniform samples," *IEEE Trans. Antennas Prop.*, vol. 41, pp. 1501-1508, Nov. 1993.

[20] O. M. Bucci, C. Gennarelli, G. Riccio, and C. Savarese, "Electromagnetic fields interpolation from nonuniform samples over spherical and cylindrical surfaces," *IEEE Proc. Microw. Antennas Prop.*, vol. 141, pp. 77-84, Apr. 1994.

[21] F. Ferrara, C. Gennarelli, G. Riccio, and C. Savarese, "NF-FF transformation with cylindrical scanning from nonuniformly distributed data," *Microw. Optic. Technol. Lett.*, vol. 39, pp. 4-8, Oct. 2003.

[22] F. Ferrara, C. Gennarelli, G. Riccio, and C. Savarese, "Far field reconstruction from nonuniform plane-polar data: A SVD based approach," *Electromagnetics*, vol. 23, pp. 417-429, 2003.

[23] F. D'Agostino, F. Ferrara, C. Gennarelli, R. Guerriero, and M. Migliozzi, "On the correction of the probe positioning errors in a non-redundant bi-polar near to far-field transformation," *Appl. Comp. Electromag. Soc. Jour.*, vol. 33, pp. 1374-1382, Dec. 2018.

[24] F. D'Agostino, F. Ferrara, C. Gennarelli, R. Guerriero, and M. Migliozzi, "Probe position errors corrected near-field-far-field transformation with spherical scanning," *Appl. Comp. Electromag. Soc. Jour.*, vol. 31, pp. 106-117, Feb. 2016.

[25] F. D'Agostino, F. Ferrara, C. Gennarelli, R. Guerriero, and M. Migliozzi, "On the compensation of probe positioning errors when using a nonredundant cylindrical NF-FF transformation," *Prog. Electromagn. Res. B*, vol. 20, pp. 321-335, 2010.

[26] F. D'Agostino, F. Ferrara, C. Gennarelli, R.

Guerriero, and M. Migliozzi, "Two efficient procedures to correct the positioning errors in the plane-polar scanning," *IET Microw., Antennas Prop.*, vol. 10, no. 13, pp. 1453-1458, 2016.

[27] F. D'Agostino, F. Ferrara, C. Gennarelli, R. Guerriero, and M. Migliozzi, "Near to far-field plane-polar transformation from probe positioning error affected data," *Appl. Comp. Electromagn. Soc. Jour.*, vol. 33, pp. 419-429, Apr. 2018.

[28] F. D'Agostino, F. Ferrara, C. Gennarelli, R. Guerriero, M. Migliozzi, and G. Riccio, "A singular value decomposition based approach for far-field reconstruction from irregularly spaced planar wide-mesh scanning data," *Microw. Optic. Technol. Lett.*, vol. 49, pp. 1768-1772, July 2007.

[29] F. D'Agostino, F. Ferrara, C. Gennarelli, R. Guerriero, and M. Migliozzi, "An SVD-based approach to reconstruct the planar wide-mesh scanning NF data from inaccurately probe-positioned samples," *IEEE Antennas Wireless Prop. Lett.*, vol. 17, pp. 641-644, Apr. 2018.

[30] O. M. Bucci, G. D'Elia, and M. D. Migliore, "Advanced field interpolation from plane-polar samples: Experimental verification," *IEEE Trans. Antennas Prop.*, vol. 46, pp. 204-210, Feb. 1998.

[31] A. D. Yaghjian, "Approximate formulas for the far field and gain of open-ended rectangular wave-guide," *IEEE Trans. Antennas Prop.*, vol. AP-32, pp. 378-384, Apr. 1984.

[32] F. D'Agostino, F. Ferrara, C. Gennarelli, R. Guerriero, S. McBride, and M. Migliozzi, "Fast and accurate antenna pattern evaluation from near-field data acquired via planar spiral scanning," *IEEE Trans. Antennas Prop.*, vol. 64, pp. 3450-3458, Aug. 2016.

[33] F. D'Agostino, F. Ferrara, C. Gennarelli, R. Guerriero, and M. Migliozzi, "An iterative technique to retrieve the planar wide-mesh scanning near-field data from those affected by an inaccurate positioning," *Proc. of MIKON*, Poznan, Poland, pp. 145-148, May 2018.

Francesco D'Agostino received the Laurea degree in Electronic Engineering from the University of Salerno in 1994, where in 2001 he received the Ph.D. degree in Information Engineering. From 2002 to 2005, he was Assistant Professor at the Engineering Faculty of the University of Salerno where, in October 2005, he was appointed Associate Professor of Electromagnetics and joined the Department of Industrial Engineering, where

he is currently working. His research activity includes application of sampling techniques to electromagnetics and to innovative NF-FF transformations, diffraction problems, radar cross section evaluations, Electromagnetic Compatibility. In this area, he has co-authored 4 books and over 230 scientific papers, published in peer-reviewed international journals and conference proceedings. He is a regular reviewer for several journals and conferences and has chaired some international events and conferences. D'Agostino is a member of AMTA, EurAAP, and IEEE.

Flaminio Ferrara was born near Salerno, Italy, in 1972. He received the Laurea degree in Electronic Engineering from the University of Salerno in 1999. Since the same year, he has been with the Research Group in Applied Electromagnetics at the University of Salerno. He received the Ph.D. degree in Information Engineering at the same University, where he is presently an Assistant Professor of Electromagnetic Fields. His interests include: application of sampling techniques to the efficient reconstruction of electromagnetic fields and to NF-FF transformation techniques; monostatic radar cross section evaluations of corner reflectors. Ferrara is co-author of more than 230 scientific papers, mainly in international journals and conference proceedings. In particular, he is co-author of 4 books on NF-FF transformation techniques and co-author of the chapter "Near-field antenna measurement techniques" of the Handbook of Antenna Technologies. He is reviewer for several international journals and member of the Editorial board of the International Journal of Antennas and Propagation. He is member of the IEEE society.

Claudio Gennarelli was born in Avellino, Italy, in 1953. He reeived the Laurea degree (*summa cum laude*) in Electronic Engineering from the University of Naples, Italy, in 1978. From 1978 to 1983, he worked with the Research Group in Electromagnetics at the Electronic Engineering Department of the University "Federico II" of Naples. In 1983, he became Assistant Professor at the Istituto Universitario Navale (IUN), Naples. In 1987, he was appointed Associate Professor of Antennas, formerly at the Engineering Faculty of Ancona University and subsequently at the Engineering Faculty of Salerno University. In 1999, he has been appointed Full Professor at the same University. The main topics of his scientific activity are: reflector antennas analysis, antenna measurements, diffraction problems, radar cross section evaluations, scattering from surface impedances, application of sampling techniques to electromagnetics and to NF–FF

transformations. Gennarelli is co-author of more than 400 scientific papers, mainly in international journals and conference proceedings. In particular, he is co-author of 4 books on NF-FF transformation techniques and co-author of the chapter "Near-field antenna measurement techniques" of the Handbook of Antenna Technologies. He is a Senior Member of the IEEE since 2002 and member of the Editorial board of the Open Electrical and Electronic Engineering Journal and of the International Journal of Antennas and Propagation.

Rocco Guerriero received the Laurea degree in Electronic Engineering and the Ph.D. degree in Information Engineering from the University of Salerno in 2003 and 2007, respectively. Since 2003, he has been with the Research Group in Applied Electromagnetics of University of Salerno, where he is currently an Assistant Professor of Electromagnetic Fields. His interests include: application of sampling techniques to the efficient reconstruction of electromagnetic fields and to near-field-far-field transformation techniques; antenna measurements; inversion of ill-posed electromagnetic problems; analysis of microstrip reflectarrays; diffraction problems. Guerriero is co-author

of about 190 scientific papers, mainly in international journals and conference proceedings. In particular, he has co-authored 3 books on NF-FF transformation techniques and is co-author of the chapter "Near-field antenna measurement techniques" of the Handbook of Antenna Technologies. He is reviewer for several international journals and member of the Editorial board of the International Journal of Antennas and Propagation. Since 2015, he is member of IEEE.

Massimo Migliozzi received the Laurea degree in Electronic Engineering from the University of Salerno in 1999. He received the Ph.D. degree in Information Engineering at the same University, where at the present time he is a Research fellow in Electromagnetic Fields. His scientific interests include: application of sampling techniques to the efficient reconstruction of electromagnetic fields and to NF-FF transformation techniques; antenna measurements; electromagnetic compatibility; antenna design; diffraction problems. Migliozzi is co-author of about 150 scientific papers, mainly in international journals and conference proceedings and reviewer for several international journals.

A Novel Finite Element Mesh Truncation Technology Accelerated by Parallel Multilevel Fast Multipole Algorithm and its Applications

Sheng Zuo [1], Yu Zhang [1], Daniel G. Doñoro [1], Xunwang Zhao [1], and Qifeng Liu [2]

[1] Shaanxi Key Laboratory of Large Scale Electromagnetic Computing
Xidian University, Xi'an, Shaanxi 710071, China
yuzhang@mail.xidian.edu.cn

[2] Science and Technology on Electromagnetic Compatibility Laboratory
China Ship Development and Design Center, Wuhan 430064, China

Abstract ─ In order to meet the highly accurate requirements of nowadays scattering and antenna problems, the finite element method requires the use of very accurate mesh truncations techniques able to absorb any outgoing wave completely. In this paper a novel implementation of the finite element mesh truncation technique called Finite Element-Iterative Integral Equation Evaluation (FE-IIEE) is studied. This method can provide a numerical exact radiation boundary condition while the original sparse and banded structure of the finite element method (FEM) matrix is retained. Also, an efficient parallel multilevel fast multipole algorithm (MLFMA) is included to drastically accelerate the time-consuming near field calculation process required by the truncation technique. In order to achieve a high parallel efficiency, both algorithms have been implemented together from scratch, being able to run over several thousands of CPU cores. Through comparisons with commercial software such as HFSS, the accuracy and efficiency of the method are validated showing excellent performance. Finally, a large 100-elements array antenna with more than 24 million unknowns is effectively analyzed using 2560 CPU cores.

Index Terms ─ Finite element method (FEM), integral equation, mesh truncation technique, multilevel fast multipole algorithm (MLFMA).

I. INTRODUCTION

Nowadays, the analysis of large radiation/scattering problems is of crucial interest in military (and civil) nautical and aeronautical industry. The use of higher working frequencies of modern radars makes the analysis, despite the constant enhancements in computer power, a challenge, especially due to the large electrical sizes of the objects.

Among other numerical techniques, the finite element method (FEM) has demonstrated to be a powerful and flexible computational tool for solving large radiation/scattering problems, even when the models present very complex materials [1, 2]. In order to analyze these open region problems, FEM requires the use of mesh truncation techniques that transform the infinite free space into a finite computation domain [3]. It is important to mention that the truncation methodologies have a great impact on the accuracy and efficiency of FEM, especially scattering objects due to their low RCS levels.

In general, the traditional finite element truncation techniques can be roughly divided into two classes: local mesh truncation technologies such as absorbing boundary condition (ABC) [3] and perfectly matched layers (PML) [4] and global mesh truncation technologies such as the finite element - boundary integral (FE-BI) method [5-7]. The formers are easy to implement, but their computational accuracy is unpredictable because of its dependence on many factors such as the distance away from the objects and the shape of truncation boundary. The latter, although can provide exact radiation boundary conditions, presents a partly full system of equations which makes the use of direct solution methods an impossible task forcing us to employ iterative solution strategies (with the consequence convergence issues).

Under this scenario, a mesh truncation algorithm called finite element-iterative integral equation evaluation (FE-IIEE) is studied in this paper [8-12]. This truncation technique provides an exact radiation boundary condition regardless the distance to the sources of the problem while the original sparse and banded structure of the FEM matrix is retained. The convergence of this method is assured by using a convex truncation boundary, moreover, as the distance of truncation boundary away from the objects is larger, faster rates of convergence are obtained [10]. Due to these advantages, it has been extensively hybridized mainly with high frequency methods in the past decades [8-9]. In recent works, authors have used it for the analysis of the unit cell of infinite array antennas as in [12]. However, its effective

application in complex and electrically large electromagnetic open region problems is still limited due to the extremely large time-consuming task requires during the near field calculation in the truncation process.

In this paper, a massively parallel efficient version of the multilevel fast multipole algorithm (MLFMA) [13] is employed to overcome this limitation, and drastically accelerate the near field calculation. In order to achieve a high parallel efficiency, both techniques have been implemented together from scratch, being able to run over several thousands of CPU cores. Also, complex numerical examples from real practical applications are analyzed to demonstrate the accuracy and efficiency of the proposed method.

The rest of the paper is organized as follows. The theory of FE-IIEE is presented in Section II. Section III describes the implementation of the parallel MLFMA for near field computing acceleration. Section IV contains the numerical results. Finally, our conclusions are gathered in Section V.

II. BASIC THEORY OF FE-IIEE

Let us start considering a typical FE-IIEE setup for a general radiation or scattering problem as illustrated in Fig. 1. The original infinite computational domain is divided into two overlapping domains: the infinite domain (Ω^{EXT}) exterior to the auxiliary boundary S' which generally is the object surface and a FEM domain (Ω^{FEM}) truncated by the surface S. Thus, the mentioned overlapping region is limited by S' and S. The boundary S may be arbitrarily shaped but typically it is selected to be conformal to S'.
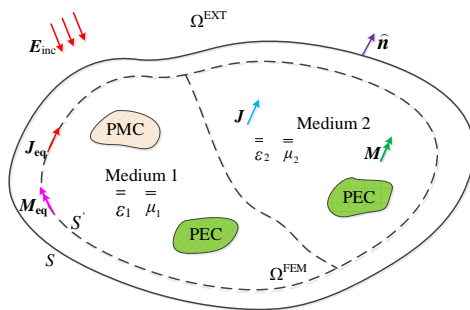

Fig. 1. A typical FE-IIEE method for general radiation or scattering problems.

The distribution of the electric field E in the domain Ω^{FEM} is obtained by solving the following equations:

$$\nabla \times (\overline{\overline{\mu}}_r^{-1} \cdot \nabla \times E) - k_0^2 \overline{\overline{\varepsilon}}_r \cdot E = -jk_0\eta_0 J^{imp} \quad \text{in } \Omega^{FEM}, \quad (1)$$

$$\hat{n} \times E = 0 \quad \text{on } \Gamma_{PEC}, \quad (2)$$

$$\hat{n} \times (\overline{\overline{\mu}}_r^{-1} \cdot \nabla \times E) = 0 \quad \text{on } \Gamma_{PMC}, \quad (3)$$

$$\hat{n} \times (\overline{\overline{\mu}}_r^{-1} \cdot \nabla \times E) - jk_0\hat{n} \times (E \times \hat{n}) = \phi^{(i)} \quad \text{on } S, \quad (4)$$

where $\overline{\overline{\mu}}_r$ and $\overline{\overline{\varepsilon}}_r$ are the relative permeability tensor and relative permittivity tensor of the medium respectively, k_0 represents the wave number in free space, η_0 refers to the free space wave impedance, J^{imp} is an impressed electric current excitation in the FEM domain, j denotes the imaginary unit, and $\hat{n}$ is the external normal unit vector of the corresponding surface. Equations (2), (3), and (4) describe Dirichlet, Neumann and Cauchy boundary conditions, respectively.

The FE-IIEE method starts its execution calculating the electric field E in the Ω^{FEM} domain by solving the system of equations introduced previously. Then, the residual of the Cauchy boundary condition expressed in (4) ($\phi^{(i)}$ term) is updated using the resulted electric field E, the equivalent electric current J_{eq} and the equivalent magnetic current M_{eq} on the boundary S'. These currents are used to calculate the electric field E field and its curl over the truncation boundary S. Thus, the residual $\phi^{(i)}$ is updated and a new iteration of the algorithm starts. This process continues until the residual $\phi^{(i)}$ satisfies an end condition (typically an error lower than 1e-5) that implies that the electromagnetic waves reaching the boundary S are completely absorbed.

It is worth mentioning that the initial value of the residual $\phi^{(0)}$ is zero for radiation problems. For scattering problems, the initial value of the residual $\phi^{(0)}$ is the result of evaluating (4) with $E=E^{inc}$ being E^{inc} the incident electric field over the boundary.

The variational formulation of the problem described previously is:

Finding $E \in \mathbf{H}(curl: \Omega^{FEM})$

$$\iiint_\Omega \nabla \times v \cdot (\overline{\overline{\mu}}_r^{-1} \cdot \nabla \times E) dv$$
$$-k_0^2 \iiint_\Omega v \cdot \overline{\overline{\varepsilon}}_r \cdot E dv + jk \oiint_{\Gamma_S} (\hat{n} \times v) \cdot (\hat{n} \times E) ds \quad (5)$$
$$= \underbrace{-jk_0\eta_0 \iiint_\Omega v \cdot J^{imp} dv - \iint_{\Gamma_P} v \cdot \phi^p ds}_{b_I} + \underbrace{(-\oiint_{\Gamma_S} v \cdot \phi^{(i)} ds)}_{b_\phi}$$

$$\forall v \in \mathbf{H}(curl: \Omega^{FEM}),$$

where $\mathbf{H}(curl; \Omega^{FEM})$ is the space of square integrable vector functions with square integrable curl, b_I term corresponds to the internal excitations, and b_ϕ term is related to the residual $\phi^{(i)}$ value of equation (4). The discretization of the above variational formulation is achieved by using second order tetrahedral curl-conforming basis functions that constitute a rigorous implementation of Nédélec first family of finite elements [14, 15].

According to (5), the final FE-IIEE system can be expressed in matrix equation block form as follows,

$$\begin{bmatrix} K_{II} & K_{IS} \\ K_{SI} & K_{SS} \end{bmatrix} \begin{bmatrix} g_I \\ g_S \end{bmatrix} = \begin{bmatrix} b_I \\ b_\phi \end{bmatrix}, \quad (6)$$

where subscripts I and S represent the degree of

freedoms (DOFs) in interior domain and the DOFs on the boundary S, respectively. It is important to note that the original sparse and banded structure of the FEM matrix is retained since the integral equation effects (full dense equation blocks) are moved to the right-hand side ($\boldsymbol{b}_{\phi}$ term). In addition, the numerical cost of the second and subsequent iterations is very small since the factorization of the FEM matrix is performed only once at the first iteration (if direct solvers are used).

III. IMPLEMENTATION OF PARALLEL MLFMA FOR NEAR FIELD COMPUTATION

A. Implementation principle of MLFMA accelerated near field calculation

As mentioned in the introduction, the FE-IIEE method still has a limitation due to the extremely large time-consuming task required during the truncation process. FE-IIEE needs to calculate the electric field distribution and its curl over the external boundary S using the following integral equations:

$$\boldsymbol{E} = -\mathrm{j}\omega\mu\iint_{S'} \boldsymbol{J}_{\mathrm{eq}} \cdot (\bar{\boldsymbol{I}} + \frac{\nabla\nabla}{k^2}) \cdot G(R)ds' + \iint_{S'} \boldsymbol{M}_{\mathrm{eq}} \times \nabla G(R)ds', \quad (7)$$

$$\nabla \times \boldsymbol{E} = -\mathrm{j}\omega\mu\nabla \times \iint_{S'} G(R)\boldsymbol{J}_{\mathrm{eq}}ds' - \omega^2\mu\varepsilon\iint_{S'} \boldsymbol{M}_{\mathrm{eq}} \cdot (\bar{\boldsymbol{I}} + \frac{\nabla\nabla}{k^2}) \cdot G(R)ds', \quad (8)$$

where $\bar{\boldsymbol{I}}$ represents the unit dyad, $G(R)$ is the Green's function for the free-space. The computational complexity of the (7) and (8) is O(MN) where M and N are the number of Gaussian sampling points on boundary S' and S respectively. The numerical cost of this process becomes extremely large when the electrical size of the model increases.

As a fast algorithm, the MLFMA has been widely used in accelerating matrix-vector operations for the method of moment (MoM). Therefore, in order to overcome the current computational bottleneck presented in the FE-IIEE, seems natural to extend the MLFMA and accelerate (7) and (8). Specific details about the MLFMA implementation used in this paper are described next.

Let us consider the two-dimensional problem depicted in Fig. 2. Firstly, the space that contains the field points and the source points is divided into small boxes by levels: the largest box is the level 0 (which surrounds the whole computational domain), then level 0 is divided into smaller boxes obtaining the level 1 and later the level 1 is divided obtaining the level 2. This process continues until the smallest box meets the standard (generally, when the side length is less than 0.5 wavelength).

Accordingly, the smallest boxes at the lowest level (here is level 3), contain three different types of non-

empty group: the group with both field and source points, the group only with field points and the group only with source points. In the current implementation in this paper, different groups are marked with different ***Iflag*** values to avoid empty loops and invalid calculations, as displayed in Fig. 2.
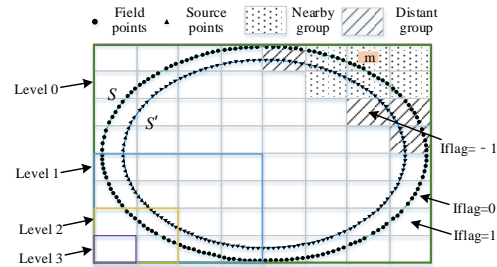
Fig. 2 Configuration for MLFAM based near-field computation.

Through the application of MLFMA, the near field computation in any non-empty groups which contains field points is divided into two categories: the field due to the nearby groups computed using (7) and (8); and, the far-region actions that are calculated through the expansion of the Green's function in (7) and (8) into multipole forms by using the addition theorem and the plane wave expansion theory. After mathematical deduction we obtain that [16],

$$\boldsymbol{E} = -\frac{k^2}{(4\pi)^2}[\eta\iint_{4\pi} \mathrm{e}^{-\mathrm{j}\boldsymbol{k}\cdot(\boldsymbol{r}-\boldsymbol{r}_m)} T_L(kR_{m'm},\hat{\boldsymbol{k}}\cdot\hat{\boldsymbol{R}}_{m'm})(\bar{\boldsymbol{I}}-\hat{\boldsymbol{k}}\hat{\boldsymbol{k}}) \, \boldsymbol{J}_{m'}(\hat{\boldsymbol{k}}) \, d^2\hat{\boldsymbol{k}}$$
$$-\iint_{4\pi} \hat{\boldsymbol{k}} \times \mathrm{e}^{-\mathrm{j}\boldsymbol{k}\cdot(\boldsymbol{r}-\boldsymbol{r}_m)} T_L(kR_{m'm},\hat{\boldsymbol{k}}\cdot\hat{\boldsymbol{R}}_{m'm})\boldsymbol{M}_{m'}(\hat{\boldsymbol{k}})d^2\hat{\boldsymbol{k}}], \quad (9)$$

$$\nabla \times \boldsymbol{E} = \frac{\mathrm{j}k^3}{(4\pi)^2}[\eta\iint_{4\pi}\hat{\boldsymbol{k}} \times \mathrm{e}^{-\mathrm{j}\boldsymbol{k}\cdot(\boldsymbol{r}-\boldsymbol{r}_m)} T_L(kR_{m'm},\hat{\boldsymbol{k}}\cdot\hat{\boldsymbol{R}}_{m'm}) \, \boldsymbol{J}_{m'}(\hat{\boldsymbol{k}}) \, d^2\hat{\boldsymbol{k}}$$
$$+\iint_{4\pi} \mathrm{e}^{-\mathrm{j}\boldsymbol{k}\cdot(\boldsymbol{r}-\boldsymbol{r}_m)} T_L(kR_{m'm},\hat{\boldsymbol{k}}\cdot\hat{\boldsymbol{R}}_{m'm})(\bar{\boldsymbol{I}}-\hat{\boldsymbol{k}}\hat{\boldsymbol{k}})\boldsymbol{M}_{m'}(\hat{\boldsymbol{k}})d^2\hat{\boldsymbol{k}}], \quad (10)$$

where $\hat{\boldsymbol{k}}$ is the unit vector of plane wave expansion direction, $\boldsymbol{r}$ represents the field point coordinates, $\boldsymbol{r}_m$ refers to the center of filed point group, $\boldsymbol{J}_{m'}(\hat{\boldsymbol{k}})$ and $\boldsymbol{M}_{m'}(\hat{\boldsymbol{k}})$ are the radiation pattern of the electric current and magnetic current, respectively, $\boldsymbol{r}'$ is the source point coordinates, $\boldsymbol{r}_m'$ denotes the center of source point group, and $T_L(kR_{m'm},\hat{\boldsymbol{k}}\cdot\hat{\boldsymbol{R}}_{m'm})$ is the translator operator between source point group m' and field point group m. By using such a scheme, the computational complexity for updating the residual $\boldsymbol{\phi}^{(i)}$ on the boundary S can be reduced from O(MN) to $O(\sqrt{MN}\log(MN))$. Figure 3 shows the flowchart of the presented mesh truncation technique where the FE-IIEE and the MLFMA algorithms are working together.
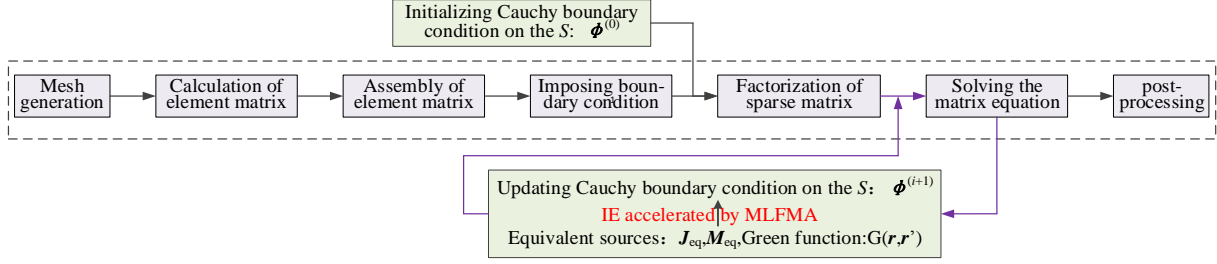
Fig. 3. The program design flow of the FE-IIEE+MLFMA implemented in this paper.

B. Parallel strategy

The parallelization process of MLFMA has two basic partitioning strategies: spatial partitioning and direction partitioning [17]. The former refers to the division of all non-empty groups in each level to each MPI (Message Passing Interface) process, and the latter refers to the distribution of the wave plane directions belonging to each group into the different MPI process. The simple use of one of these strategies usually fails when scaling on a large number of CPU cores. Therefore, in order to improve the scalability of parallel MLFMA, these two parallel partitioning strategies must be combined together.

Considering that the plane wave expansion of the electromagnetic current sources is the most time-consuming process during the nearfield calculation, the non-empty groups in lowest level are firstly divided into N_p portions according to the bisecting source point's rule, where N_p is the number of processes. Each portion is distributed to one MPI process. As an example, Fig. 4 shows the case that the tree nodes from level 2 to level 4 are distributed to 6 processes, where the process indices are denoted by $P_0 \sim P_5$. It can be seen that the non-empty group (the tree node) at a certain level may be shared by different processes except those at the lowest level. If the non-empty group exists in many processes, its corresponding outgoing and incoming plane wave directions are equally distributed among the related processes. This adaptive partitioning strategy makes our parallel MLFMA to have no special requirements when choosing the number of processes.

On the other hand, it is worth pointing out that during the translation period, if the outgoing plane waves are not in the current process, they need be received from the source group processes where they are located. However, for the near field calculation, we only need to consider the actions from the source points to the field points, in other words, the translation process does not need to be reciprocal. Thus, to avoid invalid communications messages when exchanging outgoing plane waves, a send list and a receive list are established in an earlier stage. The lists include the non-empty group indices, destination and source process indices, and the related outgoing plane wave directions.
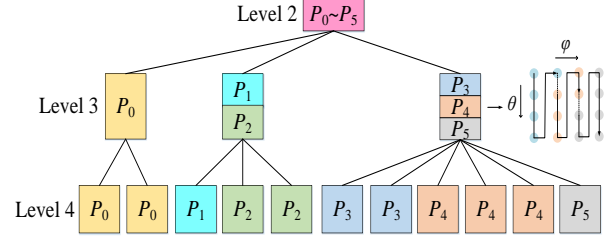
Fig. 4. The parallel strategy of MLFMA for near field computation.

IV. NUMERICAL RESULTS

In this section, the results of different numerical examples are analyzed to demonstrate the performance, versatility and accuracy of the proposed method. Comparisons with well-known commercial software such as ANSYS HFSS [18] and FEKO [19], with in-house codes and with experimental measurements are done to validate its results.

Two different computer platforms are used to complete these simulations: the first one is a Dell T7600 workstation with four 6-core 64-bit E5-2620 0 @2GHz CPUs and 192 GB of RAM; the second one is a Sugon HPC cluster with 548 compute nodes where each node has two 32-core AMD HygonGenuine 2.0 GHz processors (32×512 KB L2 Cache and 64 MB L3 Cache) and 256 GB RAM. The compute nodes are connected with InfiniBand switches to provide the highest communication speeds.

A. Low scattering carrier

The bistatic radar cross-section (RCS) analysis of a metal low scattering carrier object is considered first. Figure 5 shows the low scattering carrier model used in this benchmark.

The model is illuminated by a negative x-axis incident y-axis polarized uniform plane wave at 3.0 GHz. The overall dimensions of the model are 0.731 m by 0.524 m by 0.077 m corresponding to an electrical size of 7.31 λ by 5.24 λ by 0.77 λ. It is worth noting that due to the low scattering characteristics of the object, certain angles present very low RCS levels which are very difficult to catch numerically. For that reason, authors

consider that this model is a good benchmark to verify the level of accuracy of the proposed truncation technique.
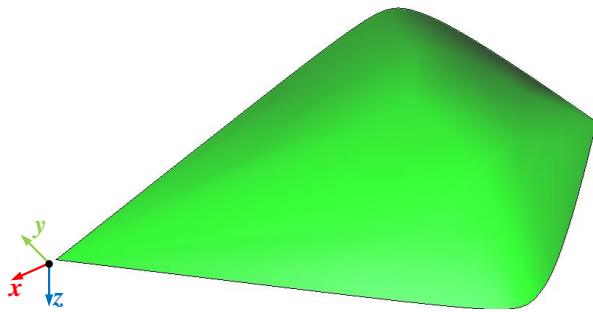
Fig. 5. The metal low scattering carrier model.

The results given by the presented FE-IIEE+MLFMA technique are compared with those given by ANSYS HFSS, FEKO and an in-house higher order method of moments (HOMoM) solver [20]. In order to perform a full comparison with HFSS, all the truncation techniques available in this software, such as ABC, PML and FE-BI, are used in the analysis. The truncation boundary is placed at 0.2 λ from the target in the proposed method. In the case of HFSS, the truncation distance is left to its default option (0.333 λ). The other techniques use method of moments, so no truncation boundary is needed.

Figure 6 shows the comparison between FEKO, the in-house HOMoM code and the proposed FE-IIEE+MLFMA method. An excellent agreement is appreciated even for lowest RCS levels. The results of the pure FE-IIEE method without acceleration are also plotted. In this way, we can see how there are no differences between both versions of the FE-IIEE method indicating that the use of the MLFMA algorithm does not result in any loss of numerical accuracy. However, as it may be seen later, the use of the proposed FE-IIEE+MLFMA technique drastically reduces the total computational time of the analysis.

The comparisons between the results given by HFSS using ABC, PML, and FE-BI as mesh truncation techniques and the proposed method are shown in Fig. 7. In this case, the adaptive convergence accuracy of HFSS was set to 10^{-3}. As aforementioned, the model presents very low RCS values in certain angles that are difficult to catch numerically. In the case of the proposed method, the RCS values for these low level angles present an excellent agreement compared with the levels given by MoM. However, in the case of HFSS, there is a loss of accuracy and cannot match the required RCS levels. It is worth noting that a lower adaptive converge value (lower than 10^{-3}) could mitigate this problem, however the amount of computational resources required to perform the simulation, makes this task almost impossible to conclude.
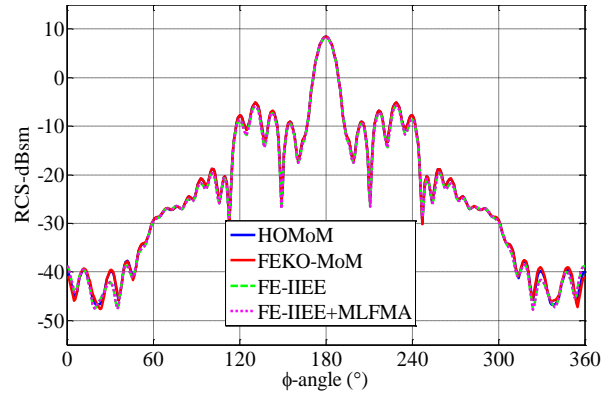
Fig. 6. Bistatic RCS results of the low scattering carrier at 3.0 GHz in the *xoy*-plane calculated by the proposed method and MoM.
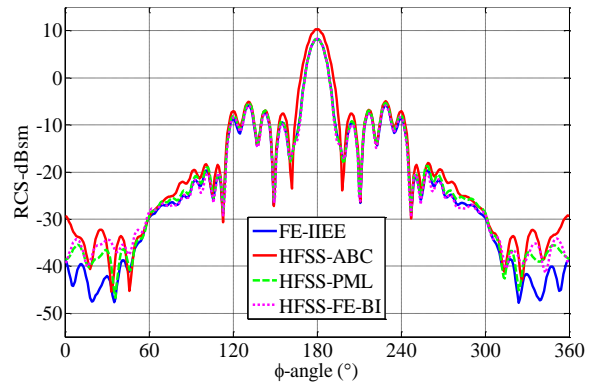
Fig. 7. Bistatic RCS results of the low scattering carrier at 3.0 GHz in the *xoy*-plane calculated by the HFSS and the proposed method.

The computational statistics for these simulations are given in Table 1. All simulations were performed using 12 CPU cores in the Dell T7600 workstation platform described above. It is worth pointing out that the residual value for the proposed method corresponds to the residual of the boundary condition given in (4) meanwhile the residual value for HFSS is its adaptive convergence accuracy. According to this data, we can see how the proposed parallel FE-IIEE+MLFMA technique drastically accelerates the simulation time while the memory level remains unchanged.

Table 1: Computational statistics of the proposed method and HFSS for the low scattering carrier

Methods	Residual	Iteration Count	Number of Tetrahedrons	Unknowns	Memory/ GB	CPU Time/s
FE-IIEE	10^{-4}	8	104,261	710,500	12.57	1639
FE-IIEE+MLFMA	10^{-4}	8	104,261	710,500	12.57	190
HFSS-ABC	10^{-2}	14	208,479	1,236,430	12.28	1100
	10^{-3}	24	2,024,208	12,458,342	154.20	42,406
HFSS-PML	10^{-2}	16	479,470	2,894,550	56.50	9291
	10^{-3}	20	1,429,104	7,069,446	148.30	27,283
HFSS-FE-BI	10^{-2}	12	92,271	586,264/30,078	2.75	924
	10^{-3}	26	1,949,894	13,324,482/290,406	121.70	22,664

B. Waveguide narrow-edge slot antenna

In order to perform a further verification of the computational accuracy and efficiency of the proposed method, the radiation analysis of a waveguide narrow-edge slot antenna is considered next. The model of this antenna is depicted in Fig. 8.

(a)

(b)
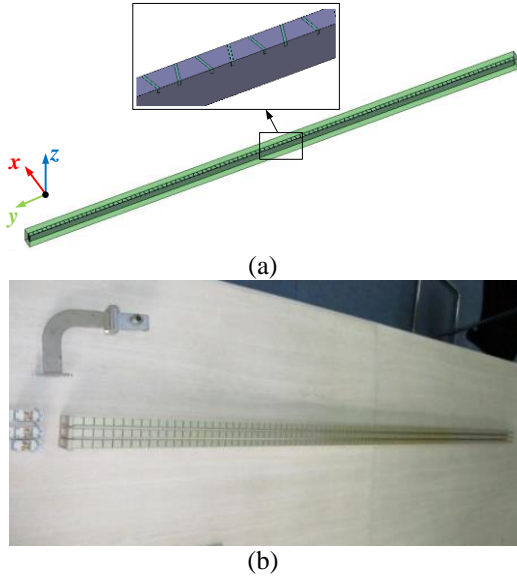
Fig. 8. The waveguide narrow-edge slot antenna model: (a) the simulation model, and (b) the measurement model.

The waveguide is a WR-90 waveguide (X-band), with dimensions of 22.86 mm by 10.16 mm, and a wall thickness of 1.00 mm. The operation frequency is 9.35 GHz and the rectangular wave ports placed on both ends of the waveguide are used to excite/match the antenna. The total number of tetrahedron used in the discretization of the model is 634,756 and the total number of unknowns is 4,055,352. This simulation is performed using 20 CPU cores in Dell T7600 workstation platform. The residual of the FE-IIEE truncation method is set to 10^{-3}.

In this case, the results are compared with measurement and those given by the in-house HOMoM code. Figure 9 shows the normalized radiation pattern

where a very good agreement between the results is appreciated. Table 2 summarizes the computational statistics of this example when using the FE-IIEE and the FE-IIEE+MLFMA method. It is worth noting that, for this moderate electrical size model, the near-field calculation takes more than 97% computation time of FE-IIEE before the MLFMA acceleration is adopted. The use of the proposed hybrid technique drastically reduces the computation time from 5777.6s to 238.4s taking the FE-IIEE capabilities to a higher level.
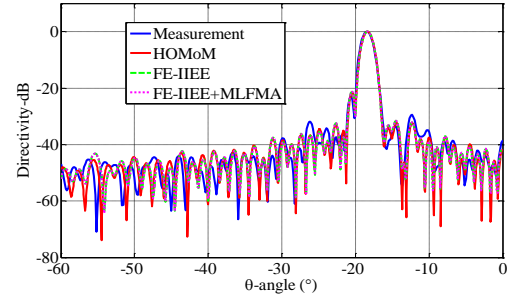
Fig. 9. Normalized radiation pattern of the waveguide narrow-edge slot antenna in the *yoz*-plane.

Table 2: Computational statistics of the FE-IIEE method and FE-IIEE+MLFMA method for the waveguide narrow-edge slot antenna

Methods	Iteration Count	Near Field Calculation Time/s	Total Time/s
FE-IIEE	8	5777.6	5916.2
FE-IIEE+MLFMA	8	238.4	374.1

C. 100-elements array antenna

A very common and typical application of FEM is the analysis of antenna arrays with complex materials and shapes. For this last example, the analysis of a large patch antenna array with 100 elements in a 5 by 20 configuration is considered. Figure 10 shows the unit structure (a) and the whole antenna array (b).

The relative permittivity of the dielectric substrate is 2.65 with a delta tangent of 0.003. Each antenna unit is

fed through two coaxial cables at the bottom in equal amplitude and phase. The operation frequency is 3.2 GHz. The total number of tetrahedron for this antenna is 3,839,140, obtaining a total number of unknowns of 24,530,828. The residual of the FE-IIEE truncation method is set to 10^{-3}. A total of 2560 CPU cores in Sugon HPC cluster were used to perform this simulation which took 3.65 hours and 6.85 TB of memory.

(a)

(b)
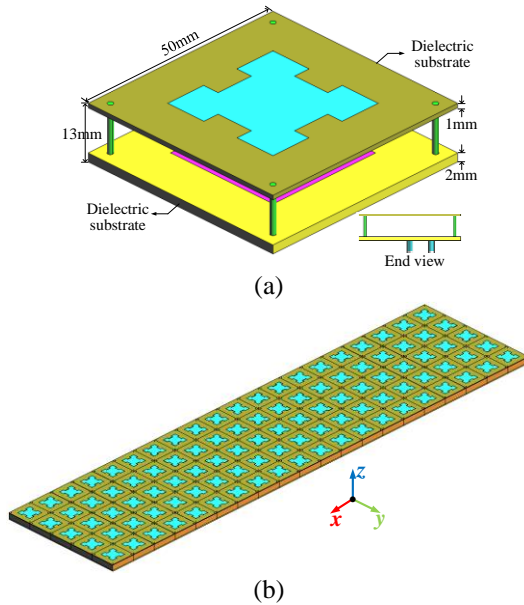
Fig. 10. The array antenna model: (a) the array unit structure, and (b) the array structure.
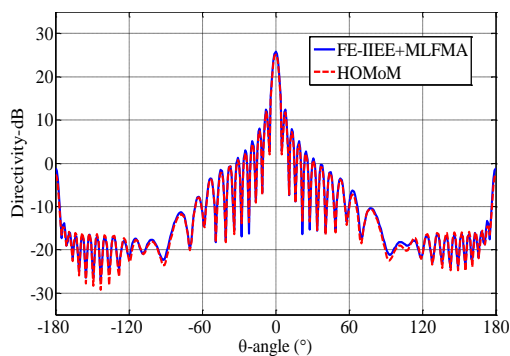
Fig. 11. Radiation pattern of the 100-elements array antenna in the *xoz*-plane.

Figure 11 shows the comparison of the radiation pattern for the elevation cut (*xoz* plane) between FE-IIEE+MLFMA and the in-house higher order method of moments (HOMoM) code. A very good agreement is appreciated confirming that the proposed method can efficiently perform full-wave simulation of challenging electromagnetic problems.

V. CONCLUSION

In this paper, a very efficient parallel FEM mesh truncation technique is presented for the truncation of radiation and scattering problems. This method provides a numerical exact radiation boundary condition while the original sparse and banded structure of the finite element method (FEM) matrix is retained. The accuracy and effectiveness of the proposed technique are demonstrated through the analysis of several practical applications. Specially, the proposed method has shown better accuracy and efficiency than the commercial software HFSS in the analysis of the low scattering objects. As a final conclusion, authors believe that this truncation method is able to meet the highly accurate requirements of nowadays scattering and antenna problems.

ACKNOWLEDGMENT

REFERENCES

[1] J. Jianming, *The Finite Element Method in Electromagnetics*. New Jersey: John Wiley & Sons, 2002.

[2] M. Salazar-Palma, T. K. Sarkar, L. E. Garcia-Castillo, T. Roy, and A. R. Djordjevic, *Iterative and Self-Adaptive Finite-Elements in Electro-magnetic Modeling*. Norwood, MA: Artech House Publishers, Inc., 1998.

[3] B. Engquist and A. Majda, "Absorbing boundary conditions for numerical simulation of waves," *Proceedings of the National Academy of Sciences*, vol. 74, no. 5, pp. 1765-1766, 1977.

[4] J. Y. Wu, D. M. Kingsland, J. F. Lee, et al., "A comparison of anisotropic PML to Berenger's PML and its application to the finite-element method for EM scattering," *IEEE Transactions on Antennas and Propagation*, vol. 45, no. 1, pp. 40-50, 1997.

[5] X. Q. Sheng and Z. Peng, "Analysis of scattering by large objects with off-diagonally anisotropic material using finite element-boundary integral-multilevel fast multipole algorithm," *IET Micro-waves, Antennas & Propagation*, vol. 4, no. 4, pp. 492-0, 2010.

[6] J. L. Volakis, J. Gong, and A. Alexanian "A finite element boundary integral method for antenna

RCS analysis," *Electromagnetic*, vol. 14, no. 1, pp. 63-85, 1994.

[7] H. Hu, Y. Tan, B. Zhu, and L. Zhou, "A hybrid FE-BI method using in antenna radiation analysis," *2008 8th International Symposium on Antennas*, Propagation and EM Theory, Kunming, pp. 898-901, 2008.

[8] R. Fernandez-Recio, L. E. Garcia-Castillo, I. Gomez-Revuelto, et al. "Fully coupled multi-hybrid FEM-PO/PTD-UTD method for the analysis of radiation problems," *IEEE Transactions on Magnetics*, vol. 43, no. 4, pp. 1341-1344, 2007.

[9] R. Fernandez-Recio, L. E. Garcia-Castillo, I. Gomez-Revuelto, et al., "Fully coupled hybrid FEM-UTD method using NURBS for the analysis of radiation problems," *IEEE Transactions on Antennas and Propagation*, vol. 56, no. 3, pp. 774-783, 2008.

[10] R. Fernandez-Recio, L. E. Garcia-Castillo, I. Gomez-Revuelto, and M. Salazar-Palma, "Convergence study of a non-standard Schwarz domain decomposition method for finite element mesh truncation in electromagnetics," *Progress In Electromagnetics Research (PIER)*, vol. 120, pp. 439-457, 2011.

[11] D. Garcia-Donoro, S. Ting, A. Amor-Martin, et al., "Analysis of planar microwave devices using higher order curl-conforming triangular prismatic finite elements," *Microwave and Optical Technology Letters*, vol. 58, no. 8, pp. 1794-1801, 2016.

[12] D. Garcia-Donoro, L. E. Garcia-Castillo, T. K. Sarkar, et al., "A non-standard Schwarz domain decomposition method for finite element mesh truncation of infinite arrays," *IEEE Transactions on Antennas and Propagation*, vol. 66, no. 11, pp. 6179-6190, 2018.

[13] A. Tzoulis, T. F. Eibert, "Efficient electromagnetic near-field computation by the multilevel fast multipole method employing mixed near-field/far-field translations," *IEEE Antennas & Wireless Propagation Letters*, vol. 4, no. 1, pp. 449-452, 2005.

[14] A. Amor-Martin, D. Garcia-Donoro, L. E. Garcia-Castillo, et al., "A finite element mesh truncation technique for scattering and radiation problems in HPC environments," *Computing & Electromagnetics International Workshop*, IEEE, 2017.

[15] L. E. Garcia-Castillo and M. Salazar-Palma, "Second-order Nédélec tetrahedral element for computational electromagnetics," *International Journal of Numerical Modelling: Electronic Networks*. Devices and Fields (John Wiley & Sons, Inc.), vol. 13, no. 2-3, pp. 261-287, Mar.-June 2000.

[16] C. W. Chew, *Fast and Efficient Algorithms in Computational Electromagnetics*. Artech House, 2001.

[17] X. Zhao, S. W. Ting, and Y. Zhang, "Parallelization of half-space MLFMA using adaptive direction partitioning strategy," *IEEE Antennas and Wireless Propagation Letters*, vol. 13, pp. 1203-1206, 2014.

[18] HFSS. Accessed: 01/06/2019. [Online]. Available: https://www.ansys.com/products/electronics/ansys-hfss, 2019.

[19] FEKO. Accessed: 01/06/2019. [Online]. Available: https://altairhyperworks.com/product/FEKO, 2019.

[20] Y. Zhang, T. K. Sarkar, Y. Zhao, et al., *Higher Order Basis Based Integral Equation Solver (HOBBIES)*. Wiley Press, USA: New Jersey, 2012.

Sheng Zuo was born in 1992 in Hunan, China. He received the B.S. degree of Electronic Information Engineering and the M.S. degree in Electronics and Communications Engineering from Xidian University in 2014 and 2017, respectively. Since September 2017 he is working toward the Ph.D. degree at Xidian University. His research activities and interests are focused in large-scale parallel finite element computation in complex electromagnetic environment, domain decomposition method and fast multipole method.

Yu Zhang received the B.S., M.S., and Ph.D. degrees from Xidian University, Xi'an, China, in 1999, 2002, and 2004, respectively. He joined Xidian University as a Faculty Member in June 2004. He was a Visiting Scholar and Adjunct Professor at Syracuse University from 2006 to 2009. As Principal Investigator, he works on projects including the project of NSFC. He authored four books, namely Parallel Computation in Electromagnetics (Xidian Univ. Press, 2006), Parallel Solution of Integral Equation-based EM Problems in the Frequency Domain (Wiley–IEEE, 2009), Time and Frequency Domain Solutions of EM Problems Using Integral Equations and a Hybrid Methodology (Wiley, 2010), and Higher Order Basis Based Integral Equation Solver (HOBBIES) (Wiley, 2012), as well as more than 100 journal articles and 40 conference papers.

Broadband Tracking of Characteristic Modes

Jianbin Zhu, Weiwen Li, and Liangcai Zhang

Department of Electronic Engineering, Xiamen University, Xiamen 361005, P. R. China
807408442@qq.com, wwl@xmu.edu.cn, 13194086664@163.com

Abstract ─ Effective mode sorting is the key to achieving characteristic mode (CM) analysis for open conductors. However, mode ordering just according to the eigenvalue magnitude may cause the mode crossing in the operating band. Mode tracking must be performed to obtain the correct mode ordering. Currently, mode tracking based on eigenvector correlation is usually only applicable to narrowband cases due to the large interval between the sampling frequency point and the first frequency. In this paper, the correlation calculation is directly performed between two adjacent frequencies, and the first frequency is not used as the anchor point. Due to the improvement of the eigenvector correlation, the broadband mode tracking is realized. Some numerical examples are used to verify the effectiveness of this algorithm.

Index Terms ─ Characteristic mode theory, broadband, eigenvector correlation, mode tracking.

I. INTRODUCTION

The characteristic mode (CM) theory is a useful tool that allows us to analyze antenna radiating properties using a systematic approach [1-4]. After the impedance matrix of the open conductor has been obtained by Galerkin method of moment (MoM), a generalized eigenvalue equation can be constructed using the real and imaginary part of the matrix. The eigenvectors physically correspond to the characteristic current wavemodes, which form a weighted orthogonal set over the conductor surface [5].

The modes can be sorted according to the eigenvalue magnitude at each frequency point. However, since the eigenvalues are sensitive to frequency variations, the ordering of modes at higher frequencies may differ from that obtained at lower frequencies [6]. Similarly, for geometrically symmetric conductors with degenerate modes, the mode ordering based on tracking eigenvalues alone cannot also work well [7]. For these reasons, it is more common to perform mode tracking based on eigenvector correlation [8, 9]. In that case, the first frequency sample is selected as the reference frequency, and the vector correlation algorithm is used to determine the mode ordering at each subsequent frequency [10].

Since the starting frequency is used as the reference point, the interval between the subsequent frequency samples and the reference frequency will increase as the frequency increases. When the operating frequency band is wide enough, the last frequency point is far away from the first one, and the mode swapping problem is prone to occur, especially for higher order modes [10]. We refer to this mode tracking algorithm based on initial frequency correlation as the original algorithm, which can be implemented by parallel operations.

To eliminate the mode swapping of wideband mode tracking, we propose to perform eigenvector pairing and correlation calculation for all directly adjacent two frequencies. In this method, the mode ordering of subsequent frequencies cannot be performed until mode sorting at the previous frequency is completed. That is to say, the mode correlation is performed by serial operation. However, mode tracking can be implemented over a wide band due to the large correlation of adjacent frequency modes. So we called it the broadband mode tracking, or the improved algorithm.

II. MODE SORTING

According to CM theory, the current distribution of the conductor surface can be expressed as the superposition of characteristic current vector J_n:

$$J = \sum_n \alpha_n J_n , \qquad (1)$$

where α_n is the complex weighting coefficient of the nth mode. The characteristic current mode J_n is determined by the generalized eigenvalue equation [5]:

$$X J_n = \lambda_n R J_n . \qquad (2)$$

The impedance matrix $Z = R + jX$ of the open conductor obtained by Galerkin MoM is a symmetric matrix. λ_n is the eigenvalue of the nth mode and is the function of frequency. Since the eigenvalue equation depends only on the impedance matrix, in the physical sense, the current wavemode eigenvectors depend only on the shape and size of the conductor structure and is not affected by the excitation source [11-14]. The eigenvalues are also determined only by the conductor structure. Moreover, since X and R are real symmetric matrices, and R also is a positive definite matrix, the eigenvalues obtained by solving (2) are real numbers. It is necessary to sort the modes within the observed frequency range to

use CM theory. At each discrete frequency sample, the modes can be sorted according to the eigenvalue, the modal significance (MS), or the characteristic angle [3]. The most intuitive method is based on the eigenvalue magnitude, which is arranged in ascending order at each frequency.

However, since the eigenvalues change rapidly with frequency, mode swapping is apt to occur. Due to the orthogonality of the characteristic modes and their slow variation with frequency, the eigenvector correlation is generally used for mode tracking to reduce the mode crossing. The correlation coefficient r between vectors A and B can be calculated using the Pearson correlation formula [8, 9]:

$$r(A,B) = \frac{1}{M-1} \frac{\sum_{i=1}^{M}(A_i - \bar{A})(B_i - \bar{B})}{\sqrt{\sum_{i=1}^{M}(A_i - \bar{A})^2 \sum_{i=1}^{M}(B_i - \bar{B})^2}}, \quad (3)$$

where (A_i, B_i) is the vector element pair to be compared, and $\bar{A}$ and $\bar{B}$ are the average of the real vector A and B, respectively. M is the dimension of the vectors A and B, that is, the number of vector elements. Correlation value r ranges between -1 and 1. The closer the absolute value of r is to 1, the higher the correlation between the two vectors. When (3) is used in the mode tracking algorithm, A is the characteristic mode obtained by calculating (2) at a certain frequency, and B is the CM at other frequencies to be paired with A.

If the correlation calculation involves all vector pairs between two frequency points, it is computationally expensive and time-consuming. However, for electrically small and intermediate size conductor bodies, the actual surface current or total radiation field is determined by only the first few characteristic modes. Therefore, we can also reduce the number of vectors used for correlation calculations. For example, to determine the first five modes, only the first 40 eigenvectors are selected for correlation calculation. Nonetheless, the total number of eigenvectors for each frequency is equal to the dimension of the conductor impedance matrix, which is determined by the structure mesh fineness. In fact, since external excitation is not required, the eigenvector results depend only on the calculation of the impedance matrix. Therefore, the accuracy of CM analysis depends mainly on the meshing density, which also determines the calculation amount of the impedance matrix and the number of eigenvalues. When higher order modes are needed in CM analysis, the high mesh density with the mesh element side length of $\lambda/30$ (λ is the wavelength in free space) is suggested. Usually, to ensure the CM analysis accuracy, the mesh fineness with side length of $\lambda/15$ is enough [10].

III. MODE TRACKING BASED ON ORIGINAL ALGORITHM

In CM theory, the mode order is defined according to the ascending eigenvalues at the first frequency. In the original algorithm, the mode order of the subsequent frequency samples is determined by calculating the correlation between the first frequency eigenvectors and those for subsequent frequencies. This algorithm process can be illustrated as shown in Fig. 1.
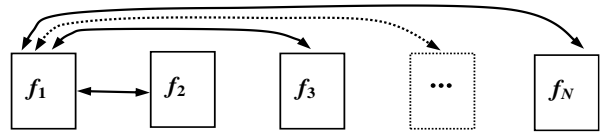
Fig. 1. Illustration of parallel correlation computing process in the original algorithm.

Using this algorithm, the mode curve can be obtained quickly, and mode crossing does not occur in a relatively narrow frequency band, especially for regular conductor structures [10]. However, for broadband situations, mode swapping may happen due to the large frequency span, especially for cases with structure irregularities. To illustrate these issues exemplarily, the algorithm is used to analyze the first five modes of rectangular and butterfly conductor plates in the range from 1 GHz to 5 GHz.

First, the 100 mm × 40 mm rectangular conductor plate is meshed into 512 triangular Rao-Wilton-Glisson (RWG) elements with side length of about $\lambda/15$, as shown in Fig. 2. Thus, we have a total of 744 triangular edges, which also corresponds to the dimension of the impedance matrix. Using (2), we can obtain 744 eigenvalues at each frequency point. The frequency step is 0.2 GHz, that is, the eigenvalue calculation is performed on 21 frequency samples. At each frequency point, the first 40 eigenvectors are selected in ascending order of eigenvalues.
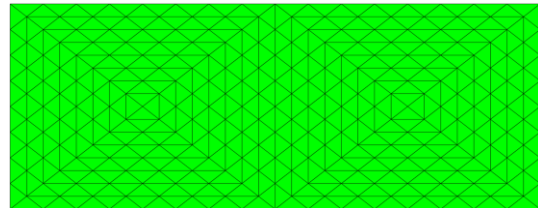
Fig. 2. Meshing of the 100 mm × 40 mm rectangular conductor plate.

Then, the correlation coefficients of the 40 eigenvector pairs between the first frequency and each

subsequent frequency are calculated, and the mode matching is performed using the correlation amplitude according to the mode order of the first frequency. This process is also called the mode arbitration.

The obtained mode tracking curve is shown in Fig. 3. Due to large frequency range, the mode 5 exhibits swapping at around 3.6 GHz. It indicates that this mode arbitration method can only achieve mode tracking in a narrower frequency band. However, this algorithm can implement fast mode tracking because, in addition to parallel operations, the eigenvector number for correlation calculations is limited. Of course, this algorithm can also be implemented by serial operation. In that case, mode sorting for this example takes 12.68 s. In this paper, all the calculations are performed on an Intel Core i7-6700HQ (2.6 GHz) machine with Windows 7 Professional 64 bit and 8 GB of RAM.
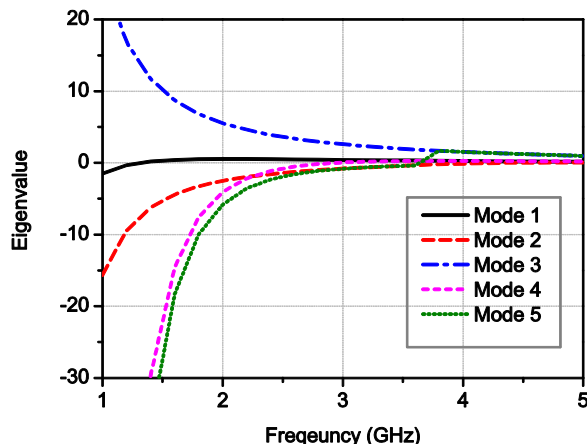
Fig. 3. Mode curves of 100 mm × 40 mm rectangular conductor plate using the original algorithm.

When there are electric field concentration regions in the conductor structure, mode swapping is easily generated, and the frequency range of mode tracking may be further reduced. For this case, tracking of the first five modes for the planar butterfly structure is performed in the range of 1.0-3.0 GHz. The frequency step is also 0.2 GHz.

To form the butterfly structure plate, as shown in Fig. 4, two isosceles triangles having the base length of 200 mm and the waist length of 141 mm are cut out from a 200 mm × 200 mm rectangular conductor plate. Strong electric fields can be concentrated on the thin waist of the butterfly structure. The butterfly plate is discretely meshed using the triangular RWG elements with the side length of approximately $\lambda/15$. Then the number of triangle elements is 720, corresponding to a total of 1025 triangular edges, also shown in Fig. 4.

Using the original tracking algorithm, the resulted mode curve for the butterfly conductor is shown in Fig.

5. It can be seen that mode swapping occurs in the mode 5 curve around 2.2 GHz. This shows that as the conductor structure becomes more complex, the mode tracking bandwidth using the original algorithm will be further reduced. By serial operation, the time for completing the mode tracking of this example is 20.84 s.
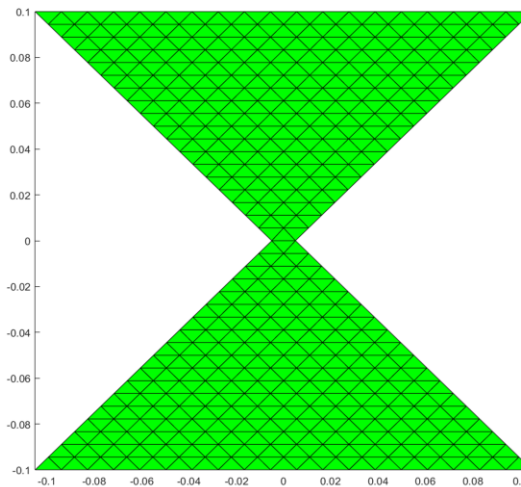
Fig. 4. Meshing model of butterfly conductor plate (unit: m).
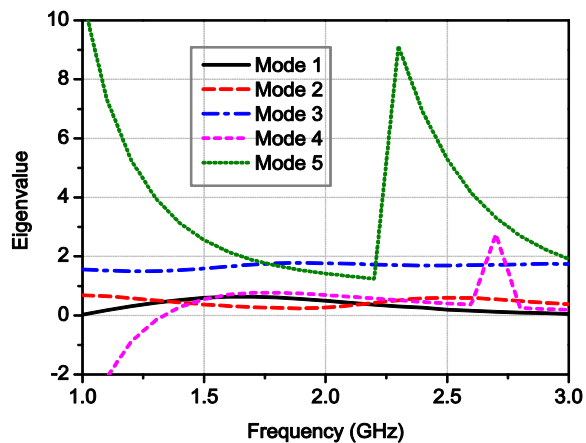
Fig. 5. Mode curves of the butterfly conductor plate based on the original algorithm.

IV. IMPLEMENTATION OF BROADBAND MODE TRACKING

Since the bandwidth of mode tracking is limited by the eigenvector correlation between two frequencies and the span between the first frequency and the last one may be large, the improved algorithm for mode arbitration based on direct adjacent two frequency points is proposed. Specifically, the eigenvectors of the first frequency match those of the second frequency, and then the eigenvectors of the second frequency match those of

the third frequency, and so on. By this way, the first five modes at all frequency samples are determined.

It can be seen that the modes of the current frequency cannot be determined until the modes of the previous frequency are sorted. This tracking process is a serial operation and its calculation speed may be reduced compared to the original parallel algorithm. However, the mode crossing can be eliminated in wide band owing to the fixed frequency interval. Figure 6 shows the mode arbitration process of this broadband mode tracking algorithm.
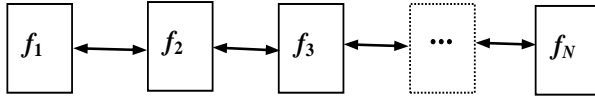
Fig. 6. Mode arbitration illustration of the broadband tracking algorithm.

As an example, the first five modes of the 100 mm × 40 mm rectangular plate are tracked using the mode arbitration method with two directly adjacent frequencies. The obtained first five modes are shown in Fig. 7. We can observe that mode 5 does not exhibit mode swapping. Here, the same mesh density, the same frequency range, and the same frequency step as the case shown in Fig. 3 is used. The mode sorting time using this algorithm is 12.79 s. It indicates that this algorithm can also implement fast mode tracking. In fact, in this example, the first five modes can be tracked in the frequency range of 1.0-10.0 GHz without the mode swapping.
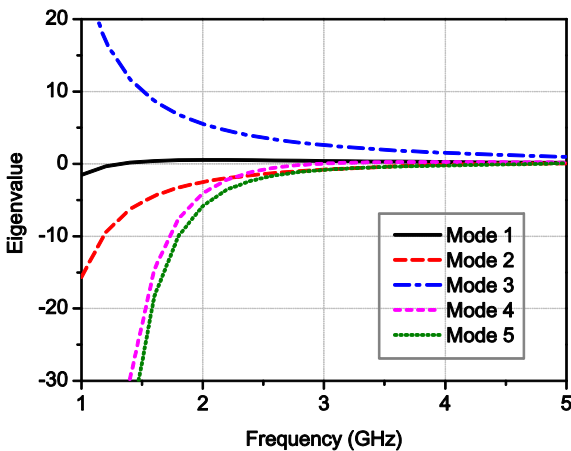
Fig. 7. First five modes of the 100 mm × 40 mm conductor plate based on the wideband algorithm.

Similarly, the butterfly structure shown in Fig. 4 is also subjected to mode tracking using the present method. When the other conditions remain completely unchanged, the resulting mode curve is shown in Fig. 8.

We can see the mode crossing is effectively suppressed in the range from 1 GHz to 3 GHz. In this case, the tracking time of the first five modes is 21.14 s. Using this algorithm, we can also verify that the first five modes can be tracked in the 1.0-4.7 GHz frequency range without the mode crossing. All of those demonstrate the effectiveness of the wideband algorithm.
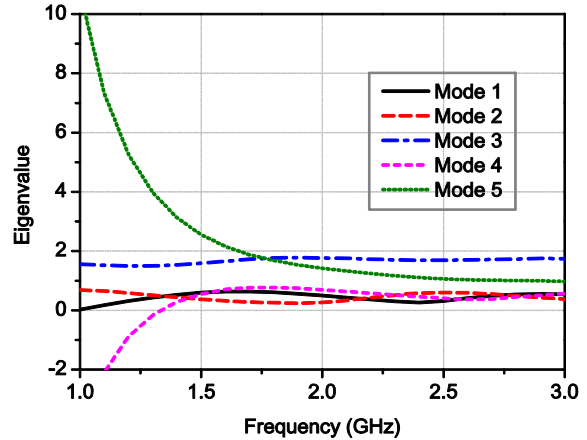
Fig. 8. Mode curves of butterfly structure obtained by using the wideband algorithm.

V. ANALYSIS AND DISCUSSION

A. Cause of mode swapping

For the original algorithm, there are two possible reasons for the occurrence of mode crossing. One is the insufficient calculation accuracy due to the low mesh density, and the other is low eigenvector correlation due to the excessive frequency spacing. The mode swapping shown in Fig. 3 and Fig. 5 is due to the excessive spacing between frequencies f_1 and f_n, rather than due to insufficient mesh density.

To further verify this point of view, the mesh density is doubled to the butterfly structure. Using the original algorithm, we still obtain the mode curves as shown in Fig. 5, which indicates that the mode crossing is not caused by meshing.

B. Number of correlation eigenvector pairs

Although only the first five modes are determined in the numerical examples, we have to calculate the correlation between 40×40 eigenvector pairs. Therefore, the amount of correlation calculation is still large. In fact, the calculation amount can be further reduced according to the number of modes to be sorted, for example, the first five modes.

First, the first five modes of the first frequency are determined with ascending order eigenvalues, and the correlation coefficients between these five modes and the first 40 modes of the second frequency are solved. Then, the first five modes of the second frequency are ordered and used to calculate their correlation with the first 40

modes of the third frequency. By this way, the first five modes for all the frequency points are determined. Thus, the eigenvector pair number of the correlation calculation between the two frequency points is reduced from 40 × 40 of the wideband algorithm to 5 × 40.

C. Parallel operation of wideband algorithm

The wideband algorithm is performed completely in series. However, since the time required for mode sorting is small, we can first calculate the correlation of all adjacent frequency modes in parallel, and then sort modes according to the correlation using serial operation. On the other hand, since there are no first five modes that have been determined beforehand, the correlation calculation is performed on all 40 × 40 eigenvector pairs of the two adjacent frequencies. Thus, the parallel operation of the wideband algorithm contradicts the number of the correlation eigenvector pairs.

D. Reference frequency and frequency step

Intuitively, the intermediate frequency can also be used as the reference point to improve the working bandwidth of the mode tracking algorithm. However, as can be seen, the eigenvalues of the starting reference frequency are greater than those of the subsequent frequencies. If the intermediate frequency is selected as the reference point, the eigenvalue decreases as the frequency decreases in the first half of the frequency band. In this case, the mode curve loses its physical meaning.

On the other hand, it is of course possible to reduce the computation amount of the algorithm by increasing the frequency step. However, if the frequency interval is too large, the vector correlation between two frequency points is weakened and the mode crossing is apt to occur. Therefore, the frequency step should be a compromise between computational speed and mode crossing control.

VI. CONCLUSION

Considering the need of broadband high-precision mode tracking, the serial operation between direct adjacent frequencies is used in mode correlation calculation. The numerical results show that this algorithm can reliably improve the bandwidth of mode tracking and effectively control the mode crossing. Since correlation calculations are performed using a limited number of eigenvectors, less time is required to complete wideband mode tracking.

The mode tracking bandwidth implemented by this algorithm is sufficient in practical applications. In fact, characteristic mode analysis should not be used in excessive bandwidth, otherwise misleading problems may occur.

REFERENCES

[1] K. K. Kishor and S. V. Hum, "Multiport multiband chassis-mode antenna design using characteristic modes," *IEEE Antenna Wirel. Propag. Lett.*, vol. 16, pp. 609-612, 2017.

[2] R. Martens and D. Manteuffel, "Systematic design method of a mobile multiple antenna system using the theory of characteristic modes," *IET Microwave Antennas Propagat.*, vol. 8, no. 12, pp. 887-893, Sept. 2014.

[3] Y. Chen and C. F. Wang, "Characteristic-mode-based improvement of circularly polarized U-slot and E-shaped patch antennas," *IEEE Antenna Wirel. Propag. Lett.*, vol. 11, pp. 1474-1477, 2012.

[4] M. Cabedo-Fabres, E. Antonino-Daviu, A. Valero-Nogueira, and M. F. Bataller, "The theory of characteristic modes revisited: A contribution to the design of antennas for modern applications," *IEEE Antenna Propag. Mag.*, vol. 49, no. 5, pp. 52-68, Oct. 2007.

[5] R. Harrington and J. Mautz, "Theory of characteristic modes for conducting bodies," *IEEE Trans. Antennas Propag.*, vol. 19, no. 5, pp. 622-628, Sept. 1971.

[6] M. Capek, P. Hazdra, P. Hamouz, and J. Eichler, "A method for tracking characteristic numbers and vectors," *Prog. Electromagn. Res.*, vol. 33, pp. 115-134, 2011.

[7] E. Safin and D. Manteuffel, "Advanced eigenvalue tracking of characteristic modes," *IEEE Trans. Antennas Propag.*, vol. 64, no. 7, pp. 2628-2636, July 2016.

[8] D. J. Ludick, J. V. Tonder, and U. Jakobus, "A hybrid tracking algorithm for characteristic mode analysis," in *Proc. Int. Conf. Electromagn. Adv. Appl.*, Palm Beach, FL, pp. 455-458, Aug. 2014.

[9] D. J. Ludick, U. Jakobus, and M. Vogel, "A tracking algorithm for the eigenvectors calculated with characteristic mode analysis," in *Proc. 8th European Conf. Antennas and Propagation (EuCAP)*, The Hague, Netherlands, pp. 569-572, Apr. 2014.

[10] W. Li, J. Zhu, B. Xu, and Z. Zeng, "Fast implementation of characteristic mode tracking," *IET Microwave Antennas Propagat.*, vol. 12, no. 14, pp. 2179-2183, Nov. 2018.

[11] Z. T. Miers and B. K. Lau, "Computational analysis and verifications of characteristic modes in real materials," *IEEE Trans. Antennas Propag.*, vol. 64, no. 7, pp. 2595-2607, July 2016.

[12] Y. Chen, "Alternative surface integral equation-based characteristic mode analysis of dielectric resonator antennas," *IET Microwave Antennas Propagat.*, vol. 10, no. 2, pp. 193-201, Jan. 2016.

[13] Q. He, Z. Gong, H. Ke, and L. Guan, "A double modal parameter tracking method to characteristic modes analysis," *ACES Journal*, vol. 32, no. 12, pp. 1069-1076, Dec. 2017.

[14] A. Araghi and G. Dadashzadeh, "Detail-oriented design of a dual-mode antenna with orthogonal radiation patterns utilizing theory of characteristic modes," *ACES Journal*, vol. 28, no. 10, pp. 952-959, Oct. 2013.

The Application of Chirp Z-Transform in Fast Computation of Antenna Array Pattern

Cheng Zhang [1], Anyong Qing [2, 1], and Yang Meng [1]

[1] School of Physics
University of Electronic Science and Technology of China, Chengdu, 610054, China
zhangcheng_uestc@163.com, mengy.1003@163.com

[2] School of Electrical Engineering
Southwest Jiaotong University, Chengdu, 610031, China
qinganyong@tsinghua.org.cn

Abstract ─ As an essential means of evaluating antenna array performance and the basis of antenna array design, numerical computation of antenna array pattern is very important. Computation of antenna array pattern by using straightforward summation is very time consuming especially for planar array with many elements. Moreover, in some applications such as antenna array synthesis, huge number of repeated pattern computations is needed that the consumed time is intolerably long. Although the computation can be accelerated by fast Fourier transform (FFT) when the elements are equally spaced by half of a wavelength because the array factor and the element excitation currents is a Fourier transform pair, in general, FFT is not applicable. In this paper, the chirp z-transform (CZT) is introduced to accurately and efficiently compute pattern of general linear or planar antenna arrays. Numerical examples confirm that CZT is flexible, efficient, and accurate.

Index Terms ─ Antenna array pattern, chirp z-transform, FFT, linear antenna array, planar antenna array.

I. INTRODUCTION

Usually antenna arrays instead of bulky single-element antennas are deployed for higher directivity, narrower beam width, anti-interference ability and so on. Numerical computation of antenna array pattern is very important because it is an essential means of evaluating antenna array performance and is the basis of antenna array design [1].

In practice, array elements are often but not necessarily identical for convenience and simplicity. In this case, the array pattern of an ideal array is usually represented by its array factor.

For the general linear antenna array with *N* elements as shown in Fig. 1, its array factor reads:

$$AF\left(u,u_0\right) = \sum_{n=1}^{N-1} I_n \cdot \exp\left[j2\pi \frac{x_n}{\lambda}\left(u-u_0\right)\right], \qquad (1)$$

where $u=\cos\theta$, $\theta \in [0, \pi]$, $u_0=\cos\theta_0$, θ_0 is the desired beam steering direction, I_n and x_n are the excitation current and the position of the nth element, respectively, λ is the wavelength.

For the general planar antenna array with N elements as shown in Fig. 2, its array factor is given by:

$$AF\left(u,v,u_0,v_0\right) = \sum_{n=0}^{N-1} I_n \cdot \exp\left[jx_n \frac{2\pi}{\lambda}\left(u-u_0\right) + jy_n \frac{2\pi}{\lambda}\left(v-v_0\right)\right], (2)$$

where u and v are defined in terms of sine space coordinates $u=\sin\theta\cos\varphi$ and $v=\sin\theta\sin\varphi$, $u_0=\sin\theta_0\cos\varphi_0$, $v_0=\sin\theta_0\sin\varphi_0$, (θ_0, φ_0) is the main beam steering direction, I_n and (x_n, y_n) are the excitation current and the position of the nth element, respectively.
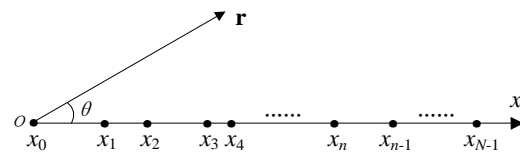

Fig. 1. General linear antenna array.
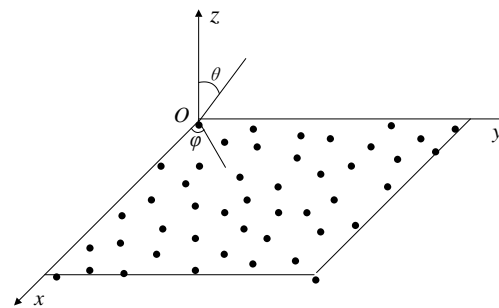
Fig. 2. General planar antenna array.

In some applications such as phased antenna array synthesis, the number of computations of array factor T might be extremely high. In general, T reads:

$$T = a \cdot b \cdot c \,, \qquad (3)$$

where a is the number of directions for a fixed array at fixed main beam direction. To evaluate the array performance, the array factor has to be calculated at as many directions as possible within a given range. b is the number of scanning angles (u_0, v_0) of interest. Different patterns might be required when the main beam scanning at different scanning angles. c is the number of antenna arrays considered during the complete synthesis process. Thousands or even more antenna arrays with fixed main beam direction and different weights need to be evaluated when optimizing array excitations by using methods such as statistical strategy optimization techniques [2-4].

For the planar antenna array considered in section 3C, calculation of array factor with $a=512\times512$ directions by using the brute-force method (BFM) will be taken about 15.2 seconds. If $b=100$ scanning angles (u_0, v_0) are considered and $c=10000$ times of array factor calculations for each scanning angle are needed, thus $T\approx2.62\times10^{11}$. The corresponding consumed time is about 1.52×10^7 and it is intolerably long. Therefore, fast computation of array factor is utmost importance.

For an array with equally spaced elements, the array factor and the element excitation currents are a Fourier transform pair as expressed in (4). The formal expression of inverse discrete Fourier transform (IDFT) is also given in (5):

$$AF(u_k) = \sum_{n=-(N-1)/2}^{(N-1)/2-1} I_n \cdot e^{j2\pi n \frac{d}{\lambda}u_k}, k = -\frac{K-1}{2},...,\frac{K-1}{2}-1, \quad (4)$$

$$x(n) = \sum_{k=-(N-1)/2}^{(N-1)/2-1} \frac{X(k)}{N} \cdot e^{j2\pi k \frac{n}{N}}, n = -\frac{(N-1)}{2}...,\frac{(N-1)}{2}-1. \quad (5)$$

It might be a feasible way by adopting fast Fourier transform (FFT) in order to accelerate the computation of array factor [5]. However, compared (4) and (5), it can be seen that one of the correspondences holds:

$$\frac{n}{N} \longleftrightarrow \frac{d}{\lambda}u_k \,. \qquad (6)$$

Expression (5) can be re-written as:

$$\frac{n}{N} \cdot \frac{\lambda}{d} \longleftrightarrow u_k \,. \qquad (7)$$

Due to $-0.5 \leq n/N \leq 0.5$ and $-1 \leq u_k \leq 1$, the condition $\lambda/d=2$ must be met. In other words, FFT can be directly used to compute pattern of array with elements spacing only equal to half of wavelength depicted in Fig. 3. For general arrays, FFT cannot be directly applied.

In this paper, a versatile, efficient, and accurate approach to compute patterns of general antenna arrays with arbitrary spacing between array elements is proposed. The novel approach is based on CZT [6-7] which provides greater flexibility compared to FFT

for calculation of array factor. The corresponding parameters of CZT for antenna array factor computation are derived. Computation processes are also explored and given in this paper. Simulation results prove that it is applicable with high accuracy and efficiency, especially for planar array with equally or unequally spaced elements.
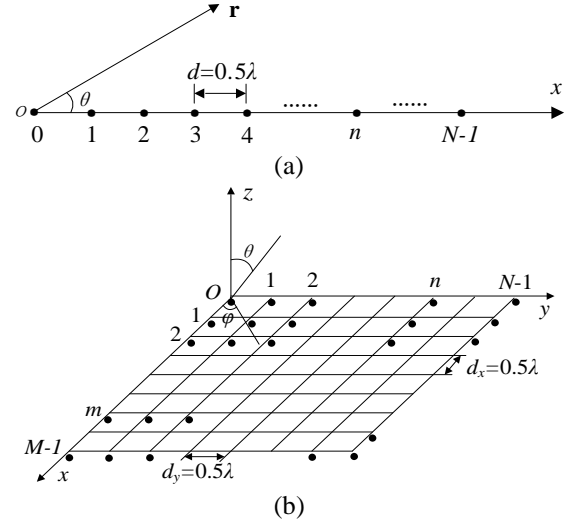
Fig. 3. Antenna arrays with elements spacing equal to half of a wavelength: (a) linear array and (b) planar array.

II. CHIRP Z-TRANSFORM FOR FAST COMPUTATION OF ARRAY FACTOR

A. One-dimension chirp z-transform

For an N-point sequence $x(n)$, CZT samples along spiral arcs in the z-plane as:

$$X(z_k) = \sum_{n=0}^{N-1} x(n) z_k^{-n} \,, \qquad (8)$$

where $z_k = AW^{-k}$, $k = 0, 1, \ldots, K-1$, K is the number of points to calculate, A is the complex starting point, and W is the complex ratio between points.

In particular, if $A = A_0 e^{j2\pi\omega_0}$ and $W = e^{j2\pi\phi_0}$, CZT can be expressed as a convolution and computed efficiently by using Rabiner's algorithm [6].

B. Two-dimension chirp z-transform

2-D CZT of sequence $x(m, n)$ was derived by Draidi [7]:

$$X(z_{1k}, z_{2l}) = \sum_{m=0}^{M-1}\sum_{n=0}^{N-1} x(m,n) z_1^{-m} z_2^{-n}$$

$$= \sum_{m=0}^{M-1}\sum_{n=0}^{N-1} x(m,n)\left(A^1\right)^{-m} W_1^{mk} \left(A^2\right)^{-n} W_2^{nl} \qquad (9)$$

where $z_{1k} = A^1 W_1^{-k}$, $z_{2l} = A^2 W_2^{-l}$, $k= 0, \ldots, K-1, l=0, \ldots, L-1$, $A^1 = A_0^1 e^{j2\pi\omega_{01}}$, $W_1 = e^{j2\pi\phi_{01}}$, $A^2 = A_0^2 e^{j2\pi\omega_{02}}$, and $W_2 = e^{j2\pi\phi_{02}}$.

The above 2-D CZT can be efficiently computed by using row-column decomposition and 1-D CZT.
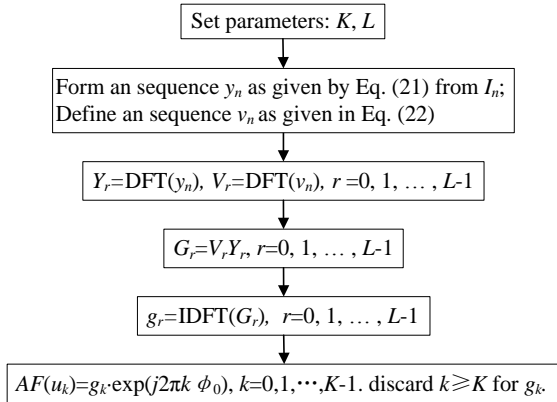
Fig. 4. The flow chart of pattern computation of linear array with equally spaced elements.

C. 1-D chirp z-transform for linear antenna array

For a linear antenna array with N equally spaced elements, (1) can be re-written as,

$$AF(u_k) = \sum_{n=0}^{N-1} I_n e^{jn\psi_k}, \qquad (10)$$

where $u_k = \cos\theta_k$, $k=0,1,\dots,K-1$, K is the total number of angles to sample, $0 \le \theta_k \le \pi$ is the kth sampled angle, $\psi_k = \beta d u_k - \psi_0$, $\beta = 2\pi/\lambda$ is the phase constant, d is the space between neighboring elements, $\psi_0 = \beta d u_0$ is the progressive phase delay between neighboring elements. Let $z_k = e^{-j\psi_k}$, we have:

$$AF(u_k) = \sum_{n=0}^{N-1} I_n z_k^{-n}. \qquad (11)$$

Obviously, CZT can be applied to compute the array factor $AF(u_k)$ efficiently if the following conditions are satisfied:

$$z_k = e^{-j(\beta d\cos\theta_k - \psi_0)} = A_0 e^{j2\pi\omega_0} e^{-jk2\pi\phi_0}. \qquad (12)$$

Equivalently, we have:

$$A_0 = 1, \qquad (13)$$

$$2\pi\omega_0 = \psi_0 - \beta d, \qquad (14)$$

$$2\pi\omega_0 - (K-1)2\pi\phi_0 = \psi_0 + \beta d, \qquad (15)$$

$$\beta d\cos\theta_k - \psi_0 = k2\pi\phi_0 - 2\pi\omega_0. \qquad (16)$$

Therefore, the parameters of CZT for computation of $AF(u_k)$ are:

$$A_0 = 1, \qquad (17)$$

$$\omega_0 = \frac{u_0 - 1}{2\pi}\beta d, \qquad (18)$$

$$\phi_0 = -\frac{\beta d}{(K-1)\pi}, \qquad (19)$$

$$\theta_k = \cos^{-1}\frac{K-1-2k}{K-1}. \qquad (20)$$

After derivation of the parameters, the calculation process addressed in [6] of CZT can be directly used to compute the linear array factor. A more detailed illustration is also given in this paper and shown in Fig. 4. In step 1, set L to be the smallest integer greater than or equal to $N+K-1$. The forms of y_n and v_n in step 2 are similar to the forms addressed in [6] and reads:

$$y_n = \begin{cases} I_n e^{-j2\pi n\omega_0} e^{j\pi n^2\phi_0}, & 0 \le n \le N-1, \\ 0, & N \le n \le L-1 \end{cases}, \qquad (21)$$

$$v_n = \begin{cases} e^{-j\pi n^2\phi_0}, & 0 \le n \le K-1 \\ e^{-j\pi(L-n)^2\phi_0}, & L-N+1 \le n \le L-1. \\ 0, & \text{other } n \end{cases} \qquad (22)$$

The convolution of y_n and v_n is the major part of the computational effort and requires a time roughly proportional to $(N+K)\log(N+K)$. It can be achieved by using DFT and the details are displayed in step 3~step 5 [8]. The DFT and inverse DFT (IDFT) can be accelerated by using FFT. Therefore, the computation speed is very fast.

In nature, the 1-D CZT imposes no limitation on element space d in regular linear array. It can be further extended to linear array with unequally spaced elements as shown in Fig. 5.
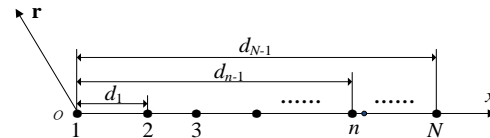
Fig. 5. A linear array with unequally spaced elements.

The extension works as follows:

1) Refine the linear array with N unequally spaced elements into a virtual one as shown in Fig. 6 with N_e equally spaced elements of space d_u, which is determined by the following expression:

$$d_u = \max\left[\min \sum_n \left| \lceil \frac{d_n}{d_u} \rfloor d_u - d_n \right| \right], \qquad (23)$$

where the symbol $\lfloor x \rceil$ stands for the integer nearest to the real number x;

2) Place the original elements to the nearest node in the virtual array without changing their excitations, and deactivate all element on other nodes by setting excitation currents $I_m = 0$;

3) Apply the 1-D CZT to compute the pattern.
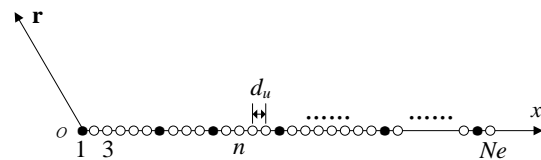
Fig. 6. The virtual linear array.

D. 2-D chirp z-transform for planar antenna array

For a planar antenna array with elements arranged in a rectangle grid at distance d_x and d_y along M rows and N column. (2) can be re-written as:

$$AF\left(u_{kl},v_{kl}\right)=\sum_{m=0}^{M-1}\sum_{n=0}^{N-1}I_{mn}e^{j\left[m\beta d_x(u_{kl}-u_0)+n\beta d_y(v_{kl}-v_0)\right]}, \quad (24)$$

where $u_{kl}=\sin\theta_{kl}\cos\varphi_{kl}$ and $v_{kl}=\sin\theta_{kl}\sin\varphi_{kl}$, $k=0,\dots,K-1$, $l=0,\dots,L-1$.

By checking the analogy between (9) and (24), it is very clear that $AF(u_{kl}, v_{kl})$ can be more efficiently computed by applying 2-D CZT if its parameters are appropriately set. Derivation of parameters is similar to the 1-D CZT. Due to page limitation, the lengthy derivation process is omitted. The parameters are:

$$A_0^1 = A_0^2 = 1, \quad (25)$$

$$\phi_{01} = \frac{-\beta d_x}{(K-1)\pi}, \quad (26)$$

$$\phi_{02} = \frac{-\beta d_y}{(L-1)\pi}, \quad (27)$$

$$\omega_{01} = \frac{u_0-1}{2\pi}\beta d_x, \quad (28)$$

$$\omega_{02} = \frac{v_0-1}{2\pi}\beta d_y, \quad (29)$$

$$\theta_{kl} = \cos^{-1}\sqrt{\left(\frac{K-1-2k}{K-1}\right)^2+\left(\frac{L-1-2l}{L-1}\right)^2}, \quad (30)$$

$$\varphi_{kl} = \sin^{-1}\frac{\frac{L-1-2l}{L-1}}{\sqrt{\left(\frac{K-1-2k}{K-1}\right)^2+\left(\frac{L-1-2l}{L-1}\right)^2}}. \quad (31)$$

The flow chart of array factor computation of planar array with equally spaced elements is shown in Fig. 7.

In this paper, 2-D CZT is efficiently performed by using 1-D CZT with row-column decomposition [7]. In step 1, set P_1 to be the smallest integer greater than or equal to $M+K-1$, and set P_2 to be the smallest integer greater than or equal to $N+L-1$. In step 2, $v(p_1, p_2)$ is similar with $g(n, m)$ addressed in [7] and given in (32). The forms of $v(p_1, p_2)$ and $vh(p_1, p_2)$ are similar with the forms of v_n illustrated in (22) and given in (33)~(34), respectively:

$$h(p_1,p_2)=\begin{cases}I_{p_1p_2}e^{j2\pi(p_1\omega_{01}+p_2\omega_{02})}e^{j\pi\left(\phi_{01}p_1^2+\phi_{02}p_2^2\right)}, & \begin{cases}0\le p_1\le M-1,\\0\le p_2\le N-1\end{cases}\\ 0, & \text{other } p_1 \text{ and } p_2\end{cases},(32)$$

$$v(p_1,p_2)=\begin{cases}e^{-j\pi\phi_{02}p_2^2}, & 0\le p_1\le M-1,0\le p_2\le L-1\\ e^{-j\pi\phi_{02}(P_1-p_1)^2/2}, & \begin{cases}0\le p_1\le M-1,\\P_2-N+1\le p_2\le P_2-1\end{cases}\\ 0, & \text{other } p_1 \text{ and } p_2\end{cases}, (33)$$

$$vh(p_1,p_2)=\begin{cases}e^{-j\pi\phi_{01}p_1^2}, & 0\le p_1\le K-1,0\le p_2\le P_2-1\\ e^{-j\pi\phi_{01}(P_1-p_1)^2/2}, & \begin{cases}P_1-M+1\le p_1\le P_1-1,\\0\le p_2\le P_2-1\end{cases}\\ 0, & \text{other } p_1 \text{ and } p_2\end{cases}. (34)$$

In step 3~step 5, we first compute the CZT of each row of $h(p_1, p_2)$, put the result into an intermediate array, and then compute the CZT of each column of the intermediate array in step 7~step 9. Similarly, FFT is used to accelerate the DFT and IDFT. Therefore, the consumed time is substantially reduced.

It can be similarly generalized to efficiently compute array factors of planar arrays with unequally spaced elements, for example, triangular arrays whose elements are arranged in a triangular grid.
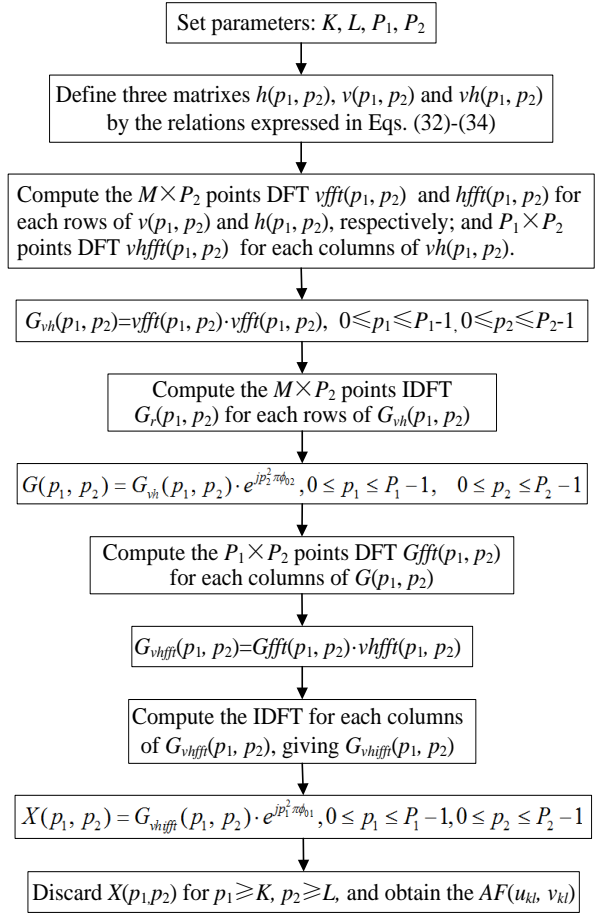
Fig. 7. The flow chart of array factor computation of planar array with equally spaced elements.

III. NUMERICAL RESULTS

### A. Linear array with unequally spaced elements

The first linear array is one with 32 equally spaced elements of $d=0.7\lambda$. The excitations follow a Chebyshev

distribution [9] with *SLL*=-35dB and θ_0=20°. The array factor computed by 1-D CZT is depicted in Fig. 8. Obviously, it agrees very well with that by BFM.

(a)

(b)
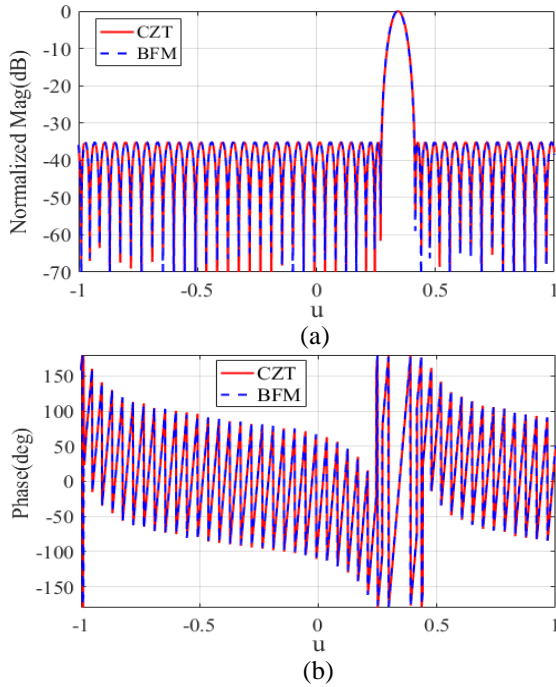
Fig. 8. Comparison of Chebyshev patterns computed by CZT and BFM: (a) magnitude and (b) phase.

The second linear array is a 40-element Woodward array [10] having a space *d*=0.32*λ* and half beam width 20°. Once again, as shown in Fig. 9, the patterns by the two approaches overlap.

Figure 10 shows the time consumed by the two methods for computing linear array factors with various number of elements. It can be seen that the consumed time grows linearly with number of elements for both methods. The slope of CZT is 0.004×10^{-3} that its consumed time is almost constant for the studied number of elements. On the other hand, the slope of BFM is 0.05×10^{-3} that the consumed time difference becomes bigger and bigger as the number of elements increases beyond 30. Therefore, CZT is more suitable for large linear arrays with equally spaced elements.

B. Linear array with unequally spaced elements

A 37-element array with uniform excitation and unequally spaced elements addressed in Table 3 of [11] is re-visited here. Distribution of elements is extremely irregular that it is hardly possible to align all elements in the refined array with the corresponding elements in the actual array regardless of d_u. From the point of view of time consumption, the above observation in Section 3A of this paper hints that it is flexible to set as small as possible d_u for better alignment and consequently better

accuracy of the computed array factor by CZT. The effect of d_u on computational accuracy and computational time is shown in Table 1. The accuracy at d_u=0.02*λ* is fairly good, as can be further demonstrated by the array factor in Fig. 11. Meanwhile, both actual computation time and its increment are negligibly small even if the virtual antenna array is 20 times denser.

(a)

(b)
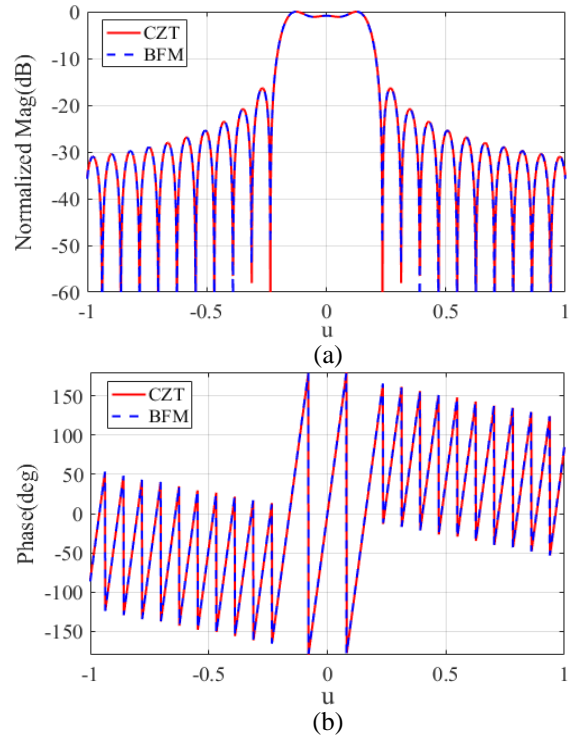
Fig. 9. Comparison of Woodward patterns computed by CZT and BFM: (a) magnitude, and (b) phase.
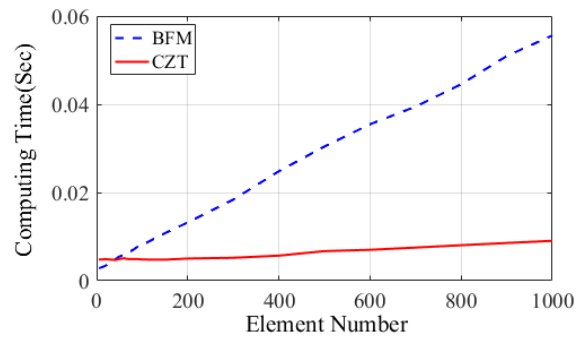
Fig. 10. Comparison of consumed time for computing array factors with equally spaced elements.

Table 1: Comparison of accuracy and consumed time

d_u	Mag. (dB)	Phase (Deg)	CZT (Sec)
0.005*λ*	0.1	1	0.031
0.01*λ*	0.19	1.5	0.022
0.05*λ*	0.45	4.5	0.014
0.1*λ*	1.1	12	0.013
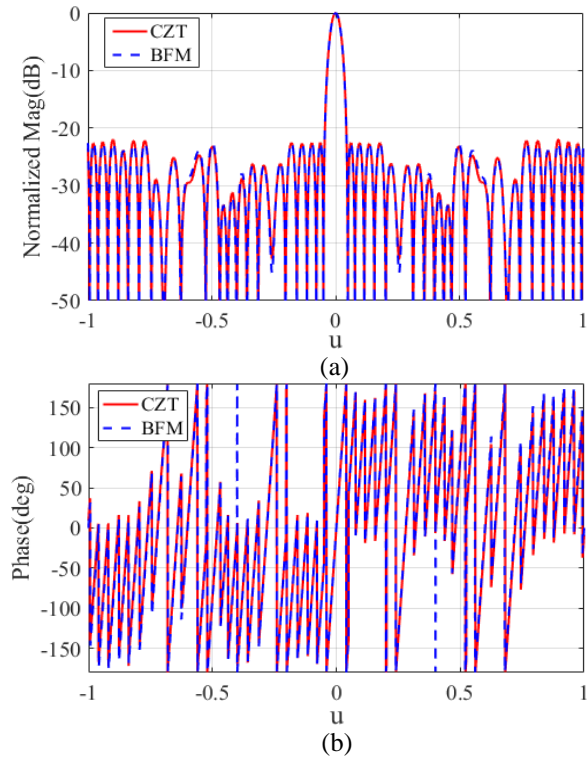
Fig. 11. Comparison of patterns of linear array with unequally spaced elements: (a) magnitude, and (b) phase.

C. Planar array with equally spaced elements

A rectangular planar array consisting of M=24 rows and N=32 columns of elements arranged along a rectangular grid with d_x=0.7λ and d_y=0.4λ is used to illustrate the capability of the 2-D CZT. Its main beam is pointed at (θ_0=20°, φ_0=45°) and a Chebyshev response is assumed to suppress the sidelobe at -35dB.

Figure 12 shows the magnitude and phase patterns computed by the 2-D CZT and BFM in the *u-v* coordinates. The patterns computed by the two methods are almost identical. For clarity, the *u*-cuts of the patterns at *v*=0.242 is drawn in Fig. 13. The differences of *PSLL* and phase are less than 0.2 dB and 3.5°.

The consumed time of the two methods for computing planar array factors with various numbers of equally spaced elements is shown in Fig. 14. The consumed time of 2-D CZT is almost constant. The consumed time is less than 0.15 second even for arrays with ten thousand elements. For BFM, the consumed time is about 176 second, which is 1173 times to 2-D CZT.
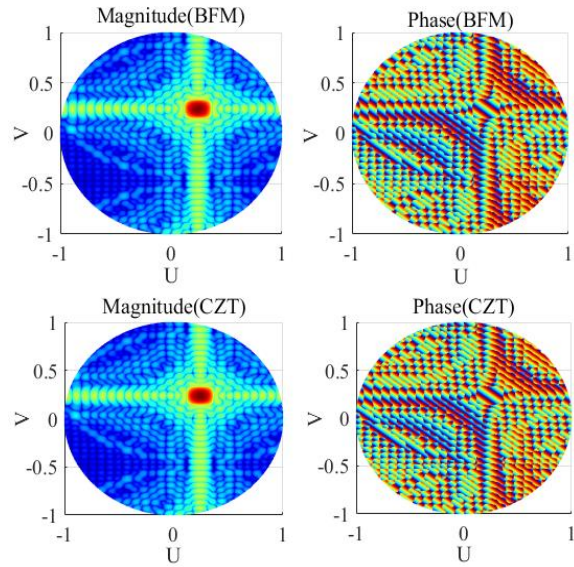
Fig. 12. Comparison of planar array patterns computed by BFM and CZT.
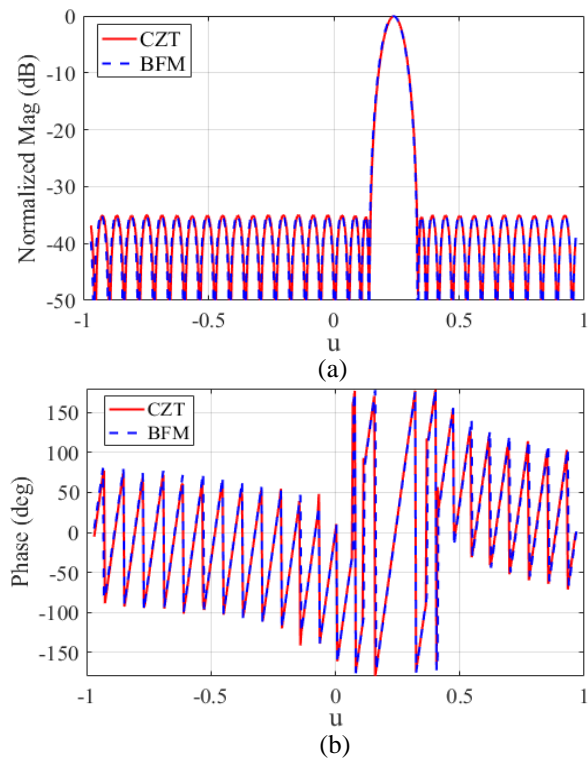
Fig. 13. *u*-cuts at *v*=0.242: (a) magnitude and (b) phase.
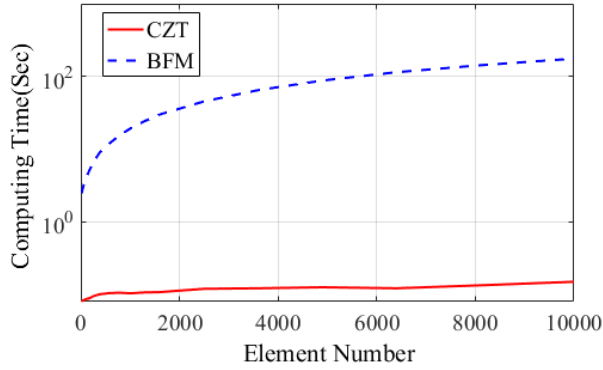
Fig. 14. Consumed time of CZT and BFM with various element numbers.

It is common sense that pattern of larger planar array has to be more finely sampled to reduce error. The consumed time with different number of sampling points of the above mentioned uniform planar array factor is listed in Table 2. Both grow as the number of sampling points increases. More importantly, the ratio between them becomes larger and larger. It can therefore be concluded that 2-D CZT is more advantageous to BFM in computing large planar array.

Table 2: Consumed time with different sampling points

Sampling Points	CZT (Sec)	BFM (Sec)
256×256	0.03	3.78
512×512	0.11	15.21
768×768	0.17	33.6
1024×1024	0.27	60.46
1536×1536	0.55	134.38

D. Planar array with unequally spaced elements

Figure 15 shows a planar phased antenna array with 576 unequally spaced elements. The array was illuminated by uniform excitation and its main beam is pointed at (θ_0=30°, φ_0=60°).

Likewise, distribution of elements here is also extremely irregular that it is hardly possible to align all elements in the refined array with the corresponding elements in the actual array regardless of d_u and d_v. Fortunately, the above observation in section 3C of this paper allows us to flexibly set as small as possible d_u and d_v for better alignment and consequently better accuracy of the computed array factor by CZT. A similar study on the effect of d_u and d_v on computational accuracy is conducted. For simplicity, only cases of $d_u = d_v$ are investigated as shown in Table 3. The accuracy at $d_u = d_v$ =0.02λ is fairly good while CZT always consumes much less time than BFM.
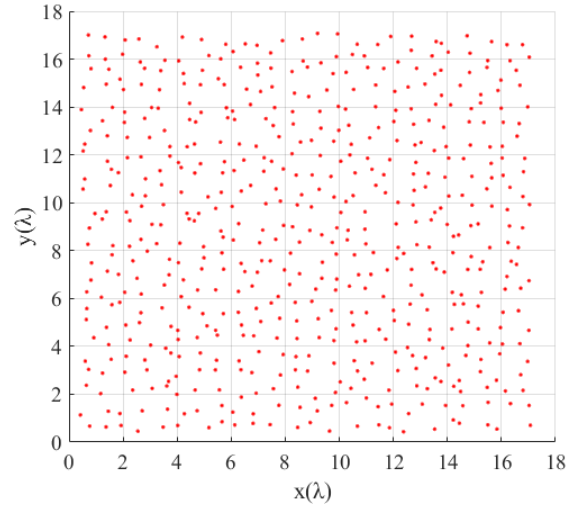
Fig. 15. A planar array with unequally spaced elements.

The actual array is accordingly refined d_u =0.02λ in x directions and d_v =0.02λ in y directions. The patterns computed by the two methods are shown in Fig. 16. For clarity, the u-cuts of the patterns at v=0.25 is drawn in Fig.17. The *PSLL* and phase differences are less than 0.05dB and 4.4°.

Table 3: Comparison of computational accuracy and computational time

d_u and d_v	Mag. (dB)	Phase (Deg)	2-D CZT	BFM (Sec)
0.01λ	0.03	2.5	2.78	12.55
0.02λ	0.05	4.4	1.21	12.55
0.05λ	0.05	6.8	0.54	12.55
0.1λ	0.06	9.5	0.33	12.55

Similarly, the consumed time with different number of sampling points of the above mentioned non-uniform planar array factor is listed in Table 4. The consumed time for both methods is proportional to the number of sampling points. More importantly, the ratio between them becomes larger and larger. It can therefore be concluded that 2-D CZT is more advantageous to BFM in computing large planar array.

Table 4: Comparison of consumed time with different sampling points

Sampling Points	2-D CZT	BFM (Sec)
256×256	0.88	2.97
512×512	1.21	12.55
768×768	1.85	27.99
1024×1024	2.35	50.66
1536×1536	3.57	108.04
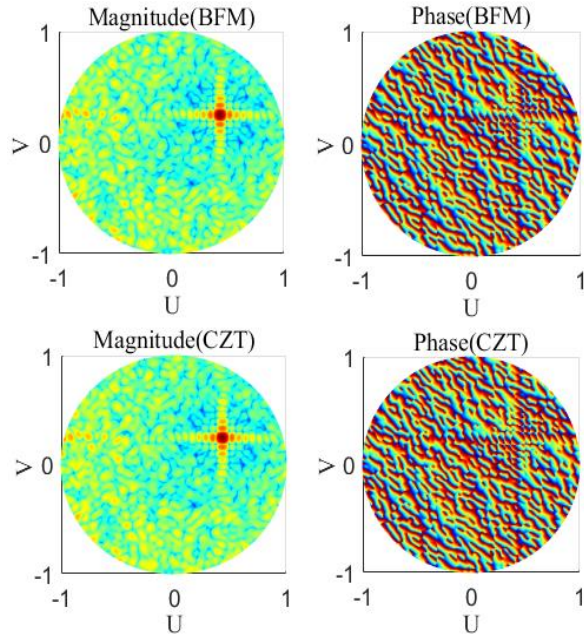
Fig. 16. Comparison of patterns computed by BFM and CZT, respectively.

(a)

(b)
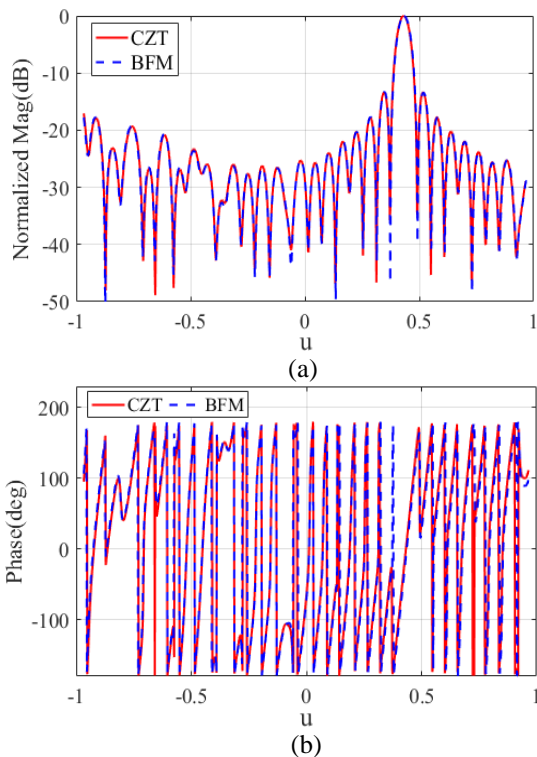
Fig. 17. *u*-cuts at *v*=0.25: (a) magnitude and (b) phase.

IV. CONCLUSION

In this paper, a novel approach based on CZT is proposed to accurately and efficiently compute pattern of general linear or planar antenna arrays. The corresponding parameters of CZT are derived, making it suitable for antenna array factor computation. Computation processes are also explored and given in this paper. Simulation results prove that it is applicable with high accuracy and efficiency, especially for planar array with equally or unequally spaced elements.

REFERENCES

[1] C. A. Balanis, *Antenna Theory - Analysis and Design*. 2nd ed., Harper & Row New York, 2005.

[2] N. Anselmi and L. Poli, "Design of simplified array layouts for preliminary experimental testing and validation of large AESAs," *IEEE Trans. on Antennas Propagation*, vol. 66, no. 12, pp. 6906-6920, Dec. 2018.

[3] Y. Ma and S. Yang, "Pattern synthesis of 4-D irregular antenna arrays based on maximum-entropy model," *IEEE Trans. on Antennas Propagation*, vol. 67, no. 6, pp. 3048-3057, May 2019.

[4] B. Zhang and Y. Rahmat-Samii, "Robust optimization with worst case sensitivity analysis applied to array synthesis and antenna designs," *IEEE Trans. on Antennas Propagation*, vol. 66, no. 1, pp. 160-171, Jan. 2018.

[5] V. V. Bhargav and G. K. Mahanti, "Minimization of side lobe level of scanned linear array antenna with fixed dynamic range ratio utilizing iterative fast Fourier transform," *IEEE Applied Electromagnetic Conf.*, Kolkata, India, Dec. 18-22, 2011.

[6] L. R. Rabiner and R. W. Schafer, "The chirp z-transform algorithm," *IEEE Trans. Audio and Electroacoustics.*, vol. 17, no. 2, pp. 86-92, June 1969.

[7] J. A. Draidi and M. A. Khasawnch, "Two-dimensional chirp z-transform and its application to zoom Wigner bispectrum," *IEEE International Symposium on Circuits and Systems*, Atlanta, GA, vol. 2, pp. 540-543, May 12-15, 1996.

[8] T. G. Stockham, "High speed convolution and correlation," *1966 Spring Joint Computer Conf.*, *AFIPS Proc.*, vol. 28, Washington, D. C.: Spartan, pp. 229-233, 1966.

[9] C. L. Dolph, "A current distribution for broadside arrays which optimizes the relationship between beamwidth and sidelobe level," *Proc. IRE*, vol. 34, no. 6, pp. 335-348, 1946.

[10] P. M. Woodward and J. D. Lawson, "The theoretical precision with which an arbitrary radiation-pattern may be obtained from a source of a finite size," *J. IEE*, vol. 95, pt. III, no. 37, pp. 363-370, Sept. 1948.

[11] C. Lin, A. Qing, and Q. Feng, "Synthesis of unequally spaced antenna arrays by using differential evolution," *IEEE Trans. on Antennas Propagation*, vol. 58, no. 8, pp. 2553-2560, Aug. 2010.

Cheng Zhang was born in Zhongwei, Ning'xia Province, China, in 1988. He received the B.S. degree in Optical Information Science and Technology and the M.Sc. degree in Electronics and Communication Engineering from the University of Electronic Science and Technology of China (UESTC), Chengdu, Sichuan, China, in 2011 and 2014, respectively. Now, he is currently pursuing the Ph.D. degree in Radio Physics at UESTC.

Anyong Qing (S'97–M'00–SM'05) was born in Hu'nan province, China, on May 27, 1972. He received the B.E. degree from Tsinghua University, in 1993, the M.E. degree from Beijing Broadcasting Institute, Beijing, China, in 1995, and the Ph.D. degree from Southwest Jiaotong University in 1997, all in Electromagnetic Theory and Microwave Technology. He was a Postdoctoral Fellow in the Department of Communication Engineering, Shanghai University, Shanghai, China, between September 1997 and June 1998 and a Research Fellow at the School of Electrical and Electronic Engineering, Nanyang Technological University, Singapore from June 1998 to June 2000. He was a Member of Scientific Staff in the Electromagnetic Theory Group at the Department of Electrical Engineering, University of Kassel, Kassel, Germany, from July 2000 to May 2001. He was a Research Scientist at Temasek Laboratories, National University of Singapore, Singapore, from September 2001 to December 2009 and a Senior Research Scientist from January 2010 to October 2012. He was a Professor with School of Physics, University of Electronic Science and Technology of China, Chengdu, China since November 2012 (part time since December 2017). He is currently chairing Department of Electrical Electronics, Southwest Jiaotong University, Chengdu, China. His research interests include terahertz theory & technology, photo acoustic theory & technology, compressive sensing, natural optimization, computational acoustics & electromagnetics, inverse acoustic & electromagnetic scattering, electromagnetic composite materials, antennas & antenna arrays, millimeter wave & terahertz imaging, and biomedical imaging. He was grated National Young Thousand Talent professorship in September 2011. He is a member of Material Research Society Singapore, and a member of the Chinese Institute of Electronics. He is an Associate Editor of Radio Science since 2017.

Yang Meng received the B.S. degree in Electronic Information Science and Technology from Chongqing University of Arts and Aciences, Chongqing, China in 2014. He is currently pursuing the Ph.D. degree in Radio Physics with University of Electronic Science and Technology of China, Chengdu, China, under the supervision of Professor Anyong Qing. His research interests include the areas of millimeter wave imaging, electromagnetic scattering, and inverse scattering.

X-Band Isoflux Concentric Circular Antenna Arrays for Image Data Download from LEO Satellites to Ground Stations

M. A. El-Hassan [1], K. F. A. Hussein [1], A. E. Farahat [1], and K. H. Awadalla [2]

[1] Electronics Research Institute (ERI), Cairo, Egypt
mayaboelhassan@yahoo.com, Khalid_elgabaly@yahoo.com, asmaa@eri.sci.eg

[2] Faculty of Electronic Eng., Menoufia University Egypt
kamal_awadalla@hotmail.com

Abstract ─ A circularly polarized isoflux beam synthesized by concentric circular arrays of printed microstrip patch antennas is proposed for X-band transmission of image data from land-imaging LEO satellites to the ground stations. This beam has a wide coverage angle of about 100° of uniform illumination. The paper introduces a novel design of a compact right-hand circularly polarized microstrip patch as an element for the concentric circular arrays. The patch antenna has impedance matching bandwidth of about 600 MHz and axial ratio bandwidth of about 170 MHz at 8.1 GHz. A prototype of the proposed patch antenna is fabricated for experimental measurements. The electromagnetic simulation and experimental results show good agreement. A computationally efficient particle swarm optimization (PSO) procedure is developed and applied to find the distribution of the excitation magnitudes over the array elements so as to generate an isoflux beam in all the elevation planes with circular symmetry in the azimuth planes. The phase of excitation is the same for all the array elements. The method proposed to apply the PSO reduces the computational resources to about 6.5% of those required by the conventional method of application. Moreover, the proposed iterative PSO procedure is shown to be very fast convergent.

Index Terms ─ Concentric circular arrays, isoflux beam, LEO satellite, particle swarm optimization, PSO.

I. INTRODUCTION

A low-earth-orbit (LEO) satellite platform is recommended to radiate a beam with homogeneous power density over the coverage area on the earth surface. For a point on the ground surface just at the satellite nadir the propagation has its minimum value, whereas for off-nadir points, the propagation path is longer. To provide homogeneous power density on the ground, the antenna must compensate the power loss due to the change of the propagation path by increasing the gain toward directions where the path is longer. That is,

the antenna gain pattern provides isoflux radiation. An isoflux pattern is omnidirectional (circularly symmetric) with the azimuth angle and has cosecant-squared dependence on the elevation angle. This produces constant signal level at all the points over the beam footprint on the ground surface. It also results in continuous and uniform signal level at the ground station at all the elevation angles during the communication session irrespective of the azimuth direction of the flying vehicle relative to the ground station. For land-imaging LEO satellites using either optical sensor or synthetic aperture radar (SAR), an X-band antenna (or antenna array) is needed for image data transmission from the satellite to the ground stations. As mentioned above, for uniform and continuous reception by the ground station, the satellite antenna should provide isoflux radiation pattern.

The work of [1] introduces the design of sparse concentric circular array to produce isoflux pattern over a visibility cone of about 100° for LEO satellites. In [2] a secant pattern (CP) antenna is designed by combining a CP generating adaptor and a secant pattern radiator. In [3] an isoflux pattern presented by a compact X-band antenna with circularly polarized for a nanosatellite platform that imposes an important volume constraint. In [4] a microstrip phased array is designed and optimized using genetic algorithm to produce isoflux pattern by two concentric ring arrays for operation in the X-band with application to LEO cubesat communications. In [5] the design of concentric ring arrays for isoflux radiation is presented, with considering the reduction of the sidelobe level for medium earth orbit (MEO) satellite using particle swarm optimization (PSO) technique. In [6], a design of a patch antenna array is introduced for a reconfigurable isoflux pattern, with fewer levels of excitations to diminish the hardware complexity using PSO and harmony search algorithm (HSA) as optimization approach. In [7], a design of concentric ring antenna arrays for isoflux radiation for geostationary earth orbit (GEO) and MEO satellites is performed using

an evolutionary multi-objective optimization technique. In [8], a phase-only synthesis algorithm is applied to design lens-array antennas to produce flat-topped and isoflux beams.

The PSO algorithm is commonly used to optimize antenna arrays to synthesize beam shapes required for various applications [9]. In this paper, a planar array of concentric circular arrays of circularly polarized microstrip patch antennas is optimized to produce circularly symmetric isoflux beam using the PSO technique. A novel X-band circularly polarized microstrip patch antenna with corner slots is designed to be the element of the proposed array. A prototype of the proposed patch antenna is fabricated for experimental measurement of the impedance matching bandwidth and the radiation patterns of the circularly polarized fields. The PSO is applied to optimize the magnitudes of excitation of the radiating elements which are arranged in 5 coplanar circular arrays with a total number of 93 elements. The magnitudes of excitation for all the elements on the same circle are kept equal to each other. Thus, the magnitudes only are allowed to vary in the radial direction to achieve the optimization goals. The numerical results of the present work are concerned with the application of the PSO to concentric circular arrays of isotropic point sources and as well as concentric circular arrays of printed microstrip patches. The presentation and discussions of the numerical results focus on the investigation of the performance of the single element as well as the optimized array. The commercially available package CST® is used for electromagnetic simulation for the purpose of ensuring the correctness and accuracy of the obtained results.

The major improvements can be addressed in the present work: (i) the reduction of computational cost (time and memory space) of the PSO algorithm, and (ii) the fast convergence of the iterative procedure to arrive at the required beam shape.

II. BEAM SHAPE FOR ISOFLUX RADIATION FROM LEO SATELLITES

A spherical model for the earth and, hence, a circular path of the satellite around the earth can be assumed as shown in Fig. 1. The function $R_s(\theta)$ indicates the relative distance of the satellite to any point of the illuminated earth surface in any cut of the azimuth plane, h represents the height of the satellite, an a_E is the equatorial radius of the earth.
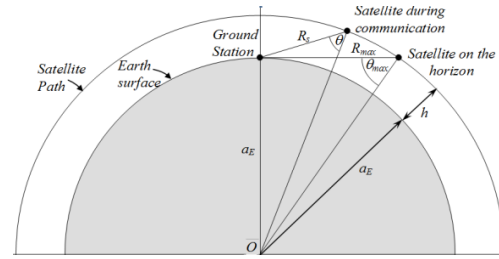
Fig. 1. Low-earth-orbit satellite path about the earth during a communication session with the ground station.

It is assumed that the communication session between the satellite and the ground station can start as soon as the satellite appears to the ground station just on the horizon and ends when the satellite disappears below the horizon. Practically, the communication session does not start unless the satellite reaches a minimum elevation angle, θ_{min}, above the horizon and ends just when the satellite elevation angle becomes lower than this value. During the communication session, the communication range R_s (the distance between the satellite and the ground station) changes according to the following relation:

$$R_s(\theta) = (h + a_E) \cos \theta - \sqrt{(h + a_E)^2 \cos^2 \theta - h(h + 2a_E)}. \quad (1)$$

To keep the power density at the ground station at a fixed level irrespective of the satellite position during the communication session, the power radiated from such an antenna should be proportional to the square of the communication range.

According to the above discussion, for a LEO satellite orbiting the earth at an altitude of 1000 km, the working sector of the main lobe of the radiation pattern should be $\approx 100° \times 100°$. The directional pattern shape, within the limits of its working sector, should be conical and close to a funnel shape, with directions of maximum radiation at angles of about $\pm 50°$ from nadir.

Thus, to provide uniform power density over the coverage area on the ground, the antenna must compensate the power loss due to the propagation path by raising the gain toward directions where the path is longer. According to the description of the isoflux pattern in the coverage sector of the radiation pattern the antenna gain should meet the requirement determined by the following expression:

$$G(\theta) = G_{max} \left(\frac{R_s(\theta)}{R_{max}} \right)^2, \quad (2)$$

where $R_{max} = 2610$ km is the maximum distance between antenna and ground station at an orbital altitude of 1000 km, θ is the observation angle versus the direction of the Earth center and elevation angle of the satellite 5°. In this case, the gain of the antenna in the directions of the maximum radiation should be about 6 dBi.

III. BEAM SHAPING USING CONCENTRIC CIRCULAR ARRAYS

Two degrees of freedom are required for the control parameters to get isoflux three-dimensional beam for uniform radiation over a given solid angle. The circularly symmetric distribution with the azimuth angle and the uniform distribution with the elevation angle require concentric circular arrays like those shown in Fig. 2. Each circular array has a number of elements proportional to its radius so as to keep equal circumferential distances between the contiguous elements on the circles. The distribution of excitation magnitudes with radial direction controls the beam shape with the elevation angle whereas the magnitudes distribution with the circumferential dimension controls the beam shape with the azimuth angle. A central element may be added to the concentric circular array. As discussed in [10] adding a central element to a circular array improves the array gain and reduces the sidelobe level.
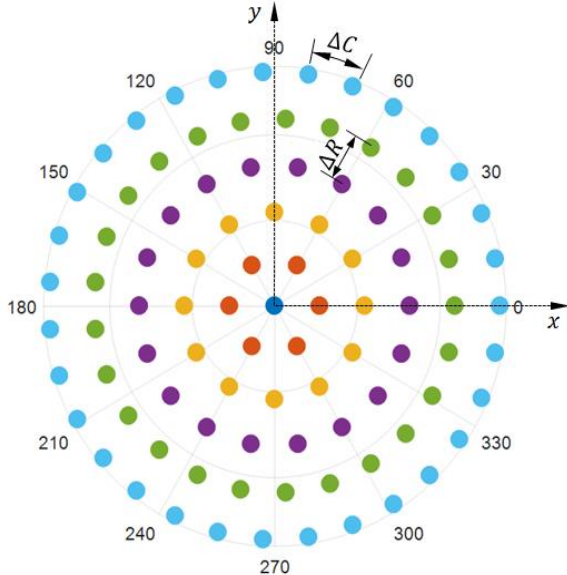
Fig. 2. Concentric circular arrays with growing size for synthesized isoflux beams with circular symmetry.

A. Radiation pattern of concentric circular arrays

For a circular array of isotropic point source radiators and that all the elements have the same phase of excitation, the radiation pattern can be calculated as

follows:
$$E(\theta, \phi) = \sum_{n=1}^{N_P} A_n \, e^{jk_o R \sin\theta \cos(\phi - \Phi_n)}, \quad (3)$$
where R is the radius of the circle, $R = N_P \Delta C / 2\pi$, ΔC is the inter-element arc spacing, Φ_n is the angular position of nth element in the $x - y$ plane, $\Phi_n = 2n\pi/N_P$ with $1 \le n \le N_P$, ϕ is the azimuth angle measured with the positive x-axis, θ is the elevation angle measured with the positive z-axis, k_0 is the free space wave number, $k_0 = 2\pi/\lambda_0$, λ_0 is the wave length in free space, A_n is the excitation coefficient (amplitude and phase) of the nth element. It can be written as $A_n = I_n \, e^{j\alpha_n}$ where, $I_n =$ excitation amplitude of the nth element and α_n is the phase excitation of the nth element (relative to the array center).

Let the antenna array be arranged as N_R concentric circular arrays with a growing number of elements. Assume that the radii of the concentric circles are uniformly increasing; this means that the radius of the circle number m, $(m = 1,2,..,N_R)$ is $R_m = m \, \Delta R$. The arrangement of the elements of such concentric circular array is shown in Fig. 2. On the mth circle, a number of $N_P(m)$ elements are uniformly arranged over the circle circumference. The circumferential distance between the contiguous elements on the mth circle can be expressed as follows:
$$\Delta C \equiv \Delta P_m = \Delta \Phi R_m = \frac{2\pi R_m}{N_P(m)} = \frac{2\pi m}{N_P(m)} \Delta R \, . \quad (4)$$
The following expression can be used to calculate $N_P(m)$,
$$N_P(m) = \text{round} \, (2\pi \, m). \quad (5)$$
According to this equation, irrespective of the value of m, the separation ΔP_m for all the circles is kept as near as possible to ΔR. Also, this equation indicates that the minimum number of elements on one circle is 6.

An extra element is located at the center of the entire array. The coefficient of the excitation voltage of the nth element on the mth circle is $A_{m,n}$. The coefficient of excitation of the central element is A_0.

Assuming that the elements are isotropic point source radiators and that all the elements have the same phase of excitation, the radiation pattern can be calculated as follows:
$$E(\theta, \phi) = A_0 +$$
$$\sum_{m=1}^{N_R} \sum_{n=1}^{N_P(m)} A_{m,n} \, e^{jk R_m \sin\theta \cos(\phi - \Phi_{m,n})}, \quad (6)$$
where, $\Phi_{m,n}$ is the angular position (with the positive x-axis) of the nth array element on the mth circular array, $\Phi_{m,n} = 2\pi n/N_P(m); m = 1, \ldots, N_R, n = 1, 2, \ldots, N_P(m)$.

B. Concentric circular arrays for circularly symmetric radiation pattern

To enforce circular symmetry of the synthesized radiation pattern, all the elements on the same circle must have the same magnitude of excitation; this means,
$$A_{m,n} = A_m, \, m = 1,2,\ldots,N_R, \, n = 1,2,\ldots,N_P(m). \quad (7)$$
Substituting from (7) into (6), the following expression

is obtained for the radiated field in the far zone,

$$E(\theta, \phi) = A_0 +$$
$$\sum_{m=1}^{N_R}\left(A_m \sum_{n=1}^{N_{P(m)}} e^{jkR_m \sin\theta \cos(\phi - \Phi_{m,n})}\right). \quad (8)$$

C. Application of the particle swarm optimization for shaping the beam of concentric circular arrays

The PSO technique achieves the required optimization by setting the positions of each individual particle within a moving swarm so as to get the overall swarm as near as possible to a predetermined goal. The algorithm developed to implement the PSO should have its goal to minimize a predefined cost function. The latter expresses the distance to a required electromagnetic objective. The movements and interactions of the particles within the swarm are considered during the calculation of the improved positions that make the overall swarm approaches the required goal. In the problem of beam shaping by an antenna array, each particle position represents a possible set of magnitudes of the feed of the elements of the array, i.e., it represents one point in the optimization space. The implementation of the PSO algorithm can be divided into four stages: (i) initialization of positions, $\mathbf{x}_n^{(0)}$ and velocities, $\mathbf{v}_n^{(0)}$, for the particles of the swarm, (ii) calculation of the local best positions, $\mathbf{y}_n$, for the particles, (iii) Calculation of the global best position, $\mathbf{g}$, (iv) Calculation of the particles velocities, $\mathbf{v}_n^{(1)}$, and positions, $\mathbf{x}_n^{(1)}$, for the next iteration[11].

The following equations are used to implement an iterative PSO algorithm:

$$\mathbf{v}_n^{(t)} = w\,\mathbf{v}_n^{(t-1)} +$$
$$c_1 r_1\left(\mathbf{y}_n^{(t-1)} - \mathbf{x}_n^{(t-1)}\right) + c_2 r_2\left(\mathbf{g}^{(t-1)} - \mathbf{x}_n^{(t-1)}\right), \quad (9)$$
$$\mathbf{x}_n^{(t)} = \mathbf{x}_n^{(t-1)} + \mathbf{v}_n^{(t)}, \quad (10)$$

where t is the iteration number (time index) and n is the particle number. For each particle, the initial position, $\mathbf{x}_n^{(0)}$, is determined by assigning random values (varying around the unity) to the amplitudes of the excitation voltages of the array elements. The initial local best position of each particle, $\mathbf{y}_n^{(0)}$, is assigned the same initial value of the particle position. The initial value of the velocity of each particle is set to zero. The local best position, $\mathbf{y}_n$, for each particle is the position of this particle that results in the minimum value of the cost function over the successive iterations during the run of the PSO algorithm. The global best position, $\mathbf{g}$, for the particles in the swarm is the position among the local best positions that results in the absolute minimum value of the cost function over the successive iterations during the run of the PSO algorithm. In each iteration, the velocity, $\mathbf{v}_n$, and position, $\mathbf{x}_n$, for each particle in the swarm are updated, as given by (9) and (10).

D. Computational improvement of the PSO algorithm

The PSO algorithm is applied to get the optimum values of only 6 magnitudes of excitation; one for all the elements in each circular array plus the central element. In this way, each particle in the swarm has its position as one-dimensional vector with only 6 real elements, which can be expressed as follows:

$$\mathbf{x}_n^{(t)} = \begin{pmatrix} A_0^{(t)} & A_1^{(t)} & A_2^{(t)} & A_3^{(t)} & A_4^{(t)} & A_5^{(t)} \end{pmatrix}^T. \quad (11)$$

Thus, instead of applying the PSO to find 93 optimum positions (the total number of the array elements) it is applied only to find 6 optimum positions (the number of concentric circular arrays). This can be considered a major improvement that considerably reduces the computational complexity of the PSO algorithm. As the swarm has 15 particles whose positions should be calculated in each iteration of the PSO algorithm, the total number of the values that should calculated in each iteration are reduced to 90 values (15×6) instead of 1395 values (15×93). As the PSO algorithm runs for about 150 iterations to arrive at accurate results, the reduction ratio of the computational time is (1395-90)/1395×100% = 93.5%. Similarly, the required memory space is reduced by the same percentage (93.5%).

The main objective of the PSO algorithm is to realize the target beam shape described by $\hat{E}(\theta)$. From (1) and (2) one can deduce the desired isoflux radiation pattern to achieve uniform distribution of the power density over the satellite footprint. This means that the desired electric field radiation pattern should take the form given by the following expression:

$$E_d(\theta) = \frac{R_S(\theta)}{R_{max}} =$$
$$E_o\left[\begin{array}{c} (h + a_E)\cos\theta \\ -\sqrt{(h + a_E)^2\cos^2\theta - h(h + 2a_E)} \end{array}\right], \quad (12)$$

where, E_o is the constant magnitude of the radiated electric field in the far zone. Thus, the target beam shape for the PSO algorithm can be defined as follows:

$$\hat{E}(\theta) = \begin{cases} E_d(\theta), & 0 < \theta \le \tfrac{1}{2}\Theta_a, \ 0 < \phi < 2\pi \\ 0, & \tfrac{1}{2}\Theta_a < \theta < \pi, \ 0 < \phi < 2\pi \end{cases}, \quad (13)$$

where Θ_a is the desired beam width.

As the main goal of the PSO during its iterations is to reduce the cost function, the latter should be increased as the achieved radiation pattern further deviates from the ideal pattern. Thus, the cost function can be, simply, the absolute difference between the achieved and the desired (ideal) patterns of the electric field as follows:

$$F_C = W_F\left(\left|E - \hat{E}\right|\right) + W_S\left(\left|E - \hat{E}\right|\right), \quad (14)$$

where W_F is a weighting coefficient of the part of the cost function ensuring the required beam shape over the illuminated angular zone defined by: $0 < \theta \le \tfrac{1}{2}\Theta_a$, W_S is a weighting coefficient for the part of the cost function

ensuring cancelation of the sidelobes over the angular zone: $\frac{1}{2}\Theta_a < \theta < \pi$.

In conclusion, the amplitudes and phases of the elements of different circles to satisfy the performance goal by the PSO algorithm so as to satisfy the required beam shape and the remaining objectives of the antenna array design such as the axial ratio and the sidelobe level.

IV. CORNER-SLOTTED MICROSTRIP PATCH ANTENNA FOR CIRCULAR POLARIZATION

This section presents a brief description of the circularly polarized microstrip patch antenna proposed for the implementation of the concentric circular array to produce the isoflux beam. The circular polarization is obtained from a square microstrip antenna by etching two symmetric L-shaped slots near two diagonally facing corners of the square patch as shown in Fig. 3. Right-hand circular polarization (RHCP) is obtained if one slot is cut near the right upper corner and the other slot is cut near the left lower corner as shown in Fig. 3. In analogous manner, LHCP is obtained if one slot is cut at the left upper corner and the other slot is cut at the right lower corner. The patch is square of side length L_P and has four side slots and two corner slots. A corner slot is L-shaped and has two arms; each of length L_{CS} and width W_{CS}. The separation between the slot edge and the patch edge is t_S. The four side slots are cut along the horizontal and vertical axes of symmetry and proposed to enhance circular polarization and make the antenna size compact. Each of the four side slots has a length of L_s and a width of W_s. The lengths of the slots and the position of the feed are set to obtain good impedance matching and to produce acceptable value of the axial ratio over the radiation zone of interest. The ground plane is square with side length G. The feeding probe is located at a distance F from the patch center ($x = 0, y = F$) as shown in Fig. 3.

V. RESULTS AND DISCUSSIONS

A planar concentric circular array with an inter-radial spacing of 0.5λ is optimized to produce isoflux beam. The array is arranged in the x-y plane and is composed of 5 coplanar circular arrays with a total number of 93 elements, where 92 elements are distributed in the 5 circles and an extra element is located at the center of the array. The elements on each circle are equispaced along its perimeter. The number of elements on the five circles arranged from the innermost to the outermost are $6, 12, 18, 25, 31$, and the radii of the circles are $\lambda/2, \lambda, 3\lambda/2, 2\lambda, 5\lambda/2$, respectively.

The PSO algorithm is applied to produce an isoflux beam from such concentric circular arrays as explained in Section 2, where the working parameters of the PSO are set as follows: the swarm size (number of particles)

is $p = 15$, the inertia coefficient, $w = 0.729$, the maximal velocity, $\mathbf{v}_{max} = 0.2$, the cognitive rate coefficient $c_1 = 1.0$, the social rate coefficient $c_2 = 2.0$. The PSO algorithm runs for 150 iterations.
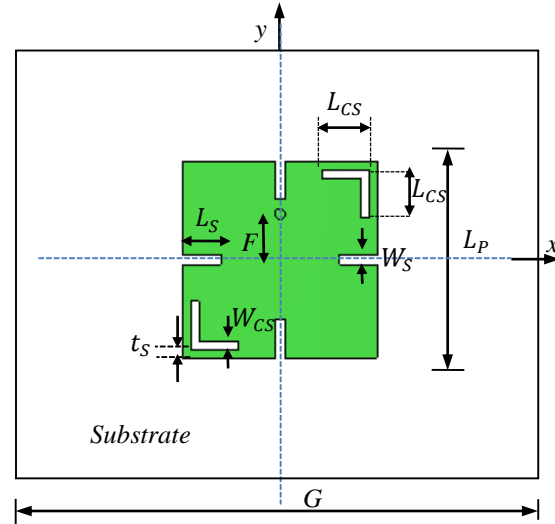
Fig. 3. The proposed compact circularly polarized corner-slotted patch antenna.

A. Assessment of the circularly polarized corner-slotted microstrip patch

The optimal design parameters of the patch antenna to produce RHCP are $L_P = 7.5$ mm, $G = 20.6$ mm, $L_s = 1.1$ mm, $L_{SC} = 1.6$ mm, $W_s = 0.36$ mm, $W_{SC} = 0.27$ mm, $t_S = 0.28$ mm, and $F = 1.6$ mm. It should be noted that in the following presentation and discussions of the numerical results the patch antenna has the same design parameters listed above unless otherwise indicated. The patch is printed on a roger TMM4 substrate with permittivity $\varepsilon_r = 4.5$, loss tangent $\delta = 0.002$, and thickness $h = 1.524$ mm.

A prototype of a single patch antenna is fabricated in the laboratory for experimental verification of the simulation results concerning the dependence of the reflection coefficient on the frequency and the radiation patterns of the circularly polarized fields. Top and bottom views of the fabricated antenna are presented in Fig. 4. The vector network analyzer of the Agilent Field Fox N9918A is used to measure S_{11} at the antenna port against the frequency. Figure 5 shows the experimental setup with the fabricated prototype of the proposed antenna. The results for the dependence of S_{11} on the frequency are plotted and presented in Fig. 6, where the comparison between the experimental and simulation results of the reflection coefficient shows good agreement. The simulation results for S_{11} show that the patch antenna has an impedance matching bandwidth of about 600MHz (7.81 – 8.42 GHz) for reflection

coefficient < - 10 dB. In the same figure the axial ratio is plotted against the frequency with a minimum axial ratio of about 0.12 dB and a 3 dB axial ratio bandwidth of about 170 MHz (8.02 − 8.19 GHz), with a maximum gain of about 6.4 dBi.

(a) Top view   (b) Bottom view
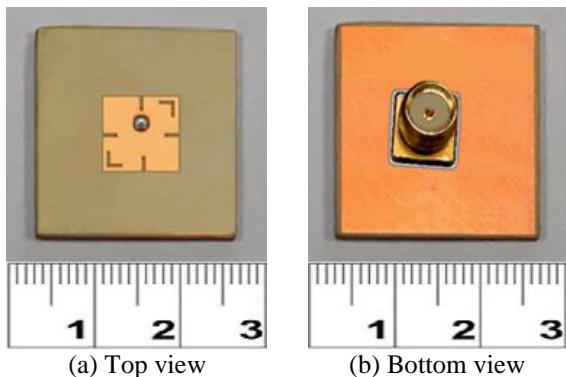
Fig. 4. A fabricated prototype of the circularly polarized patch antenna.

Fig. 5. Experimental measurements of S_{11} for the circularly polarized patch antenna using vector network analyzer of the Agilent Field Fox N9918A.
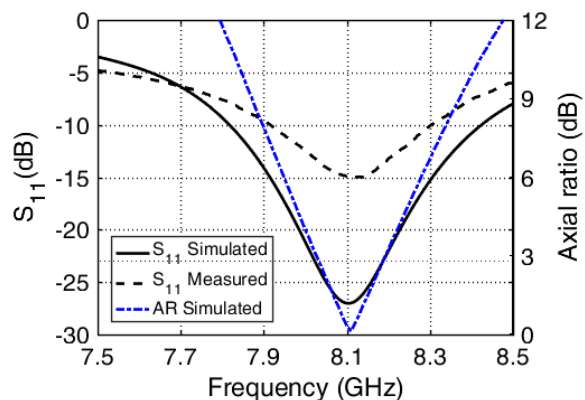
Fig. 6. Frequency dependence of S_{11} and the axial ratio for the circularly polarized patch antenna.

For experimental measurement of the RHCP radiation pattern, the dual circularly polarized antenna model JXTXLB-OSJ-20180 is used as a reference antenna and the experimental setup is made as shown in Fig. 7. The radiation patterns are measured at 8.1 GHz in the two principal planes $x − z$ ($\phi = 0°$) and $y − z$ ($\phi = 90°$). The radiation patterns obtained through simulation and experimental measurements are presented in Fig. 8 showing good agreement. It seems that the radiation is dominated by right-hand circularly polarized electric field component.

Fig. 7. Experimental setup for measurement of the antenna radiation patterns.
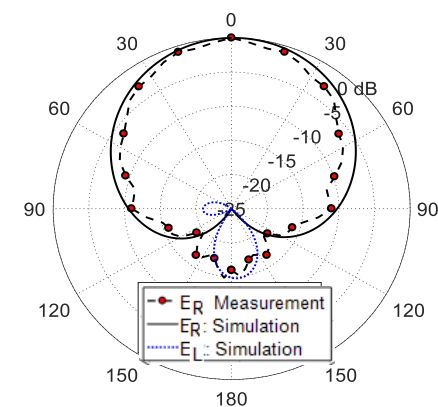
(a) Radiation pattern in the plane $\phi = 0°$
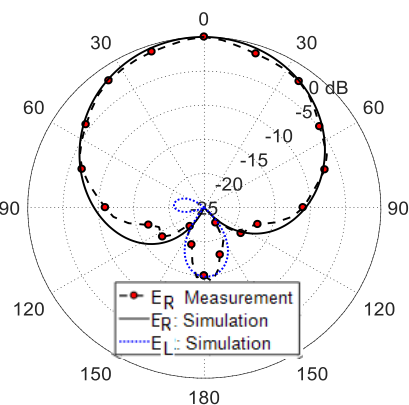
(b) Radiation pattern in the plane $\phi = 90°$

Fig. 8. Radiation patterns for the circularly polarized fields radiated by the microstrip patch.

The directional patterns for the axial ratio produced by the circularly polarized patch antenna are plotted with θ and ϕ as shown in Figs. 9 (a)-(b), respectively, at 8.1 GHz. The 3 dB axial ratio beam width is about 188° $(-123° \; to + 65°)$ in the plane $\phi = 0°$ and is about 162° $(-94 \;°to + 68°)$ in the plane $\phi = 90°$. For the elevation angles $\theta = 10°,\; 20°,\; 30°,\; 40°, 50°$ the axial ratio is maintained below 3dB for all the values of ϕ.

(a) Variation of the axial ratio with θ

(b) Variation of the axial ratio with ϕ
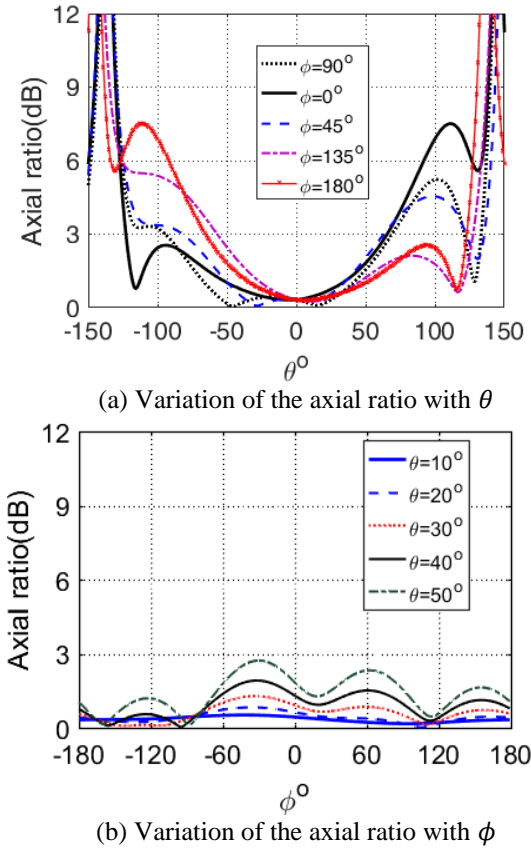
Fig. 9. Radiation pattern for the axial ratio of the patch antenna at frequency 8.1 GHz.

Table 1: Arrangement of the radiating elements in a concentric circular array with the magnitudes of excitation to produce isoflux beam

Circle Number	0	1	2	3	4	5
Number of Elements	1	6	12	18	25	31
Radius	0	ΔR	$2\,\Delta R$	$3\,\Delta R$	$4\,\Delta R$	$5\,\Delta R$
Magnitudes	1.297	2.509	-1.460	0.282	0.358	-0.245

B. Isoflux beam synthesized using concentric circular arrays of point source elements

The PSO is applied to produce isoflux beam by the concentric circular array that is arranged as described in Section III. In the present section the radiating elements of this array are taken as isotropic point sources. During the optimization procedure, all the array elements are kept in-phase. In the meantime, the magnitudes of excitation for all the elements on the same circle are kept equal to each other. Thus, the magnitudes only are allowed to vary in the radial direction to achieve the optimization goals. The optimization procedure aims to find the radial distribution of the excitation magnitudes so as to generate an isoflux beam in all the elevation planes. Consequently, the produced beam will be circularly symmetric and independent of ϕ.

(a)

(b)
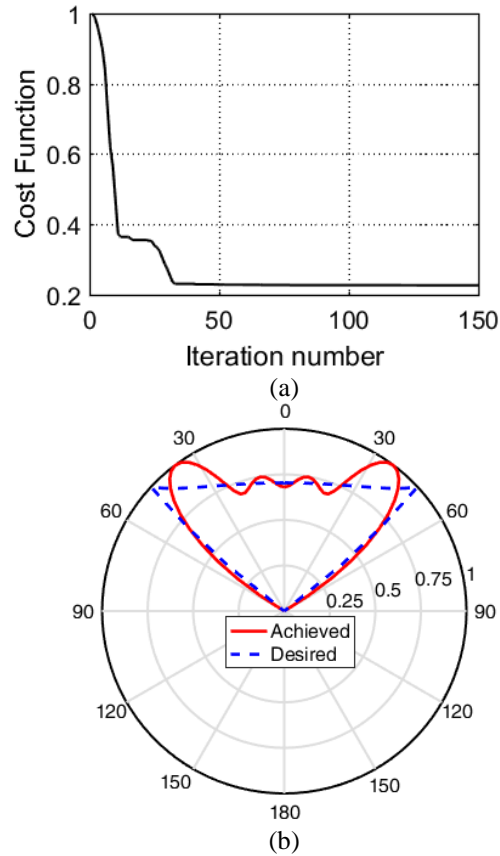
Fig. 10. The isoflux beam obtained from the application of the PSO algorithm on a concentric circular array of 92 elements arranged on 5 concentric circles plus a central element: (a) decay of the cost function while preceding with iterations, and (b) the achieved isoflux beam in the elevation plane compared with the desired one.

To produce an isoflux beam of width 100°, the excitation magnitudes of the central element and the other concentric circles are listed in Table 1. The cost function with the successive iterations of the PSO algorithm is presented in Fig. 10 (a). It is clear that the algorithm is rapidly convergent as it takes less than 70 iterations to reach a good steady state value of the cost function (about 20% of its initial value). Such fast

convergence and low value of the cost function reflect the efficiency of the applied PSO algorithm. The normalized pattern achieved by the PSO algorithm in the elevation plane (i.e., with θ) is presented in Fig. 10 (b) and compared with the desired one. The desired and achieved three-dimensional radiation patterns are presented in Figs. 11 (a)-(b), respectively. Both the polar plots and the three-dimensional plots presented in Figs. 10 and 11, respectively show satisfactory agreement between the desired beam shape and that achieved using the PSO algorithm.

(a)

(b)
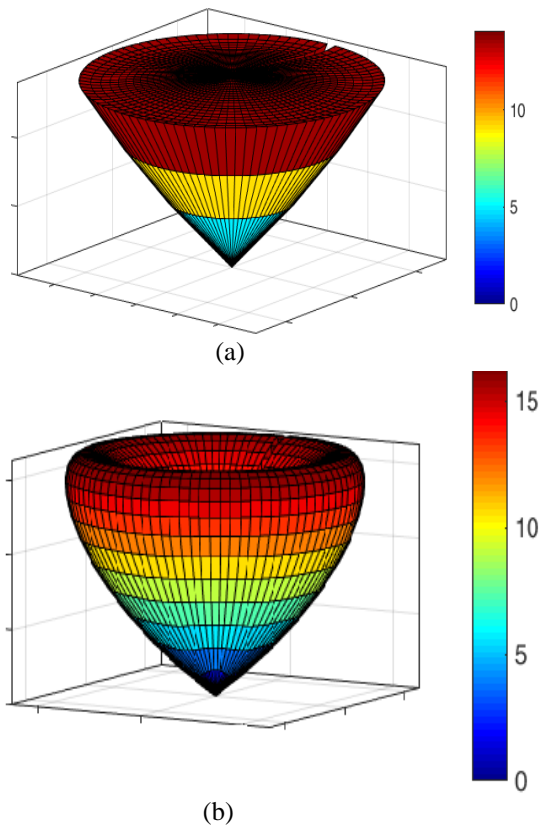
Fig. 11. 3D isoflux radiation pattern obtained by concentric circular arrays of 92 elements arranged in 5 circles plus a central element: (a) desired beam shape, and (b) achieved beam shape.

C. Circularly-polarized isoflux beam synthesized by concentric circular arrays of corner-slotted microstrip patches

To produce an isoflux beam with circular polarization, the array element should be circularly polarized. For practical considerations, it is recommended that the concentric circular array be implemented as an array of printed elements. For this purpose, the circularly polarized microstrip patch antenna described in Section IV is proposed as an element for this array. This can be

considered a practical and cost-effective implementation of the concentric circular arrays with the same distribution of the excitation magnitudes obtained for the hypothetical point source array described in Section V, B. A planar array composed of concentric circular arrays of 93 elements of such type of patches is proposed to produce the isoflux beam. The dimensions of such a planar array are 210 mm × 210 mm and, hence, it has the advantages of low profile, lightweight, and eases of manufacturing using printed circuit techniques. The 93 patch elements of the array are excited in phase with the magnitudes listed in Table 1. The achieved radiation patterns in the elevation planes $\phi = 0°$ and $\phi = 90°$ at 8.1 GHz are presented in Fig. 12.

The frequency dependence of the axial ratio of the optimized beam in the forward direction ($\theta = 0°$) is presented in Fig. 13. It is clear that the band width for axial ratio < 3dB is about 100 MHz (8.03- 8.13 GHz); whereas for axial ratio < 6dB, the bandwidth is about 260 MHz (7.94 - 8.2 GHz).

(a) Plane $\phi = 0°$

(b) Plane $\phi = 90°$
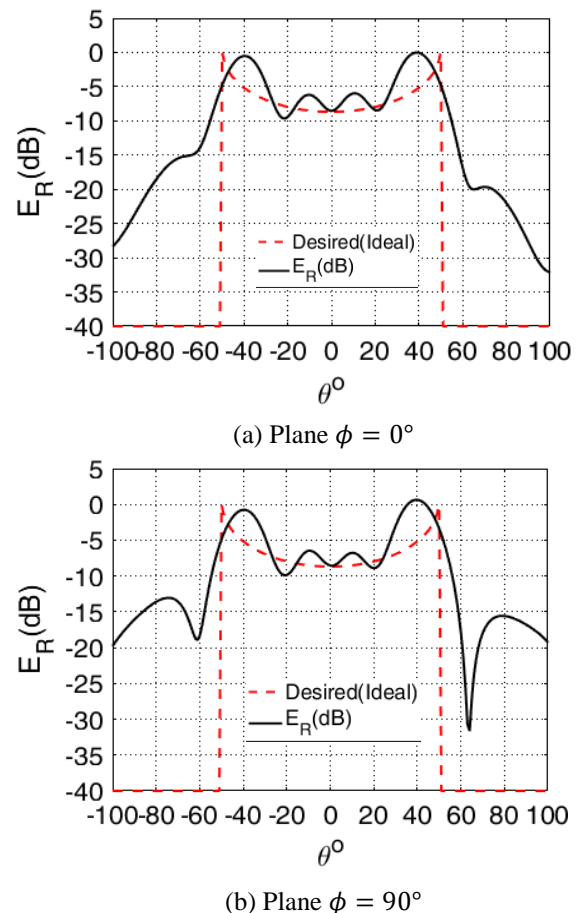
Fig. 12. The isoflux beam achieved using a 93-element concentric circular array of circularly polarized patch antennas compared with the desired shape, $f = 8.1$ GHz.
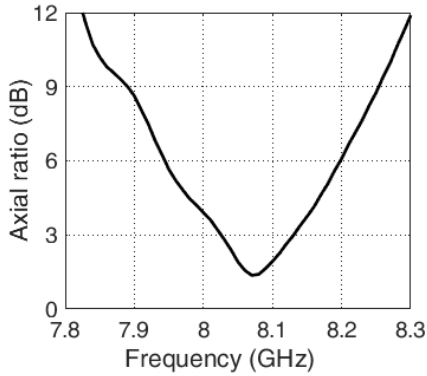
Fig. 13. Axial ratio in the forward direction ($\theta = 0°$) versus frequency for an isoflux beam produced by concentric circular arrays of circularly polarized patches, f = 8.1 GHz.

(a) Plane $\phi = 0°$

(b) Plane $\phi = 90°$
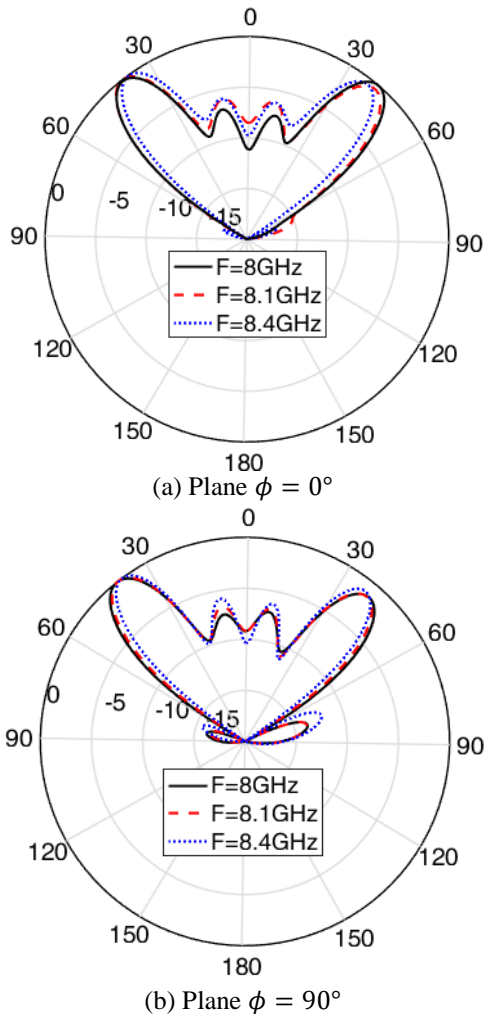
Fig. 14. Polar plots of the isoflux beam produced by concentric circular arrays of circularly polarized patch antennas at different frequencies in the elevation planes: (a) $\phi = 0°$, and (b) $\phi = 90°$.

Polar plots of the isoflux beam achieved using the concentric circular arrays described above are presented in Fig. 14 at the frequencies 8, 8.1, and 8.4 GHz. As shown in the figure, the isoflux beam is achieved over a frequency band of about 600 MHz (7.8 - 8.4 GHz) with acceptable accuracy of the beam shape.

A three-dimensional plot of the radiation pattern achieved by the concentric circular arrays described above is presented in Fig. 15. It is clear that the beam produces isoflux radiation in the elevation planes with circular symmetry in the azimuth plane.
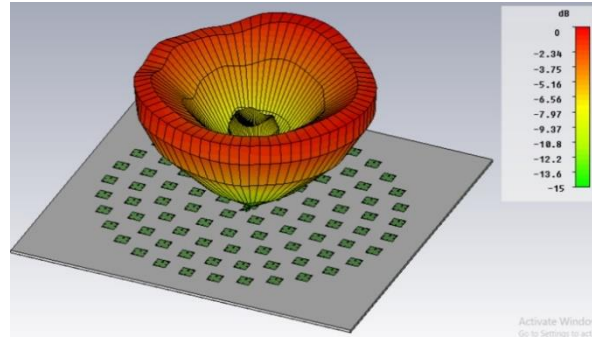
Fig. 15. Three-dimensional plot of the isoflux radiation pattern produced by optimized concentric circular arrays of circularly polarized patch antennas, f = 8.1 GHz.

VI. CONCLUSION

A planar array composed of concentric circular arrays of printed microstrip antennas is optimized to synthesize an isoflux beam for X-band transmission of image data from land imaging LEO satellites to the ground stations. A compact right-hand circularly polarized microstrip patch is designed to be an element of the concentric circular arrays. Both simulation and experimental results show that the impedance matching bandwidth of the proposed microstrip patch antenna is about 600 MHz, whereas the axial ratio bandwidth is about 170 MHz at 8.1 GHz. The radiation patterns for the circularly polarized fields are obtained through electromagnetic simulation and experimental measurement showing good agreement. The PSO is applied to find the magnitudes of excitation for the array elements, while keeping the phases equal, so as to synthesize an isoflux beam with circular symmetry. The proposed application method of the PSO is shown to be computationally efficient as it reduces the required computational resources to about 6.5% of those required by the conventional method. The iterative PSO procedure is shown to have fast convergence to arrive at the optimization goals.

REFERENCES

[1] M. Ibarra, M. A. Panduro, Á. G. Andrade, and A. Reyna, "Design of sparse concentric rings array for

LEO satellites," *Journal of Electromagnetic Waves and Applications*, vol. 29, no. 15, pp. 1983-2001, 2015.

[2] J. M. Yim, J. K. Son, T. K. Lee, J. W. Lee, and W. K Lee, "Secant pattern radiator for X-band data transmission," *Asia-Pacific Microwave Conference Proceedings* (*APMC), IEEE*, pp. 1178-1180, 2013.

[3] R. Manrique, G. Le Fur, N. Adnet, L. Duchesne, J. M. Baracco, and K. Elis, "Telemetry X-band antenna payload for nano-satellites," In *11th European Conference on Antennas and Propagation* (*EUCAP), IEEE*, pp. 549-552, Mar. 2017.

[4] J. E. Diener, R. D. Jones, and A. Z. Elsherbeni, "Isoflux phased array design for cubesats," *IEEE APS Conference*, pp. 1811-1812, 2017.

[5] A. R. Maldonado, M. A. Panduro, and C. del Rio-Bocio, "On the design of concentric ring arrays for isoflux radiation in MEO satellites based on PSO," *Progress In Electromagnetics Research*, vol. 20, pp. 243-255, 2011.

[6] A. R. Maldonado, M. A. Panduro, C. del Rio Bocio, and A. L. Mendez, "Design of concentric ring antenna array for a reconfigurable isoflux pattern," *Journal of Electromagnetic Waves and Applications*, vol. 27, no. 12, pp. 1483-1495, 2013.

[7] M. Ibarra, M. A. Panduro, and A. G. Andrade, "Differential evolution multi-objective for optimization of isoflux antenna arrays," *IETE Technical Review*, vol. 33, no. 2, pp. 105-114, 2016.

[8] S. Loredo, G. Leon, O. F. Robledo, and E. G. Plaza, "Phase-only synthesis algorithm for transmitarrays and dielectric lenses," *ACES Journal*, vol. 33, no. 3, 2018.

[9] W.-C. Weng, "Optimal design of an ultra-wideband antenna with the irregular shape on radiator using particle swarm optimization," *Applied Computational Electromagnetics Society Journal (ACES) Journal*, vol. 27, no. 5, 2012.

[10] D. Mandal, K. Kola, J. Tewary, V. Roy, and A. Bhattacharjee, "Synthesis of steered flat-top beam pattern using evolutionary algorithm," *Advanced Electromagnetics*, vol. 5, no. 3, pp. 86-90, 2016.

[11] M. A. El-Hassan, K. F. A. Hussein, and K. H. Awadalla, "Shaped beam circularly polarized circular array for SAR and satellite applications," 36th *National Radio Science Conference* (*NRSC 2019*), *AASTMT*, Port Said, Egypt, B2, Apr. 16-18, 2019.

Single Layer Transmit-array with Beam-Steering and Polarization Switching

Xiaochun Liu [1,2], Qiming Yu [1], Xiangkun Kong [1], Zhengyu Huang [1], Borui Bian [1], Shaobin Liu [1], and Jixuan Liu [1]

[1] College of Electronic and Information Engineering
Nanjing University of Aeronautics and Astronautics, Nanjing, 211106, China
liuxiaochun637@sina.com, yuqiming4919@163.com, xkkong@nuaa.edu.cn, huangzynj@nuaa.edu.cn,
borui_bian@sina.com, lsb@nuaa.edu.cn, 664031942@qq.com

[2] The Aeronautical Science Key Laboratory for High Performance Electromagnetic Windows
Jinan, 250023, China
liuxiaochun637@sina.com

Abstract － In this paper, a single layer multi-polarization transmit-array operating at C-Band is designed using ring groove with a single split as the element. The rotational orientation of each element can provide the required phase shift. The elements have identical dimensions, but the rotational orientation of each element is selected to provide a specific transmit-array function. The transmit-array has three working conditions which can change the polarization of the incident wave and set separation beam direction at the same time. The thin single-layer transmit-array without dielectric substrate is designed, simulated and measured based on a horn antenna. The measurement result shows that the transmit-array can switch the linear polarization incident wave to left-circularly polarized wave and right-handed circular polarized wave with separation beam of ± 30 azimuth angles separately. The measured results are in agreement with the theoretical and simulation results.

Index Terms － Beam steering, phase modulation, polarization switching, transmit-arrays.

I. INTRODUCTION

In the last few years, a kind of transmit-array [1-3] has attracted much attention in millimeter-wave applications. There are two types of transmit-array: one is based on them M-FSS structure [4, 5], the other one is based on the reception–transmission structure [6, 7]. Some of the current phased transmit-array research is directed towards optimization of individual phasw1e-agile elements for beam-forming antennas. The appropriated phase shift of each element creates a phase distribution across the elements of the array. This distribution of phase shift has a lensing effect if it approximates the propagation delay. Transmit-array allows the use of large feed antennas or multiple feeds without compromising the radiation aperture compared to reflect-arrays.

At present, many metamaterial antennas with bandwidth and beam tunability have been studied [8-10]. Luo et al. report a microelectromechanical system (MEMS)-modulated scanning beam metamaterial antenna based on surface micromachining process [11]. The antenna is implemented by cascading periodical metamaterial modules to make an electromagnetically homogeneous waveguide, of which the MEMS cantilevers are monolithically integrated in each unit as a radio frequency (RF) switch to modulate the phase constant, and thereby to realize the scanning beams in the fixed frequency around 8GHz. Ke et al. report a leaky-wave antenna working 9.1GHz with programmable beam scanning [12]. The leaky-wave antenna is orthogonally arranged and composed of sixteen metallic J-shaped units in the composite right-left handed (CRLH) formation to obtain tunable metamaterial properties programmable radiation patterns. The radiation patterns can be changed by controlling gap's state with open or close.

Most of the planar air-fed transmit-array antenna adopts multi-layer frequency select surface (M-FSS) element structure. In 2011, Rudi et al. [2] adopted rectangular patch and cross dipole structure as a transmit-array element, compensated phase by rotating the array element, designed a five-layer planar air-fed transmit-array antenna work at 12.4GHz. The transmit-array antenna contains 349 transmission elements, which is designed to collimate the radiation from a feed horn into a beam pointing 20˚ from broadside. In 2014, Yang Fan designed a three-layer planar air-fed transmit-array antenna in *x*-band, using swasti-type transmission array element. The insertion loss of the transmit-array element in the working band is always higher than 4.2dB. The

element can realize the transmission phase shift of 360 degree, and the transmit-array antenna has the advantages of high gain and wide band [5].

The multilayer transmit-array antenna has the disadvantage of complex array structure, the high profile and poor transmission performance, so reducing the antenna's vertical profile is an important development direction.

In this paper, a single layer transmit-array is presented to improve the complex structure of traditional multiple layers transmit-array. The single-layer metal transmit-array without dielectric substrate is designed, which is consists of ring groove with a single split. The rotational orientation of each element can provide the required phase shift. The transmit-array effect is created by the phase shifters, which collimate radiation from the feed and steer the resulting beam in the desired direction. The transmit-array is designed to work in three polarized situations: under the linear-polarization (LP), left-hand-circular-polarized (LHCP) and right-hand-circular-polarized (RHCP). When the transmit-array is placed at the front of the transmitting antenna, it can change the polarization of the incident wave and set separation beam direction at the same time, which can achieve the application of split beam detection and polarization conversion. When the transmit-array is placed at the front of the receiving antenna, the beam of the incident waves is separated as it passes through the transmit-array, that achieve low scattering. This transmit-array can be widely used and developed in detection systems of electronic warfare.

II. DESIGN PRINCIPLES AND METHODS
A. Scattering parameters of rotated element

The reflection and transmission properties of this transmit-array can be represented as a scattering matrix. When the elements are rotated with the z-axis by an angle ψ, scattering matrix can be defined as equation (1) and equation (2), which relates circularly polarized wave modes [2]:

$$B^{CP} = S_\psi^{CP} A^{CP}, \tag{1}$$

$$\begin{bmatrix} b_1^l \\ b_1^r \\ b_2^r \\ b_2^l \end{bmatrix} = \begin{bmatrix} S_{11}^{lr} & S_{11}^{ll} & S_{12}^{ll} & S_{12}^{lr} \\ S_{11}^{rr} & S_{11}^{rl} & S_{12}^{rl} & S_{12}^{rr} \\ S_{21}^{rr} & S_{21}^{rl} & S_{22}^{rl} & S_{22}^{rr} \\ S_{21}^{lr} & S_{21}^{ll} & S_{22}^{ll} & S_{22}^{lr} \end{bmatrix} \begin{bmatrix} a_1^r \\ a_1^l \\ a_2^l \\ a_2^r \end{bmatrix}. \tag{2}$$

The vector components are labeled with a superscript that indicates the hand of polarization: l indicates left-hand circular polarization (LCP) and r indicates right-hand circular polarization (RCP). The superscript and subscript of each CP scattering parameter are labeled in order: for example, S_{12}^{rl} relates the right-hand component scattered at Port 1 to the left-hand component incident on Port 2.

The scattering matrix for linearly polarized modes can be transformed into the matrix for circularly

polarized modes by:

$$S_\psi^{CP} = [T^{XY \to CP}][S_\psi^{XY}][T^{XY \to CP}]^{-1}, \tag{3}$$

where $T^{XY \to CP}$ is the coordinate transformation from cartesian to circular element vectors:

$$T^{XY \to CP} = \frac{1}{\sqrt{2}} \begin{bmatrix} 1 & -j & 0 & 0 \\ 1 & j & 0 & 0 \\ 0 & 0 & 1 & -j \\ 0 & 0 & 1 & j \end{bmatrix}. \tag{4}$$

The values of each CP scattering parameter are determined:

$$\begin{aligned} S_{11}^{lr} = S_{11}^{rl} = S_{22}^{rl} = S_{22}^{lr} &= \frac{1}{2}(\Gamma_x + \Gamma_y) \\ S_{12}^{ll} = S_{12}^{rr} = S_{21}^{rr} = S_{21}^{ll} &= \frac{1}{2}(T_x + T_y) \\ S_{11}^{rr} = S_{22}^{ll} &= \frac{1}{2}(\Gamma_x - \Gamma_y)e^{+j2\psi} \\ S_{11}^{ll} = S_{22}^{rr} &= \frac{1}{2}(\Gamma_x - \Gamma_y)e^{-j2\psi} \\ S_{12}^{rl} = S_{21}^{lr} &= \frac{1}{2}(T_x - T_y)e^{+j2\psi} \\ S_{12}^{lr} = S_{21}^{rl} &= \frac{1}{2}(T_x - T_y)e^{-j2\psi} \end{aligned} \tag{5}$$

where Γ_x and Γ_y are the reflection coefficients to x- and y-polarized waves, T_x and T_y are the transmission coefficients.

Note that the above formulas indicate that when the elemental antenna is rotated, four of the above parameters are phase advanced by twice the rotation angle, four are phase delayed by twice the rotation angle, and eight remain unchanged. The phase shifted components are all due to the polarization anisotropy of the element, they are proportional to the difference between Γ_x and Γ_y, or T_x and T_y.

When the designed transmit-array working under the LP waves, the prototype is designed to split an incident wave into left and right circularly polarized wave. The effect is similar to a Wollaston prism, which separates an incident wave into two linearly polarized beams. The transmit-array decomposes an incident wave into its CP components and redirects the power from each component into two separate beams. The prism effect occurs because S_{21}^{lr} and S_{21}^{rl} have equal magnitudes but opposite phase shifts. However, the gradient will have opposite signs for the scattered fields associated with S_{21}^{lr} and S_{21}^{rl}. When LCP and RCP modes are incident from the same direction, they will scatter into two beams in different directions. Fields scattered in the negative beam are mostly associated with the S_{21}^{lr} parameter; fields in the positive beam are mostly associated with the S_{21}^{rl} parameter. The phase of eight parameters are unaffected by element rotation and the fields they scatter will always form beams in the same direction. Ray diagrams associated with these four scattering parameters are shown in Fig. 1.
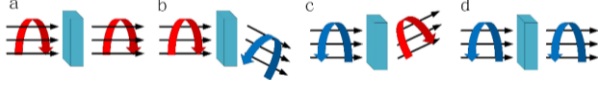
Fig. 1. Ray diagram representation of the waves transmitted through a array configured to split circular polarization. Scattering associated with: (a) S_{21}^{rr}, (b) S_{21}^{rl}, (c) S_{21}^{lr}, and (d) S_{21}^{ll}.

B. Ideal phase-shifting element

When the line polarization wave propagates along the -z direction, the main polarization direction is along the x-axis direction so that the linear polarization incident wave can be expressed as [6]:

$$\overrightarrow{E_1} = E_0 e^{jkz} \cdot \hat{u}_x. \tag{6}$$

For the transmit-array, when the antenna element is rotated ψ by the z axis, the vector equation of the transmission beam is changed:

$$\overrightarrow{E_t} = \frac{1}{2} E_0 e^{jkz} [e^{j2\psi}(T_x - T_y)\hat{u}_x) + (T_x + T_y)\hat{u}_x]. \tag{7}$$

As shown in equation (7), the transmission beam consists of two linear polarized wave components. The first part is composed of the linear polarized wave with the phase advance twice of the element rotation Angle(ψ), the second part is the linear polarization wave with the phase independent of the rotation Angle(ψ). The design goal of transmit-array is transforming the linear polarization incident wave to the left and right circular polarization beam. Therefore, it is necessary to divide the transmission array into two parts; the phase compensation is respectively carried out with the center line of the array as the axis of symmetry. When the counter-clockwise rotation is set to the positive direction for phase compensation at the right side of the array, the transmission beam can be expressed as:

$$\overrightarrow{E_t} = \frac{1}{2} E_0 e^{jkz} [e^{j2\psi}(T_y - T_x) j\hat{u}_y) + (T_y + T_x) ju_y]. \tag{8}$$

Add the equation (7) to the equation (8), the transmitted beam after superposition can be expressed as:

$$\overrightarrow{E_t} = \frac{1}{2} E_0 e^{jkz} [e^{j2\psi}(T_x - T_y)(\hat{u}_x - j\hat{u}_y) + (T_x + T_y)(\hat{u}_x + j\hat{u}_y)]. \tag{9}$$

As shown in equation (9), the transmission beam consists of two circular polarized wave components. The first part is located in the left half of the array, which is composed of left-circularly polarized waves with the phase advance twice of the element rotation Angle(ψ), The second part is located in the right half of the transmit-array, which is composed of right-circular polarization wave with the phase independent of the rotation Angle(ψ). To make the beam amplitude of the left and right circularly polarized wave closed, the array element should satisfy the following formula:

$$T_x \gg T_y. \tag{10}$$

For the beam separation transmit-array, using the rotary phase modulation technique, the transmit-array element needs to meet the requirements of a high insertion loss in x-axis polarization direction and low insertion loss in the direction of y-axis polarization. The change of element transmission phase is not twice as much as the element rotation angle, the rotation angle of each array element needs to be calculated separately.

III. DESIGN OF THE SPLIT RING ELEMENT AND TRANSMIT-ARRAY

The conceptual model diagram of planar air-fed transmit-array antenna is shown in Fig. 2 (a). The whole antenna system is illuminated by a focal source such as horn antenna. In this paper, the horn antenna is used as the feed antenna.

The feed antenna is located on the focus of the single layer transmit-array. The transmit-array is made of numerous split ring elements with variable rotation angles, as shown in Fig. 2 (a). The focal length ratio of the feed antenna in this paper is 0.8. The transmit-array element is single-layer pure metal structure. It is investigated in the C-band and can split an incident wave according to its circular polarization components. The effect of this transmit-array antenna is similar to the Wollaston prism, that a Wollaston prism divides an incident wave into two linearly polarized beams [2].
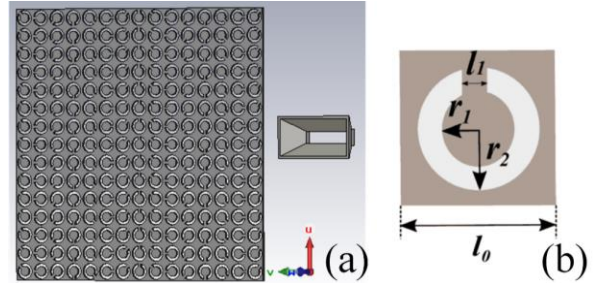
Fig. 2 (a) Conceptual model diagram of transmit-array and (b) the details of ring groove with a single split. (structure parameters: l_0=15 mm, r_2=6mm, r_1=4mm, and l_1=2mm).

A. Design of the transmit-array element

The transmission coefficients of these elements are individually designed so that the spherical phase front from the feed source is converted into a planar phase front [2]. Each element needs to satisfy the requirements of total transmission and phase compensation. In this paper, a single layer transmission element is presented, which is shown in Fig. 2 (b). The element is a square structure, the gray part of the element is copper, and the white part is a hollowed-out split ring made of air. The element is made of pure perforated metal without dielectric substrate. The array of the pure copper

structure has strong structural strength and can adapt to engineering application. The element thickness is 1 mm.

The element of ring groove with a single split mentioned above was designed to work at C-band and simulated by full-wave simulations. The simulated scattering parameter of the element is shown in Fig. 3 (a). Figure 3 (b) shows that the insertion loss of the element in the x-axis polarization direction is close to 0 near the 5GHz, the transmission performance is ideal. The insertion loss of the element in the y-axis polarization direction at 5GHz is below -10db, the transmission performance is poor, which meet the equation (10).

Figure 3 (c) shows the simulation result of the transmission phase and phase difference of the single layer element in the x-axis and y-axis. The transmission phase difference of the element in the x-axis and y-axis is about 90 degrees at 5GHz. In the frequency range of 0~9GHz, the maximum difference of transmission phase between the two orthogonal directions of x axis and y axis is 142 degrees. The transmission phase of the transmit-array element in the orthogonal directions of x and y axes does not need to satisfy the phase difference of 180 degrees. Figure 3 (d) shows the relationship between element rotation angle and the change of phase. In the subsequent transmit-array design, this relationship is used to determine the rotation angle of the element.
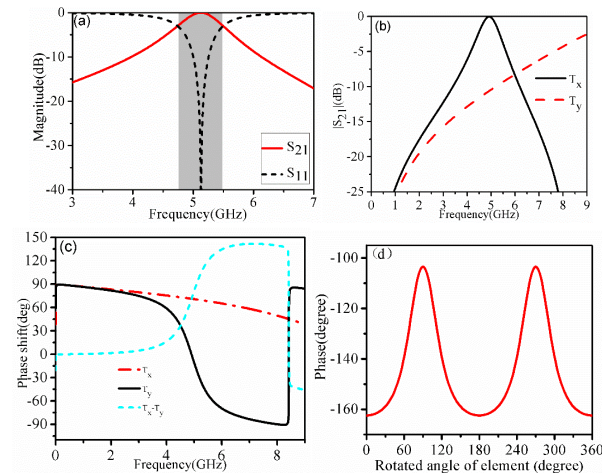

Fig. 3. (a) The scattering parameter of the element, (b) insertion loss of the element in the direction of the orthogonal polarization, (c) the transmission phase and phase difference of the element in the orthogonal direction, and (d) relationship between element rotation angle and the change of phase.

B. Design of transmit-array

After satisfying the requirement of transmission, the requirement of phase compensation needs to be met simultaneously. It is well known that the wave radiated by a horn antenna can be nearly regarded as a spherical wave [13]. When the spherical wave passes through the transmit-array, each element in the array should have phase modulation to make up for the presence of the optical path difference. The sequential rotation technique [4] is used to compensate phase for each element in the transmit-array.

The geometry of the single-layer transmit-array is shown in Fig. 4 (b). When the spacing of elements is less than one half wavelength, the mutual coupling effect between elements is strong, the overall performance of the antenna is greatly affected. When the element spacing is too large, the main lobe decreases and the sidelobe increases. In general, when l_0 stands for the cycle length of the elements, and the α represents the angle between the main beam and the vertical direction, the cycle length of the elements should be satisfied: $0.5\lambda < l_0 < \lambda /(1+sin\alpha)$. In this paper, $l_0=0.6\lambda$ is selected as the element spacing for this transmit-array.

The left and right sides of transmit-array are completely symmetric, No. 8 of transmit-array is the symmetric center line. It contains 225 elements, and their phase shift distribution is provided by the rotation. The prism effect occurs because the transmission waves have equal magnitudes but opposite phase shifts [5]. The left side elements of the transmit-array are rotated clockwise, and the right ones are counterclockwise.

Assume that the focal length is f, the cross slot at the position coordinate (x, y) needs to be rotated by an angle $\psi(x,y)$ relative to the central ones[14-18]. Element rotations are set according to:

$$\psi\left(x, y\right) = -\frac{1}{2}kx\sin 30° . \qquad (11)$$

The rotated angle of each element is shown in Fig. 4 (a).
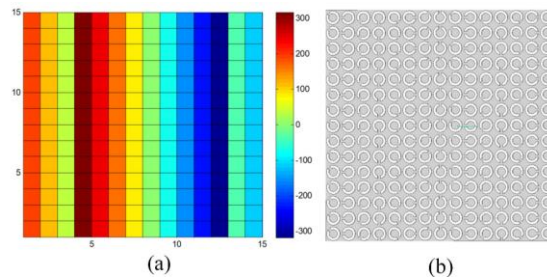
Fig. 4. (a) Rotated angle of each element and (b) Schematic diagram of transmit-array.

C. Function of designed beam array antenna

The transmit-array achieves not only polarization switching but also beam-steering. Electronic beam steering can be obtained by changing the phase distribution on the transmit-array [6]. The elements phase on both sides of the symmetry axis are adjusted independently, correction of transmission phase delay, compensate the space phase difference of the elements,

the electromagnetic waves could combine in two directions, so the separation beam is obtained in two directions.

When setting clockwise direction as the positive direction of element phase compensation, the polarization conversion array obtained by the phase compensation in a clockwise direction can only be applied to the right-handed circular polarized feed antenna. Set the counterclockwise direction as the positive direction of element phase compensation, the polarization conversion array obtained by the phase compensation in counterclockwise direction can convert the left-circularly polarized incident wave into the right circular polarized wave. Therefore, the transmit-array is divided into two parts: the left half is set clockwise as the positive direction of phase compensation, the right side is set counterclockwise as the positive direction of phase compensation.

When the waves pass through the transmit-array, the polarization of the incident wave will be changed: from LHCP to RHCP, RHCP to LHCP, LP to LHCP and RHCP. When working under the LP wave, the incident wave will scatter into two beams as LHCP and RHCP sat $\pm$ 30 azimuth angles, as shown in Fig. 5 (a); When working under the LHCP wave, the incident wave will scatter into two RHCP wave sat $\pm$ 15 azimuth angles, as shown in Fig. 5 (b); When working under the RHCP wave, the incident wave will scatter into two LHCP wave sat $\pm$ 15 azimuth angles, as shown in Fig. 5 (c). The measured radiation patterns are compared later.
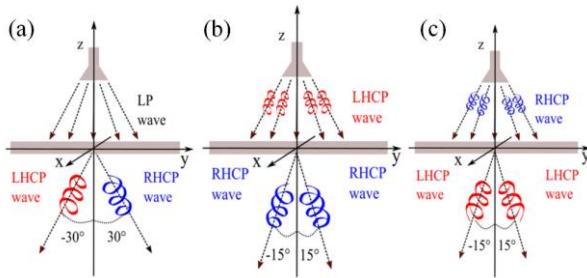

Fig. 5. Operating mode under the: (a) LP, (b) LHCP, and (c) RHCP horn antenna.

IV. SIMULATION AND MEASUREMENT OF THE TRANSMIT-ARRAY

A. Simulation of the transmit-array

Firstly, the operation of the transmit-array under the LP horn antenna is simulated by full-wave simulations. As a focal source with a gain of 12.15 dBi, a WR-187 standard waveguide horn is placed above the transmit-array [19-20]. The focal distance F is 468 mm (F/D = 0.8, Fig. 2) as a tradeoff between the spillover and taper efficiencies. The center frequency of the LP horn antenna is 5GHz. The simulated radiation pattern of the

transmit-array is shown in Fig. 6 (a). It is easy to see that the incident wave is divided into two transmission waves: LHCP at +30 azimuth angle and RHCP at -30 azimuth angle. The radiation mode with transmit-array is almost RHCP, and the major lobe points to the desired direction.

Secondly, the second working state is simulated the focal source is a 12.0 dBi right-handed circularly polarized conical horn. The focal distance F is as same as the previous one. The simulated radiation pattern of the transmit-array under the RHCP horn antenna is shown in Fig. 6 (b). The incident wave was divided into two LHCP transmission waves at ±15 azimuth angles. The radiation mode with the transmit-array is almost LHCP, and the major lobe points to the desired direction.

The simulated radiation pattern of the transmit-array under the LHCP horn antenna is shown in Fig. 6 (c), which is rather similar to the result of the RHCP horn antenna used as the feed source, except for the direction of polarization.
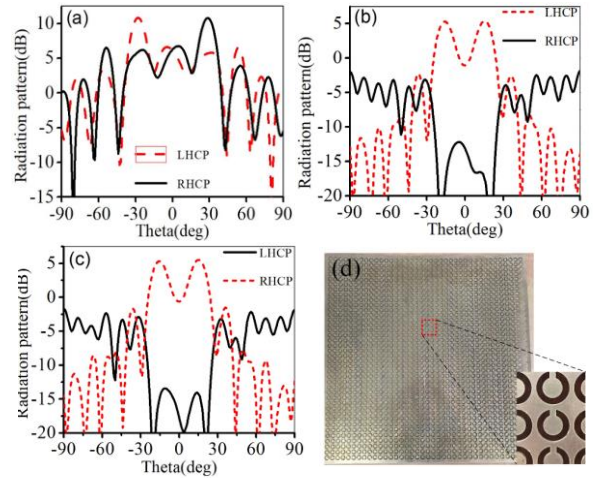
Fig. 6. (a) The simulated radiation pattern of the transmit-array under the LP horn, (b) the simulated radiation pattern of the transmit-array under the RHCP horn, (c) the simulated radiation pattern of the transmit-array under the LHCP horn, and (d) the physical samples of the transmit-array.

B. Measurement of the transmit-array

The design of the single-layer transmit-array is shown in the Fig. 6 (d). To facilitate the test, the design of the single-layer transmit-array is carried out by the periodic extension, which makes the transverse diameter bigger. The overall size of the antenna array is 525mm * 525mm, which contains 35*35=1225 elements. The transmit-array is made of the brass metal plate by laser cutting.

The overall view of test scenarios in an anechoic chamber is shown in Fig. 7 (a). Due to circular

polarization wave can be synthesized by linear polarization wave, only the working condition of the transmit-array under the LP wave has been measured. The designed transmit-array has been placed between the LP horn antenna and the waveguide probe. The LP horn antenna working in the 4-8GHz band has been used as the feed antenna, which is located 420mm away from the transmit-array center. The waveguide probe is placed on a robotic arm that can move up, down, left, and right. Performing near-field scanning measurements on the antenna that loading the transmit-array. Then the scan results can be converted into far-field radiation patterns by near-field scanning system.

The contrast of the measured and radiation pattern is shown in Fig. 7 (b) and Fig. 7 (c). The major lobe points to the desired direction (+30° and -30°) and matches the simulation results. Compared with the simulation results, the measured main lobe has a slight shift that may be caused by machining errors or experimental errors. Despite the presence of the shift, the beam-steering function of the transmit-array is well implemented.
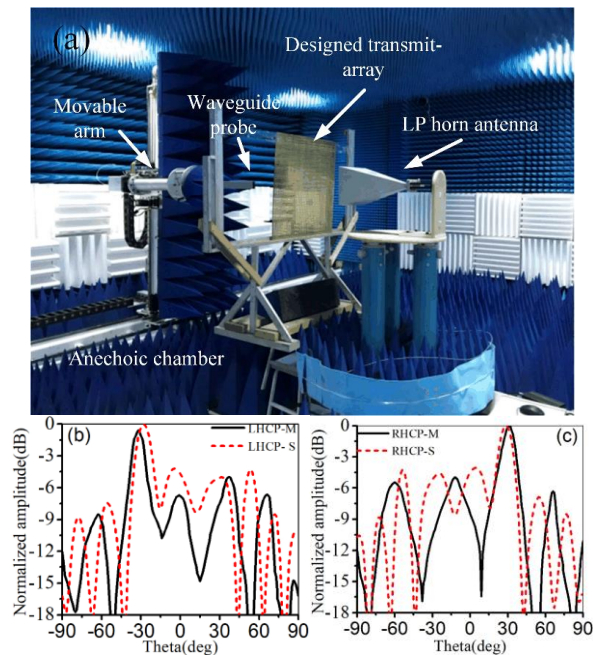

Fig. 7. (a) Overall view in an anechoic chamber, (b) measured and simulated radiation pattern of LHCP, and (c) measured and simulated radiation pattern of RHCP.

To demonstrate the performances of our proposed transmit-array, a comparison with previously published work is shown in Table 1. The transmit-array can change the polarization of the incident wave and set separation beam direction at the same time. The transmit-array has a huge advantage in the number of layers and thickness, which can reduce the disadvantage of complex array structure, the high profile and poor transmission performance.

Table 1: Performance comparison

Ref.	TAF	BSSA	Unit	NL	RS
[2]	PC and BSe	±20°	PRU	5	NO
[3]	PC and BSc	±60°	PDU	4	YES
[7]	Dual-Band Beam-Steering	50°	PDU	7	NO
This work	PC and BSe	±30°	PRU	1	NO

TAF=Transmit-array function, BSSA=Beam separation or scan angle, NL=Number of layers, RS=Reconfigurable situation, PC=Polarization conversion, BSc=beam scanning, BSe=beam separation, PRU=Phase-rotation unit, PDU=Phase-delay unit.

V. CONCLUSION

This paper presents the design and realization of a single layer multi-polarization transmit-array antenna, which is composed of a feed antenna and single layer transmit-array. It overcomes the disadvantages of the multilayer transmit-array antenna about the complex array structure, high profile and poor transmission, which only consists of pure metal transmission type elements according to the sequential rotation technique. It has three working conditions under different polarization of the incident wave, and it can switch the polarization of the incident wave and set separation beam direction at the same time, that can fully adapt to diversified work requirements. The measurement results are in agreement with the theoretical and simulation results.

ACKNOWLEDGMENT

REFERENCES

[1] X. Zhao, C. Yuan, L, Liu, S. Peng, Q. Zhang, and H. Zhou, "All-metal transmit-array for circular polarization design using rotated cross-slot elements for high-power microwave applications," *IEEE Trans. Antennas Propagat.*, pp. 3253-3256, 2017.

[2] R. H. Phillion and O. Michal, "Lenses for circular polarization using planar arrays of rotated passive elements," *IEEE Trans. Antennas Propagat.*, pp. 1217-1227, 2011.

[3] C. Huang, W. Pan, X. Ma, B. Zhao, J. Cui, and X.

Luo, "Using reconfigurable transmitarray to achieve beam-steering and polarization manipulation applications," *IEEE Trans. Antennas Propagat.*, vol. 63, no. 11, pp. 4801-4810, 2015.

[4] C. G. Ryan, M. R. Chaharmir, J. R. Shaker, J. R. Bray, Y. M. Antar, and A. Ittipiboon, "A wideband transmit-array using dual-resonant double square rings," *IEEE Trans. Antennas Propagat.*, pp. 1486-1493, 2010.

[5] A. K. Bhattacharyya, *Phased Array Antennas*, Hoboken (NJ): Wiley-Interscience, 2006.

[6] P. L. Di, A. Clemente, L. Dussopt, R. Sauleau, P. Potier, and P. Pouliguen, "Circularly-polarized reconfigurable transmit-array in Ka-band with beam scanning and polarization switching capabilities," *IEEE Trans. Antennas Propagat.*, pp. 529-540, 2017.

[7] S. A. Matos, E. B. Lima, J. S. Silva, J. R. Costa, C. A. Fernandes, N. J. Fonseca, and J. R. Mosig, "High gain dual-band beam-steering transmit array for satcom terminals at Ka-band," *IEEE Trans. Antennas Propagat.*, vol. 65, no. 7, pp. 3528-3539, 2017.

[8] Y. Luo, K. Kikuta, Z. Han, T. Takahashi, A. Hirose, and H. Toshiyoshi, "An active meta-material antenna with MEMS-modulated scanning radiation beams," *IEEE Electron. Device Lett.*, vol. 37, no. 7, pp. 920-923, 2016.

[9] M. Rahman, M. Naghshvarianjahromi, S. Mirjavadi, and A. Hamouda, "Bandwidth enhancement and frequency scanning array antenna using novel UWB filter integration technique for OFDM UWB radar applications in wireless vital signs monitoring," *Sensors*, vol. 18, no. 9, pp. 3155, 2018.

[10] M. Nejatijahromi, M. Naghshvarianjahromi, and M. U. Rahman, "Switchable planar monopole antenna between ultra-wideband and narrow band behavior," *Progress in Electromagnetics Research*, vol. 75, pp. 131-137. 2018.

[11] M. Nejatijahromi, M. Nagshvarianjahromi, and M. Rahman, "A new compact planar antenna for switching between UWB, narrow band and UWB with tunable-notch behaviors for UWB and WLAN applications," *Appl. Comput. Electromagn. Soc. J.*, vol. 33, no. 4, 2018.

[12] H. Ke, Y. He, J. Xu, and Y. Luo, "A leaky-wave antenna with programmable beam scanning," *IEEE International Conference on Computer and Communication Engineering Technology (CCET)*, pp. 138-141, Aug. 2018.

[13] M. Sazegar, Y. Zheng, C.Kohler, H. Maune, M. Nikfalazar, J. R. Binder, and R. Jakoby, "Beam steering transmit-array using tunable frequency selective surface with integrated ferroelectric varactors," *IEEE Trans. Antennas Propagat.*, pp. 5690-5699, 2012.

[14] B. Rahmati and H. R. Hassani, "Low-profile slot transmit-array antenna," *IEEE Trans. Antennas Propag.*, pp. 174-181, 2015.

[15] G. Shajan, M. Kozlov, and J. Hoffmann, "A 16-channel dual-row transmit array in combination with a 31-element receive array for human brain imaging at 9.4 T," *Magn. Reson. Med.*, pp. 870-879, 2014.

[16] R. T. Derryberry and B. Raghothaman, "Adaptive antenna transmit array with reduced CDMA pilot channel set," *U.S. Patent No. 6,728,307*, 27 Apr. 2004.

[17] P. W. Dent, "Multi-signal transmit array with low intermodulation," *U.S. Patent No. 7,027,454*, 11 Apr. 2006.

[18] T. S. Ibrahim, "Ultrahigh-field MRI whole-slice and localized RF field excitations using the same RF transmit array," *IEEE T. Med. Imaging*, pp. 1341-1347, 2006.

[19] L. Schwartzman and L. Topper, "Analysis of phased array lenses," *IEEE Trans. Antennas Propagat.*, vol. 16, no. 6, pp. 628-632, 1968.

[20] A. Munoz-Acevedo, P. Padilla, and M. Sierra-Castaner, "Ku band active transmit array based on microwave phase shifters," *Antennas and Propagation*, *EuCAP, 3rd European Conference on. IEEE*, 2009.

Xiaochun Liu was born in China, in 1962. He received the B.S. degree from Nanjing University of Aeronautics and Astronautics, Nanjing, China, in 1984. He is currently pursuing the Ph.D. degree in Nanjing University of Aeronautics and Astronautics, Nanjing, China. He has been engaged in research on radar radome technology for a long time.

Qiming Yu was born in Zhejiang Province, China, in 1992. He received the B.S. degree and M.S. degree from Nanchang University, Nanchang, China, in 2014 and 2016, respectively. He is currently pursuing the Ph.D. degree in Nanjing University of Aeronautics and Astronautics, Nanjing, China. His current research interests include frequency selective surface, rasorber and lens antenna.

A W-Band Dual-Polarization Slot Array Antenna with Low Sidelobe Level

Hao Luo [1], Yu Xiao [2], Wenhao Tan [1], Luoning Gan [1], and Houjun Sun [1]

[1] Department of Information and Electric Engineering
Beijing Institute of Technology, Beijing, 100081, China
ihlyt111@126.com

[2] Department of Electronic Engineering
Tsinghua University, Beijing, 100081, China
xiaoyummw@tsinghua.edu.cn

Abstract ─ A 94-GHz dual-polarization low-sidelobe-level slot array antenna is proposed. A 2x2-slot cavity-backed subarray is adopted as the basic unit of the array. A high-isolation orthogonal-mode transducer (OMT) with a simple structure is used to excite the dual-polarization subarray. The realization of a low sidelobe level depends on the amplitude-weighted waveguide feed network. A novel unequal power dividing ratio but equal phase (UPEP) single-ridged waveguide divider is presented for the construction of the vertical polarization (VP) array feed network. A 16x16-slot low-sidelobe-level dual-polarization array antenna is fabricated. The machining difficulties of the W-band array are reduced by using simpler structures. The measured results show that the impedance bandwidth is greater than 7.3 GHz, while the first sidelobe levels are lower than -20.1 dB for both polarization arrays within the operating bandwidth. The measured gain is higher than 30.9 dBi for the two polarization arrays with an antenna efficiency better than 64% .

Index Terms ─ Dual-polarization, low sidelobe level, slot array antenna, *W*-band.

I. INTRODUCTION

Fully polarimetric radar has advantages in anti-interference properties and has received increasing attention in recent years. The dual-polarization antenna is the key part of achieving the polarization agility of a fully polarimetric radar system [1]. The reported dual-polarization reflector antenna and lens antenna have a high gain but suffer from a high profile [2-3].

Most reported dual-polarization planar antennas are based on dielectric substrates because of their low profile and low cost [4-9]. Microstrip patch antennas were used as the dual-polarization radiating elements in [5-8]. High isolation between the two polarization arrays has been achieved by multilayer feed networks; however, these antennas have a low radiation efficiency due to the large loss of the microstrip feed network. In [8-9], a substrate-integrated waveguide feed network was used, and the antenna efficiency increased but remained at a low level because the dielectric loss could not be ignored, especially in the millimeter-wave band.

Waveguide slot antennas employ a low-loss feed network, leading to an easier realization of a low sidelobe level, which has been widely used in the milli-meter wave band [10-12]. However, these slot arrays are actually series-fed, which results in a narrow bandwidth due to the long-line effect.

The basic units of the cavity-backed slot antennas in [13-17] use the resonance mode in the cavity to feed the slots instead of a conventional feed network, which results in lower feeding loss and wider bandwidth. In addition, corporate feed networks are adopted in cavity-backed slot arrays, resulting in high-gain and wideband performance. Due to the good performance, a large number of cavity-backed slot array antennas with different radiating elements, different transmission lines and different frequencies have been studied and reported [13-21]. Few of these studies have mentioned low-sidelobe-level design in a dual-polarization array, however, for radar systems, low-sidelobe-level antennas can improve the anti-jamming ability of the system.

The goal of this paper is to present a method to design the wideband high-gain dual-polarization slot array antenna with a low-sidelobe-level design in the W-band. First, we introduce the basic unit of the dual-polarization array and analyze the working mechanism of the orthogonal-polarization feeding structure. Next, we introduce the design of the unequal power dividing ratio but equal phase single-ridge waveguide divider in detail. Finally, a 16x16-slot dual-polarization array with a low sidelobe level is fabricated and measured to verify the design method.

II. ANTENNA DESIGN

The total structure of the proposed W-band dual-

polarization 16x16-slot cavity-backed array antenna is shown in Fig. 1. The antenna consists of six metal layers. The upper two layers are the radiating part of the array, and the third and fifth layers are the 1-to-64-way amplitude-weighted feed networks of the vertical polarization and horizontal polarization arrays. The power-weighted feed-networks are composed of the UPEP rectangular waveguide dividers and UPEP single-ridge waveguide dividers. The isolation bars and coupling windows are in the fourth layer, and they are the key to realizing high isolation between the feed networks of the two polarization arrays. The sixth layer is the backboard, and two WR-10 standard waveguides with an FUGP-385 flange are used as the feeding ports.
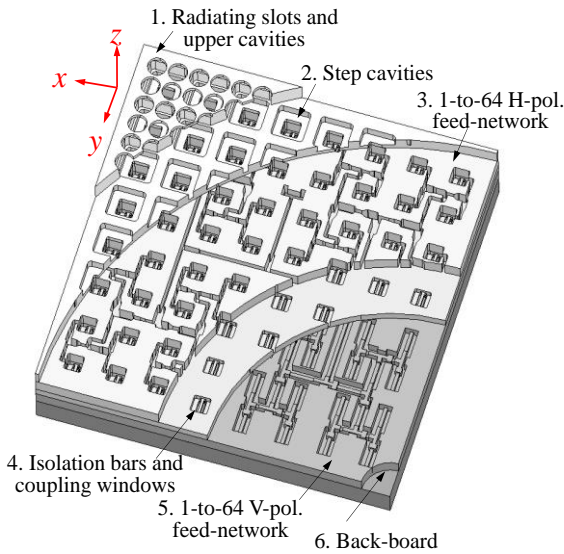

Fig. 1. Configuration of the dual-polarization array.

A. The dual-polarization cavity-backed slot subarray

As shown in Fig. 2, the basic unit of the array is a cavity-backed 2x2-slot subarray. Circular radiating slots and square cavities with large fillets are used instead of the narrow slots and irregularly shaped cavities in [13] to reduce the machining difficulties in the W-band. The radiating slots and the upper cavity have a rotationally symmetrical structure that can radiate uniformly for both polarizations. The radiating part is fed by a square waveguide, and a step cavity is adopted to improve the impedance bandwidth of the feed waveguide. The horizontal-polarization (HP) electromagnetic (EM) wave is fed from an E-plane rectangular waveguide through the z-direction coupling window etched on the sidewall of the square waveguide, and the VP EM wave is fed by a single-ridged waveguide through the y-direction coupling window on the bottom of the square waveguide.
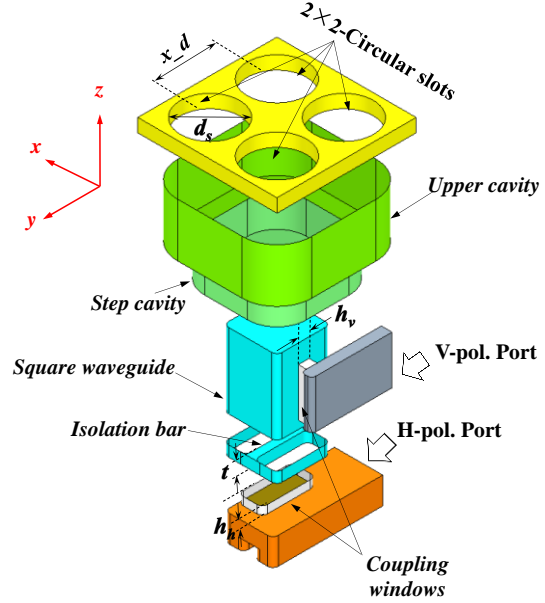
Fig. 2. Configuration of the basic unit in the array.

As shown in Fig. 3, the isolation bar can cut off the HP EM wave, while the z-direction coupling slot can cut off the VP EM wave, the isolation between the two ports can be estimated by formula (1):

$$I_s = 20\log_{10} e^{\alpha L},\tag{1}$$

where α is the attenuation constant of TE_{10} mode, L is the sum of hv, h_h and t. As depicted in Fig. 4, the isolation between HP and VP ports is lower than -45dB among 88GHz~100GHz. Compared with the feeding structure in [21], the orthogonal-mode transducer adopted in our work has a more compact structure and a higher isolation so that the two polarization feed-networks can be designed independently.
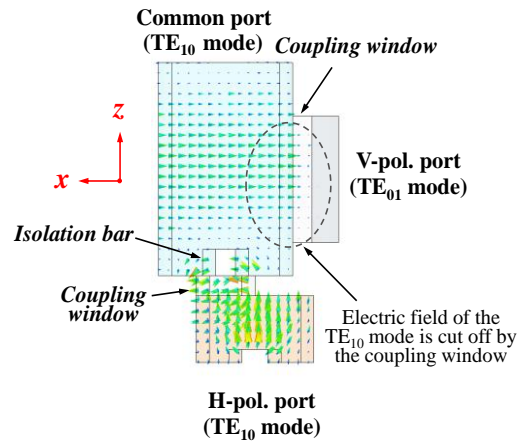
(a) Electric field distribution in the OMT (H-pol.)
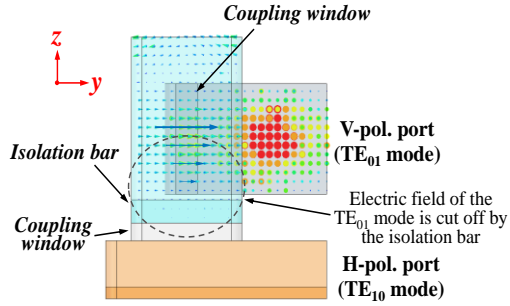
(b) Electric field distribution in the OMT (V-pol.)

Fig. 3. Working mechanism of the OMT.
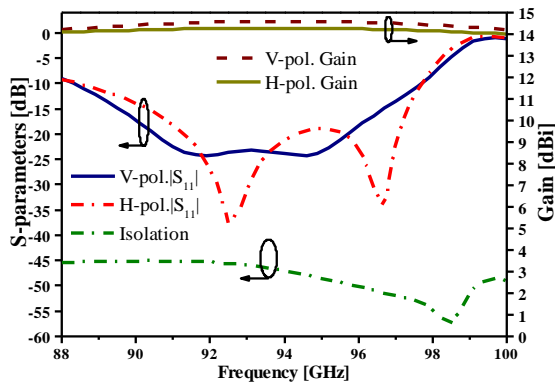
Fig. 4. Simulated performance of the subarray.

The EM simulation software Ansoft HFSS is used to analyze the performance of the antenna. The S-parameters and gain of the basic unit are depicted in Fig. 4, and the radiation patterns of the basic unit are exhibited in Fig. 5. The reflection coefficients of the VP and HP units are lower than -10 dB over the frequency range of 88.5 GHz~96.8 GHz. The simulated gain is higher than 14 dBi, and the cross-polarization discrimination (XPD) is lower than -39 dB in both planes for the two polarization units.
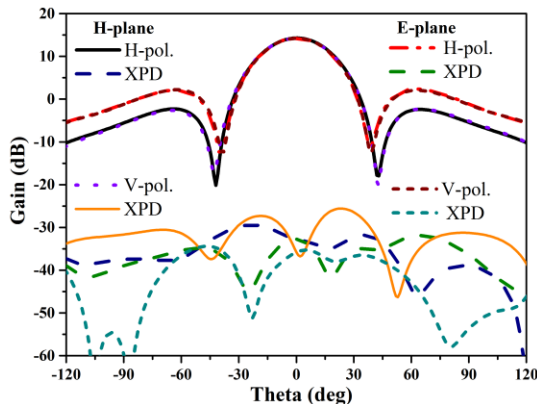
Fig. 5. Radiation pattern of the subarray (94GHz).

B. Design of the UPEP waveguide dividers

When using the 2x2-slot unit to build a wideband large-scale array, the low-sidelobe-level performance of the array antenna needs to be realized by an amplitude-weighted corporate feed network.

The UPEP waveguide divider is the basic unit of the amplitude-weighted feed network in rectangular waveguide (RWG). The characteristic impedance of Z_0 and phase constant β of the TE$_{10}$ mode in a rectangular WG are listed in (2) and (3):

$$\beta = \frac{2\pi}{\lambda}\sqrt{1-\left(\frac{\lambda}{2a}\right)^2}, \qquad (2)$$

$$Z_e = \frac{b}{a}\sqrt{\frac{\mu}{\varepsilon}}\frac{1}{\sqrt{1-(\lambda/2a)^2}}, \qquad (3)$$

where a and b are the broad wall width and narrow width of an RWG. The realization of the UPEP RWG divider is through tuning the narrow wall width of RWG. This method can be used to build the VP amplitude-weighted feed network. However, a UPEP single-ridge waveguide divider should also be designed to build the HP amplitude-weighted feed network.

Unlike the RWG, the electric field and magnetic field distributions in an SRWG are more complicated. At present, there are few studies on a UPEP single-ridge waveguide divider.

The key to realizing a UPEP divider is to find a waveguide parameter that affects the characteristic impedance (Z_e) of the waveguide but has a small effect on the guide wavelength (λ_g). Figure 6 shows curves of the characteristic impedance and guide wavelength of a single-ridge waveguide with different values of the ridge width a_2; for the SRWG, when the ridge height b_2 is close to the height of the waveguide b_2, the ridge width a_2 is proportional to the characteristic impedance Z_e but independent of the guide wavelength λ_g.
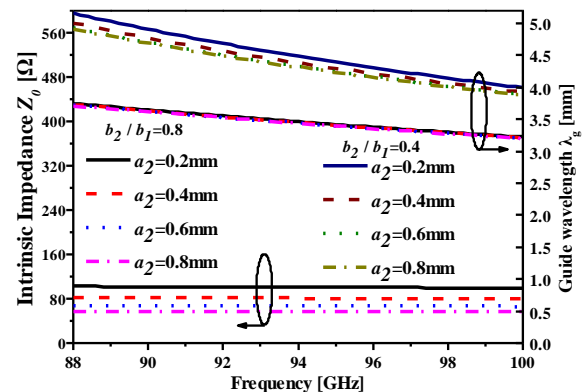

Fig. 6. Simulated results of a single-ridge waveguide.

Based on this discovery, we proposed the UPEP single-ridge waveguide divider, which is shown in Fig. 7. A power splitting SRWG section is added to both

output WGs. The ridge heights of the two SRWG sections are close to the height of the SRWG ($b_2 \approx b_1$). By adjusting the ridge width of the two SRWG sections, an unequal power dividing ratio but equal phase can be achieved. An impedance matching section is placed at the input port to broaden the bandwidth. The impedance of this section can be calculated by formula (4):

$$Z_1 = \sqrt{Z_0 Z_2 Z_3 (Z_2 + Z_3)}. \tag{4}$$
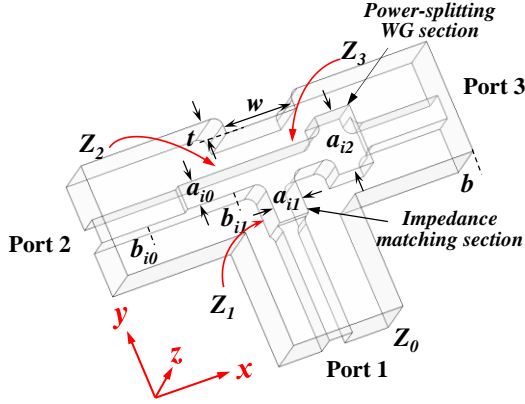
Fig. 7. The proposed UPEP single-ridge waveguide divider.

Figure 8 shows the performance of the designed UPEP single-ridge waveguide divider. The power dividing ratio is 3.5 dB, and the absolute value of the phase deviations is less than 5 degrees between the two output ports, while the reflection coefficient is less than -18 dB in the frequency range of 88 GHz~100 GHz.
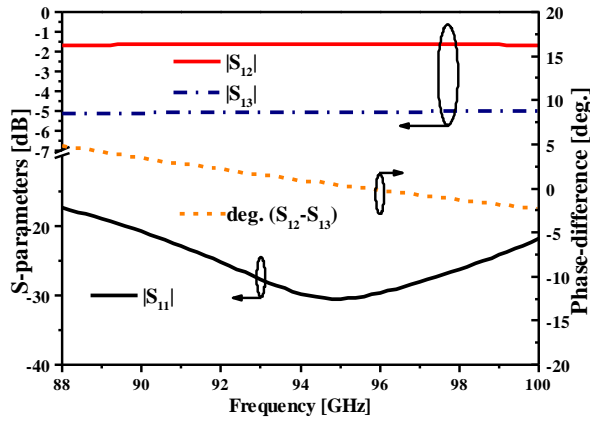
Fig. 8. S-parameters of the proposed UPEP divider.

C. Design of the amplitude-weighted feed-network

To realize the low sidelobe level of a large-scale array, we used the 2x2-slot dual-polarization subarray to build a 16x16-slot array. Two kinds of 1-to-64-way amplitude-weighted waveguide feed networks are designed in this section.

Based on the proposed UPEP single-ridge waveguide divider, a 1-to-64-way amplitude-weighted corporate feed network is built for the HP array. The amplitude-weighted feed network for the VP array consists of the UPEP rectangular waveguide divider proposed in previous work. Figure 9 shows the configuration of the H feed networks. A 25 dB Taylor synthesis is used to obtain the normalized amplitude coefficient of each output port in the two feed-networks.
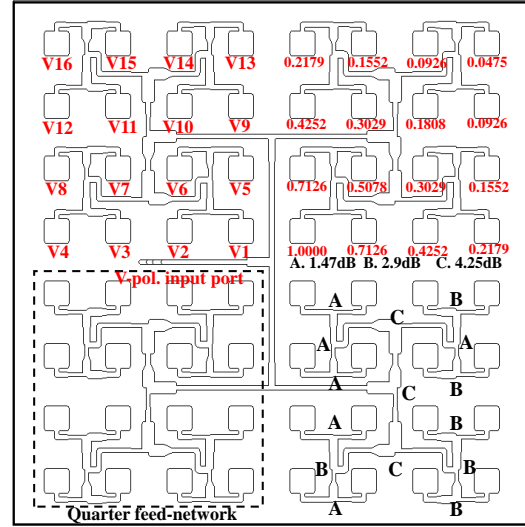
(a) Configuration of the VP array feed-network
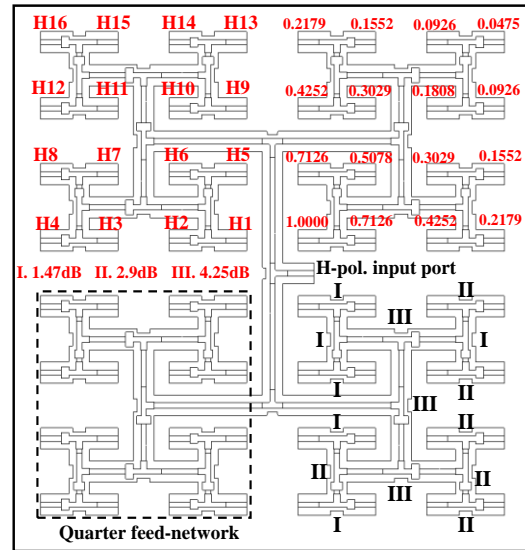
(b) Configuration of the HP array feed-network

Fig. 9. The designed amplitude-weighted feed-networks.

Three UPEP power dividers with power splitting ratios of 4.25 dB, 2.9 dB and 1.47 dB are required for each feed network. Their corresponding positions are also shown in Fig. 9.

The feed ports of the array are two WR-10 standard waveguides with an FUGP-385 flange. As shown in Fig. 10, a vertical transition from the single-ridge waveguide to the WR10 standard waveguide is introduced in the feed networks. The S-parameters of the vertical transition are shown in Fig. 11. The results indicate that the transition structure has a reflection coefficient of less than -22 dB in the frequency range of 88 to 100 GHz, a relative bandwidth of approximately 25.6%, and an insertion loss of less than 0.05 dB in the same frequency range.
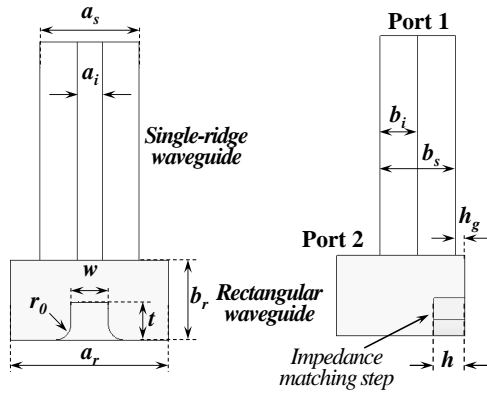
Fig. 10. Vertical transition from SRWG to RWG.
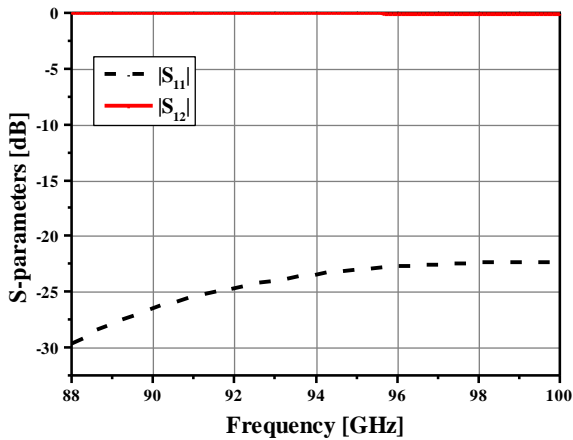
Fig. 11. Simulated performance of the vertical transition.

The simulated performance of the designed VP and HP amplitude-weighted feed networks are shown in Fig. 12. The absolute values of the phase deviation are less than 8 degrees among the 64 ports, and the absolute values of the amplitude differences are less than 0.25 dB in the frequency range of 89.2 GHz ~ 98.2 GHz. Moreover, the reflection coefficients of the HP and VP input ports are less than -10 dB from 88.5 GHz to 97.5 GHz.
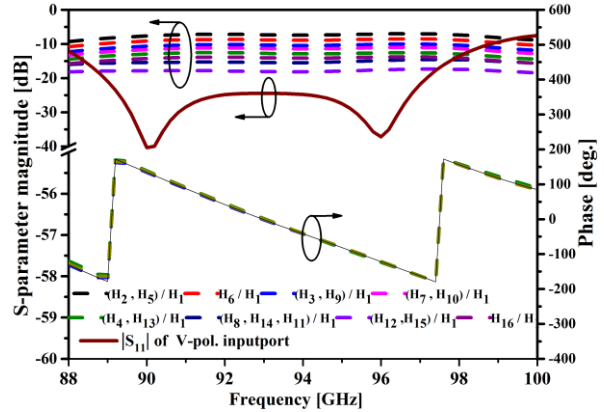
(a) Performance of the HP array feed-network
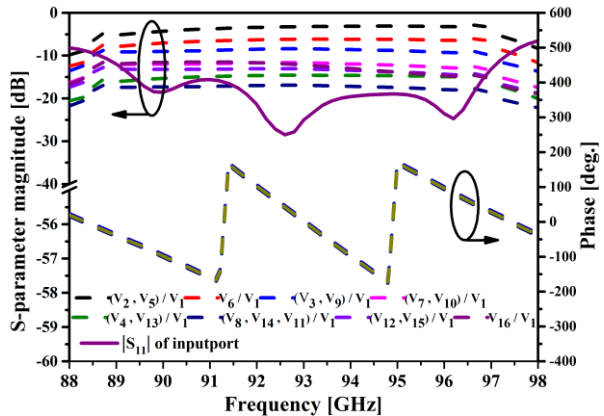
(b) Performance of the VP array feed-network

Fig. 12. Simulated results of the feed-networks.

III. MEASUREMENT AND RESULTS

The designed dual-polarization 16x16-slot cavity-backed array antenna consists of six aluminum plates and is shown in Fig. 1. These aluminum plates are machined by milling and bonded by a vacuum brazing process. The smallest milling cutter used during machining is 0.3 mm in diameter. The surface roughness inside the waveguide cavity after processing is Ra1.6. The manufacturing tolerances of the array antenna are analyzed by the HFSS software. Figure 13 shows the prototype of the proposed antenna.

The average thickness of each layer of solder after bonding is less than 0.02 mm, which is within an acceptable range. The reflection coefficient and isolation of the two polarization input ports of the array antenna were measured by the R&S ZVA-Z110 vector network analyzer. The results are shown in Fig. 14. The reflection coefficients of the HP and VP ports are less than -10 dB in the frequency range of 89.2GHz~ 96.5GHz, and the relative bandwidth is approximately 7.8%. The isolation between the two polarization feed ports is better than 45 dB in 88 GHz ~100 GHz.
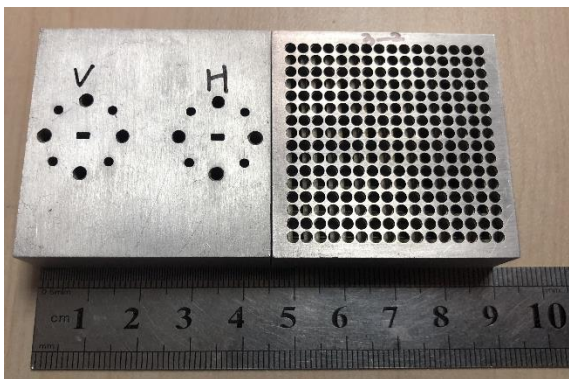
Fig. 13. Prototype of the fabricated array antenna.
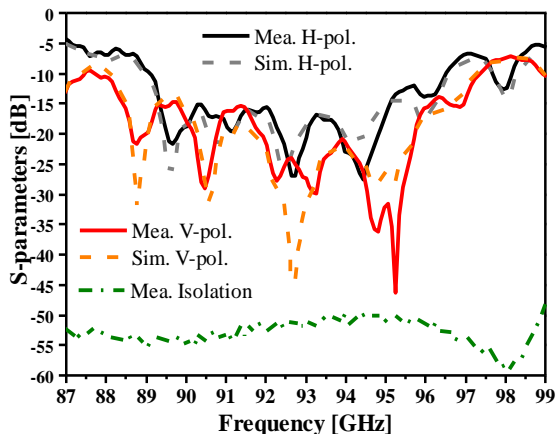
Fig. 14. Measured S-parameters of the proposed array.

The radiation performance of the dual-polarization array was measured by a W-band far-field antenna testing system in an anechoic chamber. The antenna measurement environment is shown in Fig. 15.
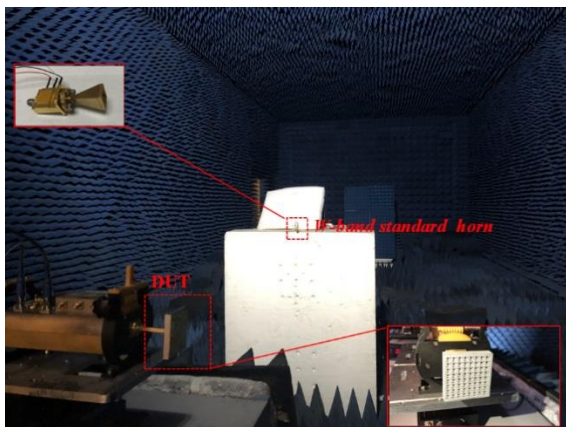
Fig. 15. Antenna measurement environment.

Figure 16 shows the measured and simulated gains of the antenna. A gain curve considering the metal loss and surface roughness is also added to the figure for a comparison. The measured gain for the VP array is higher than 31 dBi, and the measured gain for the HP array is higher than 30.9 dBi from 90 GHz to 96 GHz. The measured gain is approximately 0.6 dB lower than the simulated gain, which is caused by errors in the processing and measurement. The measured efficiency of the two polarization arrays is higher than 64% over the entire working band.
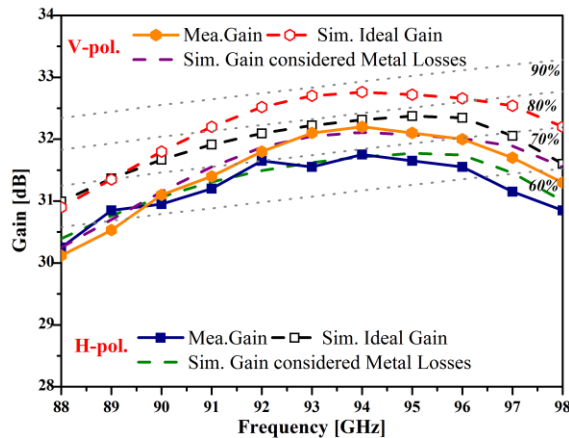
Fig. 16. Measured gain of the proposed array.

A comparison between the measured and simulated radiation patterns is shown in Fig. 17. The measured sidelobe levels for the VP and HP arrays are lower than -21 dB and -20.1 dB in both planes, respectively. The XPDs for both polarization arrays are lower than -35 dB in both planes. The measured and simulated results are highly consistent, which verifies the validity of the design method.
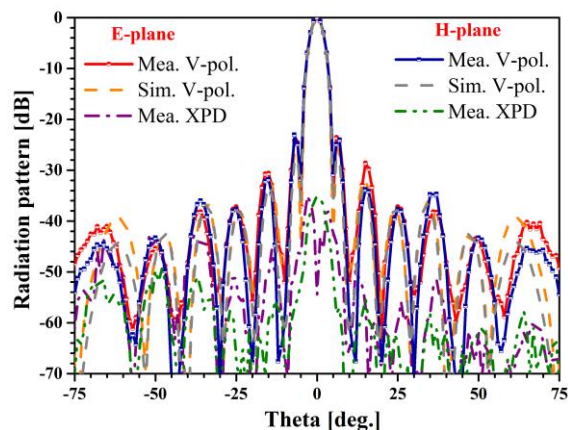
(a) Radiation pattern of the VP array (94GHz)
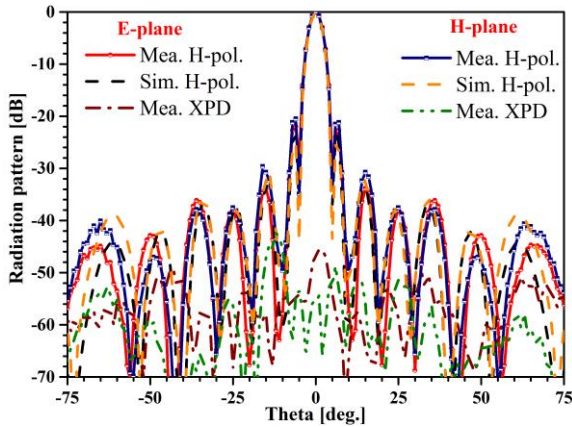
(b) Radiation pattern of the HP array (94GHz)

Fig. 17. Measured radiation pattern of the proposed array.

Table 1 presents a comparison of the antenna presented in references and our work. The performance comparison includes the center frequency, realized gain, impedance bandwidth, sidelobe-level, cross-polarization discrimination, antenna efficiency, and fabrication difficulties. The results indicate that the antenna in our work has the lowest sidelobe level with wideband and high-gain performance characteristics.

Table 1: Performance comparison of the reported planar dual-polarization antenna and our work

Ref.	[13]	[19]	[20]	[21]	[4]	Our Work
Freq. [GHz]	60	60	60	60	94	94
Gain [dB]	32.2	22.3	12.5	16.5	13.3	31.2
BW.	8%	17%	22%	15%	7%	7.8%
SLL. [dB]	-13	-12.3	-10	-13	-10	-20.1
XPD. [dB]	<-25	<-20	<-10	<-30	<-9	<-35
Effc.	80%	72%	70%	65%	50%	64%
Fabr. Diffic.	Medium	Low	Low	High	Low	Medium

IV. CONCLUSION

A 94-GHz dual-polarization low-sidelobe-level 16x16-slot cavity-backed array antenna is proposed. A high-isolation orthogonal mode transducer with a simple structure is used to excite the 2x2-circular-slot cavity-backed subarray. A new UPEP single-ridge waveguide divider is proposed for the construction of the amplitude-weighted corporate feed network. The measured first

sidelobe levels are lower than -20.1 dB for both arrays from 90 GHz to 96 GHz. The measured results indicate that the fabricated W-band array antenna has wideband and high gain performance characteristics, which commendably satisfies the requirements of the W-band fully polarimetric radar system.

REFERENCES
[1] M. Andrews and P. Mitra, "Tripling the capacity of wireless communications using electromagnetic polarization," *Nature*, vol. 409, no. 1, pp. 316-318, 2001.

[2] Z. Y. Zhang, "Design of a dual-beam dual-polarized offset parabolic reflector antenna," *IEEE Trans. Antennas Propag.*, vol. 67, no. 2, pp. 712-718, 2019.

[3] Y. Su and Z. N. Chen, "A flat dual-polarized transformation-optics beamscanning luneburg lens antenna using PCB-stacked gradient index metamaterials," *IEEE Trans. Antennas Propag.*, vol. 66, no. 10, pp. 5088-5097, 2018.

[4] Z. Chen, "A 94-GHz dual-polarized microstrip mesh array antenna in LTCC technology," *IEEE Antennas Wireless Propag. Lett.*, vol. 14, pp. 1279-1281, 2015.

[5] C. L. Deng, "A high-isolation dual-polarization patch antenna with omnidirectional radiation patterns," *IEEE Antennas Wireless Propag. Lett.*, vol. 11, pp. 1273-1276, 2012.

[6] D. Sun, "Design of broadband dual-polarized patch antenna with backed square annular cavity," *IEEE Trans. Antennas Propag.*, vol. 64, no. 1, pp. 43-52, 2016.

[7] Y. Yu and W. Hong, "E-band low-profile, wideband 45° linearly polarized slot-loaded patch and its array for millimeter-wave communications," *IEEE Trans. Antennas Propag.*, vol. 66, no. 8, pp. 4364-4369, 2018.

[8] L. Wang and Y. J. Chen, "Wideband and dual-band high-gain substrate integrated antenna array for E-band multi-gigahertz capacity wireless communication systems," *IEEE Trans. Antennas Propag.*, vol. 62, no. 9, pp. 4602-4611, 2014.

[9] Y. J. Chen, "94 GHz substrate integrated wave-guide dual-circular-polarization shared-aperture parallel-plate long-slot array antenna with low sidelobe level," *IEEE Trans. Antennas Propag.*, vol. 65, no. 11, pp. 5855-5861, 2017.

[10] H. Luo, "Design of a dual-polarization single-ridged waveguide slot array with enhanced bandwidth," *IEEE Antennas Wireless Propag. Lett.*, vol. 18, pp. 138-142, 2019.

[11] T. Li, "Design and implementation of dual-frequency dual-polarization slotted waveguide antenna array for Ka-band application," *IEEE Antennas Wireless Propag. Lett.*, vol. 13, pp. 1317-

1320, 2014.

[12] R. V. Gatti and R. Rossi, "A dual-polarization slotted waveguide array antenna with polarization-tracking capability and reduced sidelobe level," *IEEE Trans. Antennas Propag.*, vol. 64, no. 4, pp. 1567-1572, 2016.

[13] D. Kim, M. Zhang, J. Hirokawa, and M. Ando, "Design and fabrication of a dual-polarization waveguide slot array antenna with high isolation and high antenna efficiency for the 60 GHz band," *IEEE Trans. Antennas Propag.*, vol. 62, no. 6, pp. 3019-3027, 2014.

[14] A. Vosoogh and P. S. Kildal, "Corporate-fed planar 60-GHz slot array made of three unconnected metal layers using AMC pin surface for the gap waveguide," *IEEE Antennas Wireless Propag. Lett.*, vol. 15, pp. 1938-1935, 2016.

[15] D. Zarifi and P. S. Kildal, "Design and fabrication of a high-gain 60-GHz corrugated slot antenna array with ridge gap waveguide distribution layer," *IEEE Trans. Antennas Propag.*, vol. 64, no. 7, pp. 2905-2913, 2016.

[16] B. L. Cao, "W-band high-gain TE_{220}-mode slot antenna array with gap waveguide feeding network," *IEEE Antennas Wireless Propag. Lett.*, vol. 15, pp. 988-991, 2016.

[17] Y. J. Chen, "W-band large-scale high-gain planar integrated antenna array," *IEEE Trans. Antennas Propag.*, vol. 62, no. 6, pp. 3370-3373, 2014.

[18] Z. J. Chen, "High gain, broadband and dual-polarized substrate integrated waveguide cavity-backed slot antenna array for 60 GHz band," *IEEE Access.*, vol. 6, pp. 31012-31022, 2018.

[19] Y. J. Li and K. M. Luk, "60-GHz dual-polarized two-dimensional switch-beam wideband antenna array of aperture-coupled magneto-electric dipoles," *IEEE Trans. Antennas Propag.*, vol. 64, no. 2, pp. 554-563, 2016.

[20] M. F. Rocher and A. V. Nogueira, "A dual-polarized slotted-waveguide antenna based on gap waveguide technology," *11th European Conf. on Antennas and Propagat. (EUCAP)*, 19-24 March 2017.

[21] A. Jawad, T. Djerafi, and K. Wu, "A 94-GHz planar orthogonal mode transducer," *International Journal of Microwace and Wireless Tech.*, vol. 6, no. 3, pp. 313-324, 2014.

Hao Luo was born in Yunnan Province, P. R. China in 1990. He received the B. S. degree in Electrical Engineering from Beijing Institute of Technology in 2012. He received the M. S. degree in Electrical Engineering from Beijing Institute of Technology in 2015. He began his PhD degree in 2015 and his interest field is mainly in millimeter wave antenna, dual-polarization antenna, and full-polarimetric radar systems.

Yu Xiao received his Ph.D. degree in Electrical Engineering from Beijing Institute of Technology in 2017. He is now a Post-Doctor in Tsinghua University, his interest field is mainly in millimeter wave system, plannaer antennas.

Wenhao Tan was born in Anhui, China, in 1995. He received the B.S. degree in Electronic and Information Engineering from Beijing Institute of Technology, Beijing, China, in 2017. He is currently pursuing the M. Eng. degree in Electromagnetic Fields and Microwave Technology at Beijing Institute of Technology, Beijing, China. His current research interests include millimeter wave antenna and silicon antenna.

Luoning Gan was born in Liaoning, China, in 1994. He received the B.S. degree in Applied Physics from Beijing Institute of Technology, Beijing, China, in 2016. He is currently pursuing the M. Eng. degree in Electromagnetic Fields and Microwave Technology in Beijing Institute of Technology, Beijing, China. His current research interests include microwave and millimeter wave antennas.

Houjun Sun received his Ph.D. degree in Communication and Electronic Systems from BIT in 1997. He is currently a Professor in BIT, the Director of the Institute of Microwave Technology, and the Director of the Beijing Key Laboratory of Millimeter Wave and Terahertz Technology. His current research interests include the integration and application of the millimeter-wave and terahertz communication system, active antenna arrays, millimeter-wave imaging.

Broad-Band I-Shaped SIW Slot Antenna for V-Band Applications

M. Nandakumar and T. Shanmugnantham

Department of Electronics Engineering
Pondicherry University, Pondicherry-605014, India
nanda.mkumar12@gmail.com, shanmugananthamster@gmail.com

Abstract — In this article, the broad-band SIW slot antenna is proposed for V-band applications, I shaped slot is used in this design and useful for millimeter-wave communication applications. The material used in this design is RT-Duriod 5880 with ε_2=2.2 with a thickness of 0.381mm and copper thickness is 35um. The proposed antenna is designed, simulated, printed and tested. The antenna has an impedance bandwidth of 5.1GHz ranges from 57GHz to 62.1GHz and discusses the parameters like VSWR, radiation patterns, gain. The antenna has validated with comparison of simulation and measured results.

Index Terms — Gigabit fidelity (GIFI), millimeter waves (MMWs), substrate integrated waveguide (SIW), system on substrate (SoS), waveguide (WG).

I. INTRODUCTION

The microwave frequency is not sufficient to fulfill the requirements of the present day to day scenario and need to switch next frequency is called millimeter-wave [2, 11] and covers a frequency range from 30 to 300GHz. In the last decade, the trends of the millimeter-waves were rapidly growing due to growth of academia, industry and personal applications. The millimeter wireless communication application is one unlicensed band in the millimeter-wave frequency with 7GHz bandwidth: covers a frequency range 57-64GHz [2, 4-5] and named has 60GHz band for automotive radar applications discussed in [1].

The researchers and academics have more interest in 60GHz band due to its huge availability of bandwidth. The wireless system plays a predominant role in gigabit-fidelity (GiFi) in wireless communication [2]. The 60GHz communication limits its range due to high levels of rain attenuation, oxygen absorption in 60GHz propagation characteristics and it is striking for short range applications [3]. This is also a highly secure and interference free communication due to operating for short range applications.

The high frequency applications, mostly preferred transmission line is SIW [4], one from of substrate integrated circuits (SICs). It has etched two rows of vias connected in top to bottom plane through substrate and also implemented for active, passive components, antenna due to system on substrate (SOS) technology used for development.

The cut off frequency of dielectric filled rectangular waveguide is represented in equation 1.The dominant mode of the rectangular waveguide is TE$_{10}$ and simplified formulae for a width of the rectangular waveguide as mentioned in equation 2:

$$f_c = \frac{c}{2\pi*\varepsilon_r} \sqrt{\left(\frac{m\pi}{a}\right)^2 + \left(\frac{n\pi}{b}\right)^2}, \qquad (1)$$

$$a = \frac{c}{2*f_c*\varepsilon_r}. \qquad (2)$$

DFW is filled with two rows of holes is called SIW and their representation as shown in Fig. 1 (c). The standard equation is used to find the width of the SIW is represented in equation 3:

$$a_R = a_S - \frac{d^2}{0.95s}. \qquad (3)$$

The diameter of vias (d) and spacing between vias (s) plays very important role in SIW, reduce radiation as well conductor loss. The standard conditions are revealed in equation 4. [5-7]:

$$d \leq \frac{\lambda_g}{5} \quad \text{and} \quad s \leq 2d. \qquad (4)$$

The some of the literature discussed has follows, Tomas et al. [6] introduced array based microstrip patch antenna fed by microstrip for high gain applications with 6x8 array. It has an impedance bandwidth of 1.1GHz, gain is 21.6dBi. Shrivastava et al. [7] proposed a SIW feed antipodal linear tapered slot antenna (ALTSA) for millimeter wireless applications that has a resonant frequency of 60GHz with 1.5GHz bandwidth, gain is 16.3dBi and slot loaded with different dielectric shapes for gain improvement; rectangular, triangular, and exponential are reported.

The SIW feed SIW based slot antenna is proposed by Gong and his team [8] for millimeter wireless applications. They are investigated wide width slot to satisfy the operating band of millimeter wireless applications, impedance bandwidth is 3.25GHz and gain is 6dBi. Ramesh et al. [9] introduces a SIW feed exponentially tapered slot antenna for 60GHz applications with a bandwidth of 0.8GHz and gain of 10dBi. The 1x2 array based exponentially tapered slot antenna is invented by Ramesh et al. [10] for V-band

applications and resonates at 60GHz; impedance bandwidth is 1.3GHz and gain is 11.2dBi.

Yue et al. [11] proposed a slot antenna with CPW to slot transition for polarization reconfigurability. It has 600MHz bandwidth at 2.4GHz and pin diode used to generate two polarizations those are horizontal and vertical polarization. Yui et al. [12] proposed a CPW fed slot antenna for dual polarization, one as 670MHz bandwidth at 2.4GHz and another as 840MHz bandwidth at 2.4GHz. The monopole fed with hybrid slot was presented by Guoping et al. [13] for wireless communication applications. This design has more bandwidth compared to slot, monopole and has a bandwidth of 3.8GHz.

The detail enlargement of the article is as follows. The design appraisal of an antenna, the optimal parameters is used for the design is represented in Section 2. The Section 3 give the clear outline of the generalized antenna parameters and also discuss the comparison of simulation, measurement results. Finally, the conclusion is explored in Section 4 followed by the references.

II. GEOMETRIC CONFIGURATION

The Fig. 1 represents schematic representation of the proposed antenna, length of microstrip is quarter wavelength ($\lambda/4$) and tapering wavelength can be considered any value to improve the performance [15]. The Fig. 1 (a) shows a top view of two antennas, antenna 1 has rectangular slot and indicated with symbol $1. The antenna 2 has shape of I shaped slot, indicated as $2. The width (W3) and length (L3) of the slots are represented below:

$$\lambda/4 \leq W_3 \leq \lambda/2, \qquad (5)$$
$$L_s \leq W_3. \qquad (6)$$

The rectangular slot achieves a 2.1GHz bandwidth. To improve bandwidth, two parallel rectangular slots are introduced and finally, shape is modified to I shape, indicated as $2. This structure has a bandwidth of 5.1GHz and their design parameters are described in Table 1. The Fig. 1 (b) and Fig. 1 (c) represent the bottom view and side view of an antenna. The material used in this design is Rogers substrate with dielectric value of 2.2 and thickness is 0.381mm.

Table 1: Specifications used for the design

Parameters	Dimensions (mm)	Parameters	Dimension (mm)
W1/W2/W3	0.85/2.4/1.93	L1/L	5.6/7.1
W	14	L2=L3	0.85
W5	4.755	L4/Ls	0.95/1.2
D2/D/S	1/0.3/0.6	L5/L6	0.87/2.02
Ws	2.93	W4	0.15
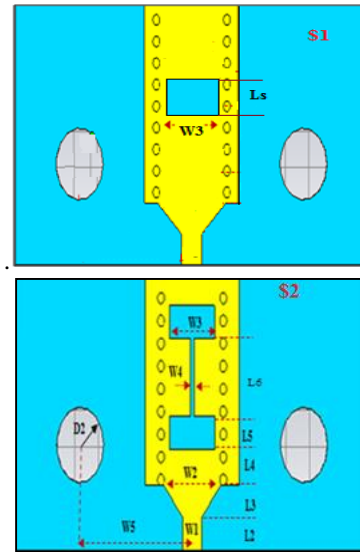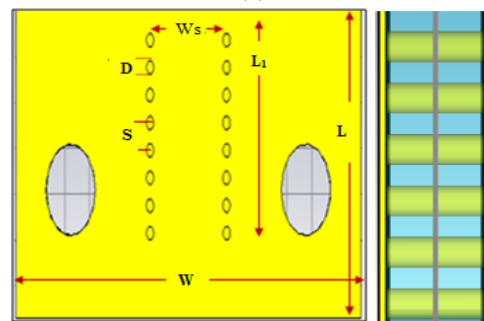
Fig. 1. Proposed antenna structure: (a) top view, (b) bottom view, and (c) side view.

The fabricated prototype of a proposed antenna is represented in Fig. 2 and 1.85mm diameter female connector model is used to measure the results. The diameter D_2 in both sides of structure was introduced to hold the connector and is separated by W_5 from the middle of the feed.
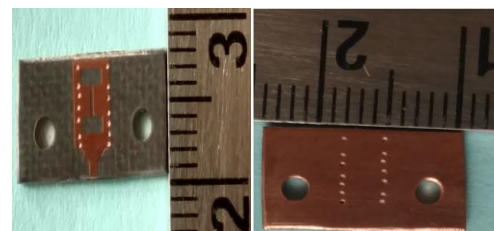
(a) Top view   (b) Bottom view

Fig. 2. Fabricated prototype: (a) top view and (b) bottom view.

III. RESULT AND DISCUSSION

The computer simulation technology studio suite software is used to design and simulate the antenna. The simulation results of this design in terms of S_{11} and VSWR is revealed in Fig. 3.

(a) Reflection coefficient
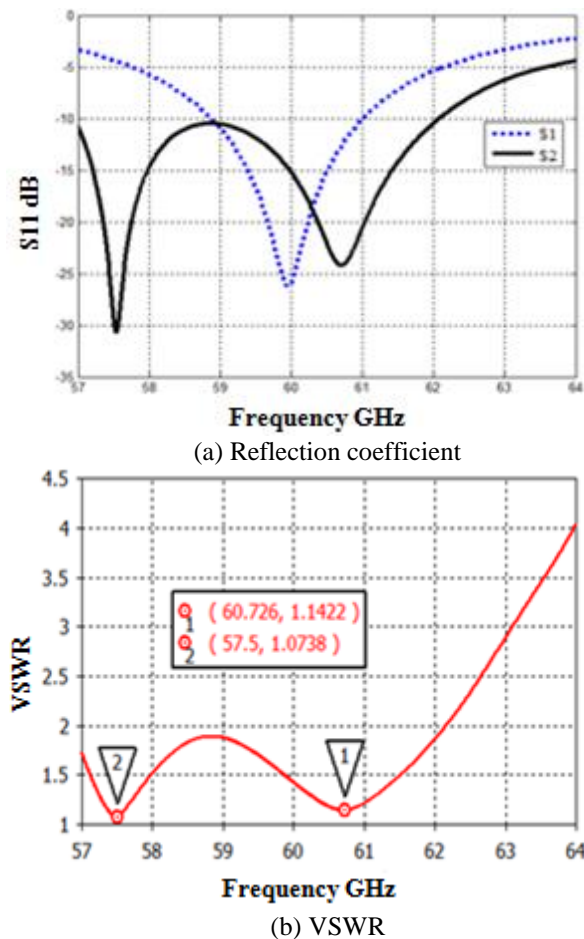
(b) VSWR

Fig. 3. Simulation results: (a) reflection coefficient and (b) VSWR.

The Fig. 3 (a) represents the reflection coefficient of two antennas, those are rectangular slot and I shaped slot. The antenna 1 ($S1$) has an impedance bandwidth of 2.1GHz with a resonant frequency of 60GHz and their S_{11} is -31dB. The proper alignment of antenna 2 ($S2$) that is I shaped slot will produce an impedance bandwidth of 5.1GHz and ranges from 57GHz to 62.1GHz. It resonates 57.493GHz, 60.7GHz frequencies respectively and their reflection coefficient values are -29.137dB, -23.604dB. The main aim is to improve the bandwidth and antenna 2 (I shaped slot) results are discussed in further. The Fig. 3 (b) describes the VSWR of a proposed antenna and it also produces 5.1GHz bandwidth with reference of the VSWR=2 line. The VSWR values are 1.0738 at 57.493GHz and 1.1422 at 60.70GHz.

A. Parameter optimization

The Fig. 4 represents the parameter optimization of a proposed design those are SIW length (L_1), slot length (L_5), and the gap between two slots (L_6). The Fig. 4 (a) represented S_{11} for SIW length (L_1) for three values 5.2mm, 5.6mm, 6mm respectively. The change of L_1 will affect the resonant frequency and moves upward to the -10dB reference line. The increasing length will decrease the bandwidth due to moving above the -10dB line. The main aim of the design is to improve the bandwidth and L_1=5.6mm is best optimized parameter compared to another two values.

The Fig. 4 (b) represents S_{11} for different values of slot length (L_5) those are 0.85mm, 0.87mm, 0.9mm and their bandwidth are 4GHz, 5.1GHz, 5GHz. Based on the bandwidth, L_5=0.87mm chosen for the design. The S_{11} for different values of L_6 (gap between two rectangular slots) is described in Fig. 4 (c) and three values are considered for analyzation of S_{11} performance and mainly bandwidth is considered for a chosen of L_6 value. The change in L_6 will affect the bandwidth and L_6=2.02mm is chosen for this design and provides the better bandwidth.

(a) L_1

(b) L_5
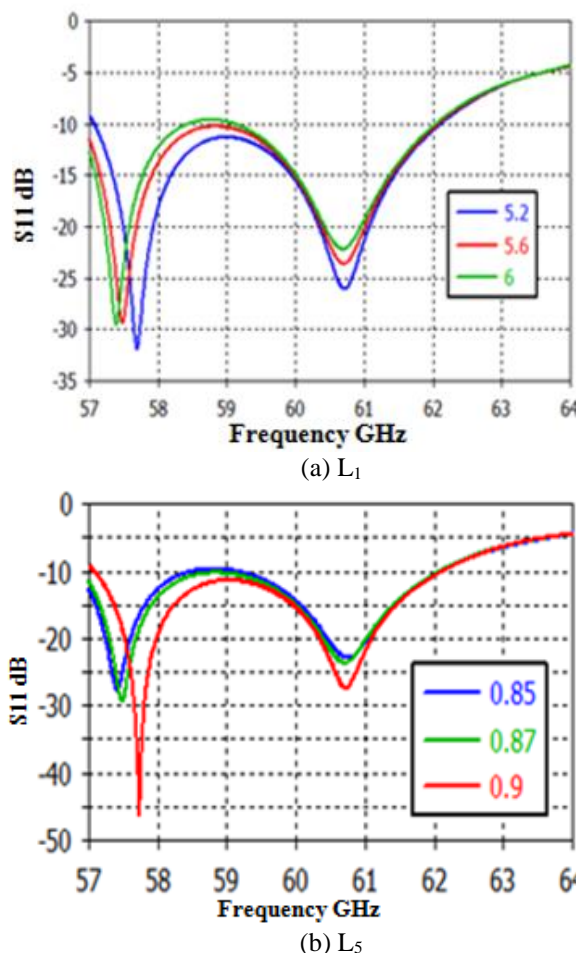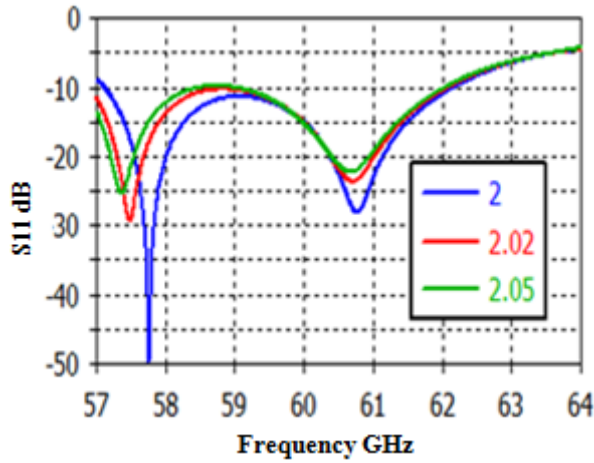
(c) L_6

Fig. 4. Frequency versus S_{11}: (a) L_1, (b) L_5, and (c) L_6.

B. Simulation versus measurement results

The comparison of simulated and measured result is represented in Fig. 5 and the Fig. 5 (a) indicate frequency versus S_{11}. The simulation and measurement bandwidth value (5.1GHz) is same but differ resonant frequency values. The Fig. 5 (b) represent VSWR result, match with reflection coefficient and clear differences of simulated, measured results are tabulated in Table 2. Where SR representes simultion results and MR representes meaasurment results.

The radiation pattern at two resonant frequencies (57.5GHz and 60.7GHz) is represented in Fig. 6. The Figs. 6 (a) and 6 (b) describes the E-field, H-field pattern and different colors are used to differentiate the results. The E-field provides bi-directional radiation patterns and H-field provides omini directional pattern. The stable radiation pattern are observed and fit to use in millimeter wireless applications.
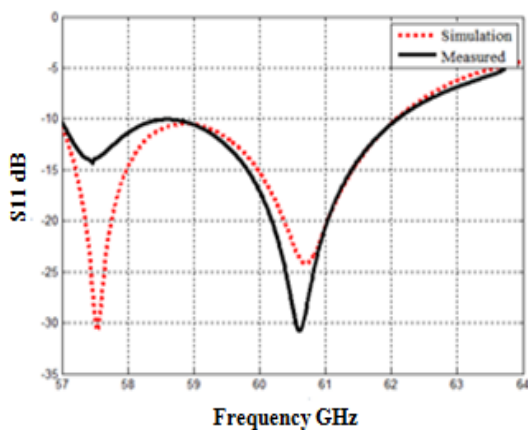
(a) Reflection coefficient
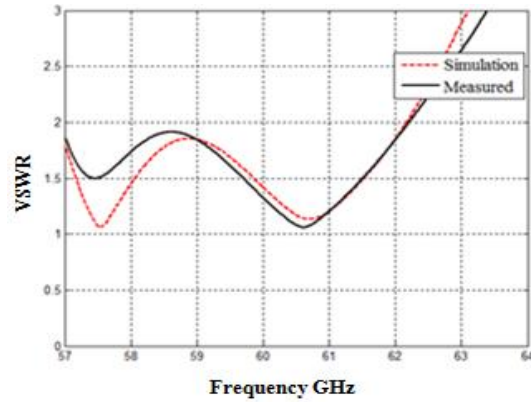
(b) VSWR

Fig. 5. The comparison of simulation and measurement results: (a) reflection coefficent and (b) VSWR.

57.5 GHz   60.7GHz

(a) E-Field

57.5 GHz   60.7GHz
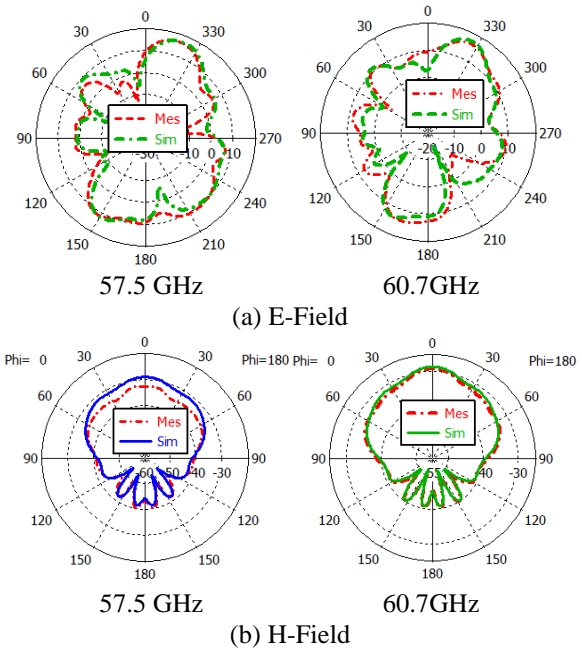
(b) H-Field

Fig. 6. Farfield patterns at resonant frequencies: (a) E-Field and (b) H-Field.

The frequency versus gain (dBi) of a proposed antenna is represented in Fig. 7 and different color lines are used to distinguish the simulation (blue) and measurement (red) results. The close match is observed between simulation, measured results and their values are 7.6dBi, 7.61dBi at 57.5GHz, 9dBi, 8.9dBi at 60GHz and 8.75dBi, 8.65dBi at 60.75GHz. The comparison of existing literature with proposed design is tabulated in the Table 3 and observed that the proposed design as improved bandwidth is around two times with existing literature, size miniaturization and average gain.
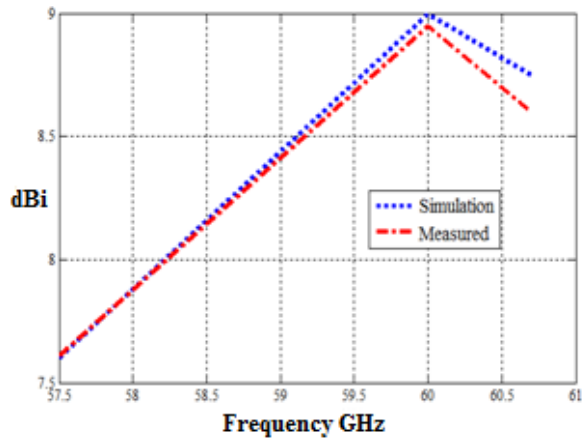
Fig. 7. Frequency vs. gain (dBi).

Figure 8 represents the E-field pattern of two antennas at 60GHz and shows the flow of fields. The efficiencies of this design has been revealed in Fig. 9 with a frequency between 57GHz to 62GHz; observed radiation efficiency is approximately 86% and 82% of transmission efficiency.
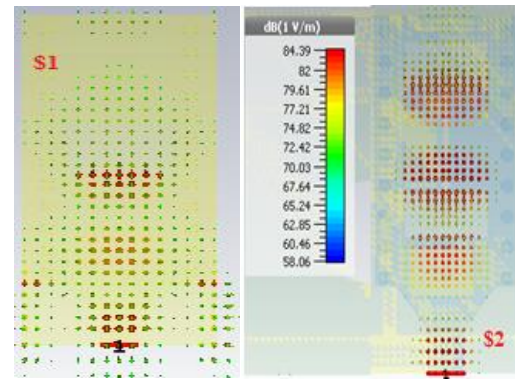
Fig. 8. E-field distribution at 60GHz.

Table 2: Comparision of simulation and measurement

S.No.	Method	Resonant Frequency (GHz)	Reflection Coefficient (dB)	VSWR
1	SR	57.493	-29.173	1.0738
	MR	57.48	-13.99	1.498
2	SR	60.70	-23.604	1.1422
	MR	60.71	-30.75	1.06

Table 3: Comparison with existing literature

S.No.	Ref.	Antenna Size [mm^3]	Substrate used in the Design	Gain (dBi)	Bandwidth (GHz)
1.	[11]	34 x 24.75 x 0.85	Rogers, ε_r =2.2	21.6	1.1
2.	[12]	44.61 x 9.93 x 0.381	Rogers, ε_r =2.2	13.7	3
3.	[13]	25 x 16 x 0.635	Rogers, ε_r =2.2	6	3
4.	[14]	33.5 x 18 x 0.787	Rogers, ε_r =2.2	10	0.8
5.	[15]	35.5 x 18 x 0.787	Rogers, ε_r =2.2	11.2	1.3
6.	Proposed	15 x 10.7 x 0.381	Rogers, ε_r =2.2	9	5.1
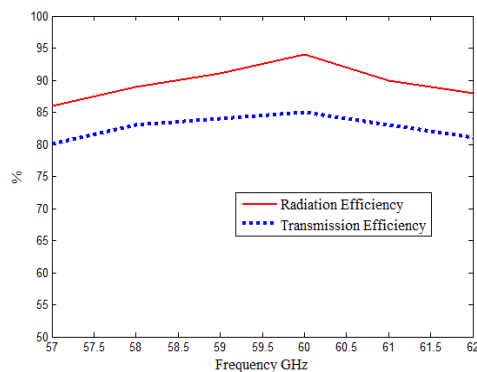
Fig. 9. Efficiencies of an proposed antenna.

IV. CONCLUSION

The I shaped SIW slot antenna has been introduced for millimeter-wave wireless applications and size is 15x10.7x0.381mm. The antenna is designed, simulated by computer simulation technology (CST) studio suite and tested generalized parameters of antenna like reflection coefficient, VSWR, radiation pattern, and gain are discussed. The measured impedance bandwidth is around 5.1GHz ranges from 57.02 to 62.09 GHz and gain at 60GHz is 8.9dBi. The antenna has good agreement between simulation and measurement results. This antenna is suitable for short-range, broadband, high data rate due to its operating frequency and used for applications like WLAN, GIFI, WPAN.

REFERENCES

[1] M. N. Kumar and T. Shanmugnantham, "Division shaped SIW slot antenna for millimeter wirelesss/ automotive radar applications," *Journal of Computer and Electrical Engineering*, vol. 71, pp. 667-675, 2018.

[2] S. K. Yong, P. Xia, and A. V. Garcia, *60 GHz Technology for Gbps WLAN and WPAN*, 1st ed., Chichester, UK: John Wiley and Sons Ltd, 2011.

[3] P. Smulders, "Exploiting the 60 GHz band for local wireless multimedia access: Prospects and future directions," *IEEE Communication. Magazine*, vol. 2, no.1, pp 140-147, 2002.

[4] Y. Li and K. M. Luk, "Low cost high gain and broadband substrate integrated waveguide fed patch antenna array for 60GHz band," *IEEE Transactions on Antennas and Propagation*, vol. 62, no. 11, pp. 5531-5538, 2014.

[5] Z. Zhang, X. Cao, J. Gao, S. Li, and J. Han, "Broadband SIW cavity-backed slot antenna for end fire applications," *IEEE Transactions on Antennas and Propagation*, vol. 17, no. 8, pp. 1271-1275, 2018.

[6] T. Mikulasek, J. Lacik, J. Puskely, and Z Raida, "Design of aperture coupled microstrip patch antenna array fed by SIW for 60 GHz band," *IET Microwave Antennas Propagation*, vol. 10, no. 3, pp. 288-292, 2016.

[7] P Shrivastava and T. R. Rao, "60 GHz radio link characteristic studies in hallway environment using antipodal linear tapered slot antenna," *IET Microwave Antennas Propagation*, vol. 9, no. 15, pp. 1793-1802, 2015.

[8] K. Gong, Z. N. Chen, X. Qing, P. Chen, and W. Hong, "Substrate integrated waveguide cavity-backed wide slot antenna for 60GHz bands," *IEEE Transactions on Antennas and Propagation*, vol. 60, no. 12, pp. 6023-6026, 2012.

[9] S. Ramesh and T. R. Rao, "Planar high gain dielectric loaded exponentially TSA for millimeter wave wireless communications," *Wireless Press Communication (Springer)*, pp. 3179-3192, June 2015.

[10] S. Ramesh and T. R. Rao, "High gain dielectric loaded exponentially tapered slot antenna array based on substrate integrated waveguide for V-band wireless communications," *International Journal of Electronics and Communications*, vol. 69, pp. 48-55, 2015.

[11] M. N. Kumar and T. Shanmugnantham, "Design of substrate integrated waveguide back to back π-shaped slot antenna for 60GHz applications," Journal: *Lecturer Notes in Electrical Engineering (Springer)*, pp. 215-224, 2018.

[12] Y. Li, Z. Zhang, W. Chen, and Z. Feng, "Polarization reconfigurable slot antenna with a novel compact CPW-to-slotline transition for WLAN application," *IEEE Antennas Wireless Propagation Letters*, vol. 9, pp. 252-255, 2010.

[13] Y. Li, Z. Zhang, W. Chen, and M. F. Iskander, "A dual-polarization slot antenna using a compact CPW feeding structure," *IEEE Antennas Wireless Propagation Letters*, vol. 9, pp. 191-194, 2010.

[14] G. Pan, Y. Li, Z. Zhang, and Z. Feng, "A compact wideband slot-loop hybrid antenna with a mono-pole feed," *IEEE Trans. Antennas Propagation*, vol. 62, no. 7, pp. 3864-3868, July 2014.

[15] M. N. Kumar and T. Shanmugnantham, "Broad-band H-spaced head shaped slot with SIW based antenna for 60GHz wireless communication applications," *Microwave and Optical Technology Letters*, John Wiley, vol. 61, pp. 1911-1916, Feb. 2019.

Nandakumar M received his B.Tech. degree in ECE from the JNTUA, Ananthapuram, M.Tech. degree in Communication Systems from JNTUA, Ananthapuram and presently working towards the Ph.D. in the Department of Electronics Engineering, School of Engineering & Technology, Pondicherry University, Pondicherry. His research interest includes microwave/millimeter wave circuits and devices, meta-materials and antennas.

T. Shanmuganatham received his B.E. degree in ECE from the University of Madras, M.E. degree in Communication Systems from Madurai Kamaraj University, and Ph.D. (Gold Medal) in the area of Antennas from the National Institute of Technology, Tiruchirappalli, India. He has 22 years of teaching experience in various reputed engineering colleges. Presently, he is working as an Associate Professor in the Department of Electronics Engineering, Pondicherry University, Pondicherry. His research interest includes antennas, microwave/millimeter-wave engineering, MEMS/NEMS. He has published more than 500 research papers in various national/international journals and conferences.

A Bowtie Slotted Quad-Band Notched UWB Antenna with Defected Ground Structure

Aisha Javed [1], Syeda I. Naqvi [1], Farzana Arshad [1], Yasar Amin [1], and Hannu Tenhunen [2,3]

[1] ACTSENA Research Group
University of Engineering and Technology (UET), Taxila, 47050, Pakistan
aishah.javed@yahoo.com, iffat.naqvi@uettaxila.edu.pk, Farzana.arshad@uettaxila.edu.pk,
Yasar.amin@uettaxila.edu.pk

[2] Department of Electronic Systems
Royal Institute of Technology (KTH), Isafjordsgatn 39, Stockholm, SE-16440, Sweden

[3] TUCS, Department of Information Technology
University of Turku, Turku-20520, Finland
hannu@kth.se

Abstract ─ A novel compact bowtie slotted circular patch antenna with quad-band notched characteristics is demonstrated in this work. The presented prototype is ascertained on FR-4 substrate. Initially, an Ultra-Wideband (3.1-10.6 GHz) antenna is achieved. Later, undesirable bands between 3.55-5.16, 5.52-5.73, 6.44-6.78 and 7.61-10.6 GHz are eliminated by incorporating slots in the patch. By proper optimization of the patch as well as ground plane, four resonant bands are achieved between 2.56-3.53, 5.22-5.5, 5.7-6.4 and 6.81-7.53 GHz supporting LTE2500, WiMAX, WLAN, and X-band applications. For good impedance matching, the antenna employs a very unique bat-shaped defected ground plane structure. The peak gain of 3.7 dB is obtained by the proposed radiator. A good agreement is observed between the measured and simulated results.

Index Terms ─ Bowtie slotted antenna, defected ground structure (DGS), notched bands, WiMAX, WLAN, X-band.

I. INTRODUCTION

In recent years, a lot of attention is acquired by UWB systems for commercial applications. For Ultra-wideband (UWB) systems, the band between 3.1-10.6 GHz is allocated by FCC (Federal communication commission) which has attracted the researchers from the academic and industrial background for current and future small range wireless applications. Recent works exhibit intensive research on UWB antennas due to features such as low cost, high data throughput, low power consumption, and small size. [1-6]. In order to design an UWB antenna, there are certain challenges which antenna designers have to deal with. As the operating range of the UWB antenna is wide so there is a possibility of interference of different frequency bands such as LTE 2500, Wi-Max at 3.5/5.5 GHz (3.3 to 3.7 GHz and 5.15-5.85 GHz), WLAN2 systems at 5.2/5.8 GHz (5.15-5.35 and 5.725-5.825 GHz), and X-band at 660 MHz/7.10-7.76 GHz [7-9]. To mitigate this problem, rather than using an extra filter, UWB antennas with inherent band notch characteristics are deployed which reduces the area, complication and cost of an UWB system.

Recent work reports several UWB antennas with one or more notch bands [10-18] by using different band notching techniques. A fork shaped antenna with a total size of $42 \times 24 \times 1.6$ mm^3 and a defective ground structure (DGS) is demonstrated for ultra-wideband applications with triple notch bands [10]. A J and U-shaped slotted antenna with an overall substrate size of $47 \times 40 \times 1.6$ mm^3 is reported with WLAN and WiMAX band notch function [11]. In [12], a dual band-notched antenna consisting of half ring-shaped resonator and a trapezoidal ground is presented. A rectangular notched-band antenna with overall dimensions of $48 \times 50 \times 1$ mm^3 with electromagnetic bandgap structures on CPW feed-line is presented [13]. A UWB antenna featuring triple notch bands using a C-shaped and U-shaped inversion slots and a modified ground plane with L-shaped slot is reported [14]. In [15], an UWB antenna with two split ring resonators (SRRs) to obtain notch filters in 5-6 GHz WiMAX/WLAN bands is demonstrated with a substrate size of 44.6×78 mm^2. A diamond-shaped SIR (stepped impedance resonator) ultra-wideband antenna with CPW-feed with dual rejected bands is reported [16]. By inserting a rectangular slot in the radiation patch and a slot in the feedline, a UWB antenna with a compact size of $33 \times 32 \times 1.5$ mm^3 is

obtained with suppression of the dual bands [17]. A $30\times40\times1.6$ mm³ circular UWB antenna with WLAN band rejection characteristic is proposed by engraving rectangular split ring resonators (RSRRs) structure in the radiator [18].

In this work, a miniaturized microstrip-fed circular notched band antenna is presented and realized. The quad notched bands are obtained by incorporating bowtie and U-shaped slots in the circular patch. A bat shaped defected ground and a rectangular structure at the bottom layer of the substrate also contributes in obtaining the notch bands. By modifying and optimizing the size and the positions of the slots, the band-notched characteristics of the antenna can be achieved to reject the complete operating bands of the 3.55-5.16, 5.52-5.73, 6.44-6.78 and 7.61-10.6 GHz. The proposed antenna thus rejects the WLAN, WiMAX, X-band and 8 GHz ITU bands.

II. ANTENNA STRUCTURE

Figures 1 (a) and (b) show the layout of the proposed antenna. CST®MWS® is used for design and simulation purposes. A circular radiating patch of radius, a=11 mm fed by 50 Ω microstrip feeding line is proposed. The circular radiating structure consists of optimized bowtie and inverted U-shaped slot. A bat like defected structure is incorporated at the ground plane. The antenna also employs a rectangular optimized structure above the bat-shaped ground plane, whose placement and size is adjusted. The following equations are used to design the antenna [19]:

$$a = \frac{F}{\left\{1+\frac{2h}{\pi \varepsilon_r F}\left[\ln\left(\frac{\pi F}{2h}\right)+1.7726\right]\right\}^{1/2}}, \qquad (1)$$

$$F = \frac{8.791\times10^9}{f_r\sqrt{\varepsilon_r}}, \qquad (2)$$

$$a = a\left\{1+\frac{2h}{\pi a \varepsilon_r}\left[ln\left(\frac{\pi a}{2h}\right)+1.7726\right]\right\}^{1/2}, \qquad (3)$$

$$(f_{re})_{110} = \frac{1.8412 V_o}{2\pi a_e\sqrt{\varepsilon_r}}. \qquad (4)$$

(a)

(b)
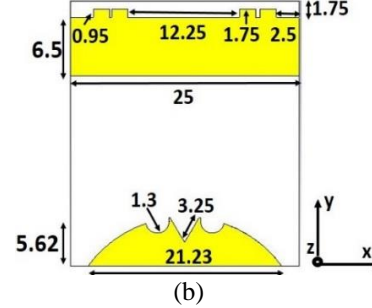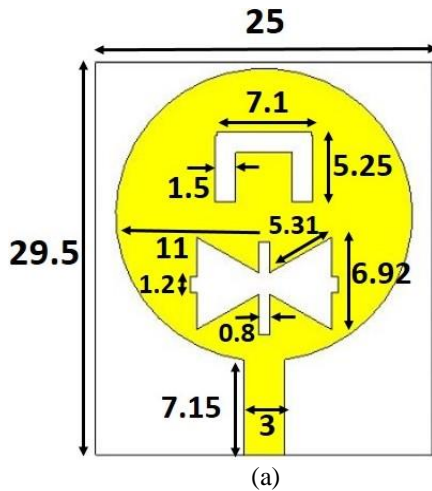
Fig. 1. (a) Top and (b) bottom (all dimensions are in mm).

In the above equations, the radius of the radiating patch is represented by a, height of the substrate by h, the relative permittivity of the substrate by ɛr whereas the resonant frequency is denoted by f_r. The proposed design with overall dimensions of 29.5×25 mm² is realized on 1.59 mm thick FR4 substrate with ɛr=4.3 and tan δ=0.025.

III. DESIGN CONFIGURATION AND WORKING MECHANISM

Figure 2 (a) shows the step by step progression of the proposed prototype. Figure 2 (b) illustrates the S_{11} for all the stages of the design to understand the working mechanism of the proposed antenna.

First of all, antenna 1 is designed which is a simple circular patch above the substrate. The initial structure of the antenna is designed to achieve the UWB (3.1-10.6 GHz) as demonstrated in Fig. 2 (b). The ground located at the substrate's bottom-layer is modified to a bat like structure to attain UWB and to enhance wideband impedance matching. Afterwards, the required notch bands are achieved by further optimization. Antenna 2 is obtained by inclusion of a bowtie-shaped slot in the circular patch to obtain notch band at X-band. The notch band achieved at this step is depicted in Fig. 2 (b). The dimensions and placement of the bowtie slots are optimized to get the desired results along with sustaining good impedance matching. In the next step, a U-shaped slot is subtracted from the patch, thus obtaining antenna 3. The incorporation of U-shaped slot in addition to previously obtained antenna 2 provides two notches at WLAN and WiMAX bands. Shifting of notch bands is observed at the inclusion of slots due to mutual coupling between existing and newly incorporated slots. Finally, the proposed antenna is achieved by adding a rectangular structure above the defected bat-shaped ground structure. The structure is modified to obtain the desired notch bands thus stopping the X band and 8 GHz ITU band. It is clear that proposed antenna has quad notch bands ranging from 3.5-5.2 GHz, 5.5-5.7 GHz, 6.45-6.7 GHz, and 7.6-11 GHz, thus filtering out potential interference from WiMAX, WLAN, X band and 8GHz ITU bands.

(a)

(b)
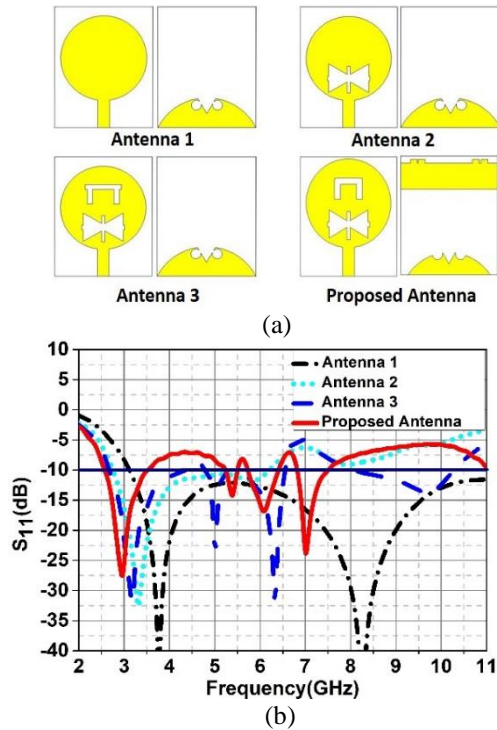
Fig. 2. (a) Stepwise progression of the proposed antenna, and (b) S-plot (S_{11}).

In order to demonstrate the working technique of proposed antenna, the surface current density at four notch frequencies, i.e., 4.3, 5.6, 6.5 and 9.1 is shown in Figs. 3 (a)-(d). It is clearly evident in Fig. 3 (a) that current density is around the U-shaped slot at 4.3 GHz. Figure 3 (b) illustrates the major current distribution around the rectangular structure for 5.6 GHz. Current is mainly centered at the bowtie slot and ground structure for 6.6 GHz frequency as shown in Fig. 3 (c). Figure 3 (d) depicts that at 9.1 GHz notch frequency, the concentration of current is at the rectangular structure, ground plane and around the edges of the bowtie slot.

(a)   (b)

(c)   (d)
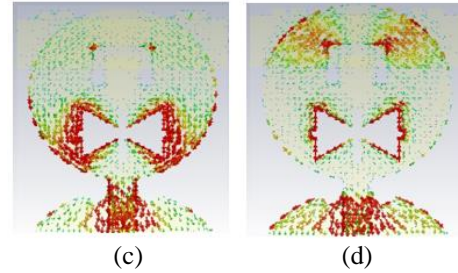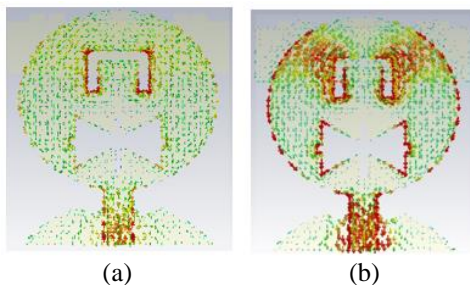
Fig. 3. Current distribution at: (a) 4.3 GHz, (b) 5.6 GHz, (c) 6.6GHz, and (d) 9.1 GHz.

IV. RESULTS AND DISCUSSION

According to the optimized parameters of the prototype the proposed antenna is fabricated and measured to validate the performance. Figure 4 illustrates the top and bottom view of the prototype. Measured results are obtained by the Agilent (Key sight) Technologies PNA-E8362 Vector Network Analyzer.

A. S-parameters

The S_{11} plots for measured and simulated results of the presented antennae are shown in Fig. 5. A suitable consistency is perceived between measured and simulated results; nevertheless, dissimilarities also exist because of the unpreventable usage of SMA-connector and coaxial-cable for measurement purposes [20]. Substrate losses and fabrication imperfections also contribute to the dissimilarities.

B. Antenna far-field results

The proposed bowtie slotted antenna's E (yz) and H (xz) plane radiation patterns are depicted Figs. 6 (a)-(d). The gain, current-densities, and the S_{11} are well explaining the band-rejection features. The radiation patterns are presented only for substantiation of the UWB characteristics at 2.9, 5.37, 6.09 and 7.02 GHz. The radiation pattern in E plane is bidirectional while in H-plane omnidirectional pattern is obtained. It can be seen that the cross-polarization level is less than -20 dB over the E-plane of the four frequency bands and for the H-plane the cross-polarization level is less than -20 dB for the lower frequency bands i.e. 2.94 GHz and 5.37 GHz but for the upper frequency bands i.e. 6.09 GHz and 7.02 GHz, the cross polarization level is between -20 dB and -10 dB. Thus, it is apparent from the radiation patterns of the proposed design, a stable behavior is obtained for the resonating frequencies.

(a)   (b)
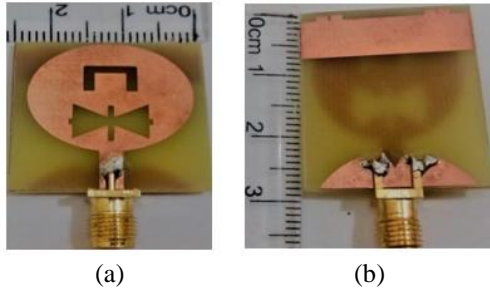
Fig. 4. Fabricated prototype: (a) top and (b) bottom
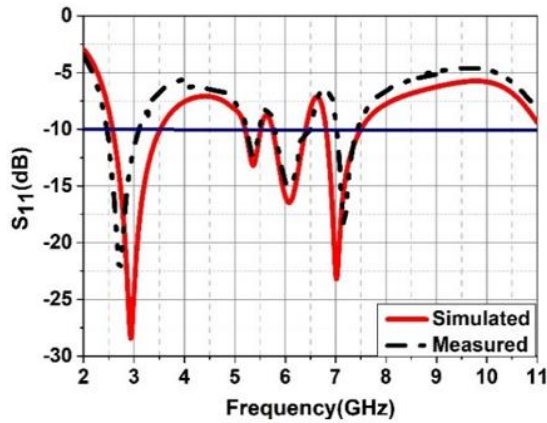
Fig. 5. Simulated and measured S_{11}

C. Antenna gain

The gain of the proposed notched band UWB antenna is illustrated in Fig. 7. It provides clear evidence that the peak gain of 3.7 dB is obtained for the resonant bands. Therefore, the proposed bowtie slotted antenna can deliver a reasonable gain over the entire range of ultra-wideband except at the notched bands.

V. SUBSTRATE ANALYSIS

The proposed antenna's performance is analyzed by changing the substrate's material. The analysis is depicted in terms of S_{11} plots in Fig. 8. The substrates used for the analysis purpose are Rogers RT Duriod 5880, Rogers RT6010 and FR-4. The thickness of all the substrates is kept same that is 1.6 mm. The detail of the substrate analysis in term of permittivity, no. of achieved notch bands and maximum gain achieved has been presented in Table 1. After the complete analysis of the outcomes, it can be seen that the working of the proposed antenna on FR-4 substrate is much reasonable as compared to the other substrates with a peak gain of 3.7 dB and quad notch bands. Rogers 5880 with permittivity

of 2.2 has achieved 2 notch bands. Whereas for Rogers RT6010, the number of notch bands is 3.
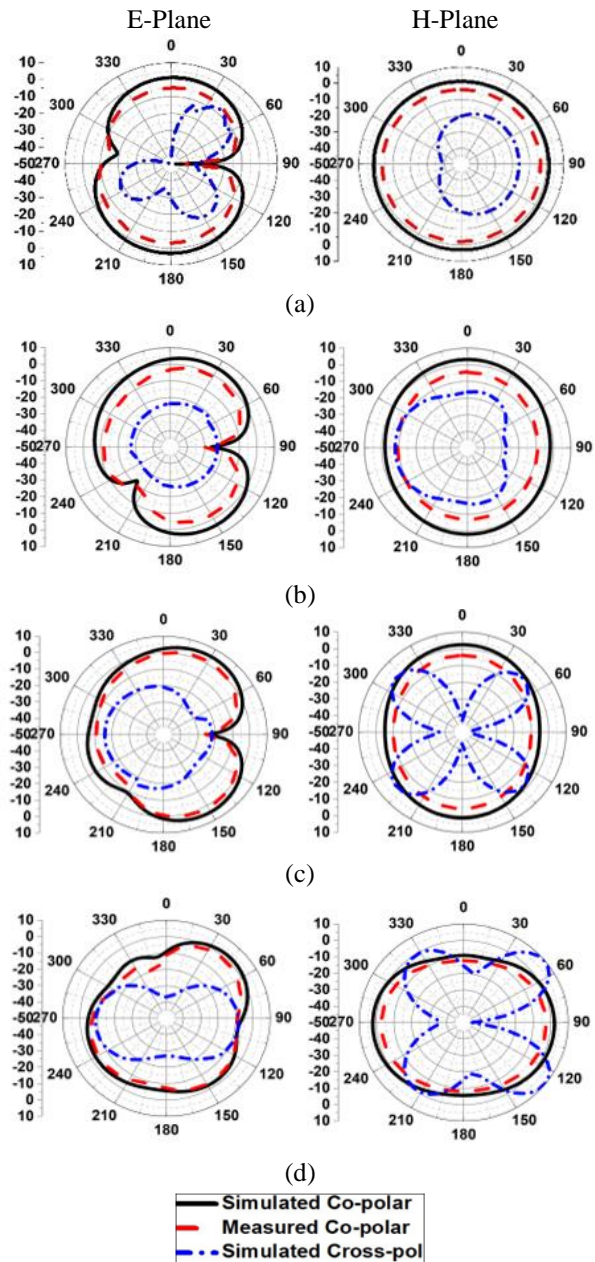
Fig. 6. Measured and simulated radiation patterns at: (a) 2.94, (b) 5.37, (c) 6.09, and (d) 7.02.

Table 2 provides the comparison with the related work. It is evident that the presented work exhibits better performance in terms of compactness, notch bands achieved, and gain.
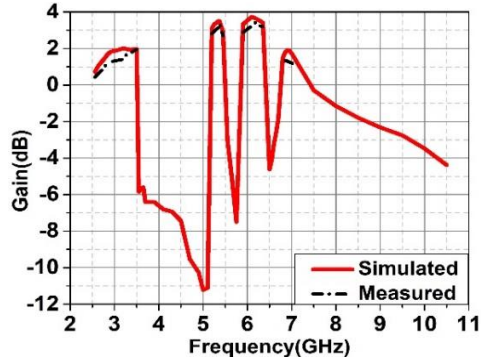
Fig. 7. Simulated and measured gain.
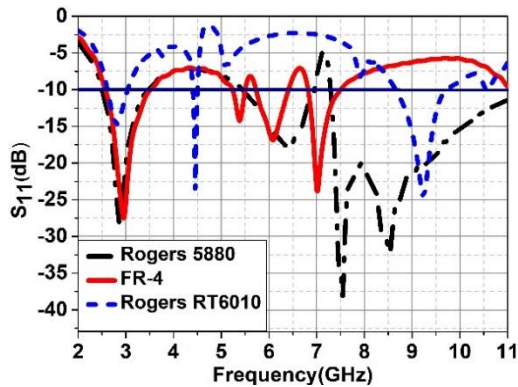
Fig. 8. Substrate analysis of the proposed antenna.

Table 1: Parameters of substrates

Substrate	Permittivity	Notch Bands	Peak Gain (dB)
Rogers 5880	2.2	2	3.505
FR4	4.3	4	3.7
Rogers RT6010	10.2	3	3.37

Table 2: Comparison with related work

References	Size (mm)	Notch Bands	Peak Gain (dB)
[8]	24×42	3	3.6
[12]	25×30.2	3	4
[16]	30*40	1	2
[19]	30*35	2	3.2
Proposed	25*29.5	4	3.7

VI. CONCLUSION

This work presents the design of a compact bowtie slotted circular patch antenna with the quad band-notched characteristics. Good impedance matching of the antenna is accomplished by using a very unique bat-shaped defected ground structure. The undesirable bands between 3.55-5.16, 5.52-5.73, 6.44-6.78 and 7.61-10.6 GHz have been eliminated by incorporating slots in the patch. Thus WiMAX, WLAN and X-band are rejected. A peak gain of 3.7 dB is attained. A reasonable agreement is achieved between simulated and measured results.

ACKNOWLEDGMENT

REFERENCES

[1] A. P. Singh, R. Khanna, H. J. M. Singh, and O. T. Letters, "UWB antenna with dual notched band for WiMAX and WLAN applications," *Microwave and Optical Technology Letters*, vol. 59, no. 4, pp. 792-797, 2017.

[2] Y. Kong, Y. Li, W. Yu, and K. J. A. C. E. S. J. Yu, "A quadruple band-notched UWB antenna by using arc-shaped slot and rotated E-shaped resonator," *Applied Computational Electromagnetics Society Journal*, vol. 31, no. 11, 2016.

[3] J. R. Panda and R. S. Kshetrimayum, "A 3.4/5.5GHZ dual-band notched UWB printed monopole antenna with two open-circuited stubs in the microstrip feedline," *Microwave and Optical Technology Letters (Wiley)*, vol. 53, no. 12, pp. 2973-2978, Dec. 2011.

[4] W. Ding and G. J. M. Wang, "Miniaturized band-notched ultra-wideband antenna," *Microwave and Optical Technology Letters*, vol. 58, no. 11, pp. 2780-2786, 2016.

[5] S. Doddipalli and A. Kothari, "Compact UWB antenna with integrated triple notch bands for WBAN applications," *IEEE Access*, 2018.

[6] N. Gad and M. Vidmar, "Design of a microstrip-fed printed-slot antenna using defected ground structures for multiband applications," *Applied Computational Electromagnetics Society Journal*, vol. 33, pp. 854-860, 2018.

[7] P. S. Bakariya, S. Dwari, and M. Sarkar, "Triple band notch UWB printed monopole antenna with enhanced bandwidth," *AEU-International Journal of Electronics and Communications*, vol. 69, no. 1, pp. 26-30, 2015.

[8] T. Arshed and F. A. Tahir, "A miniaturized triple band-notched UWB antenna," *Microwave and Optical Technology Letters*, vol. 59, no. 10, pp. 2581-2586, 2017.

[9] H. S. Singh and S. Kalraiya, "Design and analysis of a compact WiMAX and WLAN band notched planar monopole antenna for UWB and Bluetooth applications," *International Journal of RF and Microwave Computer-Aided Engineering*, pp. e21432, 2018.

[10] M. Elhabchi, M. N. Srifi, and R. Touahni, "A tri-

band-notched UWB planar monopole antenna using DGS and semi arc-shaped slot for WIMAX/WLAN/X-band rejection," *Progress In Electromagnetics Research*, vol. 70, pp. 7-14, 2017.

[11] R. A. Abdulhasan, R. Alias, A. Awaleh, and A. Mumin, "Design of circular patch microstrip ultra-wideband antenna with two notch filters," in *Computer, Communications, and Control Technology (I4CT)*, International Conference, pp. 464-467 2015.

[12] L. Peng, B. J. Wen, X. F. Li, X. Jiang, and S. M. Li, "CPW fed UWB antenna by EBGs with wide rectangular notched-band," *IEEE Access*, vol. 4, pp. 9545-9552, 2016.

[13] A. Syed and R. W. Aldhaheri, "A new inset-fed UWB printed antenna with triple 3.5/5.5/7.5-GHz band-notched characteristics," *Journal of Electrical Engineering & Computer Sciences*, vol. 26, no. 3, pp. 1190-1201, 2018.

[14] X. Chen, F. Xu, and X. Tan, "Design of a compact UWB antenna with triple notched bands using non-uniform width slots," *Journal of Sensors*, 2017.

[15] L. C. Tsai and W. J. Chen, "A UWB antenna with band-notched filters using slot-type split ring resonators," *Microwave and Optical Technology Letters*, vol. 58, no. 11, pp. 2595-2598, 2016.

[16] M. Sefidi, Y. Zehforoosh, and S. Moradi, "A novel CPW-fed antenna with dual band-notched characteristics for UWB applications," *Microwave and Optical Technology Letters*, vol. 57, no. 10, pp. 2391-2394, 2015.

[17] A. Sohail, K. S. Alimgeer, A. Iftikhar, B. Ijaz, K. W. Kim, and W. Mohyuddin, "Dual notch band UWB antenna with improved notch characteristics," *Microwave and Optical Technology Letters*, vol. 60, no. 4, pp. 925-930, 2018.

[18] G. Mishra and S. Sahu, "Compact circular patch UWB antenna with WLAN band notch characteristics," *Microwave and Optical Technology Letters*, vol. 58, no. 5, pp. 1068-1073, 2016.

[19] C. A. Balanis, *Antenna Theory Analysis and Design*, 3rd ed, Hoboken NJ (USA): John Wiley & Sons, 2005. ISBN: 0-471-66782-X.

[20] L. Liu, S. W. Cheung, Y. F. Weng, and T. I. Yuk, "Cable effects on measuring small planar UWB monopole antennas," *Ultra-Wideband - Current Status and Future Trends*, available from: http://dx.doi.org/10.5772/46080, 2012.

Aisha Javed received her Bachelor's degree in Telecommunication Engineering from UET, Taxila in 2017. Currently, she is enrolled as a part time M.S. Scholar at the University of Engineering and Technology (UET), Taxila, Pakistan. Her research interests include band notched and ultra-wideband antenna systems.

Syeda Iffat Naqvi is a part time Ph.D. Scholar in the UET Taxila, Pakistan. She is also a member of ACTSENA research group. Her current research interests include low profile flexible multiband antenna design. She is a member of IEEE and ACES.

Farzana Arshad is working towards her Ph.D. degree in Telecommunication Engineering from UET Taxila. She is also a member of ACTSENA research group. Her current research interests include low profile Multi-band and reconfigurable antenna design.

Yasar Amin is a Chairman and Associate Professor of Telecom. Engineering Dept., UET Taxila, Pakistan. He is Founder of ACTSENA Research Group at UET Taxila, Pakistan. He is a member of IEEE, IET, ACM and ACES.

Hannu Tenhunen is a Chair Professor of Electronic Systems at the Royal Institute of Technology (KTH), Stockholm, Sweden. He has held Professor position as Full Professor, Invited Professor or Visiting Honorary Professor in Finland (TUT, UTU), Sweden (KTH), USA (Cornel U), France (INPG), China (Fudan and Beijing Jiatong Universities), and Hong Kong.

A Compact Dual-band MIMO Antenna for 5G Mobile Communications

Jianxun Su, Zhengyu Dai, Jianhe Du *, Jiayong Yu, Zeqiang Chen, and Zengrui Li *

School of Information and Engineering
Communication University of China, Beijing, 100024, China
sujianxun_jlgx@163.com, zrli@cuc.edu.cn*, dujianhe1@gmail.com*

Abstract ─ In this paper we propose a compact dual-band MIMO antenna for 5G mobile communications. Its element is a dual-band monopole working at 3.4 GHz and 4.9 GHz. In order to cover the commercial 5G communication band of sub-6 GHz (3.3-3.6 GHz and 4.8-5.0 GHz), an inverted L-shaped strip is added on the ground of the monopole to achieve a band-notch of S_{11} at 3.4 GHz and a quasi-directional radiation pattern. The proposed MIMO antenna has a compact size of $50*50*0.8\text{mm}^3$ and it's composed of four improved monopoles mentioned above with mutually orthogonal placement. Long strips are loaded on the ground layer and antenna layer to obtain a better port isolation at 3.3-3.6 GHz. The measured results show that the reflection coefficient (S_{ii}) of the MIMO antenna is less than -10 dB at the lower band and less than -20dB at the higher band. Its -10dB-bandwidth covers the band of 3.3-5.8 GHz and the mutual coupling (S_{ij}) between ports keeps lower than -20dB within the dual-band. The envelope correlation coefficients (ECC) of the MIMO antenna are also measured and they're below 0.01. A channel model is used to calculate the MIMO channel capacity and the results show this MIMO channel performs best at 5 GHz.

Index Terms ─ Channel capacity, dual-band monopole antenna, envelope correlation coefficient (ECC), fifth generation (5G) communication, multiple-input-multiple-output (MIMO) antenna, mutual coupling.

I. INTRODUCTION

In the past decades, wireless communication technology has got rapid and unprecedented development. At the same time a lot of problems emerged as there were growing appetites for safer and faster data transmission. In addition, with the development and standards' building of the fifth-generation (5G) mobile communication, more and more researches have been carried into related technologies with the hope of higher transmission rate, lower cost and higher gain. Multiple-input-multiple-output (MIMO) technology is the key to realize a higher transmission rate.

By using MIMO technology, we can establish multiple independent channels on the original spectrum by diversity method and reduce multipath fading, so as to improve data transmission rate [1].

MIMO antenna is the significant facility to improve channel capacity of MIMO system. For traditional single-port antenna, the reflection coefficient (S_{ii}) is used to describe reflection loss of input; while for MIMO antenna, the mutual coupling (S_{ij}) is also important to indicate the energy from port-j to port-i. Strong mutual coupling will worsen the receiving/sending performance of MIMO antenna.

In order to suppress the mutual coupling, a lot of attempts have been tried to improve the isolation between ports in MIMO antenna [2-10]. Such as the defected ground structures (DGS) proposed in [3-4], decoupling network structures presented in [5-6] and electromagnetic band-gap (EBG) structures shown in [7-10]. Researches in [11-12] presented the applications of polarization diversity technology in MIMO communication system and its improvement of channel capacity in detail. By the way, many kinds of 5G MIMO antennas have been put forward in recent years [13-17].

In this paper, a compact dual-band 4-port MIMO antenna works within 3.3-3.6 GHz and 4.8-5.0 GHz (sub-6 GHz) is proposed. The MIMO antenna has a good performance and its measured results agree well with simulated results. In designs of many MIMO antennas, it's common to avoid placing elements in parallel and choose to place them vertically, which can avoid strong mutual couplings caused by the same polarization mode. However, in this paper the antenna elements are perpendicular to each other and parallel to each other. In addition, the MIMO antenna achieves not only low mutual couplings but also compact size.

The paper is organized as follows: the design of the antenna element and the final MIMO antenna are introduced in Section II. Section III discusses the measured and calculated results of the S-parameters, radiation patterns and channel capacity etc. Section IV gives a conclusion of this paper.

II. THE DUAL-BAND MIMO ANTENNA

A. Antenna element configuration

The MIMO antenna's element is an improved monopole and its structure is shown in Fig. 1 with the small size of 25*25*0.8mm³. The upper layer is a circular monopole fed by microstrip line and they are printed on a FR4 substrate (permittivity=4.4±0.1 and loss tangent=0.02±0.001) [18]. Inspired from the isolation enhancement ability of the L-shaped strip used in [19-20], we use the L-shaped strip to acquire a dual-band monopole and configure the proposed 4-port MIMO antenna. The inverted L-shaped strip extending from the ground and the detailed dimensions of the improved monopole are shown in Fig. 1 and Table 1. The L-shaped strip works as a radiator at 3.4 GHz and a reflector at 4.9 GHz.
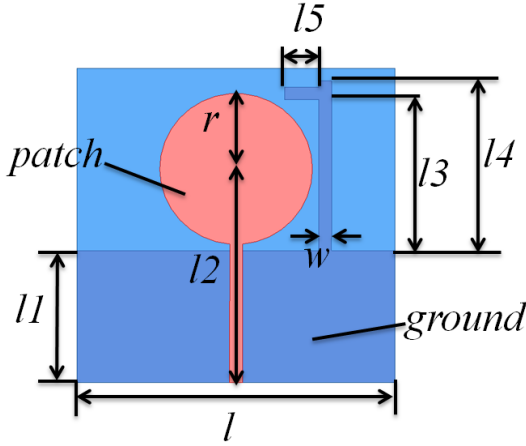
Fig. 1. Geometry of the improved monopole.

Table 1: Dimensions of the improved monopole

l	l1	l2	l3
25mm	10.5mm	17mm	12mm
l4	l5	r	w
13.5mm	2.7mm	6mm	1mm

The 3D radiation patterns and the S-parameters of the monopole with/without inverted L-shaped strip are shown in Fig. 2 and Fig. 3. The monopole without inverted L-shaped strip works at 5.45 GHz, and its radiation pattern is symmetrical. However, after adopting the inverted L-shaped strip on ground, S_{11} can achieve a band-notch at 3.4 GHz and its original resonance point of 5.45 GHz moves to 4.9 GHz. It's worth noting that the direction of maximum radiation steers to left side, which is important for the configuration of MIMO antenna in the next.
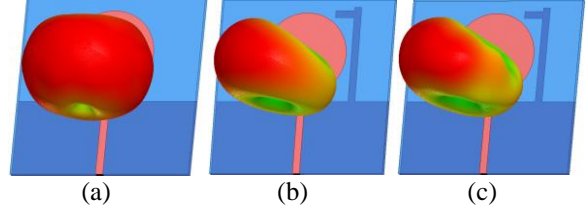
Fig. 2. 3D radiation patterns of the monopole: (a) without inverted L-shaped strip at 5.45 GHz, (b) with inverted L-shaped strip at 3.4 GHz, and (c) 4.9 GHz.
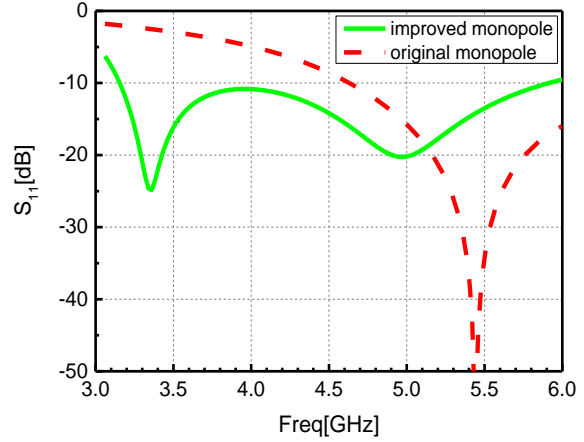
Fig. 3. S_{11} of improved monopole and original monopole.

In order to have a better illumination about the working mechanism of improved monopole, its simulated current distributions at 3.4 GHz and 4.9 GHz are shown in Fig. 4 respectively: when the antenna works at 4.9 GHz, the current is mainly distributed near the circular patch and the L-shaped strip acts as a reflector, which makes the maximum radiation direction shift to the left side; while at 3.4 GHz, the current can be coupled to the L-shaped strip from right side of the circular patch, which makes it act as a 0.4λ length radiator. And the L-shaped strip itself shows a left steering radiation pattern at 3.4 GHz due to the bending at the top.
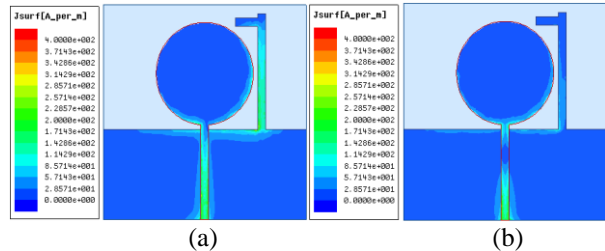
Fig. 4. Current distributions of the improved monopole antenna at: (a) 3.4 GHz and (b) 4.9 GHz.

B. Four-port MIMO antenna

Four improved monopoles mentioned above were placed in two orthogonal directions to form a four-port MIMO antenna with a size of 50*50*0.8mm^3. Its structure is shown in Fig. 5 (a). Figure 6 (a) shows the S-parameters of the antenna in Fig. 5 (a). It can be observed that isolations between ports (S_{21} & S_{41}) are close to 11 dB within 3.3-3.6 GHz. That's because the main radiation elements at 3.4 GHz are the L-shaped strips but they are spread too tightly on the ground, which results strong mutual couplings. In addition, within 4.8-5.0 GHz, mutual couplings are less than -20 dB.

(a)

(b)
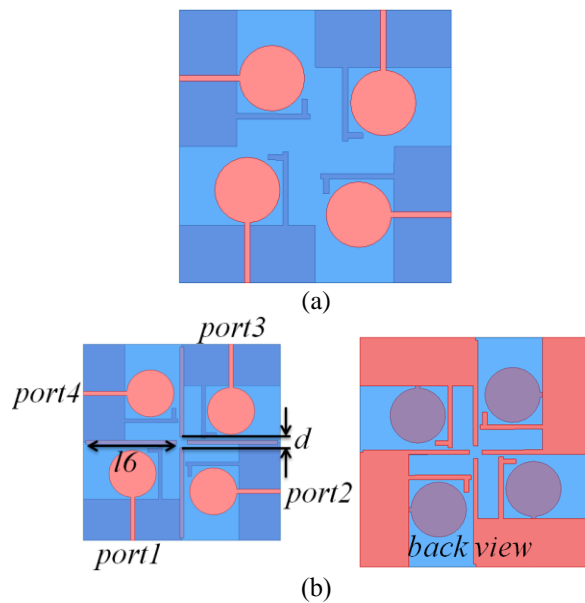
Fig. 5. Four-port MIMO antenna: (a) without long strips, and (b) with long strips ($l6$=23, d=2.7. unit: mm).

To reduce the mutual couplings within 3.3-3.6 GHz, we employ eight long strips with a length of 23mm (about 0.55λ at 3.5 GHz). As shown in Fig. 5 (b), four strips are loaded on antenna layer and another four are placed at the same place but on the ground layer. The L-shaped strips are located at the maximum radiation direction of adjacent elements, thus generating coupling energy to adjacent ports. Those long strips can work as a parasitic resonator to add the coupling path between elements and then reduce the mutual couplings. Figure 6 (b) shows the S-parameters of MIMO antenna shown in Fig. 5 (b). It can be inferred that the S_{21} & S_{41} are successfully reduced to -15 dB within 3.3-3.6 GHz, and its S_{11} is nearly unaffected.

(a)

(b)
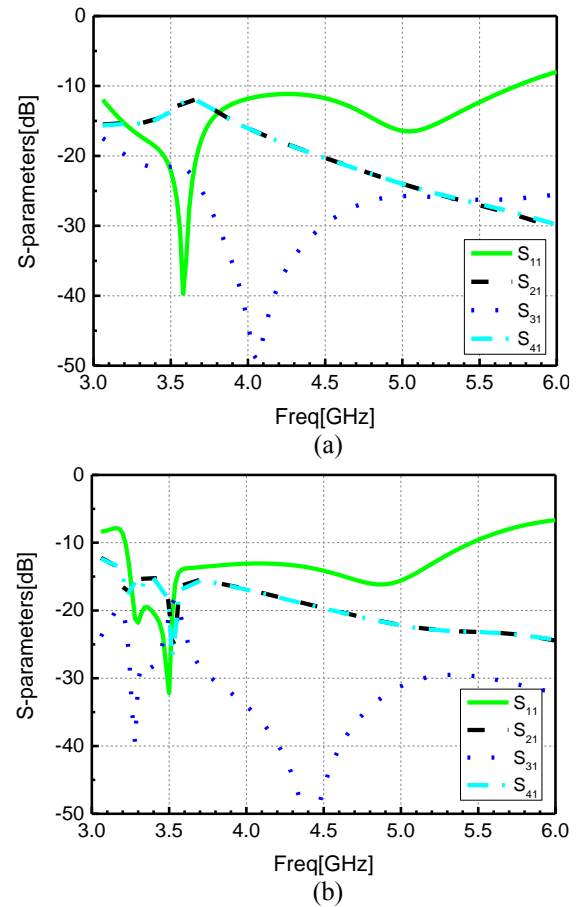
Fig. 6. Simulated S-parameters of MIMO antenna shown in Fig. 5: (a) without long strips, and (b) with long strips.

Figure 7 presents the simulated current distributions of the MIMO antenna without/with the long strips at 3.5 GHz and 4.9 GHz respectively, in which Port 1 is excited and other ports are terminated with a 50-Ω load. When the MIMO antenna without the long strips works at 3.4 GHz, there is strong current distributed near the L-shaped strips of port 2 and port 4, which leads to the high S_{21} and S_{41}, as shown in the simulated results of Fig. 6 (a). However, after loading these long strips on MIMO antenna the coupling current mostly distribute alone the strips, which can dramatically avoid the energy coupled from port1 to port2 & port4 directly and make S_{21} and S_{41} reduced consequently at 3.3-3.6 GHz. By the way, the mutual couplings between antenna elements are still less than -20 dB when the MIMO antenna works at 4.9 GHz.

(a) 3.4 GHz   (b) 3.4 GHz

(c) 4.9 GHz   (d) 4.9 GHz
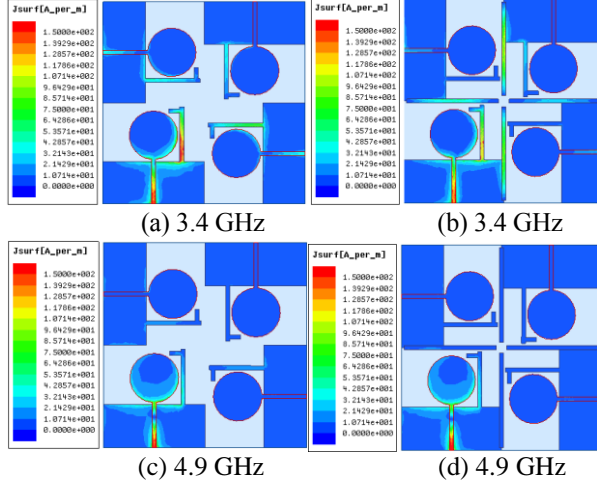
Fig. 7. Current distributions of the MIMO antenna without/with long strips at: (a)-(b) 3.4 GHz, and (c)-(d) 4.9 GHz.

III. RESULTS AND DISCUSSION

A. Experiment verification

In order to verify the simulated results mentioned above, the MIMO antenna was fabricated and measured. A vector network analyzer (Agilent PNA-L N5234A) was used to measure the antenna in our research. The fabricated MIMO antenna and the measured results of S-parameters are given in Fig. 8. As we know, the permittivity of FR4 varies a lot in practical application of microwave. Inferred from the analysis and measurement of [18], the measured resonance points of antenna based on FR4 are very close to the theoretical values within 2-8 GHz, but it varies a lot at higher frequencies like 10 GHz. So, in our measured results of 3-6 GHz, the change of FR4's properties have little impact.
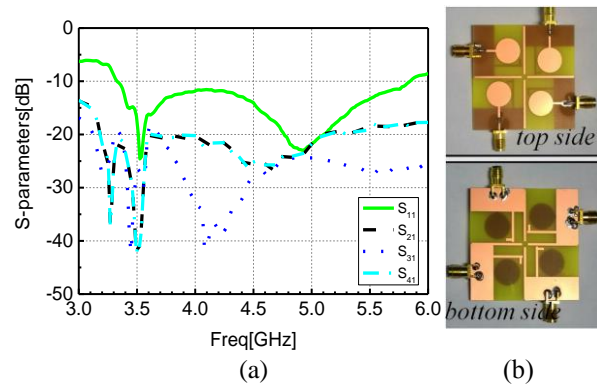
Fig. 8. (a) Measured S-parameters of MIMO antenna, and (b) fabricated antenna's top side and bottom side.

In Fig. 8 (a), the MIMO antenna can cover the dual-band of sub-6 GHz: it provides a quite good impedance bandwidth ($S_{11} < $ -10 dB within 3.3-3.6 GHz and $S_{11} < $ -20 dB within 4.8-5.0 GHz), and its -10 dB-bandwidth can even cover 3.3-5.8 GHz. However, in the simulation we don't consider the connection of transmission line and welding of SMA connector, which may explain why the measured results of S_{11} are higher than simulation results at 3.3-3.6 GHz. Meanwhile, the mutual couplings between the ports keep low enough: the $S_{ij} < $ -20 dB within the dual-band, that's because the measured results of S_{11} are higher than simulated results (more energy are reflected, and less energy are coupled to other ports). Others measured results agree well with the simulated results in Fig. 6 (b).

Compared with the 5G MIMO antennas proposed in recent years [13-17] and some traditional 4-port MIMO antennas [21-23], our antenna has a better performance in impedance match (S_{ii}) and ports isolation (S_{ij}), and its size keeps at a satisfactory level, as shown in Table 2 and Table 3.

Table 2: Performance comparison with previously reported 5G MIMO antennas

Ref.	Number of Elements	S_{ij} (dB)	S_{ii} (dB)	Size (mm²)
[13]	4	< -12	< -6	130*74
[14]	8	< -10	< -13	145*75
[15]	8	< -15	< -10	130*100
[16]	4	< -12	< -6	120*50
[17]	8	< -20	< -10	150*75
This work	4	< -20	< -10	50*50

Table 3: Performance comparison with traditional 4-port MIMO antennas

Ref.	Bandwidth (GHz)	S_{ij} (dB)	Size (mm²)
[21]	0.68-0.72&1.75-2.45	< -12	150*250
[22]	7.25-10.25	< -19	45*45
[23]	1.45-2.25&3.71-4.71	< -23	263*263
This work	3.3-5.8	< -20	50*50

Measured and simulated radiation patterns of E-plane (xoy-plane) and H-plane (xoz-plane) are shown in Fig. 9. When measuring radiation patterns, we keep port 1 excited and other ports loaded with a 50-Ω load. In measurement of radiation patterns, the MIMO antenna is used as the receiver, and a horn antenna with working bandwidth of 3-5 GHz is used as the transmitter. The

horn antenna remains fixed, and the receiver antenna rotates 360° to obtain a pattern of one plane. The cross-polarization in patterns is measured after the horn antenna rotates 90°. At 3.5 GHz and 4.9 GHz, the *E*-plane radiation patterns of the antenna element are quasi-directional. That means with the orthogonal placement of the four elements, this MIMO antenna can nearly cover all directions in *E*-plane. The co-polarization radiation patterns are quasi-omnidirectional in *H*-plane, and there are high-level of cross-polarization, but this won't affect the MIMO antenna's performance because the propagation paths in mobile wireless communication are generally multipath in diversity reception.
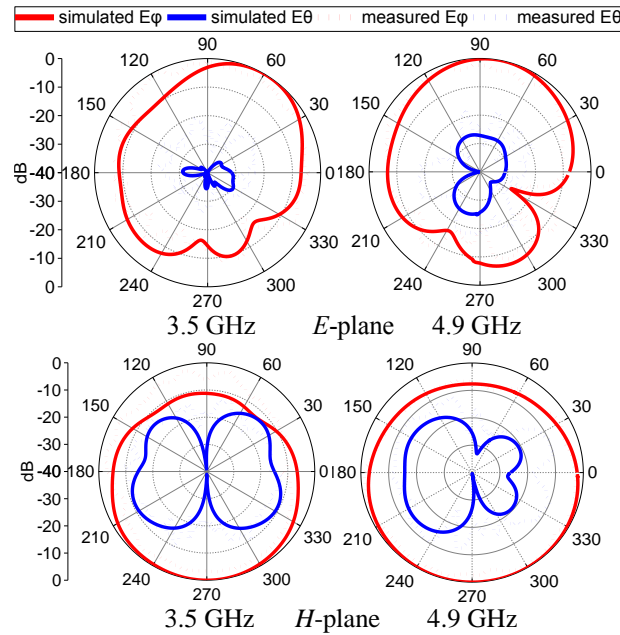
Fig. 9. Measured and simulated radiation patterns of *E*-plane and *H*-plane.

Another important parameter to evaluate the property of MIMO antenna is the envelope correlation coefficient (ECC). It's used to describe how much the communication channels are isolated or correlated with each other [4]. A low ECC means a good isolation between ports as well as high channel capacities. It can be calculated by the formula mentioned in [24] and [25]:

$$ECC_{ij} = \frac{\left| S_{ii}^{*}S_{ij} + S_{ji}^{*}S_{jj} \right|^2}{\left(1 - \left|S_{ii}\right|^2 - \left|S_{ji}\right|^2\right)\left(1 - \left|S_{jj}\right|^2 - \left|S_{ij}\right|^2\right)\eta_{rad,i}\eta_{rad,j}}, \quad (1)$$

the S-parameters and radiation efficiency η of antenna are involved in (1). As it shows in Fig. 10 the ECC of this MIMO antenna is less than 0.01 within the band, which means this antenna is competent for diversity reception/transmission in the MIMO channels. The

simulated peak gains and total efficiency of the MIMO antenna are also respectively given in Fig. 11, within the range of 3-6 GHz (0.5 GHz/step): the peak gains can reach 5.0 dBi at 5 GHz and 2.5 dBi at 3.5 GHz; the total efficiency ranges within 51% - 79%.
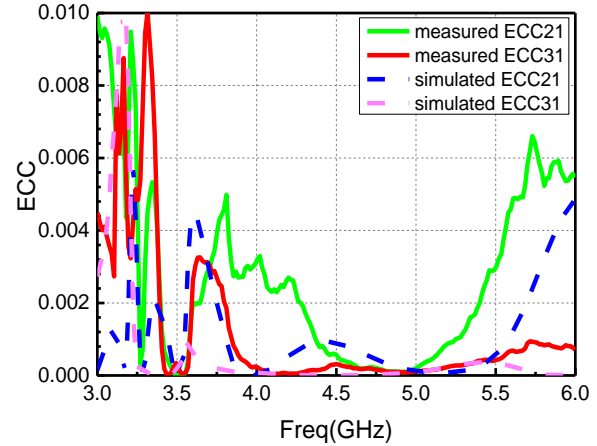
Fig. 10. Measured and simulated ECC.
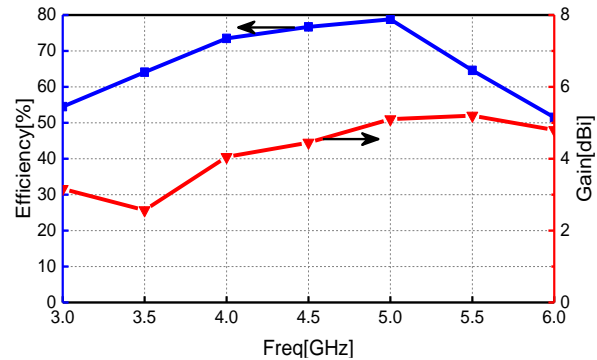
Fig. 11. Simulated peak gains and total efficiency.

B. Calculated channel capacity and CDF

Channel capacity means the maximum information transmission rate of this system, it's an important index to evaluate the quality of MIMO system and its unit is bps/Hz. The calculation of channel capacity is generally given by:

$$C = \log_2 \det(\mathbf{I}_N + \frac{\rho}{N_T}\mathbf{HH}^H). \quad (2)$$

$\mathbf{I}_N$ means the identity matrix, ρ is the average of the signal-to-noise ratio (SNR) at receiver, N_T is the number of antenna elements at transmitter, $\mathbf{H}$ denotes the channel matrix and H represents the Hermitian transpose of matrix.

In [26], Hiroyuki Arai et al. proposed a MIMO antenna that can be used for 5G indoor base station; they calculated and measured its channel performance in indoor environment. In their work, the signal

transmission path of indoor base station antenna to the target was generally line-of-sight (LOS) channel with Ricean fading environment. But for the mobile terminal antenna, the transmission path of the general signal is non-line-of-sight (NLOS). In this case, the signal transmission path follows the Rayleigh fading distribution, such as the channel model established by Yong-ling Ban et al. in [27] used to calculate the channel capacity of mobile MIMO antenna. In order to calculate the capacity of the MIMO channel in this paper, we assume that two identical MIMO antennas as the receiver and transmitter with Rayleigh fading channel environment. Given the channel model in [28] as following:

$$\mathbf{H} = \mathbf{R}_{Rx}^{1/2}\mathbf{H}_w\mathbf{R}_{Tx}^{1/2}, \qquad (3)$$

where $\mathbf{R}_{Tx}$ is the correlation matrix indicating the correlation between the transmitting antennas. Similarly, $\mathbf{R}_{Rx}$ is the correlation matrix indicating the correlation between the receiving antennas. $\mathbf{H}_w$ is the channel gain matrix with i.i.d. (independent identically distributed) Rayleigh fading. Referred from [28], $\mathbf{R}_{Tx}$ and $\mathbf{R}_{Rx}$ can be approximately expressed by:

$$\mathbf{R}_{Tx} = \mathbf{I} - \mathbf{S}_{Tx}^H\mathbf{S}_{Tx}, \qquad (4)$$

$$\mathbf{R}_{Rx} = \mathbf{I} - \mathbf{S}_{Rx}^H\mathbf{S}_{Rx}, \qquad (5)$$

where $\mathbf{S}_{Rx}$ and $\mathbf{S}_{Tx}$ are S-matrix of receiving and transmitting antennas respectively. Thus, (2) can be expressed as:

$$C = \log_2 \det\left(\mathbf{I}_{N_{Rx}} + \frac{\rho}{N_{Tx}}\mathbf{R}_{Rx}^{1/2}\mathbf{H}_w\mathbf{R}_{Tx}\mathbf{H}_w^H\mathbf{R}_{Rx}^{H/2}\right), \qquad (6)$$

in our channel model, $N_{Tx}=N_{Rx}=4$, if the SNR is high enough, then formula (6) could be approximated as:

$$C \approx \log_2 \det\left(\frac{\rho}{N_{Tx}}\mathbf{H}_w\mathbf{H}_w^H\right) + \log_2 \det\left(\mathbf{R}_{Rx}\right) + \log_2 \det\left(\mathbf{R}_{Tx}\right). \qquad (7)$$

Since in our channel model the SNR is not as high as to be negligible, so we used formula (6) to calculate the channel capacity of the MIMO system composed of two MIMO antennas. Figure 12 shows the results of calculated channel capacity changing with SNR at different frequencies and gives the i.i.d. channel capacity as a comparison. It can be seen the MIMO channel performs best at 5.0 GHz while worst at 4.5 GHz. It's worth noting that at 5.0 GHz, the capacity is very close to the capacity of the i.i.d. channel.

However, if there are data transmission links in the channel, the communication interruptions are likely occurred. That is, the probability receiver cannot receive information correctly, and the cumulative distribution function (CDF) is used to describe it. Figure 13 shows the CDF of this MIMO channel under different SNR conditions at 3 GHz. It can be seen that the higher the SNR is, the lower the CDF and the probability of interruption are.

IV. CONCLUSION

A compact dual-band MIMO antenna is proposed in this paper, it works within the dual-band of 5G communications (sub-6 GHz): 3.3-3.6 GHz and 4.8-5.0 GHz. The antenna has an excellent overall performance. Its -10 dB-bandwidth can cover 3.3-5.8 GHz and the isolation between the ports can keep higher than 20 dB. The simulated results agree well with measured results and the antenna's ECC, peak gain, radiation patterns and total efficiency are given in the paper as well. The calculated channel capacity is close to the i.i.d. channel when antenna works at 5.0 GHz and the probability of communication interruption could be small when the SNR is high enough. But there are still some drawbacks on this MIMO antenna: the radiation pattern of single element cannot cover the entire E-plane and can't receive/radiate signals in some specific directions; its total efficiency is not very ideal, only 60% in some frequency bands.
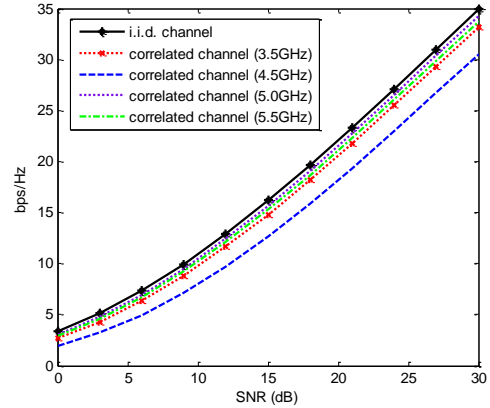

Fig. 12. Calculated channel capacity.
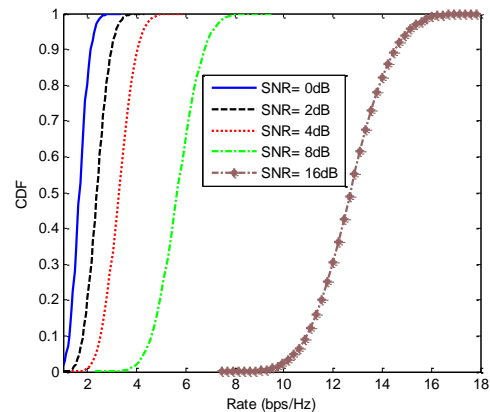
Fig. 13. Cumulative distribution function (CDF) of MIMO channel at 3 GHz.

ACKNOWLEDGMENT

REFERENCES

[1] A. J. Paulraj, D. A. Gore, R. U. Nabar, and H. Bolcskei, "An overview of MIMO communications - A key to gigabit wireless," in *Proceedings of the IEEE*, vol. 92, no. 2, pp. 198-218, Feb. 2004.

[2] X.-L. Liu, Z.-D. Wang, Y.-Z. Yin, J. Ren, and J.-J. Wu, "A compact ultra-wideband MIMO antenna using QSCA for high isolation," in *IEEE Antennas and Wireless Propagation Letters*, vol. 13, pp. 1497-1500, 2014.

[3] J. Deng, J. Li, L. Zhao, and L. Guo, "A dual-band inverted-F MIMO antenna with enhanced isolation for WLAN applications," in *IEEE Antennas and Wireless Propagation Letters*, vol. 16, pp. 2270-2273, 2017.

[4] C. Luo, J. Hong, and L. Zhong, "Isolation enhancement of a very compact UWB-MIMO slot antenna with two defected ground structures," in *IEEE Antennas and Wireless Propagation Letters*, vol. 14, pp. 1766-1769, 2015.

[5] L. Kang, H. Li, X. Wang, and X. Shi, "Compact offset microstrip-fed MIMO antenna for band-notched UWB applications," in *IEEE Antennas and Wireless Propagation Letters*, vol. 14, pp. 1754-1757, 2015.

[6] S. Zhang and G. F. Pedersen, "Mutual coupling reduction for UWB MIMO antennas with a wideband neutralization line," in *IEEE Antennas and Wireless Propagation Letters*, vol. 15, pp. 166-169, 2016.

[7] F. Yang and Y. Rahmat-Samii, "Microstrip antennas integrated with electromagnetic band-gap (EBG) structures: a low mutual coupling design for array applications," in *IEEE Transactions on Antennas and Propagation*, vol. 51, no. 10, pp. 2936-2946, Oct. 2003.

[8] S. Ghosh, T. Tran, and T. Le-Ngoc, "A dual-layer EBG-based miniaturized patch multi-antenna structure," *2011 IEEE International Symposium on Antennas and Propagation (APSURSI)*, Spokane, WA, pp. 1828-1831, 2011.

[9] X. Tan, W. Wang, Y. Wu, Y. Liu, and A. A. Kishk, "Enhancing isolation in dual-band meander-line multiple antenna by employing split EBG structure," in *IEEE Transactions on Antennas and Propagation*, vol. 67, no. 4, pp. 2769-2774, Apr. 2019.

[10] M. Al-Hasan, I. B. Mabrouk, E. R. F. Almajali, M. Nedil, and T. A. Denidni, "Hybrid isolator for mutual-coupling reduction in millimeter-wave MIMO antenna systems," in *IEEE Access*, vol. 7, pp. 58466-58474, 2019.

[11] P. Qin, Y. J. Guo, and C. Liang, "Effect of antenna polarization diversity on MIMO system capacity," in *IEEE Antennas and Wireless Propagation Letters*, vol. 9, pp. 1092-1095, 2010.

[12] L. Dong, H. Choo, R. W. Heath, and Hao Ling, "Simulation of MIMO channel capacity with antenna polarization diversity," in *IEEE Transactions on Wireless Communications*, vol. 4, no. 4, pp. 1869-1873, July 2005.

[13] W. Zhang, Z. Weng, and L. Wang, "Design of a dual-band MIMO antenna for 5G smartphone application," *2018 International Workshop on Antenna Technology (iWAT)*, Nanjing, pp. 1-3, 2018.

[14] K. Yan, P. Yang, F. Yang, L. Y. Zeng, and S. Huang, "Eight-antenna array in the 5G smartphone for the dual-band MIMO system," *2018 IEEE International Symposium on Antennas and Propagation & USNC/URSI National Radio Science Meeting*, Boston, MA, pp. 41-42, 2018.

[15] Y. Li, H. Zou, M. Wang, M. Peng, and G. Yang, "Eight-element MIMO antenna array for 5G/Sub-6GHz indoor micro wireless access points," *2018 International Workshop on Antenna Technology (iWAT)*, Nanjing, pp. 1-4, 2018.

[16] I. Dioum, K. Diallo, M. M. Khouma, I. Diop, L. Sane, and A. Ngom, "Miniature MIMO antennas for 5G mobile terminals," *2018 6th International Conference on Multimedia Computing and Systems (ICMCS)*, Rabat, pp. 1-6, 2018.

[17] A. Zhao and Z. Ren, "Size reduction of self-isolated MIMO antenna system for 5G mobile phone applications," in *IEEE Antennas and Wireless Propagation Letters*, vol. 18, no. 1, pp. 152-156, Jan. 2019.

[18] A. A. Qureshi, M. U. Afzal, T. Tauqeer, and M. A. Tarar, "Performance analysis of FR-4 substrate for high frequency microstrip antennas," *2011 China-Japan Joint Microwave Conference*, Hangzhou, pp. 1-4, 2011.

[19] M. Liang, F. Zhang, G. Zhang, and Q. Li, "Broadband dual-polarized antennas with high port isolation for portable devices," *Proceedings of 2014 3rd Asia-Pacific Conference on Antennas and Propagation*, Harbin, pp. 359-362, 2014.

[20] B. P. Chacko, G. Augustin, and T. A. Denidni, "Compact uni-planar antenna with polarization diversity for UWB applicaton in portable devices," *2014 IEEE Antennas and Propagation Society International Symposium (APSURSI)*, Memphis, TN, pp. 1809-1810, 2014.

[21] Y. Lu, Y. Chan, H. Li, Y. Lin, S. Lo, and G. C. Chuang, "Design and system performances of a dual-band 4-Port MIMO antenna for LTE applications," *2011 IEEE International Symposium*

on *Antennas and Propagation (APSURSI)*, Spokane, WA, pp. 2227-2230, 2011.

[22] J. Motohashi and M. Yamamoto, "A wideband 4-port MIMO antenna using leaf-shaped notch antennas," *2016 International Symposium on Antennas and Propagation (ISAP)*, Okinawa, pp. 1070-1071, 2016.

[23] S. S. Jehangir, A. Hassan, and M. S. Sharawi, "A 4-element dual wideband circular Yagi MIMO antenna system with loop excitation," *2016 IEEE International Symposium on Antennas and Propagation (APSURSI)*, Fajardo, pp. 69-70, 2016.

[24] P. Hallbjorner, "The significance of radiation efficiencies when using S-parameters to calculate the received signal correlation from two antennas," in *IEEE Antennas and Wireless Propagation Letters*, vol. 4, pp. 97-99, 2005.

[25] S. Blanch, J. Romeu, and I. Corbella, "Exact representation of antenna system diversity performance from input parameter description," in *Electronics Letters*, vol. 39, no. 9, pp. 705-707, 1 May 2003.

[26] B. Rohani, K. Takahashi, H. Arai, Y. Kimura, and T. Ihara, "Improving channel capacity in indoor 4×4 MIMO base station utilizing small bi-directional antenna," in *IEEE Transactions on Antennas and Propagation*, vol. 66, no. 1, pp. 393-400, Jan. 2018.

[27] Y. Ban, C. Li, C. Sim, G. Wu, and K. Wong, "4G/5G multiple antennas for future multi-mode smartphone applications," in *IEEE Access*, vol. 4, pp. 2981-2988, 2016.

[28] N. Honma, H. Sato, K. Ogawa, and Y. Tsunekawa, "Accuracy of MIMO channel capacity equation based only on S -parameters of MIMO antenna," in *IEEE Antennas and Wireless Propagation Letters*, vol. 14, pp. 1250-1253, 2015.

Anti-Jamming Front-End Design of Satellite Navigation Receiver

Fan Wang, Haipeng Liu, and Chuanfang Zhang

School of Information and Electronics
Beijing Institute of Technology, Beijing, 100081, China
zcf@bit.edu.cn, wangfan@bit.edu.cn

Abstract ─ In this paper, an anti-jamming front-end is proposed for the satellite navigation receiver. Firstly, a seven-element receiving antenna array and an eight-channel (seven receiving channels and one calibration channel) radio frequency (RF) module are devised. Then, the interference suppression module based on the linear constraint minimum variance (LCMV) criterion are designed and analyzed. By using the LCMV-PI algorithm, the spatial domain information of the signal can be used to effectively suppress the interference. In addition, considering that the channel inconsistency will adversely affect the interference suppression algorithm and subsequent signal acquisition and tracking, a channel equalization scheme is devised to correct the channel inconsistency.

Index Terms ─ Antenna array, anti-jamming, channel equalization, LCMV-PI algorithm, RF module.

I. INTRODUCTION

During the last several decades, the satellite navigation system has been widely used in aerospace, navigation, transportation, meteorology, measurement and other areas. It plays a more and more important role in social and economic development with huge value. However, after the satellite signal reaches the ground, the power is as low as only about -130dBm which submerges under the noise of the satellite navigation receiver. In addition, with the electromagnetic propagation environment becoming more complex, the weak navigation signal is more susceptible to intentional or unintentional interference, which causes the failure for the receiver to locate accurately. Therefore, as an important indicator to measure the performance, the interference suppression capability of the satellite navigation receiver must be strong. Nowadays, the interference suppression technology has become one of the research focuses in the satellite navigation field.

There are two interference suppression techniques for satellite navigation receiver. One is based on single antenna and the other is based on antenna array [1-3]. Li and Milstein [4] applied a linear transversal filter to the spread-spectrum system and suppressed the narrow-band interference. Milstein [5] then proposed a method based on fast Fourier transform to suppress interference in the frequency domain. Rao and Kung [6] proposed an adaptive constrained infinite impulse response (IIR) filter for the enhancement and tracking of sinusoids in additive noise. Poor [7] made a summary of two code-aided method including linear code-aided method and maximum-likelihood code-aided method. Chang et al. [8] raised that the single antenna-based interference suppression method has a simple structure. But only narrow-band interference can be suppressed. For this reason, antenna array interference suppression technology is introduced, and the spatial domain characteristics of the signal are used to suppress the interference. Fante and Vaccaro [9] applied the spatial domain adaptive filtering algorithm based on the minimum power criterion to the satellite navigation receiver, which improved the ability of the receiver to suppress interference. Goldstein et al. [10] proposed a Multistage Wiener Filter method based on orthogonal projections. This method reduced the amount of computation caused by matrix inversion and improved the convergence speed of the interference suppression algorithm. In this paper, an anti-jamming front-end is designed in order to improve the interference suppression performance of satellite navigation receiver. Li et al. [11] developed a new reweighted l_1-norm and an l_p-norm based normalized least mean square algorithms for sparse adaptive array beamforming control applications. Choi et al. [12] described a new direct data domain least squares (D^3LS) method using real weights, which utilized only a single snapshot of the data for adaptive processing.

In this paper, the LCMV-PI interference suppression algorithm is firstly mathematically deduced. The Monte-Carlo simulation is used to analyze the effectiveness of the algorithm for two special cases. For the first case, the angle between the useful signal and interference signal is small; for the second case, the power of interference signal is extremely large. Then an anti-jamming receiving front-end is designed. The RF module is designed with a calibration channel to achieve the calibration of the amplitude and the phase consistency of the down-conversion channel. This design improves

the interference suppression performance in the actual use of the interference suppression algorithm. By comparing with the related literature, the performance of the LCMV-PI algorithm and the rationality of the front-end design are verified.

This paper is organized as follows. Section II introduces the LCMV-PI interference suppression algorithm and carries on simulations by Matlab. Section III briefly presents the architecture of anti-jamming front-end. And then the specific design of antenna array, RF module and interference suppression module are presented, respectively. The performance of the proposed anti-jamming front-end is tested in Section IV. Finally, section V gives the conclusion.

II. SPACE ADAPTIVE INTERFERENCE SUPPRESSION ALGORITHM DESIGN

A. Signal model of antenna array

An arbitrary antenna array structure of M array elements is shown in Fig. 1. The spatial three-dimensional coordinates of the mth array element are $\rho_m = [x_m, y_m, z_m]$. The incident angles of the signal are (θ, φ), where θ is the pitch angle and φ is the azimuth angle. R_0 is the distance between the source and the reference point. R_m is the distance between the source and the mth element. It can be seen that the distance from the mth array element to the reference point is $\vec{R_m} \triangleq R_m - R_0$. The propagation delay τ_m of the signal from the mth array element to the reference point is:

$$\tau_m = \frac{\vec{R_m}}{c} = \frac{1}{c}\left(x_m sin\theta cos\varphi + y_m sin\theta sin\varphi + z_m cos\theta\right)$$
$$m=0,1,\cdots,M-1. \tag{1}$$

The corresponding spatial phase difference is:

$$\phi_m(\theta,\varphi) = \frac{2\pi}{\lambda}\left(x_m sin\theta cos\varphi + y_m sin\theta sin\varphi + z_m cos\theta\right)$$
$$m=0,1,\cdots,M-1. \tag{2}$$

Thus, the steering vector of the antenna array is:

$$a(\theta,\varphi) = \left[e^{-j\phi_0(\theta,\varphi)} \ e^{-j\phi_1(\theta,\varphi)} \ \cdots \ e^{-j\phi_{M-1}(\theta,\varphi)}\right]^T. \tag{3}$$
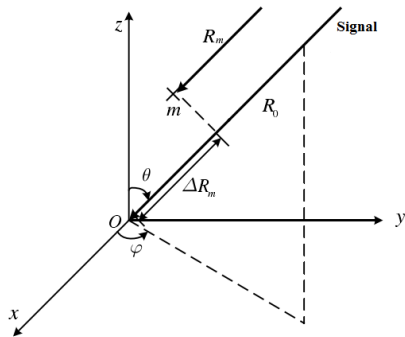
Fig. 1. Schematic diagram of arbitrary antenna array structure.

B. Analysis of LCMV-PI algorithm

The space adaptive anti-jamming processing consists of the antenna array and the adaptive processing algorithm. Figure 2 depicts the principle of the space adaptive anti-jamming processing. It can be seen that the basis of the adaptive processing is to adjust the weight vectors of the array elements according to the adaptive processing algorithm. By weighting and summing the signals received by each array element, the antenna array beam is "guided" to a certain direction where the useful signals are enhanced, and the interference signals are suppressed [13-17]. The output of the array is:

$$y(t) = \sum_{m=1}^{M} w_M^H x_m(t) = w^H x(t). \tag{4}$$
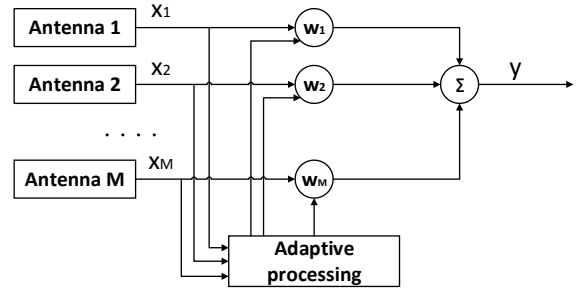
Fig. 2. The principle of the space adaptive anti-jamming processing.

The LCMV criterion is to minimize the output power of the array under some linear constraints. The cost function of the LCMV criterion is:

$$\min_w w^H R_{xx} w \quad s.t. \ w^H C = f, \tag{5}$$

where, C is the constraint matrix and f is the constraint response vector.

Based on the Lagrange multiplier method, the objective function is constructed as:

$$L(w) = w^H R_{xx} w - \lambda(f^H - C^H w), \tag{6}$$

where λ is the Lagrange multiplier.

Let $\nabla_w L(w) = 0$, the optimal weight vector is:

$$w_{opt} = R_{xx}^{-1} C(C^H R_{xx}^{-1} C)^{-1} f^H. \tag{7}$$

PI algorithm is based on the LCMV criterion. Let $C = [1,0,\cdots,0]^T = s_0$, $f = 1$, (5) can be rewritten as:

$$\min_w w^H R_{xx} w \quad s.t. \ w^H s_0 = 1. \tag{8}$$

Then, the optimal weight vector can be obtained as:

$$w_{opt} = \frac{1}{s_0^H R_{xx}^{-1} s_0} R_{xx}^{-1} s_0. \tag{9}$$

The PI algorithm ensures that the weight of the first channel is always 1, while the weights of the other channels are constantly modified during the iteration to meet the LCMV criterion. In the satellite navigation receiving system, the power of the interference signal is much larger than the useful signal, using the PI algorithm can form a deep zero-trap in the direction of interference

signal to achieve the suppression of interference and improve the SINR of the system.

C. Simulation of LCMV-PI algorithm

The performance evaluation of LCMV-PI interference suppression algorithm is conducted by simulation verification analysis based on Matlab. It is assumed that both the antenna array and the RF channel are ideal. The Monte-Carlo simulation is performed on the algorithm for three cases: the general case, the case in which the angle between the useful signal and the interference signal is very small, and the case in which the amplitude of the interference signal is extremely large.

For the general case, the simulation parameters are designed as:

(1) Antenna array setting: seven-element central circular array with the radius of 0.8λ;

(2) Useful signal direction: (10°, 10°);

(3) Interference signal direction: (80°, 80°);

(4) Interference signal setting: INR=80dB, ISR=100dB.

The radiation patterns of the antenna array are shown in Fig. 3. It can be seen that the radiation pattern forms a deep zero-trap in the direction of the interference signal, reaching -104dB. The effectiveness of the LCMV-PI algorithm for interference suppression is verified.

(a) Three-dimensional radiation pattern

(b) Color map

(c) Profile @phi=80°

(d) Profile @theta=80°
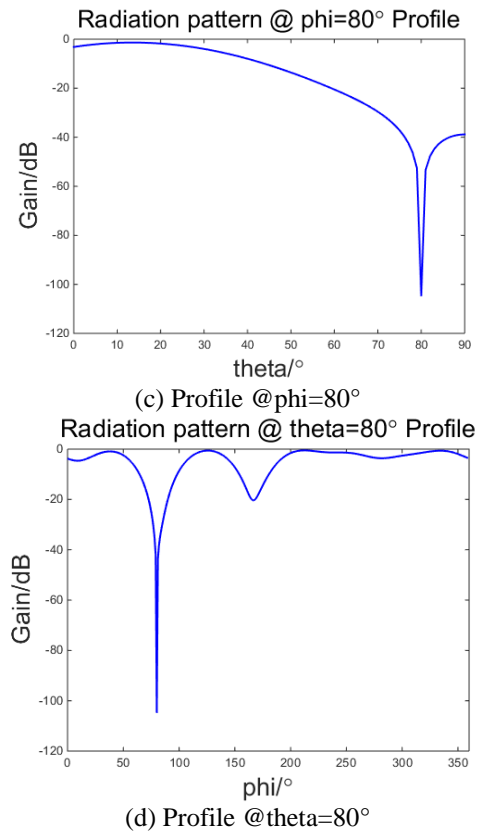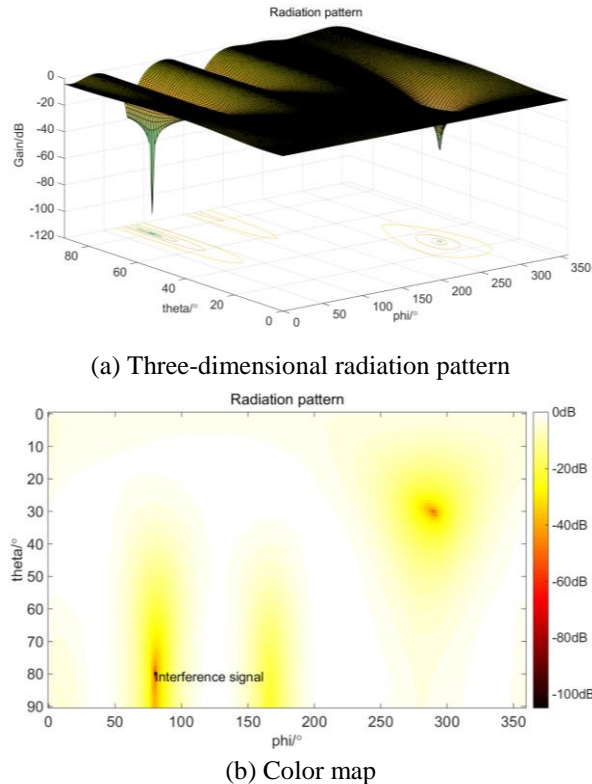
Fig. 3. The radiation patterns of the antenna array by using LCMV-PI algorithm.

For the second case, the direction of the useful signal is set as (0°, 0°), and the angle between the useful signal and the interference signal is less than 5°. The remaining parameters remain unchanged. Figure 4 shows the radiation pattern in this case. It can be seen that a deep zero-trap is formed in the direction of the interference, reaching more than -95dB, which verifies the effectiveness of the algorithm.

For the third case, the ISR is set as 200dB, 250dB and 300dB, respectively. The remaining parameters remain unchanged. The Monte-Carlo simulation results are shown in Fig. 5. From the radiation pattern, it can be seen that the larger the amplitude of the interference signal is, the deeper the zero-trap formed by the algorithm will be. The effectiveness of the LCMV-PI algorithm is also verified. However, in practice, when the interference signal power is extremely large, the receiving channel is highly likely to be saturated. At this time, the AD cannot effectively sample the receiving signal, which in turn causes the failure of the interference suppression algorithm. To cope with this situation, multi-stage automatic gain control (AGC) can be added to the receiving channels to improve the dynamic range of the

receiving channels.
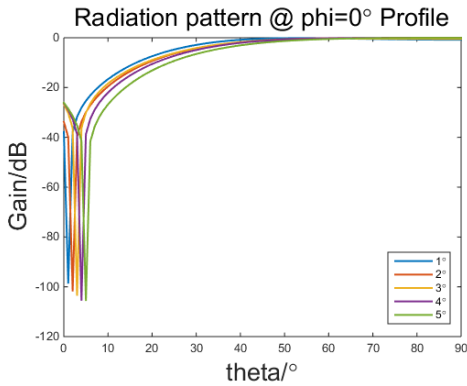
Fig. 4. The radiation pattern when the angle between the useful signal and the interference signal is small by using LCMV-PI algorithm.
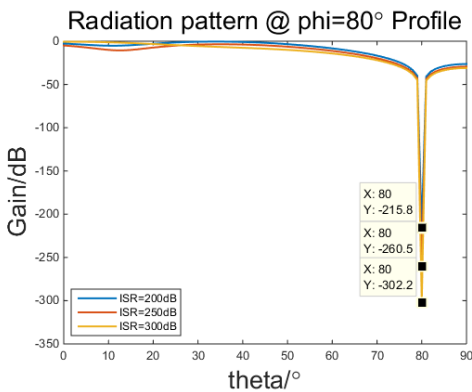
Fig. 5. The radiation pattern when the magnitudes of the interference signals are extremely large by using LCMV-PI algorithm.

III. ANTI-JAMMING FRONT-END DESIGN

The anti-jamming front-end is mainly composed of an antenna array, a RF module and an interference suppression module. The antenna array consists of seven antenna elements for receiving satellite navigation signals. The RF module consists of eight channels, seven of which are mainly used to down-convert the seven signals received by the antenna array to the IF and then send them to the interference suppression module for anti-jamming processing. The remaining channel up-converts the IF calibration signal of the baseband module to the L-band and adjusts the signal to an appropriate power level range. Thus, the signal can be used as a calibration signal for the seven receiving channels. The interference suppression module implements two functions of channel correction and interference suppression. It also transmits the anti-jamming processed IF signal to the back-end baseband module for acquisition and tracking. Figure 6 depicts the block

diagram of the receiver system.
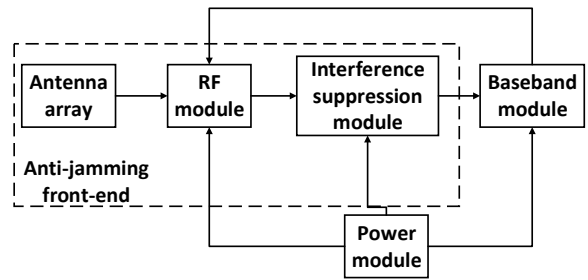
Fig .6. The block diagram of the receiver system.

A. Antenna array design

The antenna array is in the form of a seven-element central circular array, as shown in Fig. 7. The physical structure of the antenna array, that is, the relative position between the array elements, has a great influence on the performance of the entire system. When selecting the relative distance, the coupling effect between the antenna elements should be considered. When the spacing of the array elements is too small, a serious mutual coupling phenomenon will occur, which makes the interference suppression algorithm form a wider range and shallower depth of the zero-trap. And then the performance of interference suppression is reduced. When the spacing is too large, a large-scale scanning in the upper half of the antenna array may generate grating lobes, which is also undesirable for the system. On account of the considerations above and anti-jamming requirements, the mutual coupling should be minimized and the grating lobes appearing in the scanning space should be prevented in the simulation. Thus, the spacing is chosen as $R = 0.8\lambda$, where λ is the free space wavelength.
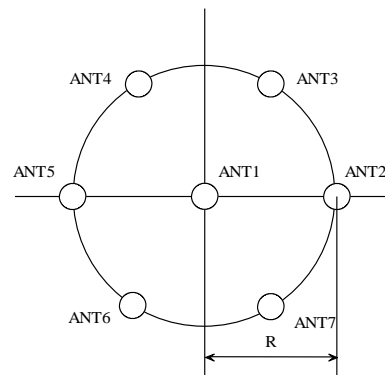
Fig. 7. Schematic diagram of the antenna array arrangement.

The consistency of the antenna elements has a certain impact on the performance of interference

suppression. Therefore, the seven antenna elements are designed in a unified form, and the un-roundness of the antenna elements and the isolation between the antenna elements are improved. The antenna element is in the form of the microstrip patch, as shown in Fig. 8.

(a) The dimensions of the antenna element

(b) The photo of the antenna element
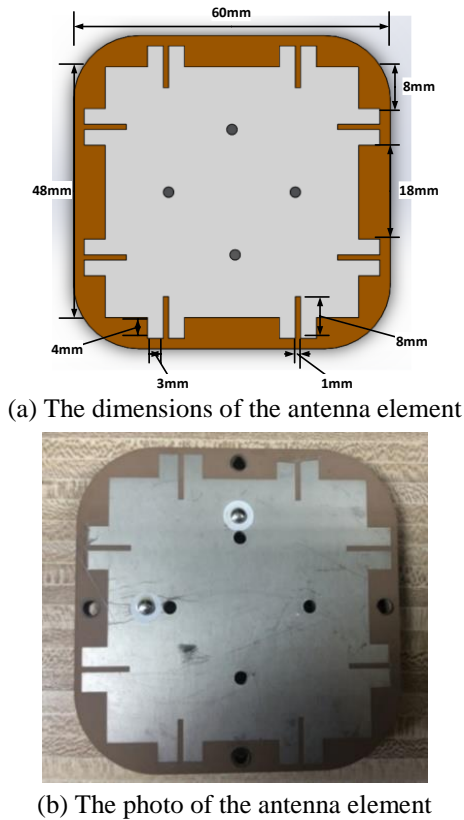
Fig. 8. The prototype of the antenna element.

As shown in Fig. 9, ABS plastic (dielectric constant 3.3, loss tangent 0.001) is chosen to be the material of the radome. The thickness of the radome is 3mm. The overall height of the antenna array is 120mm and the diameter of the bottom aluminum substrate disk is 530mm.

(a) Top view

(b) Side view
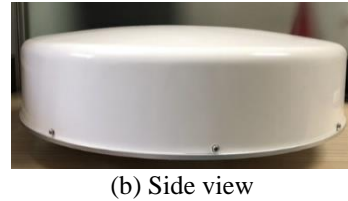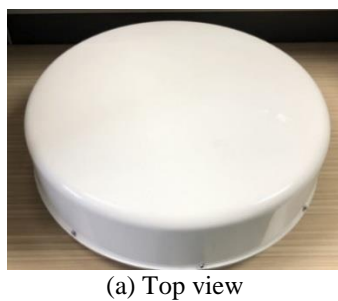
Fig. 9. The prototype of the seven-element antenna array with radome.

When the center frequency is 1340.13MHz, the radiation pattern of the antenna element is shown in Fig. 10. The un-roundness of the antenna element on theta=60° is shown in Fig. 11. From these two graphs, it can be gained that the zenith gain of the antenna element reaches 7.68dB; the 3dB lobe width reaches 75°; the 6dB lobe width reaches 110°; the front-to-back ratio is -22.2dB; the un-roundness is better than 2dB on theta=60°.
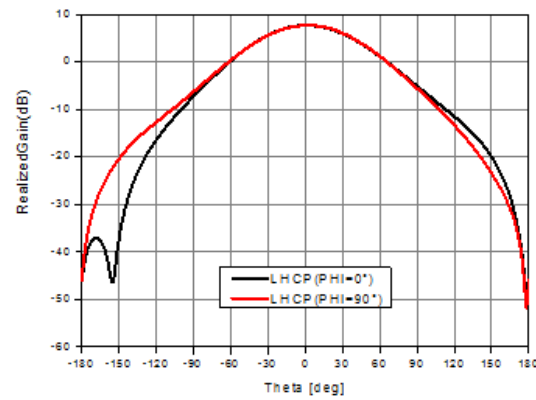
Fig. 10. The radiation pattern of the antenna element at 1340.13MHz.
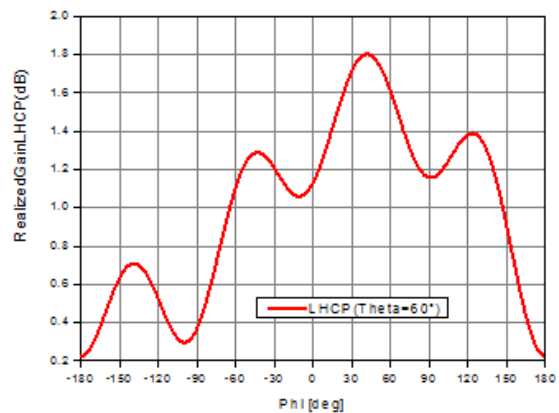
Fig. 11. The un-roundness of the antenna element on theta=60° at 1340.13MHz.

Figure 12, Fig. 13 and Fig. 14 depict the radiation pattern, the isolation and the axial-ratio of the antenna array, respectively. It can be obtained that the zenith gain of the antenna array reaches 16.39dB; the 3dB lobe width reaches 26°; the 6dB lobe width reaches 36°; the isolation is better than -26dB; the axial-ratio is better than 0.6dB.

B. RF module design

As shown in Fig. 15, the RF module is mainly composed of three sub-modules: receiving down-conversion module, transmitting up-conversion module and local oscillator module. Figure 16 shows the prototype of the RF module.
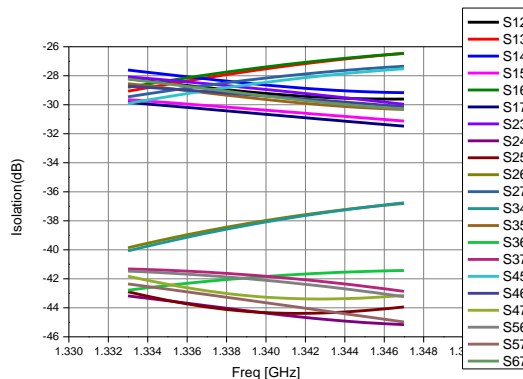
Fig. 13. The isolation between the antenna elements.
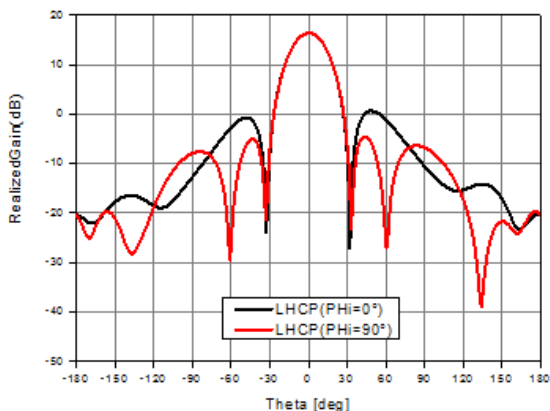
Fig. 12. The radiation pattern of the antenna array at 1340.13MHz.
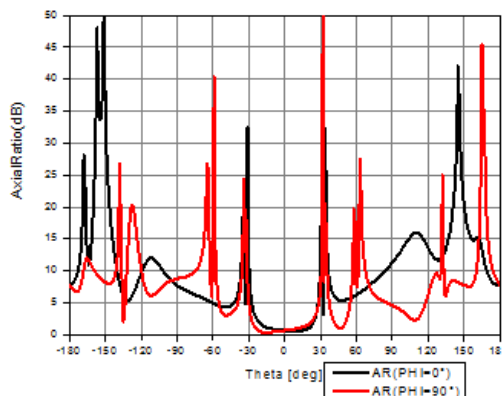
Fig. 14. The axial-ratio of the antenna array at 1340.13MHz.
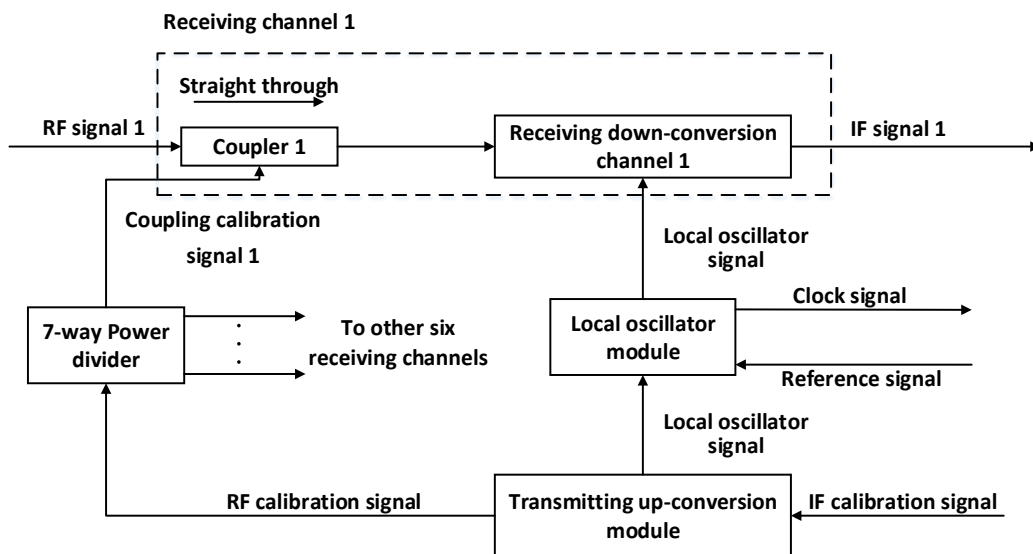
Fig. 15. The block diagram of the RF module.
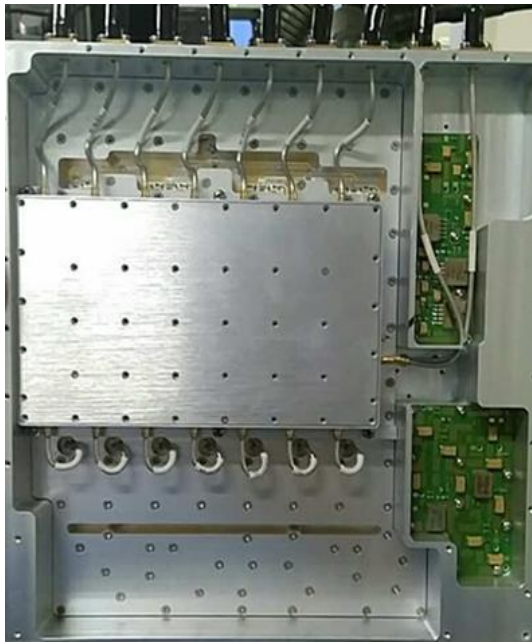
Fig. 16. The prototype of the RF module.

The receiving down-conversion module consists of seven receiving channels with same frequency and gain configuration. The receiving channel adopts the classic super-heterodyne structure. The L-band RF signal of 1340.13MHz received by the seven-channel L-band receiving antenna array is converted to the 70.13MHz IF signal and then transmitted to the interference suppression module for anti-jamming processing.

The working principle of the receiving channel is shown in Fig. 17. After the RF signal entering the receiving channel, the first stage is an isolator (Hongda's HGD09S1.25-1.35G) that guarantees the standing wave indicator of the RF port. The second stage is a coupler (RN2's RCP1500A30) for coupling the calibration signal. The third stage is a low noise amplifier (LNA, Qorvo's TQP3M9036), which is cascaded by a two-stage amplifier to ensure the noise figure (NF) of the receiving channel. A two-stage band-pass filter (Jiangjia's MC4A1340F16FCA) and an isolator are placed after the two-stage amplifier to ensure the out-of-band rejection of the channel. The temperature compensation attenuator is used to adjust the gain variation under temperature changes. The mixer (MINI's MCA1-24MH+) is a double-balanced mixer. A low-pass filter (MINI's XLF-151+) is cascaded after mixing to avoid excessive leakage of the local oscillator at the IF port, which results in channel saturation. An amplifier (MINI's PGA-103+) is added to the IF, so that the total channel gain can meet the design requirements. The channel finally uses an LC band-pass filter to ensure the out-of-band rejection indicator.
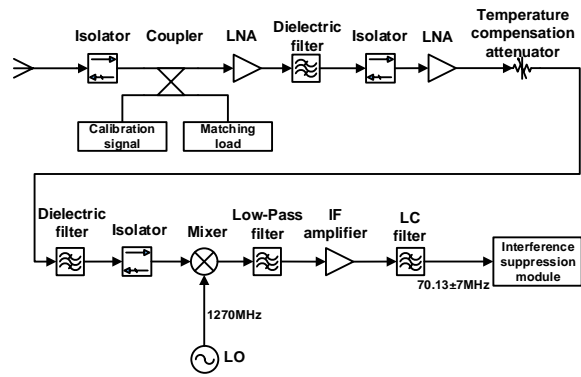
Fig. 17. The working principle of the receiving channel.

The NF of the receiving channel, the amplitude and phase consistency between the receiving channels and the isolation of the channels have great influences on the interference suppression performance. In the current design, the NF of the receiving channel is better than 1.5dB; the amplitude consistency between receiving channels is better than 0.5dB; the phase consistency is better than 5°. By using the metal sub-cavity design for each receiving channel, the isolation between channels is better than 70dB.

The transmitting up-conversion module includes a transmitting channel which converts the 70.13 MHz IF calibration signal output by the baseband module to the 1341.13MHz RF signal and adjusts the output signal to a suitable power level range. After power dividing and coupling, they act as the calibration signal for the seven receiving channels. The working principle of the transmitting channel is shown in Fig. 18. The local oscillator signal frequency is 1270MHz. The device has a high isolation between local oscillator and RF. The IF signal power is not high, which can guarantee the linearity. The filters are designed before and after the mixer to ensure the purity of the signal after mixing. The RF amplifier is Qorvo's TQP3M9036 and the local oscillator driver amplifier is NC3046S.
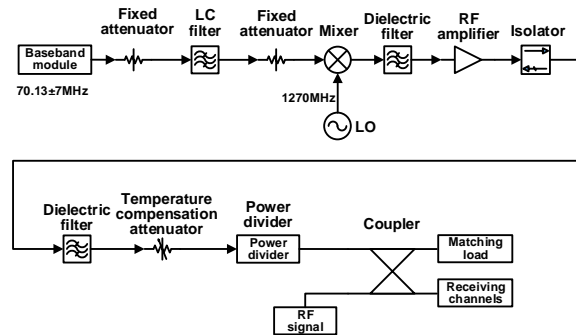
Fig. 18. The working principle of the transmitting channel.

The local oscillator module consists of a phase-locked crystal oscillator (Haichuang's PDS100MHz) and a phase-locked point source. The working principle of the local oscillator module is shown in Fig. 19. To generate 100MHz reference signals for both the phase-locked point source and baseband module, the 10MHz reference signal is phase-locked by using a thermostatic phase-locked crystal, ensuring low phase noise. After the 100MHz reference signal being amplified and filtered, it is used as the clock signal of the baseband and interference suppression module of the latter stage. The phase-locked point source locks the 100MHz reference signal generates a 1270MHz RF signal. After power dividing and amplification, they are used as the local oscillator signal of the mixers for the receiving and transmitting channels. The function of the attenuator is to control the power of the local oscillator signal and prevent the local oscillator signal input end of the mixer from being overloaded.
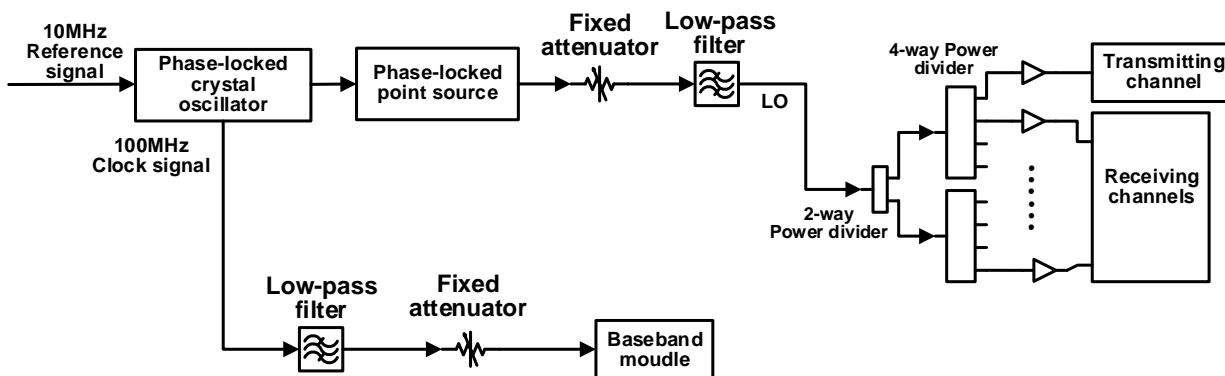
Fig. 19. The working principle of the local oscillator module.

C. Interference suppression module

The interference suppression module has two working modes of channel correction and interference suppression. Figure 20 depicts the block diagram of the interference suppression module. And the prototype of the interference suppression module is shown in Fig. 21.
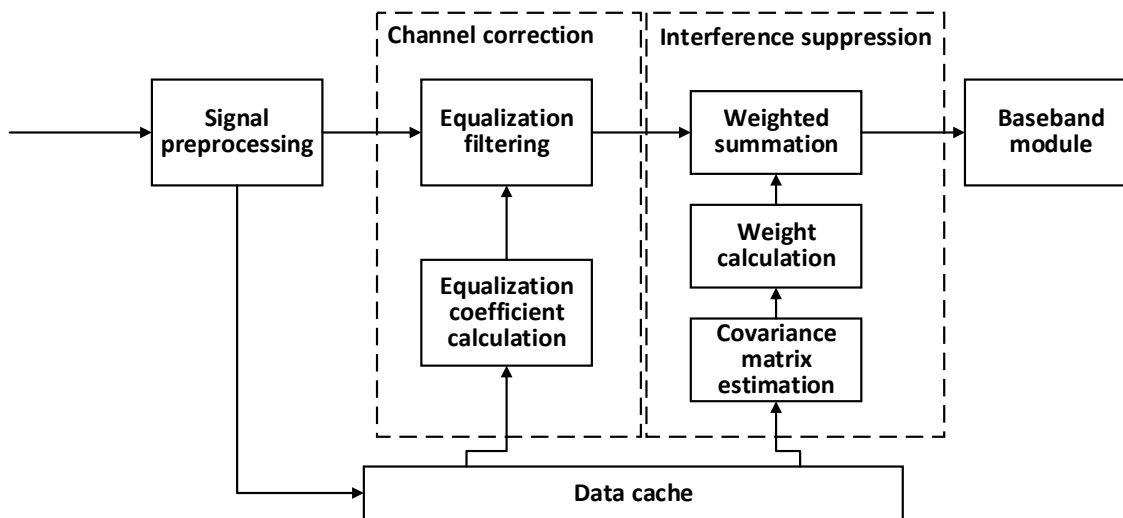
Fig. 20. The block diagram of the interference suppression module.
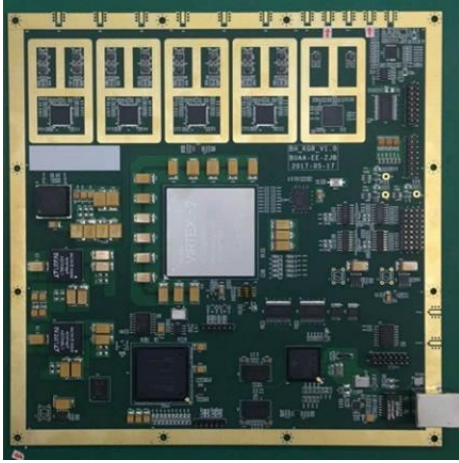
Fig. 21. The prototype of the interference suppression module.

The interference suppression module hardware board includes seven high-speed AD input channels, one high-speed DA output channel, FPGA logic unit, DSP control unit, clock management unit and power management unit. The bit-width of AD determines whether the sampling of the signal is complete or not. And the data processing resources of FPGA and DSP determine whether the interference suppression operation can be performed on the sampled data or not. The device selected in this paper can meet the requirements of interference suppression. The maximum sampling rate, bit-width, and channel isolation of the AD (ADS42LB69) input channel are 250MSPS, 16Bit, and 80dB, respectively. The maximum sampling rate, bit-width, and channel isolation of the DA (AD9142A) output channel are 1600MSPS, 16Bit, and 80dB, respectively. The FPGA is Xilinx's XC7V690T, and the DSP is TI's TMS320C6747.

In the channel correction mode, the baseband module generates the IF calibration signal. The signal is up-converted to the RF through the transmitting channel. Then the power is divided to seven channels, and coupled to each of the receiving channels. Based on the time domain channel equalization algorithm, the coefficients of the equalization filters of each channel are calculated. These coefficients are written into the FPGA by the DSP to complete the channel correction.

In the interference suppression mode, the LCMV-PI algorithm is used to perform anti-jamming processing on the received signal. The processed data is transmitted to the back-end baseband module for acquisition and tracking.

IV. IMPLEMENTATION AND RESULTS

In order to verify the performance of the algorithm and the design accuracy of the anti-jamming front-end,

the performance of channel equalization and interference suppression of the proposed device are tested after the design and production. The prototype and the test environment of the proposed anti-jamming front-end are illustrated in Fig. 22 and Fig. 23 respectively.
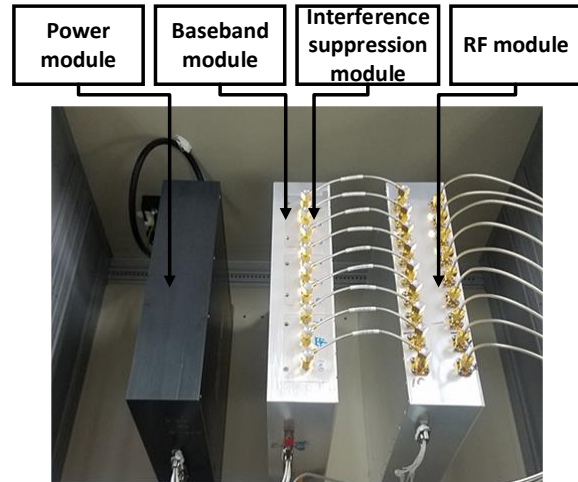
Fig. 22. The prototype of the proposed anti-jamming front-end.
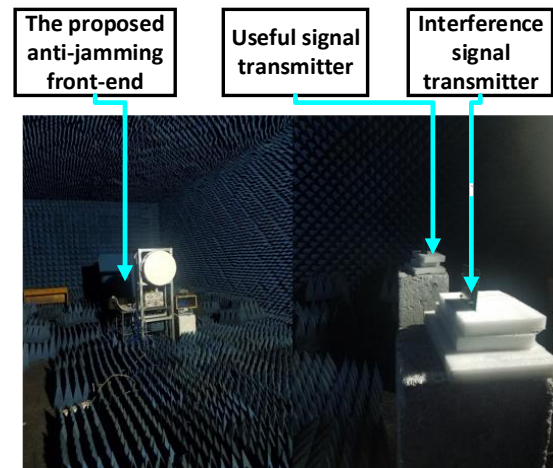
Fig. 23. The test environment of the proposed anti-jamming front-end.

A. The performance of channel equalization

The test method is as follows. Firstly, the same equalized signal are input to seven RF receiving channels. Then, the cancellation ratio (CR) of the output signals with and without the equalizing filter are compared. The test results are shown in Table 1. It can be seen that, the channel equalization has an improvement of more than 20 dB on the channel inconsistency, which will help improve the anti-jamming performance.

Table 1: The test results of the CR

Receiving Channel	2	3	4	5	6	7
CR before equalization (dB)	-13.4275	-8.9577	-22.9154	-16.7140	-7.3931	-15.5315
CR after equalization (dB)	-37.4985	-34.2868	-40.7181	-40.1475	-33.6433	-38.8989

B. The performance of interference suppression

We first start the useful signal transmitter, gradually reduce the signal power, and test the threshold of the receiver system. Then, the signal is fixed to the threshold power, and the interference signal transmitter is turned on. The interference signal power is gradually increased, and the interference suppression capability of the receiver system is tested. Through testing, we obtained that when the angle between the useful signal and the interference signal is 8°, 12°, and 16°, the interference suppression capability of the device reaches 69dB, 74dB, and 80.5dB, respectively. Table 2 lists the performance comparison among the anti-jamming front-end, including the algorithm, the angle between directions of the useful signal and interference signal and the interference suppression capability. Results indicate that the present work has better interference suppression capability at the smaller angle.

Table 2: Performance comparison of the anti-jamming front-end

Item	[18]	[19]	[20]	Our Work
Algorithm	Sub-band adaptive filter	LMS	SWGQR-RLS	LCMV-PI
ΔΦ	90°	10°	30°	8°
Interference suppression capability	ISR=84dB	ISR=60dB	ISR=40dB	ISR=69dB

It can be seen that the proposed anti-jamming front-end can effectively suppress the interference, and then improve the performance of the satellite navigation receiver.

V. CONCLUSION

In this paper, we proposed an anti-jamming front-end prototype for satellite navigation receiver. The interference suppression technique based on the LCMV-PI algorithm is applied to the interference suppression module. Considering that the channel inconsistency may have a bad influence on the interference suppression effect and the back-end signal acquisition and tracking, the channel correction function based on the channel equalization algorithm is designed. The test results show that the designed anti-jamming front-end can effectively suppress the interference signal and improve the anti-jamming performance of the satellite navigation receiver.

REFERENCES

[1]   M. Cuntz, A. Konovaltsev, and M. Meurer, "Concepts, development, and validation of multi-antenna GNSS receivers for resilient navigation," *Proceedings of the IEEE*, vol. 104, no. 6, pp. 1288-1301, June 2016.

[2]   I. J. Gupta, I. M. Weiss, and A. W. Morrison, "Desired features of adaptive antenna arrays for GNSS receivers," *Proceedings of the IEEE*, vol. 104, no. 6, pp. 1195-1206, June 2016.

[3]   C. Fernández-Prades, J. Arribas, and P. Closas, "Robust GNSS receivers by array signal processing: Theory and implementation," *Proceedings of the IEEE*, vol. 104, no. 6, pp. 1207-1220, June 2016.

[4]   L. M. Li and L. B. Milstein, "Rejection of narrow-band interference in PN spread-spectrum systems using transversal filters," *IEEE Transactions on Communications*, vol. 30, no. 5, pp. 925-928, May 1982.

[5]   L. B. Milstein, "Interference rejection techniques in spread spectrum communications," *Proceedings of the IEEE*, vol. 76, no. 6, pp. 657-671, June 1988.

[6]   D. B. Rao and Sun-Yuan Kung, "Adaptive notch filtering for the retrieval of sinusoids in noise," *IEEE Transactions on Acoustics, Speech, and Signal Processing*, vol. 32, no. 4, pp. 791-802, Aug. 1984.

[7]   H. V. Poor, "Active interference suppression in CDMA overlay systems," *IEEE Journal on Selected Areas in Communications*, vol. 19, no. 1, pp. 4-20, Jan 2001.

[8]   Q. Chang, H. Wang, and X. X. Li, "The review of interference suppression algorithms about navigation receiver navigation," *Position and Timing*, vol. 4, no. 05, pp. 83-88, 2017.

[9]   R. L. Fante and J. J. Vaccaro, "Wideband cancellation of interference in a GPS receive array," *IEEE Transactions on Aerospace and Electronic Systems*, vol. 36, no. 2, pp. 549-564, Apr. 2000.

[10] J. S. Goldstein, I. S. Reed, and L. L. Scharf, "A multistage representation of the Wiener filter based on orthogonal projections," *IEEE Transactions on Information Theory*, vol. 44, no. 7, pp. 2943-2959, Nov. 1998.

[11] W. L. Shi, Y. S. Li, and J. W. Yin, "Improved constraint NLMS algorithm for sparse adaptive array beamforming control applications," *Applied Computational Electromagnetics Society Journal*,

34.3, 2019.

[12] W. Choi, T. K. Sarkar, Hong Wang, and E. L. Mokole, "Adaptive processing using real weights based on a direct data domain least squares approach," *IEEE Transactions on Antennas and Propagation*, vol. 54, no. 1, pp. 182-191, Jan. 2006.

[13] Y. Xiao-bo, "An improved GPS receiver anti-jammer algorithm based on space-time adaptive processing," *2012 International Conference on Computer Distributed Control and Intelligent Environmental Monitoring*, Hunan, pp. 106-109, 2012.

[14] S. Leng and Wee Ser, "Adaptive null steering beamformer implementation for flexible broad null control," *Signal Processing*, 91.5, pp. 1229-1239, 2011.

[15] L. Zhao, Y. Mao, and J. Ding, "A STAP interference suppression technology based on subspace projection for BeiDou signal," *2016 IEEE International Conference on Information and Automation (ICIA)*, Ningbo, pp. 534-538, 2016.

[16] S. Daneshmand, A. Jahromi, A. Broumandan, and G. Lachapelle, "GNSS space-time interference mitigation and attitude determination in the presence of interference signals," *Sensors*, 15.6, pp. 12180-12204, 2015.

[17] H. Wang, L. Yang, Y. Yang, and H. Zhang, "Anti-jamming of Beidou navigation based on polarization sensitive array," *2017 International Applied Computational Electromagnetics Society Symposium (ACES)*, Suzhou, pp. 1-2, 2017.

[18] Y. T. Liu, "Satellite navigation antenna and adaptive anti-jamming technology," *Beijing University of Posts and Telecommunications*, 2019.

[19] J. H. Xiang, "Research on application of GPS nulling technology based on space-time adaptive processing," *Harbin Engineering University*, 2009.

[20] B. B. Shi, "Research on the technologies of high degrees of freedom interference suppression for GNSS receiver," *National University of Defense Technology*, 2011.

Improved Gaussian Process Modelling of On-Axis and Off-Axis Monostatic RCS Magnitude Responses of Shoulder-Launched Missiles

Warren P. du Plessis and Jan P. Jacobs

Department of Electrical, Electronic and Computer Engineering
University of Pretoria, Hatfield, 0028, South Africa
jpjacobs@up.ac.za, wduplessis@ieee.org

Abstract ─ An improved Gaussian-process-based technique is described for modelling both on-axis and off-axis monostatic RCS magnitude responses of shoulder-launched missiles. The RCS responses are complicated, oscillatory, quasi-periodic functions of frequency, with the oscillation periods being related to the spacings of the scatterers comprising the missiles. The updated modelling approach employs a spectral-mixture covariance function, whose components explicitly include distinct oscillations. The proposed technique is evaluated by means of two example missiles. For the six rotations considered, average predictive normalised RMSE ranged from 0.34% to 0.87% and from 0.95% to 1.53% for the two missiles respectively.

Index Terms ─ Gaussian processes, modelling, radar cross-section.

I. INTRODUCTION

A radar system has little or no influence over the radar cross-section (RCS) of a target [1, 2], making RCS the driving factor behind a variety of radar design decisions (e.g., [2, 3]). RCS magnitude strongly affects radar performance via SNR, and influences countermeasure performance via the jammer-to-signal ratio (JSR) [2].

The majority of radar targets have dimensions which are significantly larger than a wavelength, so RCS simulations normally require vast quantities of memory and take a long time, even when high-frequency techniques such as physical optics (PO) are used. Unfortunately, the fact that radar targets are so much larger than the wavelength means that the RCS magnitude varies rapidly with frequency and rotation [1], so RCS must be determined at a large number of frequencies and rotations. Accurately modelling RCS magnitude as a function of frequency would reduce the number of frequency points at which RCS must be determined (e.g., via costly simulations), thereby reducing the time required to reliably obtain platform RCS.

Despite the clear value of RCS magnitude modelling, it has received surprisingly little attention in the literature (studies concerned with modelling RCS magnitude as a function of frequency include [4-10]), and in most cases, the targets considered either have very specific attributes (e.g., strong resonances), have simpler responses than the missiles considered here, or only consider angular interpolation. There is a relatively large body of literature which attempts to extract accurate models of targets from RCS responses (e.g., [11-14]), but the emphasis in these studies is on target characterisation rather than RCS modelling. There is thus a need to consider the modelling of RCS responses of realistic targets, like missiles.

It has recently been demonstrated that Gaussian process (GP) regression [15] can be used to create accurate models of monostatic RCS magnitude responses of shoulder-launched missiles [10]. Integral to the models was the use of a specially constructed composite covariance function formed by taking the product of standard squared-exponential and periodic covariance functions [15]. It was shown that GP regression outperformed support vector regression, a GTD-based approximation technique, and spline interpolation in modelling the highly oscillatory RCS magnitude responses of Stinger and Strela missile models. GP regression has also been used in conjunction with a Bayesian committee machine to model RCS responses as a function of object shape [16], further demonstrating the value of the GP approach to RCS modelling. However, these investigations did not consider RCS frequency response [16]. Furthermore, similar to [10], only frontal-incidence (on-axis) RCS responses were considered.

In the present study, the technique described in [10] is extended to account for monostatic RCS responses involving an additional missile type, as well as different angles of incidence (i.e., off-axis). These challenging additional test cases expose limitations of the composite SE×PER covariance function used previously [10]. The structure of the frequency response of the RCS magnitude suggests that using a spectral-mixture covariance function [17] (not previously used for

electromagnetic modelling) will produce better results, and experimental results confirm that this is indeed the case.

II. GAUSSIAN PROCESS MODELLING

The goal is to model the response of the RCS magnitude as a function of frequency, i.e., a one-dimensional latent function that is assumed to be noise-free.

Consider a training set $\{(x_i, g_i) \mid i = 1, \ldots, n\}$ consisting of observations of the latent function, where the inputs x_i and outputs (targets) g_i are frequency and RCS magnitude respectively. In order to make predictions at new (test) inputs $\{x_{*,j} \mid j = 1, \ldots, n_*\}$, the first step is to define a jointly Gaussian prior distribution over the n training outputs (vector $\mathbf{g}$) and the n_* unknown test outputs (vector $\mathbf{g}_*$) [15]:

$$\begin{bmatrix} \mathbf{g} \\ \mathbf{g}_* \end{bmatrix} \sim \mathcal{N}\left(\mathbf{0}, \begin{bmatrix} K(\mathbf{x}, \mathbf{x}) & K(\mathbf{x}, \mathbf{x}_*) \\ K(\mathbf{x}_*, \mathbf{x}) & K(\mathbf{x}_*, \mathbf{x}_*) \end{bmatrix} \right), \quad (1)$$

where $\mathcal{N}(\mathbf{u}, V)$ denotes a multivariate normal distribution with mean vector $\mathbf{u}$ and covariance matrix V, while $\mathbf{x}$ and $\mathbf{x}_*$ are vectors containing the training and test inputs respectively. The shape of the prior is determined by the covariance matrix with sub-matrices $K(\cdot)$, where for example, $K(\mathbf{x}, \mathbf{x}_*)$ is an $n \times n_*$ covariance matrix holding the covariances between all pairs of training and test outputs, and the remaining $K(\cdot)$ are similarly defined.

Elements of the covariance matrices in (1) are given by a covariance function $k(x, x')$, which gives the covariance between the values of the process at x and x'. A popular standard covariance function which is frequently used for antenna modelling [18] is the squared-exponential (SE) covariance function:

$$k_{SE}(x, x') = \sigma_f^2 \exp\left[-0.5 \left(\frac{x - x'}{\tau} \right)^2 \right], \quad (2)$$

where σ_f^2 is a parameter that governs the variance of the process and τ is a positive length-scale parameter [15]. To make predictions, it is required that a posterior distribution be constructed by conditioning the test outputs $\mathbf{g}_*$ on the known training outputs $\mathbf{g}$; the posterior is given by $\mathbf{g}_* \mid \mathbf{x}_*, \mathbf{x}, \mathbf{g} \sim \mathcal{N}(\mathbf{m}, \Sigma)$ [15]. The mean $\mathbf{m}$ of the posterior is given by,

$$\mathbf{m} = K(\mathbf{x}_*, \mathbf{x}) K(\mathbf{x}, \mathbf{x})^{-1} \mathbf{g}, \quad (3)$$

and contains the most likely RCS magnitudes at the test frequencies in $\mathbf{x}_*$. Alternatively, the prediction at a point x_* may be expressed in terms of a sum of weighted

covariance functions placed at the training points [15]:

$$m_* = m(x_*) = \sum_{i=1}^{n} \alpha_i k(x_i, x_*), \quad (4)$$

where vector $\alpha = K(\mathbf{x}, \mathbf{x})^{-1} \mathbf{g}$, and $k(x_i, x_*)$ is the covariance function situated at training point x_i. The hyperparameters of the covariance function (e.g., σ_f^2 and τ in (4)) are optimised during training, which involves minimising the negative log marginal likelihood with respect to the hyperparameters [15, eq. (2.29)].

Used by itself, the above-mentioned SE covariance function is incapable of accurately modelling oscillatory responses of shoulder-launched missiles such as those shown below in Figs. 2 and 3. Previously [10], this difficulty was addressed by combining the SE covariance function, k_{SE}, with the standard periodic covariance function, k_{PER}, given by [15]:

$$k_{PER}(x, x') = \exp\left[-\frac{2}{\theta^2} \sin^2\left(\pi \frac{x - x'}{\lambda} \right) \right], \quad (5)$$

where the intervals between repetitions are determined by λ, while θ is a length-scale parameter. The resulting composite covariance function is given by [10]:

$$k_{SE \times PER} = k_{SE} \times k_{PER}, \quad (6)$$

$$= \sigma_f^2 \exp\left[-0.5 \left(\frac{x - x'}{\tau} \right)^2 \right] \times$$
$$\exp\left[-\frac{2}{\theta^2} \sin^2\left(\pi \frac{x - x'}{\lambda} \right) \right] \quad (7)$$

which has four hyperparameters, σ_f, τ, θ, and λ. While the results obtained using $k_{SE \times PER}$ for models of the Strela and Stinger missiles for front-on incidence were good [10], it is demonstrated in Section III below that predictive performance was significantly poorer when extended to rotated versions of the Strela as well as an Igla missile (front-on incidence and rotations).

The RCS responses of shoulder-launched missiles are intricate, oscillatory, quasi-periodic functions of frequency. In physics-based approaches to calculating RCS response approximations, the target is often modeled as a collection of point scatterers placed at defining structural positions of the target [1]. This approach leads to a model comprising sinusoidal oscillations whose periods are related to the spacings of the scatterers (see (1) below). Broadly speaking, the notion that multiple periods need to be taken into account suggests that a covariance function that explicitly allows multiple distinct sinusoidal oscillations might be a better modelling tool than $k_{SE \times PER}$ for RCS responses such as those shown in Fig. 3.

The spectral mixture (SM) covariance function, k_{SM} [17] is such a covariance function. For one-dimensional inputs, k_{SM} can be expressed as [17]:

$$k_{SM}(x, x') = \sum_{q=1}^{Q} w_q^2 \exp\left[-2\pi\sigma_q^2 (x - x')^2\right] \times$$
$$\cos\left[2\pi\mu_q (x - x')\right], \quad (8)$$

where Q is the number of spectral mixtures, and the hyperparameters w_q, μ_q, and σ_q^2 are respectively the weight, mean, and variance of the Gaussians comprising the qth mixture. This nomenclature arises as Bochner's theorem allows k_{SM} to be interpreted as the inverse Fourier transform of the sum of Q scale-location Gaussian spectral density mixtures, with each mixture containing two Gaussians centered symmetrically about the spectral origin [15, 17]. By comparison, the SE covariance function is the inverse Fourier transform of only a single Gaussian spectral density centered at the origin. The number of hyperparameters to be optimised for k_{SM} is $3Q$, compared to four hyperparameters for $k_{SE\times PER}$ used in [10].

In Section III, it is demonstrated that GP regression using k_{SM} gives very accurate results, significantly improving on those obtained using GP regression with $k_{SE\times PER}$. It was previously demonstrated that the point-scatterer concept in the form of a GTD-based approach was significantly less accurate than GP regression employing $k_{SE\times PER}$ in modelling the front-on RCS responses of missiles [10]. Tables 1 and 2 below show that k_{SM} in turn outperformed $k_{SE\times PER}$ for all rotations (including front-on incidence) of the Strela and Igla missiles considered. The apparent accuracy difference (k_{SM} versus point-scatterer concept) is perhaps surprising in light of the fact that both k_{SM} and the point-scatterer model make use of a number of sinusoidal terms with differing periods. It is therefore informative to compare the GP regression using k_{SM} in (3) after training to the point-scatterer view.

Under the latter approach, the reflections from the scatterers are combined with phase shifts which depend on the distances between the scatterers from the perspective of a radar, giving an RCS magnitude of,

$$RCS \approx \left| \sum_{i=1}^{S} a_i e^{j\phi_i} e^{j\beta d_i} \right|^2, \quad (9)$$

where S is the number of scatterers, each with magnitude a_i, phase φ_i, and position d_i, with $\beta = 2\pi f/c$ being the propagation phase constant where f is the frequency and c is the propagation velocity. It can be shown that the RHS of (9) reduces to:

$$RCS \approx \sum_{i=1}^{S} \sum_{j=1}^{S} k_{1ij} \cos\left[k_{2ij} + k_{3ij}(d_i - d_j)f\right], \quad (10)$$

where k_{nij}, $n=1$, 2, 3 are constants. In other words, (1) approximates the RCS magnitude by a sum of sinusoidal

functions of frequency. Each term takes effect over the whole frequency range (e.g., 5 to 15 GHz in Fig. 3), which suggests limited flexibility compared to the use of k_{SM} in (8). The summed, weighted multiple frequency components of k_{SM} (i.e., the mixtures) fulfil a similar role to that of basis functions (see (4)), but only have a significant effect in the vicinity of the training points they are placed at due to the decaying squared exponential component of k_{SM}. The placement of multiple mixtures locally at each training point makes GP regression using k_{SM} in (3) far more powerful than the point-source approximation in (1) despite the apparent similarity of these two models.

III. VERIFICATION EXAMPLES

Models of the F9K32 Strela-2 (SA-7 Grail) and Igla-S (SA-24 Grinch) missiles constructed from information freely available on the internet are shown in Fig. 1.[1]
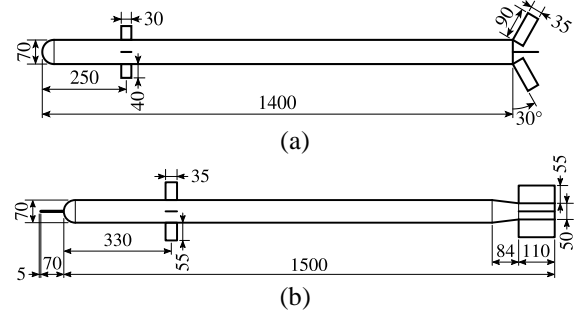
Fig. 1. The dimensions of: (a) Strela and (b) Igla missile models in mm.

FEKO release 2017.1 [19] was used to establish the ground truth data with 501 frequencies being simulated from 5 to 15 GHz (20-MHz steps) per missile using the method of moments (MoM) solver with default settings. Simulations included frontal on-axis incidence (defined as the 0° rotation), as well as incidence at rotations of 3°, 6°, 9°, 12°, and 15° in the horizontal plane measured relative to the missile axis from the front. This angular range covers hypothetical cases with the target ranging from a hovering helicopter (0°) to a cruising propellor-driven transport aircraft (15°). The incident wave was horizontally polarised, and the horizontal component of the reflected wave was considered for the RCS calculation.

Simulation run times and memory requirements were reduced by using electrical and magnetic symmetry where applicable. Maximum triangle edge lengths of a tenth of a wavelength were used, and further run-time reduction was achieved by generating separate meshes at each frequency. It was not possible to use high-frequency techniques such as PO as the main features

---

[1] The Igla proved more challenging to model than the Stinger considered in [10] and was thus used instead. For example, for front-on incidence the SE×PER function yielded a mean RMSE of 7.27% for the Igla (see Table 2) versus 1.24% for the Stinger [10].

are smaller than five wavelengths even at the highest frequencies [1]. A maximum of 285 GB of memory and a grand total of 670 hours of simulation time were required to simulate the two missiles, despite the small target sizes. Each simulation used a cluster of five computers, each with a minimum of 64 GB of memory and two 12-core Intel Xeon E5-2690 v3 processors running at 2.60 GHz.

Twenty sets of training data points (subsets of the ground truth simulation data) were compiled for each missile to verify that results were independent of specific configurations of training points [10]. To ensure that input frequency points were spread over the entire frequency range rather than being clumped together (cf. Fig. 3), the interval of 5 to 15 GHz was divided into equal sub-intervals, and one frequency point was uniformly randomly selected from each of these sub-intervals. The extreme frequency values (5 and 15 GHz) were then added if not yet present, giving a total of about 166 (Strela) or 168 (Igla) points.

A frequency step of 50 MHz or less is necessary to ensure that 1.5-m separation of the nose and tail of a missile can be resolved by the RCS magnitude [1, 10]. However, this estimate is somewhat optimistic as the nose-to-tail distance decreases with rotation, and interactions between other features of a target (e.g., the missile wings in Fig. 1) can produce variations over smaller frequency ranges. The use of 166 to 168 points is thus significantly lower than the estimated 201 required points.

Training consisted of gradient-based optimisation of the negative log marginal likelihood [15, eq. (2.29)], which is highly multi-modal. This necessitated considering multiple sets of hyperparameter starting values to ensure satisfactory results [10, 20]. For the spectral mixture covariance function in (8), a choice of $Q = 3$ mixtures gave a good compromise between flexibility and time required to optimise the hyperparameters. Experiments revealed that 750 sets of initial hyperparameter sets reliably gave satisfactory results for all runs; i.e. the hyperparameter set with the lowest negative log-likelihood always gave the best predictions, suggesting that model selection was robust.

Initial values of hyperparameters in (8) were selected according to a procedure suggested in [20]. The weights w_q, where $q = 1, ..., Q$, were set equal to the standard deviation of the training targets (i.e., simulated RCS magnitude values) divided by the number of mixtures Q. The repetition rates μ_q were uniformly randomly selected from a range which had zero as lower bound, and an upper bound that was proportional to the reciprocal of the smallest frequency spacing between the randomly-selected training points. The hyperparameters σ_q are the inverse length scales of the squared exponentrial constituent functions in (8). The initial length scales were taken to be the absolute values of random numbers drawn from a zero-mean normal

distribution that had a standard deviation that was equal to the overall range of the training data (length scales are defined as positive). It is worth noting that the length scale parameters σ_q determine the effective range of frequencies which are affected by each term of (8) for each training point.

The longest per-run training times was on the order of 60 minutes, which is far lower than the FEKO simulation time. For the SE×PER covariance function with four unknown hyperparameters, 300 sets of random starting values were used as a larger number did not improve results. Results for the hyperparameter sets with the lowest negative log-likelihood are reported below.

The errors obtained by each model were quantified using the normalised RMSE defined by:

$$\text{RMSE} = \frac{\sqrt{\dfrac{1}{n_*}\sum_{l=1}^{n_*}\left[\text{RCS}_p\left(l\right) - \text{RCS}_s\left(l\right)\right]^2}}{\max_l\left[\text{RCS}_s\left(l\right)\right] - \min_l\left[\text{RCS}_s\left(l\right)\right]}, \quad (11)$$

where the predicted and simulated linear RCS magnitudes at frequencies l are denoted $\text{RCS}_p(l)$ and $\text{RCS}_s(l)$ respectively. The results reported below only consider the test points (i.e., the subsets of the 501 available points remaining after the training points were removed) as the errors at the training points are negligible for GP regression with noise-free observations.

Tables 1 and 2 provide RMSE statistics for 20 runs of GP regression with the SE×PER and SM3 (SM with three mixtures) covariance functions for the Strela and Igla missiles, respectively.

The importance of considering different rotations is demonstrated by the fact that the most accurate results for the Strela in Table 1 are obtained when the rotation is small. However, these missiles may approach their targets at larger rotations, so errors in the RCS magnitude need to be small over the full range of rotations which will be encountered in practice.

The importance of considering different rotations is demonstrated by the fact that the most accurate results for the Strela in Table 1 are obtained when the rotation is small. However, these missiles may approach their targets at larger rotations, so errors in the RCS magnitude need to be small over the full range of rotations which will be encountered in practice.

The results in Table 1 indicate that both covariance functions provide accurate results for the Strela, with SM3 reducing the mean RMSE obtained by SE×PER by 50% or more for most rotations. The situation changes dramatically for the Igla in Table 2, where the accuracy of SM3 is considerably better than SE×PER, with mean RMSE varying from 3.26% to 7.27% for SE×PER and from 0.95% to 1.53% for SM3.

Tables 1 and 2 also show that SE×PER performance was more strongly influenced by the training data configurations associated with particular runs than SM3.

For example, the RMSEs at a 9° rotation varied from 0.83% to 5.17% for SE×PER versus 0.23% to 1.71% for SM3 in Table 1, and from 2.14% to 6.82% for SE×PER and from 0.37% to 3.59% for SM3 in Table 2.

Figure 2 compares SE×PER and SM3 predictive responses for the Strela missile at 9° rotation for a particular training data configuration (i.e., the same training points were used in both cases). For this run, the random selection of training points in the region 5 to 5.5 GHz produced no points at consecutive response maxima, which causes substantial inaccuracies in the SE×PER predictions. On the other hand, the expressive power of the SM3 covariance function allows the regression to infer the underlying response structure more effectively, yielding significantly better predictions over this range in spite of the unfavourably placed training points.

Figure 3 provides results for the Igla missile at 12° rotation that are representative of the GP models' mean predictive performance (i.e., the solution with the RMSE closest to the mean is shown in each case). While the SE×PER model follows the simulated response reasonably well, there are several frequencies with large errors, and some predictions even have negative values, which are not physically possible. Comparing the SE×PER and SM3 models in Fig. 3 clearly demonstrates the superior performance of SM3, which has both fewer and smaller significant deviations from the simulated response.

(a)

(b)
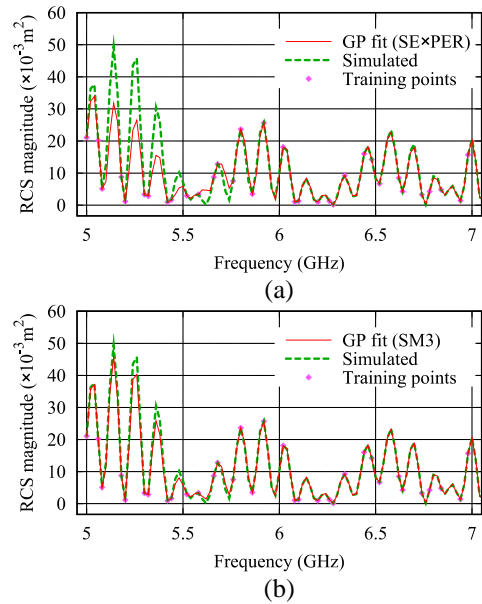
Fig. 2. GP predictive results for the Strela missile at 9° rotation using: (a) SE×PER (RMSE = 5.17%), and (b) SM3 (RMSE = 1.42%) covariance functions, compared to the simulated (true) RCS magnitude. Only the lower 2 GHz of the 10-GHz range is shown as errors over the remainder of the frequency range are negligible.

Table 1: RMSEs of Strela test data

Cov. Rot. Func.		Mean	Best	Median	Worst
SE×PER	0°	0.93%	0.66%	0.88%	1.57%
	3°	0.74%	0.50%	0.71%	1.46%
	6°	1.07%	0.63%	0.97%	2.02%
	9°	1.83%	0.83%	1.41%	5.17%
	12°	1.80%	1.00%	1.73%	3.55%
	15°	1.10%	0.45%	0.98%	3.29%
SM3	0°	0.49%	0.19%	0.49%	1.12%
	3°	0.34%	0.15%	0.30%	0.64%
	6°	0.52%	0.20%	0.45%	1.11%
	9°	0.87%	0.23%	0.75%	1.71%
	12°	0.86%	0.46%	0.64%	1.90%
	15°	0.81%	0.25%	0.62%	2.43%

Table 2: RMSEs of Igla test data

| Cov. Rot. Func.		Mean	Best	Median	Worst
SE×PER	0°	7.27%	3.94%	7.63%	10.08%
	3°	5.68%	3.09%	5.97%	7.66%
	6°	3.26%	1.94%	3.10%	5.11%
	9°	3.71%	2.14%	3.22%	6.82%
	12°	6.35%	5.12%	6.47%	7.96%
	15°	4.96%	2.78%	5.09%	7.50%
SM3	0°	1.33%	0.52%	1.20%	2.37%
	3°	0.95%	0.37%	0.87%	1.86%
	6°	1.08%	0.64%	1.00%	1.79%
	9°	1.32%	0.37%	1.18%	3.59%
	12°	1.53%	0.65%	1.29%	3.31%
	15°	1.35%	0.51%	1.25%	2.82%
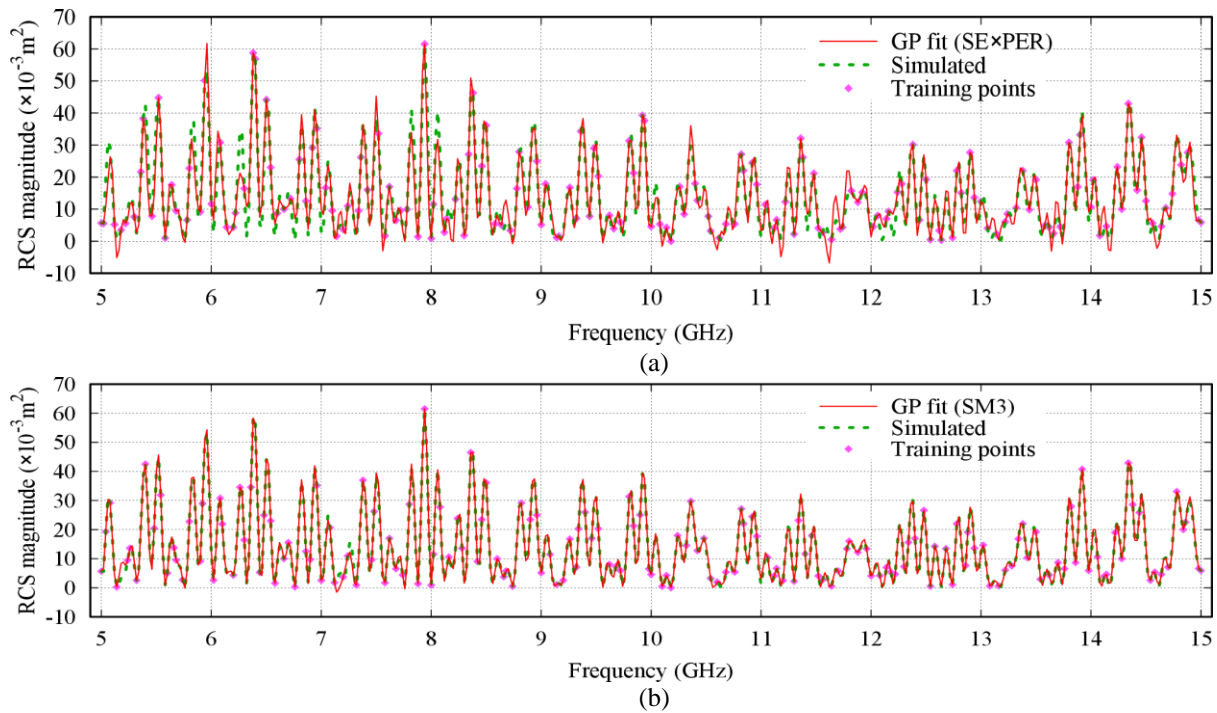
Fig. 3. Typical GP predictive results for the Igla missile at 12° rotation using: (a) SE×PER (RMSE = 6.35%), and (b) SM3 (RMSE = 1.50%) covariance functions, compared to the simulated (true) RCS magnitude.

VI. CONCLUSION

GP regression with an SM covariance function was used to model RCS magnitude responses of shoulder-launched missiles. The SM covariance function was selected since its constituent functions render it sufficiently flexible to account for oscillatory responses such as those shown in Figs. 2 and 3. Even using only three mixtures, the SM covariance function was demonstrated to yield very high predictive accuracies for all missiles and angles of incidence considered, significantly improving on results previously obtained for the same problem using a hybrid SE×PER covariance function. It was further shown that successful gradient-based optimisation of the covariance function hyperparameters could be carried out in spite of a severely multimodal negative log-likelihood function for the data considered. Significantly, the accuracy of the predictive results was shown to be almost independent of the configuration of the training points used.

ACKNOWLEDGMENT

REFERENCES

[1]   E. Knott, J. Schaeffer, and M. Tulley, *Radar Cross Section*. SciTech, Rayleigh, NC, Second ed., 2004.

[2]   G. W. Stimson, H. D. Griffiths, C. J. Baker, and D. Adamy, *Stimson's Introduction to Airborne Radar*. SciTech, Edison, NJ, Third ed., 2014.

[3]   A. A. Black, "Pulse doppler for missile approach warning," *J. Electron. Defence (JED)*, vol. 14, no. 8, pp. 44-52, Aug. 1991.

[4]   J. Yang and T. K. Sarkar, "Interpolation/extra-polation of radar cross-section (RCS) data in the frequency domain using the Cauchy method," *IEEE Trans. Antennas Propag.*, vol. 55, no. 10, pp. 2844-2851, Oct. 2007.

[5]   L. de Tommasi, B. Gustavsen, and T. Dhaene, "Accurate macromodeling Based on Tabulated Magnitude Frequency Responses," in *2008 12th IEEE Workshop on Signal Propagation on Inter-connects*, pp. 1-4, May 2008.

[6]   J. Yang, M. C. Taylor, Y. Zhang, and T. K. Sarkar, "Efficient interpolation of high-frequency domain data by phase smoothing," *Radio Sci.*, vol. 43, no. 04, pp. 1-15, Aug. 2008.

[7]   B. Persson and M. Norsell, "On modeling RCS of aircraft for flight simulation," *IEEE Antennas Propag. Mag.*, vol. 56, no. 4, pp. 34-43, Aug. 2014.

[8]   Y. Yang, Y. Ma, and L. Wang, "The simultaneous interpolation of target radar cross section in both the spatial and frequency domains by means of Legendre wavelets model-based parameter estimation," *Int. J. Aerospace Eng.*, vol. 2015,

2015.

[9] J. Yang and T. K. Sarkar, "Accurate interpolation of amplitude-only frequency domain response based on an adaptive Cauchy method," *IEEE Trans. Antennas Propag.*, vol. 64, no. 3, pp. 1005-1013, Mar. 2016.

[10] J. P. Jacobs and W. P. du Plessis, "Efficient modeling of missile RCS magnitude responses by Gaussian processes," *IEEE Antennas Wireless Propag. Lett.*, vol. 16, pp. 3228-3231, Nov. 2017.

[11] R. Carrière and R. L. Moses, "High resolution radar target modeling using a modified Prony estimator," *IEEE Trans. Antennas Propag.*, vol. 40, no. 1, pp. 13-18, Jan. 1992.

[12] L. C. Potter, D.-M. Chiang, R. Carriere, and M. J. Gerry, "A GTD-based parametric model for radar scattering," *IEEE Trans. Antennas Propag.*, vol. 43, no. 10, pp. 1058-1067, Oct. 1995.

[13] M. J. Gerry, L. C. Potter, I. J. Gupta, and A. Van Der Merwe, "A parametric model for synthetic aperture radar measurements," *IEEE Transactions on Antennas and Propagation*, vol. 47, no. 7, pp. 1179-1188, July 1999.

[14] W. Lee, T. K. Sarkar, H. Moon, and M. Salazar-Palma, "Computation of the natural poles of an object in the frequency domain using the Cauchy method," *IEEE Antennas Wireless Propag. Lett.*, vol. 11, pp. 1137-1140, 2012.

[15] C. E. Rasmussen and C. K. I. Williams, *Gaussian Processes for Machine Learning*. MIT Press, Cambridge, MA, 2006.

[16] K. Wang, D. Ding, and R. Chen, "A surrogate modeling technique for electromagnetic scattering analysis of 3-D objects with varying shape," *IEEE Antennas Wireless Propag. Lett.*, vol. 17, no. 8, pp. 1524-1527, 2018.

[17] A. G. Wilson, E. Gilboa, A. Nehorai, and J. P. Cunningham, "GPatt: Fast multidimensional pattern extrapolation with Gaussian processes," *arXiv preprint arXiv:1310.5288*, 2013.

[18] J. P. Jacobs and S. Koziel, "Two-stage framework for efficient Gaussian process modeling of antenna input characteristics," *IEEE Trans. Antennas Propag.*, vol. 62, no. 2, pp. 706-713, Feb. 2014.

[19] Altair Hyperworks, *FEKO User Manual*, 2017.

[20] A. G. Wilson, "Scalable kernel learning and Gaussian processes – Spectral mixture kernels," https://people.orie.cornell.edu/andrew/pattern/#spectral, Oct. 2018.

Warren P. du Plessis received the B.Eng. (Electronic) and M.Eng. (Electronic) and Ph.D. (Engineering) degrees from the University of Pretoria in 1998, 2003, and 2010 respectively, winning numerous academic awards including the prestigious Vice-Chancellor and Principal's Medal.

He spent two years as a Lecturer at the University of Pretoria, and then joined Grintek Antennas as a Design Engineer for almost four years, followed by six years at the CSIR. He is currently a Professor at the University of Pretoria, and his primary research interests are cross-eye jamming and thinned antenna arrays.

Jan Pieter Jacobs received the B.Eng., M.Eng., and Ph.D. degrees in Electronic Engineering from the University of Pretoria, Pretoria, South Africa, and a doctorate in Music from Yale University, New Haven, CT, USA.

He is a registered Professional Engineer in South Africa and is an Associate Professor in the Department of Electrical, Electronic and Computer Engineering at the University of Pretoria. His research interests include modelling and optimization of microwave antennas and devices, computational electromagnetics, slot antennas and arrays, and pattern recognition in music.

An Analytical Approach for a Miniaturized Unequal Wilkinson Power Divider with Filtering Response

Y. Torabi and G. Dadashzadeh

Department of Electrical Engineering
University of Shahed, Tehran, 3319118651, Iran
y.torabi@shahed.ac.ir, gdadashzadeh@shahed.ac.ir

Abstract ─ In this paper, a closed-form design method for a novel compact unequal filtering Wilkinson power divider, WPD, based on symmetric and asymmetric right/left-handed (CRLH) coupled-line circuit structures is proposed and investigated. The structure is composed of an input asymmetric CRLH coupled-line (A-CRLH) section along with two output symmetric CRLH coupled-line band-pass filter transformers to provide unequal filtering performance. The analytical design equations along with ideal closed-form expressions for scattering parameters are derived for the proposed structure by using in- and anti-phase (c/π-mode) decomposition method. To theoretically verify the proposed design approach, two filtering unequal WPDs with different high-power dividing ratios of 1:10 and 1:15 are designed and simulated. Finally, as a typical example, a practical filtering WPD with a power-splitting ratio of 1:15 operating at 1.4 GHz, is implemented with more than 55.5% size reduction as compared to conventional one. Good agreement between calculated, simulated and measured results verifies the effectiveness of the proposed power divider for miniaturized, large power dividing ratio and filtering applications.

Index Terms ─ CRLH, filtering, scattering parameters, unequal power divider.

I. INTRODUCTION

Various Wilkinson power dividers (WPD) with simultaneously filtering and unequal response are important components for microwave subsystems. As it is well known, for industrial systems and other applications like phased-array systems and beam-forming networks, compact unequal power dividers with arbitrary power division ratios and filtering response are required as key components. To date, the filtering performance of WPDs has been motivation of many research works and different techniques have been used in practice to provide unequal power dividing function with favorable selectivity [1]-[4], however, all the proposed topologies are primarily limited to lower power division ratios and/or non-exact analytical design

equations. Recently, the authors introduced in [5], that asymmetric composite right/left handed (A-CRLH) coupled-line structure, realized by loading host coupled transmission line medium with series capacitors and shunt inductors to the ground, has the capability to be flexibly designed for any desired modal characteristic impedances and frequency dispersion without manufacturing difficulty as opposed to the conventional coupled lines. By using this fact, a novel unequal WPD with high power splitting ratio is proposed, however, it is not able to effectively suppress the undesired frequency signals out of its operating bandwidth [5].

This paper documented here and in an earlier work published by the authors as the conference paper [6], is the first report on the application of symmetric and asymmetric CRLH coupled lines for the designing of a novel filtering WPD with the ability to simultaneously provide sharp filtering response with high power-dividing ratio as 1:15. The current study, presents a substantially expanded analysis of the briefly introduced earlier work [6], with analytic and measurement verifications. Particularly, synthesis equations along with ideal closed-form expressions for scattering parameters, which allow the designer to conveniently design and simulate the proposed structure, are derived. Furthermore, to demonstrate the proposed analytical design approach, two examples including unequal filtering WPDs with 1:10 and 1:15 power splitting ratios supported by S-plots obtained from analytical closed-form equations are presented. Finally, a prototype filtering 1:15 unequal WPD is implemented and tested for validation. The measured results verify the application of the proposed structure, experimentally.

II. THEORY AND DESIGN

Figure 1 (a) shows the outline of the proposed WPD. It comprises an A-CRLH coupled-line section as a quarter-wavelength transformer between input and output ports to provide unequal power division ratio and two output symmetric CRLH coupled-line band-pass filter transformers to fulfill the matching condition for the system impedance of 50 Ω as well as to obtain the

favorite selectivity in each transmission path. Typical A-CRLH coupled line as depicted in Fig. 1 (b), consists of two different CRLH transmission lines which can be assembled from N unit cells with right-handed (RH) and left-handed (LH) sections [5]. The LH section is based on lumped loading series capacitors (C_{La} and C_{Lb}) and shunt inductors (L_{La} and L_{Lb}) and the RH section is realized with conventional microstrip coupled lines as seen in Fig. 1 (b). Since each A-CRLH coupled-line section is implemented by periodically chaining N number of unit cells with electrical length 'p' much smaller than the wavelength, it can be regarded effectively homogeneous and characterized by the general coupled-mode differential equations [7]. To derive closed-form design equations, first of all, the power dividing ratio and filtering response analyses are investigated using coupled-mode formulation in sections A and B, respectively, then, the generalized scattering parameters are obtained in a closed-form in section C.
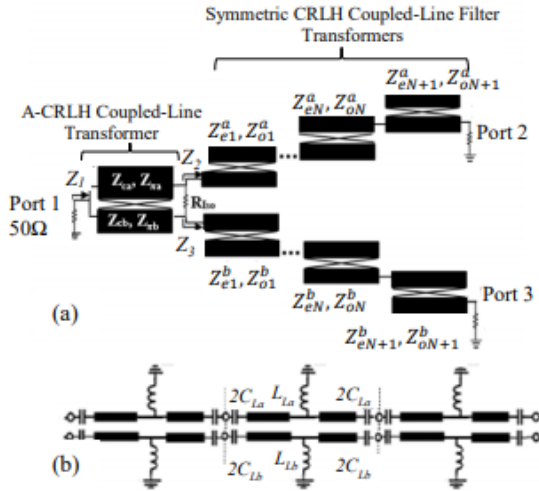

Fig. 1. (a) Schematic representation of a proposed unequal filtering WPD based on symmetric and asymmetric CRLH coupled lines, and (b) a typical structure of the asymmetric CRLH coupled lines.

A. Power-dividing ratio analysis

Based on in- and anti-phase (c/π-mode) decomposition method, the equivalent c-mode characteristic impedances of the A-CRLH coupled-line section (Z_{ca} and Z_{cb}) and isolation resistor (R_{Iso}) can be obtained as following to satisfy the demanding power dividing ratio, k^2, ($P_2/P_3=k^2$), with perfect input and output matching and isolation between output ports:

$$Z_{ca} = \sqrt{\frac{1+k^2}{k^2} Z_1 Z_2},$$

$$Z_{cb} = \sqrt{(1+k^2) k^2 Z_1 Z_2} = k^2 Z_{ca}, \quad (1)$$

$$R_{Iso} = (1+k^2) Z_2.$$

Here, Z_1 and Z_2 are the input and output impedances seen from ports 1 and 2, respectively, as indicated in Fig. 1 (a). From equation (1), the values of Z_{ca} and Z_{cb} can be estimated based on desired power-dividing ratio of k^2. The demanded modal characteristic impedances, Z_{ca} and Z_{cb}, can be straightforwardly tuned for wide-ranging values by proper choosing the loading element values of A-CRLH coupled-line section, $C_{La/b}$ and $L_{La/b}$, as well as coupling capacitance value, C_m, without manufacturing complexity based on following equations [5]:

$$C_{La/b} = \frac{Np(Z_{\pi a/b} + Z_{ca/b})}{\omega \pi Z_{\pi a/b} Z_{ca/b} + \omega^2 L_R Np(Z_{\pi a/b} + Z_{ca/b})}, \quad (2)$$

$$L_{La/b} = \frac{4NpZ_{\pi a/b} Z_{ca/b}}{\omega \pi (Z_{\pi a/b} + Z_{ca/b}) + 4Np\omega^2 C_R Z_{\pi a/b} Z_{ca/b}}, \quad (3)$$

$$C_m = \frac{\pi}{4Nk\omega p}\left(\frac{1}{Z_{\pi a}} - \frac{1}{Z_{ca}}\right) = \frac{k\pi}{4N\omega p}\left(\frac{1}{Z_{\pi b}} - \frac{1}{Z_{cb}}\right). \quad (4)$$

Here, parameters L_R, C_R and C_m are per unit cell self-inductance, self-capacitance, and mutual capacitance, respectively that model the edge-coupled interconnecting transmission line segments. For estimating loading element values, RH-parameters including C_R and L_R as two degrees of freedom can be assumed arbitrary, resulting in the favorite TL characteristic impedances for intersecting transmission lines. This avoids the fabrication limitation to realize high power division ratios in conventional coupled lines. With selected values of C_R and L_R and determined values of N and p, the loading element values can be easily calculated from equations (2) and (3).

B. Filtering response analysis

As well as unequal performance, the proposed WPD supports the filtering response by using two symmetric CRLH coupled-line filter transformers near the output ports as shown in Fig. 1 (a). The structure of CRLH coupled-line band-pass filter employed in the design of output filter transformers is shown in Fig. 2, wherein symmetric CRLH coupled-line sections with equivalent even- and odd-mode characteristic impedances of Z_{ei} and Z_{0i}, $i = 1,\ldots, N+1$, and electrical length of θ have been used in a cascaded form to develop a narrowband band-pass filter. Its equivalent circuit is also represented in Fig. 2, where each CRLH coupled-line section is roughly modeled using two CRLH transmission line sections with characteristic impedance of Z_0 and the electrical length of $\theta = -\pi/2$, added on both ends of an inverter J_i ($i=1,\ldots, N+1$). By equating their propagation constants and image impedances, the following equation is found for even- and odd-mode characteristic impedances of each CRLH coupled-line section:

$$Z_{ei/oi} = Z_0(1 \pm J_i Z_0 \pm (J_i Z_0)^2) \quad i = 1,\ldots, N+1. \quad (5)$$

The equation (5) indicates that the even-mode and odd-mode characteristic impedances of a CRLH coupled-line section can be described by the system impedance

of Z_0 and the admittance inverter of J_i, which has the same depiction of those of conventional coupled-line filters [7]. Therefore, the design equations of a typical couple-line filter can be assumed to design the CRLH coupled-line filter transformer. The values of admittance inverters for a band-pass filter are given by [7]:

$$Z_0 J_1 = \sqrt{\frac{\pi\Delta}{2g_1}}, Z_0 J_i = \frac{\pi\Delta}{2\sqrt{g_{n-1}g_n}}, Z_0 J_{N+1} = \sqrt{\frac{\pi\Delta}{2g_N g_{N+1}}}. \quad (6)$$

Here, g_0, g_1,..., g_{n+1} are the elements of an equal-ripple low-pass prototype with a normalized cutoff $\Omega_c=1$ and Δ is the fractional bandwidth of the band-pass filter. Consequently, the transmission matrix of the CRLH coupled-line filter can be written for even-order and odd-order, N, as following:

$$T_{N=odd} = \begin{bmatrix} T0 & 0 \\ 0 & T1 \end{bmatrix}, T_{N=Even} = \begin{bmatrix} 0 & T2 \\ T3 & 0 \end{bmatrix},$$

$$T0 = (-1)^{N+1/2}\left(\frac{\prod\limits_{n=1}^{N+1/2} J_{2n-1}}{\prod\limits_{n=1}^{N+1/2} J_{2n}}\right), T1 = (-1)^{N+1/2}\left(\frac{\prod\limits_{n=1}^{N+1/2} J_{2n}}{\prod\limits_{n=1}^{N+1/2} J_{2n-1}}\right), \quad (7)$$

$$T2 = (-1)^{N/2} jZ_0^2\left(\frac{\prod\limits_{n=1}^{N/2+1} J_{2n-1}}{\prod\limits_{n=1}^{N/2} J_{2n}}\right), T3 = (-1)^{N/2} \frac{j}{Z_0^2}\left(\frac{\prod\limits_{n=1}^{N/2} J_{2n}}{\prod\limits_{n=1}^{N/2+1} J_{2n-1}}\right).$$

Since in the proposed power dividing circuitry, such CRLH coupled-line filter is employed instead of the conventional output transformers in the ideal WPD, hence, its transmission matrixes should be approximately equal to transmission matrix of ideal impedance transformer to satisfy matching condition which can be determined as following:

$$T_{Ideal} = \begin{bmatrix} 0 & j(-1)^n Z_{0j} \\ j(-1)^n / Z_{0j} & 0 \end{bmatrix}, \quad (8)$$

where, Z_{0j}, $j = 2, 3$, is the characteristic impedance of the conventional transmission line functioning as an impedance transformer at output 2 or 3:

$$Z_{02} = \sqrt{50Z_2} = 50\sqrt{\frac{1}{k}}, \quad Z_{03} = \sqrt{50Z_3} = 50\sqrt{k}. \quad (9)$$

Equating (7) and (8) implies that the even-order CRLH coupled-line filter with system impedance of Z_0 equal to Z_{0j}, $j = 2, 3$, should be employed for satisfying matching conditions and improving the selectivity in each transmission path. The design guideline for the proposed WPD can be briefly summarized as:

Step1) Calculate Z_{Ca} and Z_{Cb} of A-CRLH coupled-line transformer based on equation (1) for preferred power dividing ratio (k^2). **Step2**) Calculate $Z_{e/oi}^a$ and $Z_{e/oi}^b$ ($i = 1, ..., N + 1$) of output CRLH coupled-line filter transformers based on equation (5) for desired selectivity in each transmission path and satisfying

matching condition. **Step3**) Find the corresponding mutual capacitance value, C_m, from equation (4) and Set suitable values for the strip width, w, and separation, s, using the approximate coupled-line formula [8] and appropriate circuit simulator for required C_m. **Step4**) Calculate the values of RH parameters, C_R and L_R, for determined values of w and s. **Step5**) Determine the capacitance and inductance values of chip or distributed loading element values L_L and C_L from equations (2) and (3).
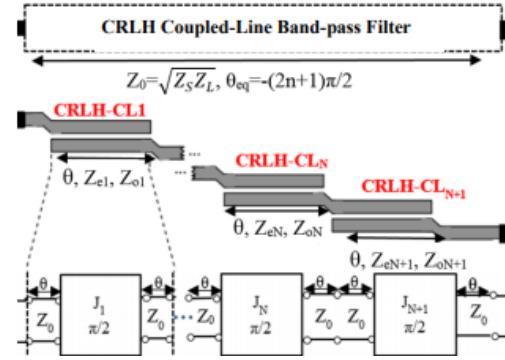
Fig. 2. CRLH coupled-line band-pass filter with its equivalent circuit.

C. Analytical closed form scattering parameters for the proposed WPD

As the common circuit simulators like Agilent Advanced Design System (ADS) do not have electrical parameter-based transmission line models for the asymmetric coupled lines without physical dimensions, hence, these circuit simulation tools, cannot give the accurate and lossless scattering parameters for the proposed WPD. In order to have convenient accurate analysis, it is necessary to study the theoretical scattering parameters of the presented WPD. In this section, the closed-form mathematical expressions for scattering parameters are presented. Consequently, once the design parameters are defined based on theoretical analysis in sections A and B, the scattering parameters of the power divider can be conveniently obtained using the ideal-closed form equations. Due to the asymmetric nature of the proposed WPD, in- and anti-phase (c/π-mode) analysis is adopted to analyze the proposed structure. After using c/π-mode analysis, Fig. 1 can be simplified to two half circuits as depicted in Figs. 3 (a) and 3 (b). Here, $\theta_c = \beta_c Np$ and $\theta_\pi = \beta_\pi Np$ represent the equivalent c- and π-mode electrical lengths of the A-CRLH coupled-line section consisting of N unit-cells of p-length. $Z_{Ca/b}$ and $Z_{\pi a/b}$, are the equivalent c- and π-mode characteristic impedances of the asymmetric CRLH coupled-line section calculated from equation (1). Moreover, for easy analysis, each output filter transformer composed of the cascade connection of $N+1$

CRLH coupled-line sections is represented by its transmission matrix, $[A_{eq}^{a/b}, B_{eq}^{a/b}, C_{eq}^{a/b}, D_{eq}^{a/b}]$, which is equal to the product of the $[A, B, C, D]$ matrices of individual two-port CRLH coupled-line sections, $[A_k^{a/b}, B_k^{a/b}, C_k^{a/b}, D_k^{a/b}]$ as:

$$\begin{bmatrix} A_{eq}^{a/b} & B_{eq}^{a/b} \\ C_{eq}^{a/b} & D_{eq}^{a/b} \end{bmatrix} = \prod_{k=1}^{N+1} \begin{bmatrix} A_k^{a/b} & B_k^{a/b} \\ C_k^{a/b} & D_k^{a/b} \end{bmatrix}. \quad (10)$$

The $[A, B, C, D]$ matrix for each two-port CRLH coupled-line section, which is approximately modeled by using two transmission lines added on both ends of an inverter, $J_i^{a/b}$, is thus given by equation (11):

$$\begin{bmatrix} A_k^{a/b} & B_k^{a/b} \\ C_k^{a/b} & D_k^{a/b} \end{bmatrix} = \begin{bmatrix} \cos\theta & jZ_0^{a/b}\sin\theta \\ j\dfrac{\sin\theta}{Z_0^{a/b}} & \cos\theta \end{bmatrix} \times$$
$$\begin{bmatrix} 0 & -j/J_k^{a/b} \\ -jJ_k^{a/b} & 0 \end{bmatrix} \begin{bmatrix} \cos\theta & jZ_0^{a/b}\sin\theta \\ j\dfrac{\sin\theta}{Z_0^{a/b}} & \cos\theta \end{bmatrix}. \quad (11)$$

Where, $Z_0^{a/b}$ and θ are the characteristic impedance and electrical length of the added CRLH transmission lines. In the abovementioned expressions, 'a' and 'b' subscripts refer to the output transformers of path 'a' and path 'b', respectively. To the c-mode equivalent circuit, Fig. 3 (a), the ABCD–matrix between two ports (Port 1 and Port 2) can be obtained as:

$$\begin{bmatrix} A_c^{a/b} & B_c^{a/b} \\ C_c^{a/b} & D_c^{a/b} \end{bmatrix} = \begin{bmatrix} \cos(\theta_c) & jZ_{ca/b}\sin(\theta_c) \\ j\dfrac{\sin(\theta_c)}{Z_{ca/b}} & \cos(\theta_c) \end{bmatrix} \begin{bmatrix} A_{eq}^{a/b} & B_{eq}^{a/b} \\ C_{eq}^{a/b} & D_{eq}^{a/b} \end{bmatrix}. (12)$$

According to the transformation between *ABCD* matrix and scattering parameters, the closed-form c-mode scattering parameters can be calculated as equation (13). The final input scattering parameter, S_{11}, and transmission parameters, S_{12} and S_{13}, of Fig. 1 can be derived as:

$$S_{11} = \frac{S_{11,c}^a + S_{11,c}^b}{2}, \quad S_{21} = \frac{kS_{21,c}^a}{\sqrt{1+k^2}}, \quad S_{31} = \frac{S_{21,c}^b}{\sqrt{1+k^2}}. \quad (14)$$

Considering the π-mode sub-circuits in Fig. 3 (b),

the output scattering parameters of π-mode can be also obtained as equation (15), where $Z_{in}^{a/b}$ is the input impedance looking into the equivalent half-circuit at the output port as indicated in Fig. 3 (b). To calculate this impedance, first, the π-mode ABCD–matrix from port 2 to port 1 is obtained as equation (16), shown in the following, then as the two-port sub-network is terminated with a short circuit at port 1 in π-mode excitation, $Z_{in}^{a/b}$ can be derived based on ABCD parameters as equation (17):

$$S_{22,\pi}^{a/b} = \frac{Z_{in}^{a/b} - 50}{Z_{in}^{a/b} + 50}, \quad (15)$$

$$\begin{bmatrix} A_\pi^{a/b} & B_\pi^{a/b} \\ C_\pi^{a/b} & D_\pi^{a/b} \end{bmatrix} = \begin{bmatrix} A_{eq}^{a/b} & B_{eq}^{a/b} \\ C_{eq}^{a/b} & D_{eq}^{a/b} \end{bmatrix} \begin{bmatrix} 1 & 0 \\ \dfrac{1}{R_{Iso}^{a/b}} & 1 \end{bmatrix} \times$$
$$\begin{bmatrix} \cos(\theta_\pi) & jZ_{\pi a/b}\sin(\theta_\pi) \\ j\dfrac{\sin(\theta_\pi)}{Z_{\pi a/b}} & \cos(\theta_\pi) \end{bmatrix}, \quad (16)$$

$$Z_{in}^{a/b} = \frac{B_\pi^{a/b}}{D_\pi^{a/b}} = \frac{j(A_{eq}^{a/b} + \dfrac{B_{eq}^{a/b}}{R_{Iso}^{a/b}})Z_{\pi a/b}\sin(\theta_\pi) + B_{eq}^{a/b}\cos(\theta_\pi)}{j(C_{eq}^{a/b} + \dfrac{D_{eq}^{a/b}}{R_{Iso}^{a/b}})Z_{\pi a/b}\sin(\theta_\pi) + D_{eq}^{a/b}\cos(\theta_\pi)}, (17)$$

The final output scattering parameters, S_{22} and S_{33}, and the isolation parameter, S_{23}, can be expressed by:

$$S_{22} = \frac{k^2 S_{22,c}^a + S_{22,\pi}^a}{1+k^2}, S_{33} = \frac{S_{22,c}^b + k^2 S_{22,\pi}^b}{1+k^2}, S_{23} = \frac{k(S_{22,c}^b - S_{22,\pi}^a)}{1+k^2}. (18)$$

To demonstrate the proposed design method, 2 examples including WPDs with 1:10 and 1:15 power dividing ratios and fractional bandwidth of 15% comprising an A-CRLH coupled-line section with two 2th order symmetric CRLH coupled-line filters are designed. The corresponding S-plots obtained from the analytical closed-form equations, (13)-(18), for RO4003 substrate with dielectric constant of 3.55 and thickness of 0.813 mm are presented in Fig. 4. It is seen that the proposed structure can function as an unequal power divider with high-selectivity band-pass responses.

$$\begin{bmatrix} S_{11,c}^{a/b} & S_{12,c}^{a/b} \\ S_{21,c}^{a/b} & S_{22,c}^{a/b} \end{bmatrix} = \frac{\begin{bmatrix} \begin{array}{cc} [50(A_{eq}^{a/b} - Z_1^{a/b}C_{eq}^{a/b}) + B_{eq}^{a/b} - Z_1^{a/b}D_{eq}^{a/b}]\cos(\theta_c) + & \\ j[50(C_{eq}^{a/b}Z_{ca/b} - Z_1^{a/b}\dfrac{A_{eq}^{a/b}}{Z_{ca/b}}) + D_{eq}^{a/b}Z_{ca/b} - \dfrac{Z_1^{a/b}B_{eq}^{a/b}}{Z_{ca/b}})]\sin(\theta_c) & 2\sqrt{50Z_1^{a/b}} \\ & \\ 2\sqrt{50Z_1^{a/b}} & [-50(A_{eq}^{a/b} + Z_1^{a/b}C_{eq}^{a/b}) + B_{eq}^{a/b} + Z_1^{a/b}D_{eq}^{a/b}]\cos(\theta_c) + \\ & j[-50(C_{eq}^{a/b}Z_{ca/b} + Z_1^{a/b}\dfrac{A_{eq}^{a/b}}{Z_{ca/b}}) + D_{eq}^{a/b}Z_{ca/b} + \dfrac{Z_1^{a/b}B_{eq}^{a/b}}{Z_{ca/b}})]\sin(\theta_c) \end{array} \end{bmatrix}}{[50(A_{eq}^{a/b} + Z_1^{a/b}C_{eq}^{a/b}) + B_{eq}^{a/b} + Z_1^{a/b}D_{eq}^{a/b}]\cos(\theta_c) + j[50(C_{eq}^{a/b}Z_{ca/b} + Z_1^{a/b}\dfrac{A_{eq}^{a/b}}{Z_{ca/b}}) + D_{eq}^{a/b}Z_{ca/b} + \dfrac{Z_1^{a/b}B_{eq}^{a/b}}{Z_{ca/b}})]\sin(\theta_c)}. \quad (13)$$
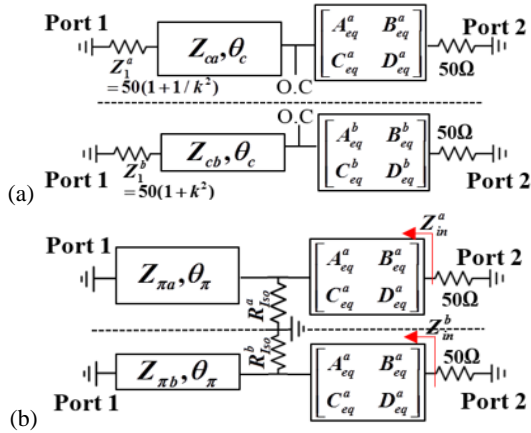
Fig. 3. Equivalent half-circuits of the proposed WPD: (a) c-mode half-circuit and (b) π-mode half-circuit.

III. CIRCUIT IMPLEMENTATION

To experimentally verify the proposed design method, a prototype filtering unequal WPD with high power dividing ratio of 1:15 and fractional bandwidth of 15% is fabricated for operating at 1.4 GHz as shown in Fig. 5. It is implemented on R04003 substrate with dielectric constant of 3.55 and thickness of 0.813mm. It consists of an A-CRLH coupled-line transformer compromises conventional coupled lines loaded by surface mount technology (SMT) components with inductance and capacitance values derived for preferred power dividing ratio of k^2 and two output CRLH coupled-line impedance transformers composed of three symmetric CRLH coupled lines formed of coupled lines loaded by distributed elements including shorted stub inductors and series interdigital capacitors (IDCs) with inductance and capacitance values derived for the desired selectivity based on aforementioned design principle. The geometrical parameters of IDCs and shorted stub inductors meeting the required electrical LC parameters can be determined with the help of established approximate formulas, [8], as a starting guess for design and then applying a suitable optimization algorithm in a full-wave software like high frequency structure simulator (HFSS) for accurate realizing the desired characteristics. The designed values of lumped loading elements with geometrical dimensions are as following: C_{La} = 3.2 pF, C_{Lb} = 0.3 pF, L_{La} = 3.2nH, L_{Lb} = 16nH, $w'_{1a} = w'_{3a} = 0.3mm$, $w'_{2a} = 0.4mm$, $w'_{1b} = w'_{3b} = 0.8mm$, $w'_{2b} = 0.9mm$, $s'_{1a} = s'_{3a} = 0.2mm$, $s'_{2a} = 0.4mm$, $s'_{1b} = s'_{3b} = 0.9mm$, $s'_{2b} = 0.4mm$, $s_{1a} = s_{3a} = 0.1mm$, $s_{2a} = 0.6mm$, $s_{1b} = s_{3b} = 0.2mm$, $s_{2b} = 0.4mm$, $l^{IDC}_{1a} = l^{IDC}_{2a} = l^{IDC}_{3a} = 8.7mm$, $l^{IDC}_{1b} = l^{IDC}_{3b} = 8.7mm$, $l^{IDC}_{2b} = 7.7mm$, $l^{stub}_{1a} = l^{stub}_{3a} = 13mm$, $l^{stub}_{2a} = 12.5mm$, $l^{stub}_{3b} = l^{stub}_{1b} = 9.4mm$, $l^{stub}_{2b} = 8.9mm$.

To avoid confusion, the geometrical values are denoted by their corresponding CRLH coupled-line section number, i.e., the dimensions that correspond to CRLH coupled-line section represented by C_{L2a} are denoted by $w'_{2a}, s'_{2a}, s_{2a}, l^{IDC}_{2a}, l^{stub}_{2a}$ and the same for other sections.

The measurement results along with full-wave and analytical theory simulations using high frequency structure simulator (HFSS) and MATLAB are depicted in Fig. 6. As shown, there is a good agreement between HFSS, theory and measurement data and the desired power division ratio with relatively sharp band-pass responses is achieved. The measured insertion loss of S_{21} and S_{31}, are about -1.3 and -13.1 dB, respectively. The measured center frequency is 1.4 GHz, with the fractional bandwidth of 15.5%. The in-band return loss, $|S_{22}|$, $|S_{33}|$ and $|S_{11}|$, are better than 30 dB. The isolation, $|S_{23}|$, is greater than 35 dB over the whole band. The measured in-band phase difference between output ports is between -2.5° and 2.8°. The performance comparison of the proposed power divider with other compact unequal WPDs in terms of power splitting ratio, filtering response, relative occupied area and isolation between output ports is summarized in Table 1. As the results show, the proposed WPD has the most compact size and the highest power division ratio, since the circuit size is reduced to 44.5% of the conventional one and the power splitting ratio is enhanced to 1:15. Additionally, despite power ratio, the proposed design has a filtering function with a steep skirt selectivity and high isolation in a wide frequency range.
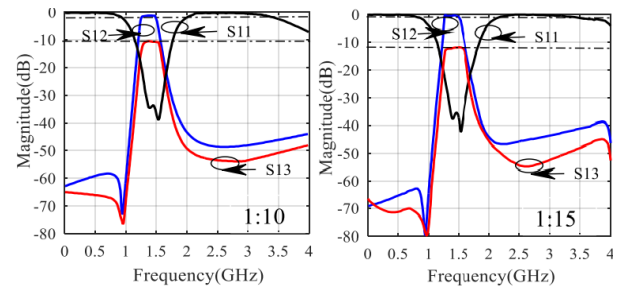

Fig. 4. Theoretical results of WPDs with (left) 1:10 and (rigth) 1:15 power dividing ratios.
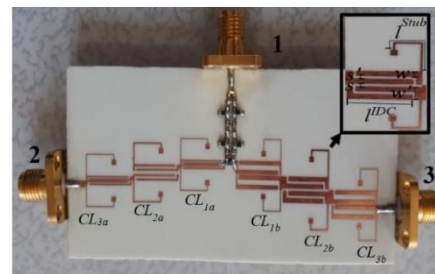
Fig. 5. Photograph of the proposed filtering 1:15 WPD fabricated on RO4003.

Table 1: Performance comparison with the previous works

Ref.	Filtering Response	Dividing Ratio	Relative Area (%)	Isolation (in-band)
[1]	Yes	1:3/2	200	>23 dB
[3]	Yes	1:8	40	N/A
[4]	Yes	1:2	200	>20 dB
[5]	No	1:15	41.3	>25 dB
[9]	No	1:6	100	>20 dB
[10]	No	1:4	100	>20 dB
[11]	No	1:10	100	>20 dB
This work	Yes	1.15	44.5	>35 dB
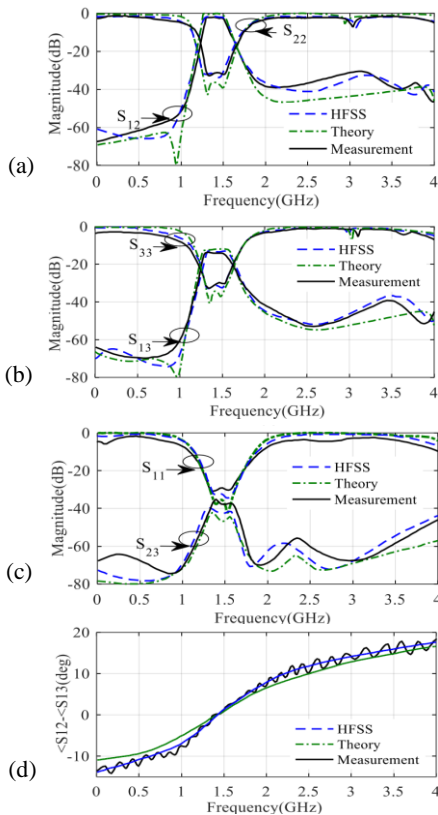


Fig. 6. Measured and simulated results of the filtering power divider: (a) S_{12} and S_{22}, (b) S_{13}, and S_{33}, (c) S_{23}, and S_{11}, and (d) phase difference of output ports.

IV. CONCLUSION

This paper presents a new compact filtering unequal WPD with high power-splitting ratio application using symmetric and asymmetric CRLH coupled lines. The analytical design equations along with ideal closed-form expressions for scattering parameters are derived for the proposed structure by using in- and anti-phase (c/π-mode) decomposition method. To verify the theoretical design procedure, an unequal compact WPD with a high-power division ratio of 1:15 is designed, simulated and fabricated at 1.4 GHz. The measurement results along with theoretical and simulation data validate that the proposed WPD not only exhibits a sharp frequency selectivity but also a large power splitting ratio with desired performance.

REFERENCES

[1] P. H. Deng and L. C. Dai, "Unequal Wilkinson power dividers with favorable selectivity and high-isolation using coupled-line filter transformers," *IEEE Transactions on Microwave Theory and Techniques*, vol. 60, no. 6, pp. 1520-1529, June 2012.

[2] L. Gao and X. Y. Zhang, "Novel 2:1 Wilkinson power divider integrated with bandpass filter," *Microwave and Optical Technology Letters*, vol. 55, no. 3, pp. 646-648, 2013.

[3] M. Danaeian, A. R. Moznebi, K. Afrooz, and H. Hakimi, "Miniaturised equal/unequal SIW power divider with bandpass response loaded by CSRRs," *Electronics Letters*, vol. 52, no. 22, pp. 1864-1866, 2016.

[4] Z. Zhuang, Y. Wu, L. Jiao, W. Wang, and Y. Liu, "Wideband balanced-to-unbalanced filtering unequal power divider with wide stopband and isolation," *Electronics Letters*, vol. 53, no. 13, pp. 892-894, 2017.

[5] Y. Torabi and G. Dadashzadeh, "A compact 1:15 unequal Wilkinson power divider using A-CRLH coupled lines," *Microwave and Optical Technology Letters*, vol. 60, no. 1, pp. 117-122, 2017.

[6] Y. Torabi and G. Dadashzadeh, "Compact filtering unequal Wilkinson power divider with 1:15 power dividing ratio using composite right/left handed-coupled lines," *International Conference on Electromagnetics in Advanced Applications (ICEAA)*, 2017.

[7] R. Mongia, I. Bahl, and P. Bhartia, *RF and Microwave Coupled-Line Circuits*. Norwood, MA: Artech House, 1999.

[8] C. Caloz and T. Itoh, *Electromagnetic Meta-materials: Transmission Line Theory and Microwave Applications: the Engineering Approach*. Hoboken, N.J: John Wiley & Sons, 2006.

[9] C.-P. Chang, C.-C. Su, S.-H. Hung, Y.-H. Wang, and J.-H. Chen, "A 6: 1 unequal Wilkinson power divider with EBG CPW," *Progress In Electromagnetics Research Letters*, vol. 8, pp. 151-159, 2009.

[10] M. Moradian and H. Oraizi, "Application of grooved substrates for design of unequal Wilkinson power dividers," *Electronics Letters*, vol. 44, no. 1, June 2008.

[11] B. Li, X. Wu, and W. Wu, "A 10:1 unequal Wilkinson power divider using coupled lines with two shorts," *IEEE Microwave Wireless Component Letter*, vol. 19, no. 12, pp. 789- 791, Dec. 2009.

Yalda Torabi was born in Zanjan, Iran in 1987. She received her B.Sc. degree in Electrical Engineering from Tabriz University, Tabriz, Iran in 2009 and the M.Sc. degree from the Iran University of Science and Technology (IUST), Tehran, Iran in 2012 and is currently working towards the Ph.D. degree in Electrical Engineering at Shahed University, Tehran, Iran.

Gholamreza Dadashzadeh was born in Urmia, Iran, in 1964. He received the B.Sc. degree in Communication Engineering from Shiraz University, Shiraz, Iran in 1992 and M.Sc. and Ph.D. degree in Communication Engineering from Tarbiat Modarres University (TMU), Tehran, Iran, in 1996 and 2002, respectively. He is currently a Professor in the Department of Electrical Engineering at Shahed University, Tehran, Iran.

Active Inductor Design for Reconfigurable Bandpass Microstrip Filter Applications

Mehmet A. Belen [1] and Peyman Mahouti [2]

[1] Department of Electric and Electronic Engineering
University of Artvin Çoruh, Artvin, Turkey
mehmetalibelen@artvin.edu.tr

[2] Department of Electrical and Electronics Engineering
Istanbul Arel University, Buyukcekmece, Istanbul, Turkey
pmahouti@arel.edu.tr

Abstract ─ Herein, the design of an active inductor and its typical application for a reconfigurable band-pass filter circuit are presented. The Active Inductor design consists of a passive variable phase and amplitude compensating network and a highly linear inverting amplifier in order to form a gyrator-C design. The design allows a wide frequency range for tuning the equivalent inductance and resistance values that enable it to be used as a filter design where the inductor equivalent resistance increases and improves signal rejection for band-pass filter applications. As a typical application, first-order active band-pass filter had been designed and prototyped. The simulation and measurement results of the design are compared with the performance results of counterpart designs in literature. From the experimental results, it can be concluded that the proposed design is a suitable model for design of tunable band pass filter circuits. The design has an operation band of 0.7-2.1GHz with the equivalent inductance value of 2.6nH.

Index Terms ─ Active inductor, band-pass filter, gyrator-C, reconfigurable, UHF Band.

I. INTRODUCTION

A challenge for research is now to design devices that are reconfigurable and adaptive (or tunable) for their characteristics to switch from one standard to another [1-2]. Moreover, whether it is in transmission or receiver mode, the signal filtering is a core function of the processing chain because it realizes the separation of useful signals that one wishes to deal and of out-of-band signals that one wishes to reject. Similarly, the important development of RF equipment imposes new constraints on microwave channels. One of the most critical functions is the re-configurability in the RF filtering. This requires a wide band tuning to meet new specifications, whether technical or financial, and can adapt the model associated with different standards.

Most of traditional architectures of tunable band pass filters use the spiral inductors that include many limitations such as a low Q factor, small and not-tunable inductance, a low self-resonant frequency and a large silicon area [3-4]. Therefore, in order to resolve these crucial problems, realization of Active Inductors (AI) becomes a more promising option having the particular advantage of wide frequency tuning, necessary for multi-standard systems [5-8]. AI shows small silicon area (it only takes about 1% -10% of passive inductor area), a higher inductance value, efficient frequency tuning range, and higher Q factor which make AI a suitable solution for design of tunable filter.

In this work, design of an AI for a typical application of tunable band-pass filter circuit had been studied. Firstly, an AI design which is consist of a passive variable phase, amplitude compensating network and a highly linear inverting amplifier in order to form a gyrator-C design has been studied. The proposed AI design achieves a wide frequency range for tuning the equivalent inductance and resistance values, which make it a suitable solution for being the tuning element in a band pass filter design. In Section IV, a typical application of a first-order active band pass filter circuit has been presented, using the AI model deigned in Section III. The simulated results had been justified with the experimental results. Furthermore, the proposed AI based band-pass filter design had been compared with the counterpart design in literature. From the experimental results, it can be concluded that the proposed design is a suitable model for design of tunable band pass filter circuits.

II. GYRATOR PROPERTIES AND NON-IDEALITIES

The realization of an active inductor relies on the basic gyrator theory [9-13], where two trans-conductors are connected end-to-end and one end of the gyrator is

bonded to a capacitor as shown in Fig. 1 [14].
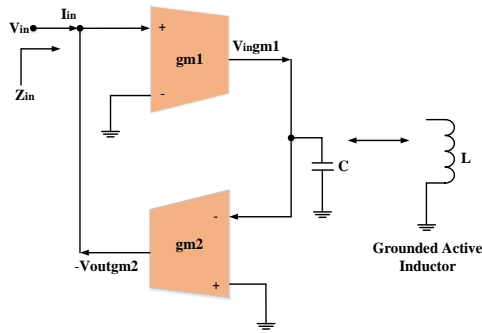
Fig. 1. Basic concept of a gyrator-C.

The expression of its input impedance Z_{in} is expressed as follows:

$$Z_{in} = \frac{V_{in}}{I_{in}} = \frac{j\omega C}{g_{m1}g_{m2}} \ . \tag{1}$$

Then the equivalent inductance is given by:

$$L = \frac{C}{g_{m1}g_{m2}} \ . \tag{2}$$

In this case, the realization of an active inductance can be performed by using simple trans-conductance transistors having a similar effect of gyrator. Since these transistors have intrinsic parasitic capacitances, the simulation of the inductance is based on the idea of using these parasites. So, we have no need of external capacity, which is an important technique for minimizing the circuit size.

III. ACTIVE INDICTOR

In Fig. 2 a schematic for an AI design using medium-power bipolar transistors are given. The design consists of a common collector non-inverting and a common emitter inverting trans-conductance amplifiers using BFP450 BJT transistors. In Table 1, a list of the elements used in AI design is presented.
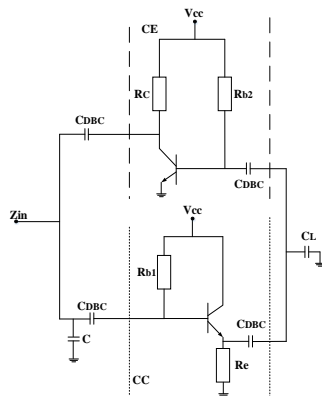

Fig. 2. Simplified schematic of AI design.

Table 1: List of the elements used in AI design

R_{b1}	10 Ω	C	4.7pF
R_{b2}	200 Ω	C_L	15 pF
R_e	100 Ω	C_{DCB}	10pF
R_c	220 Ω	Substrate	FR4,1.56mm

The BFP450 [15] is a high linearity wideband NPN bipolar RF transistor. The collector design supports voltages up to $V_{CEO}=$ 4.5 V and currents up to $I_C=$ 170 mA. With its high linearity at currents as low as 50 mA the device supports energy efficient designs. The typical transition frequency is approximately 2.4 GHz, hence the device offers high power gain at frequencies up to 3 GHz in amplifier applications. The simulated input impedance results of the design is given in Fig. 3, where the real values of the input ımpedance has a variation around of 2-3 Ω and the imaginary part has a variation of 2-60 Ω over the frequency band.
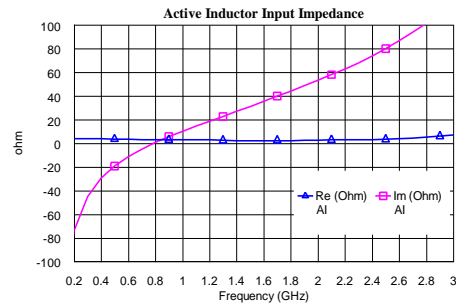
Fig. 3. Simulated input impedance for $V_{CC}=$ 3 V.

In Fig. 4 the simulated results of different input power of -20 dBm to +20 dBm with step width of 10 dBm is applied to the input of the AI design to analyse the power consumption. The design's power consumption is stable within the range of -20dBm to 10dBm which is around 65mW while the design start to consume 10% more power (72mW) with +20dBm input power. Thus, it can be concluded that the transistors used in design enter in saturation state after 10 dBm input power.

(a)

(b)
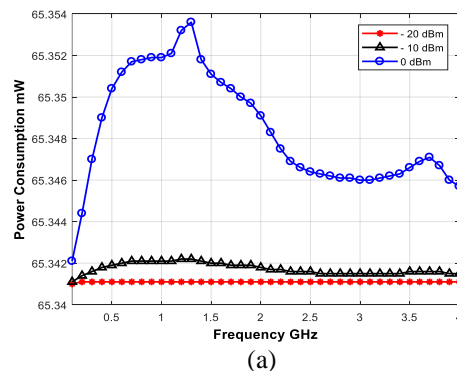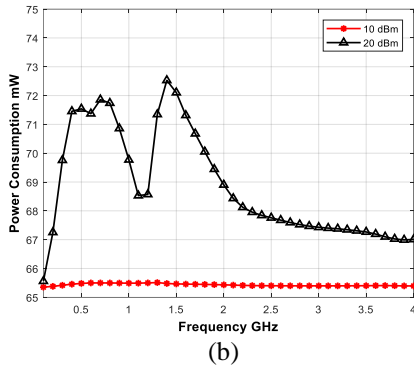
Fig. 4. Power consumption for input power of: (a) -20dBm, 0dBm and (b) 10dBm, 20dBm for V_{CC}= 3 V.

In Fig. 5 (a) the schematic of a first-order band pass filter with AI is given where with this concept it is possible to achieve high Q value in designs. Moreover since usage of a spiral inductor requires larger space in substrate, has narrow band, impedance and interference usage of active inductor which provides higher band and higher Q factor value is much efficient than the traditionally spiral inductors. Also in Fig. 5 (b), the schematic layout of the AI filter is given.

(a)

(b)
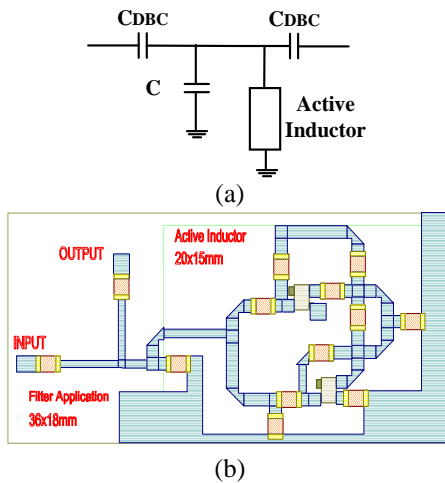
Fig. 5. AI based filters: (a) schematic and (b) layout.

IV. A TYPICAL APPLICATION: ACTIVE BAND-PASS FILTER

Herein, the measurement results of the fabricated first-order active Band-Pass filter design given in Fig. 6 are studied. The filter design has been fabricated on a FR4 substrate using standard SMD passive components and two BFP450 transistors. The measured S_{11} & S_{21} parameters of the prototyped filter have been obtained using an Anritsu 37397d vector network analyzer and had been presented in Fig. 7 alongside of the simulated results.
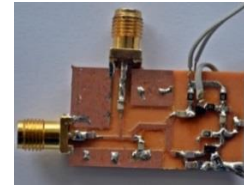
Fig. 6. Fabricated AI-based band-pass filter.
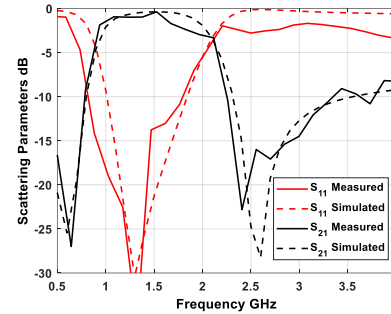
Fig 7. Simulated and measured scattering parameters for V_{CC}= 1V.

As it can be observed from Fig 8, by changing the DC bias voltage value of AI from 1-3 V it is possible to shift the frequency of the band pass filter by 300MHz. Furthermore, in Table 2 a compression of the proposed AI based filter with counterpart design has been presented.

(a)

(b)
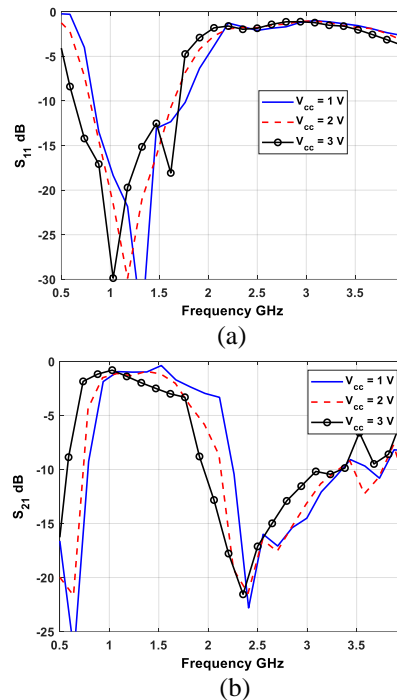
Fig. 8. Measured: (a) return loss and (b) insertion loss, with respect to the variation of voltage.

Table 2: Comparison of the proposed filter design with counterpart models in literature

| Model	Type	Order	f_c or Tunining Range GHz	Bandwidth GHz	Voltage Range
Here	SiGe	1	1.165-1.435	~1	1 to 3
[5]	SiGe	1	0.6	0.3	---
[14]	0.35um CMOS	4	0.52-0.72	0.25	2.7
[16]	0.45um CMOS	2	2.56	0.03	+/-1
[17]	0.35um CMOS	2	0.980-1.09	---	2.7

V. CONCLUSION

As it can be seen from the measurement results, a suitable model for design of a tunable AI had been achieved. The design has an operation band of 0.7-2.1GHz with the equivalent inductance value of 2.6nH. Also, for a typical application example for the designed AI, it implementation for a first order band-pass active filter is studied. The measured scattering parameter performance of the tunable band pass filter make it a suitable candidate for use in practical system applications.

REFERENCES

[1] W. Elhamdani, F. Temcamani, B. Delacressonniere, and M. Alami, "Filtre actif accordable À base d'inductance active en technologie CMOS," In: *Workshop Sur Les Technologies, De l'Information Et De La Communication*, WOTIC 09, pp. 1-4, 2009.

[2] P. Mahouti, "Design optimization of a pattern reconfigurable microstrip antenna using differential evolution and 3D EM simulation-based neural network model," *Int J RF Microw. Comput. Aided Eng.*, 29:e21796. https://doi.org/10.1002/mmce.21796, 2019.

[3] T. Bakken and J. Choma, "Gyrator-based synthesis of active on-chip inductances," *Analog Integrated Circuits and Signal Processing*, vol. 34, no. 3, pp. 171-181, 2003.

[4] H. Xiao and R. Schaumann, "A 5.4-Ghz high-Q tunable active-inductor bandpass filter in standard digital CMOS technology," *Analog Integrated Circuits and Signal Processing*, vol. 51, no. 1, pp. 1-9, 2007.

[5] G. Leuzzi, V. Stornelli, and S. Del Re, "A tunable active inductor with high dynamic range for band-pass filter application,"' *IEEE Trans. Circuits Syst. II, Exp. Briefs*, vol. 58, no. 10, pp. 647-651, 2011.

[6] L. Pantoli, V. Stornelli, and G. Leuzzi, "Class AB tunable active inductor," In *Electronics Letters*, vol. 51, no. 1, pp. 65-67, DOI:10.1049/El.2014.3877, 2015.

[7] S. Saad, M. Mhiri, A. B. Hammadi, and K. Besbes, "A 5-Mw, 1.2–3.5-Ghz capacitive degeneration in LC-digitally-controlled oscillator for nano-satellite frequency synthesizers in 90-Nm CMOS," *Journal of Circuits, Systems and Computers*, vol 25, no. 12, pp. 1650159, Dec. 2016.

[8] J. A. Torres and J. C. Freire, "K band sige HBT single ended active inductors," *Integration, The VLSI Journal*, vol. 52, pp. 272-281, 2016.

[9] T. Bakken and J. Choma, "Gyrator-based synthesis of active on-chip inductances," *Journal of Analog Integrated Circuits and Signal Processing*.

[10] B. D. Tellegen, "The gyrator: A new electric network element," *Phillips Research Reports*, vol. 3, pp. 81-101, 1949.

[11] M. M. Reja, K. Moez, and I. Filanovsky, "A wide frequency range CMOS active inductor for UWB bandpass filters," *52nd IEEE Int. Midwest Symp. Circuits and Systems*, MWSCAS'09, (Cancun, Mexico), pp. 1055-1058, Aug. 2009.

[12] L. C. Ler, A. K. Bi A'ain, and A. V. Kordesch, "Compact, high-, and low-current dissipation CMOS differential active inductor," *IEEE Microwave and Wireless Components Letters*, vol. 18, no 10, P. 683-685, 2008.

[13] Z. Guo, W. Zhang, H. Xie, C. Ding, Z. Lu, G. Xing, and Y. Zhang, "Improved quality-factor of cascode-grounded active inductor," *In Proceedings of the ICMMT (IEEE, Shenzhen)*, pp. 1-3, 2012.

[14] Y. Wu, X. Ding, M. Ismail, and H. Olsson, "RF bandpass filter design based on CMOS active inductors," *IEEE Transactions on Circuits and Systems II: Analog and Digital Signal Processing*, vol. 50, no 12, pp. 942-949, 2003.

[15] https://www.infineon.com/cms/en/product/rf-wireless-control/rf-transistor/high-linearity-si-and-sigec-transistors-for-use-up-to-6-ghz/bfp450/

[16] V. Kumar, R. Mehra, and A. Islam, "A 2.5 GHz low power, high-Q, reliable design of active bandpass filter," in *IEEE Transactions on Device and Materials Reliability*, vol. 17, no. 1, pp. 229-244, Mar. 2017. doi: 10.1109/TDMR.2017.2652142.

[17] S. Bantas and Y. Koutsoyannopoulos, "CMOS active-LC bandpass filters with coupled-inductor Q-enhancement and center frequency tuning," in *IEEE Transactions on Circuits and Systems II: Express Briefs*, vol. 51, no. 2, pp. 69-76, Feb. 2014. doi: 10.1109/TCSII.2003.821521.

Mehmet Ali Belen received his Ph.D degree in Electronics and Communication Engineering from the Yıldız Technical University in 2016. His current research interests are in the areas of, device modeling, computer aided microwave circuit design, monolithic microwave integrated circuits, and antenna arrays, active/passive microwave components especially in the field of metamaterial-based antennas and microwave filters.

Peyman Mahouti received his Ph.D. degree in Electronics and Communication Engineering from the Yıldız Technical University in 2016. The main research areas are analytical and numerical modelling of microwave devices, optimization techniques for microwave stages, and application of artificial intelligence based algorithms.

Analysis of Lossy Multiconductor Transmission Lines (MTL) Using Adaptive Cross Approximation (ACA)

A. Mueed, Y. Zhao*, Y. Wei, Z. B. Zhu, and Q. L. Liu

Department of Electrical and Automation Engineering
Nanjing Normal University, Nanjing, 210046, China
engr.mueed@live.com, zhaoyang2@njnu.edu.cn*, 61197@njnu.edu.cn, 1822628862@qq.com,
2668265779@qq.com

Abstract ─ In this article, an efficient adaptive cross approximation (ACA) algorithm is employed for the lossy of MTL such as propagation matrix, attenuation loss, dielectric loss and characteristic impedance are evaluated. ACA solver is stable and convenient to solve the compression and approximation of low-rank matrix because adaptive refinement is used to generate the optimal mesh. The integral equation (IE) solver along with adaptive cross approximation (ACA) is used to reduce the computational time and memory size. In the proposed algorithm, the complexities become linear. Therefore, the ACA provides less memory size and less computation cost. The results are compared with the latest state of the art existing work for validation.

Index Terms ─ Adaptive cross approximation, attenuation constant, characteristic impedance, integral equation, losses in multiconductor transmission line (MTL), propagation constant.

I. INTRODUCTION

In the past few decades, electromagnetic compatibility (EMC) has received considerable attention in the scientific community. The numerical schemes are used for the analysis of frequency dependent multiconductor transmission line (MTL) problems. The MTL parameters are generally attained from the computational electromagnetics. The traditional and advanced techniques for MTL are applied in various fields. But the integral equations have some numerical difficulties associated with its integral formula, singularity problems, complex assembly of the populated matrix and time-consuming [1-7].

In the existing literature, various mathematical methods for the simulation of MTL are discussed, for example, finite difference time domain (FDTD) [8], finite element method (FEM) [9] and method of moment (MOM) [10]. The integral equation with the MOM is widely used in EMC problems [11-12].

MOM is a powerful method for solving complex geometries such as those found in EMC problems. The algebraic integral equation method is used for conducting and non-conducting surface under the boundary condition. The discretization process is carried out with the help of MOM, which is considered the most efficient technique. MOM is used to discretize the integral equation into matrix form with subblock basis function [13-15].

The singular value decomposition (SVD) method reduces the computational complexities of deficient low-rank matrix [16]. ACA is an algebraic nature algorithm, which relies on the rank-deficient property between the orders of the basis function of well-separated groups. The grouping of basis function for the iterative solver is used to overwhelm the shortcomings of the traditional method. Therefore, the basis function for the block structure of the dense matrix is developed. Moreover, the groups (subblocks) have the low-rank matrix attribute and the ACA is applied on these properties to reduce the computational performance [17-23].

Based on the existing literature, it can be concluded that ACA is an efficient methodology for the numerical analysis of MTL, therefore used in this paper. The S-matrix, Z-matrix and Y-matrix are achieved from the ACA approach which are used for the analysis of MTL parameters. The lossy transmission line parameters such as dielectric loss, propagation constant loss and characteristic impedance are calculated through the proposed algorithm. The active impedance matching technique, FET transistors named as CGH40006P, is used for the matching of transmission line. To validate effectiveness of the ACA approach, the simulations are carried out in the ANSYS EM-environment and the ADS software. Finally, the results are compared to validate the dominant performance of proposed scheme.

The organization of the rest of the paper is as follows. In Section I, literature review is discussed about MTL. In Section II, the mathematical equation of MTL is described. Section III covers the comprehensive procedure about the adaptive cross approximation, implementation of dielectric constant, characteristic impedance and propagation constant. In Section IV,

lossy model simulation and validation of results are presented. Finally, Section V concludes the work.

II. MULTICONDUCTOR TRANSMISSION LINE MODEL

In this section, we considered a MTL having M-conductors with one conductor grounded. The total length of the transmission line (TL) is L which is divided into small number of segmets. However, a unit meter length is considered for the analysis. According to the Telegram's equation, lossy transmission line constraints are given [6].

$V(z)$ is the line voltage of $(n \times 1)$ vectors and $I(z)$ is the line current of n vectors. The ith element under the test is voltage V_i and current I_i, respectively. The second order simultaneous equation of the MTL is:

$$\begin{cases} \dfrac{\partial^2 V(z)}{\partial z^2} = ZYV(z), \\ \dfrac{\partial^2 I(z)}{\partial z^2} = YZI(z), \end{cases} \quad (1)$$

where:

$$\begin{cases} Z = R + j\omega L \\ Y = G + j\omega C \end{cases}.$$

The basic model of the MTL line is illustrated in Fig. 1.
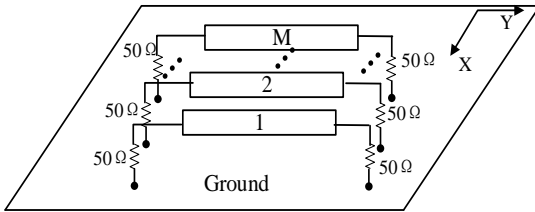
Fig. 1. Simple MTL model.

The Green's function of the MTL for the Helmholtz equation is:

$$E_r(z) = \dfrac{-jk_1}{2\pi} \int_\Omega G(r,r') \dfrac{\partial E(r')}{\partial n} dl' - \dfrac{-j}{2\pi k_1} \int_\Omega G(r,r')E(z)dl', \quad (2)$$

where:

$$G(r,r') = \dfrac{1}{|r-r'|}\left(e^{-jk_1|r-r'|}\right).$$

$K_1 = \omega\sqrt{\varepsilon\mu_0} = \omega\sqrt{\mu_0\,\sigma^r}$ is a constant, ω is the angular frequency, μ_0 is the permeability, σ^r is the conductivity of the conductor, S^r is the cross sectional area of under test conductor, $\dfrac{\partial E(r)}{\partial z}$ is the electric voltage of the excited field and ε is complex permittivity of the lossy line.

The basis function for the MTL is:

$$E_z = \sum_{r=1}^{M}\sum_{i=1}^{N^{(r)}} \alpha_i^{(r)} b_i^{(r)}(r), \quad (3)$$

where b_i is the basis function, $N^{(r)}$ is the total number of

segments and α is the coefficient.

A. Dielectric loss model

In this subsection, the dielectric loss model is presented. The MTL model is frequency dependent. The material for the models are lossy and the properties of the material are shown in the Table 1. The properties of the dielectric material are taken as same for all cables and calculated with the help of ACA techniques. The characteristic of lossy material verses frequency is shown in Fig. 2.

From the equation (2), the dielectric parameter is $K_1 = \omega\sqrt{\mu_0\,\sigma^r}$. The complex conductivity for the lossy model is:

$$\sigma_c = Y_c \dfrac{d}{A}, \quad (4)$$

where:

$$\sigma_c = \sigma + j\omega\varepsilon_r.$$

The complex permittivity at the angular frequency is:

$$\varepsilon_c = \varepsilon' - j\varepsilon'' = \varepsilon' - j\dfrac{\sigma_c}{\omega\varepsilon_0}. \quad (5)$$

The kth iteration of the lossy model for complex permittivity is:

$$\varepsilon_c = \sum_{i=1}^{k}\left(\dfrac{j\omega\tau\varepsilon_h}{1+j\omega\tau}\right). \quad (6)$$

where:

ε_h is the dielectric at high frequency,
ε_l is the low frequency dielectric constant,
$\omega = 2\pi f$ is an angular frequency,
τ is the relaxation time.

The loss tangent for the lossy model is:

$$\tan(\delta) = \dfrac{\varepsilon_l - \varepsilon_h}{(\omega\tau\varepsilon_h + \dfrac{\varepsilon_l}{\omega\tau})}. \quad (7)$$
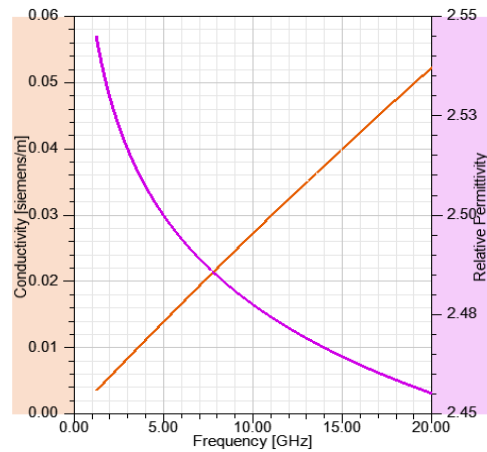

Fig. 2. Lossy material property.

Table 1: Properties of lossy material

Parameter	Value
Relative Permeability	2.5
Relative Permitivity	1
Bulk Conductivity	0
Dielectric Loss Tangent	0.1
Magnetic Loss Tangent	0
Landa G Factor	2

B. Characteristics impedance and propagation constant

The equation (1), describes the compact form of the MTL. The condition for the lossy MTL is $R \ll \omega L$ and $G \ll \omega C$. The propagation loss matrix is:

$$\gamma = \frac{R}{2}\sqrt{\frac{C}{L}} + \frac{G}{2}\sqrt{\frac{C}{L}} + j\omega\sqrt{LC}, \qquad (8)$$

where:

$$\mathrm{Re}(\gamma) = \alpha = \frac{R}{2}\sqrt{\frac{C}{L}} + \frac{G}{2}\sqrt{\frac{C}{L}},$$
$$\mathrm{Im}(\gamma) = \beta + j\omega\sqrt{LC},$$

α is the attenuation constant which consists of two losses. The first and second terms describe the conductor loss and the dielectric loss respectively. β is the propagation constant. The characteristic impedance for the lossy MTL is:

$$Z_c = \sqrt{\frac{L}{C}}\left\{1 - \frac{jR}{2\omega L} + \frac{jG}{2\omega C}\right\}, \qquad (9)$$

where Z_c is characteristics impedance.

B.1. Perfectly matched

In this subsection, the perfectly matched condition of transmission line is discussed. The condition for the perfectly matched load is $Z_o = Z_L$, which means that no energy is reflected back, and maximum power is delivered to the load.
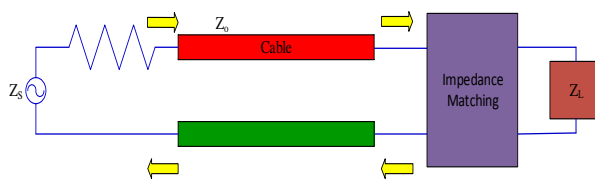

Fig. 3. Simple impedance matching model.

The active impedance matching technique is used for the perfectly matched transmission line in Fig. 3. The FET transistor CGH40006P [24] is used for the active matching technique. The high electron mobility transistor (HEMT), gallium nitride (GaN) is a type of FET unmatched transistor. The HEMT offers high gain and broad bandwidth capabilities for making the ideal and linear compressed amplifier. The HEMT has high power and high reliability, which provides a high degree of freedom and the versatile nature of properties. This FET transistor works in a wide range of frequencies between 1GHz-10GHz. The complex source impedance and load impedance are according to the datasheet.

III. ADAPTIVE CROSS APPROXIMATION

ACA is an iterative procedure for approximation of the low-rank matrix and approximate the original matrix without filling the entire matrix entries. However, ACA is a suboptimal algorithm, which gives a more significant number of independent vectors than other optimal algorithms.

In this paper, the sparse matrix is obtained from the integral equation of the MTL. This matrix is fully populated. The sparse matrix is converted into low-rank matrix. ACA technique is used to compress the matrix and evaluate the useful information, which is relevant for the low-rank matrix. This low-rank matrix is also called the Subblocks. This low-rank matrix is very suitable to calculate the behavior of transmission line at different frequencies with the help of an ACA approach. Therefore, the ACA approach is more suitable to solve the low-rank matrix. The post-processing calculation gives the S-Matrix, Z-Matrix, characteristic impedance, propagation, and attenuation constant. In this paper, the ACA is implemented for the low-rank matrix $P^{p \times q}$, which gives better compression quality. The matrices obtained from the ACA are propagation loss matrix, dielectric loss matrix, and characteristic impedance matrix.

Let $P := \{p_1, p_2, \ldots \ldots, p_M\}$ and $Q := \{q_1, q_2, \ldots \ldots, q_M\}$ be the two low-rank matrix. ACA approximation is a rank deficient matrix by a product of two matrices in an iterative process:

$$A = [P]^{p \times k}[Q]^{k \times q}. \qquad (10)$$

Let $p \times q$ block matrix which is compressed by ACA in k steps (number of iterations), where k is less than M. So the matrix P has $p \times k$ dimension, and the matrix Q has $q \times k$ dimension. At every step of the algorithm (number of iteration), each row and column are calculated by the previous value (last iteration). Each number of entries are updated and then calculate the approximation error. This process continues until the approximation error is smaller than the predefined value. The convergence criteria for the ACA algorithm are maximum delta and number of passes. The improvement of solution needs more number of passes per refinement to concise the solution. Therefore, the ACA algorithm has less memory size and computation cost. ACA is more efficient, so the memory requirement and computation time becomes linear which is $k(p + q)$ and $k^2(p + q)$ respectively. A number of operations are required for the approximation of the low-rank matrix by the ACA are $\varphi(PQ)$.

The matrix $p \times q$ is divided into subblocks $p_1 \times q_1$, $p_2 \times q_2$ which is geometrically well-separated. The admissible condition for the dense populated matrix is:

$$\eta dist(p_1, q_1) \geq \min\{diamp_1, diamq_1\}. \quad (11)$$

The subblock concerning to $p_1 \times q_1$, is called admissible block. The block patches must satisfy (10), If not satisfied, this matrix cannot be compressed and the process should be repeated to fulfill the admissible condition. For an admissible pair, the ACA provides the vector $p_k := \frac{\hat{p}_k}{(\hat{p}_k)_{ik}} \epsilon P^p$ and $q_k \epsilon P^q$ with the iteration process:

$$\hat{p}_k := p_{jk} - \sum_{i=1}^{k}(q_i)_{jk} \, p_i, \quad (12)$$

$$p_k := p_{ik} - \sum_{i=1}^{k}(p_i)_{jk} \, q_i. \quad (13)$$

The maximum condition for the number of entries as:

$$0 \neq \left|(\hat{p}_k)_{ik}\right| \geq \left|(\hat{p}_k)_i\right|. \quad \forall \; i=1,2,.....M. \quad (14)$$

The accuracy ε can be found by inspecting the norm of p_k and q_k to satisfy the required k-rank of approximation if:

$$\left\|p_{k+1}\right\|_2 \left\|q_{k+1}\right\|_2 \leq \varepsilon \left\|PQ^T\right\|. \quad (15)$$

The simple flow diagram for the adaptive cross approximation is shown in Fig. 4.
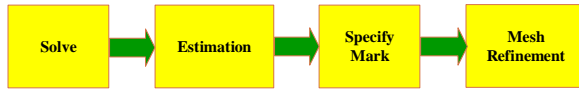
Fig. 4. Simple flow chart of ACA.

IV. NUMERICAL SIMULATION

In this section, numerical simulations are performed to check the effectiveness and correctness of the ACA algorithm for the frequency dependent losses parameters. The simulations of proposed algorithm are carried out in ANSYS HFSS, which is based on MOM. The FEM is implemented based on Q2D-Quasi solver. Both results are compared to check the validity of the algorithm. For proposed model, there are 14-conductors in the MTL. The start and stop frequencies are 0.5GHz and 10GHz respectively. The tolerance for the ACA is 0.002 (maximum value of delta, which is helpful for the convergence to solution). The specification of each cable is in Table 2. The model of MTL is in Fig. 5. The efficiency in term of memory computation is shown in Fig. 6.

A. Dielectric loss

The dielectric loss has a vital role in the performance of MTL. Dielectric loss depends upon the properties of the material such as imperfect conductivity and imperfect conductor. The dielectric loss is calculated through ACA algorithm. The results are compared with the lossless and losses at Tan(0.1) and Tan(0.2). The compared result is shown in Fig. 7.
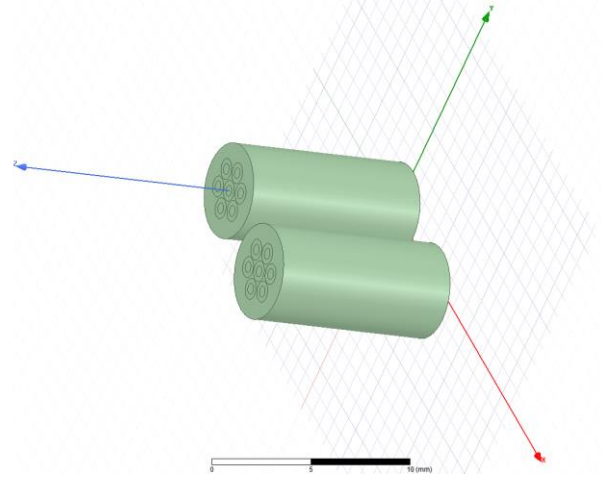

Fig. 5. Simulation model of the stranded cable.
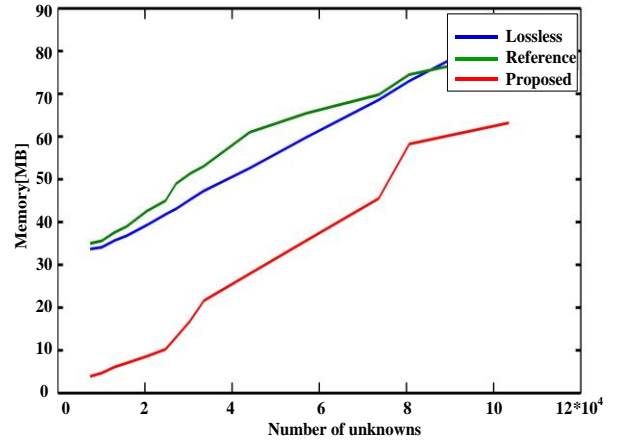
Fig. 6. Memory comparison of ACA.

Table 2: Parameters of lossy MTL model

| Parameter	Value
Conductor Diameter	2mm
Dielectric Diameter	4mm
Conductor Material	PEC
Dielectric Material	Lossy Material
Height	10mm
Transparency	0.6
Frequency	10GHz
Number of Adaptive Passes	15
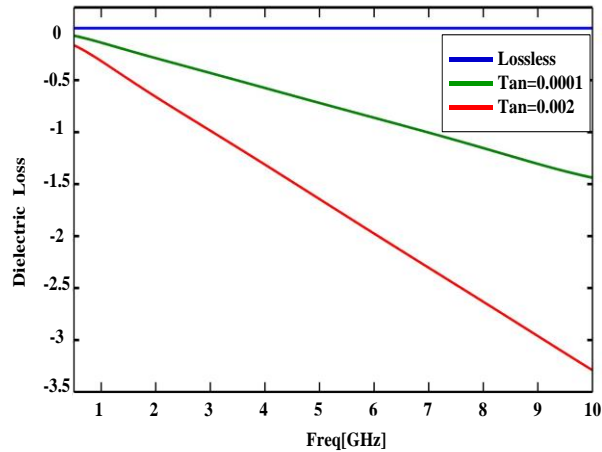
Fig. 7. Dielectric Loss of MTL.

B. Characteristics impedance and attenuation loss

In this subsection, the propagation matrix and characteristic impedance matrix of the MTL are calculated. The parameters of lossy MTL model are shown in Table 1. In this simulation, number of iterations

(number of adaptive passes) is 15 with frequency ranges from 0.5 to 10GHz and 951-sweep point steps. The number of adaptive passes and maximum delta value can be adjusted according to the convergence of solution. This data gives the real and imaginary point to analyze the propagation loss (attenuation loss and phase loss) and characteristic impedance. To verify the algorithm result, comparison takes place with the commercial software, Quasi 2D solver, finite element method [25] and the IEEE paper [26]. Both models are drawn in ANSYS environment with same parameters and is compared the result. The comparison is shown in Fig. 8 which depicts the numerical result for the propagation loss. The X- and Y-axis are normalized values.

The magnitude and angle of characteristic impedance are shown in Fig. 9 and Fig. 10. Adaptive cross approximation summary in Table 3 shows lossless and lossy model behavior at different tangent loss. Moreover, the memory usage is also given in Table 3 which shows the required memory to compute the matrix assembly and structure assembly (Tetrahedra) at different number of passes.

Table 3: ACA algorithm

| Adaptive Passes	Lossless			Lossy Model (Tanα=0.1)			Lossy Model (Tanα=0.0001)		
	Matrix Assembly (MB)	Matrix Size	Tetrahedra	Matrix Assembly (MB)	Matrix Size	Tetrahedra	Matrix Assembly (MB)	Matrix Size	Tetrahedra
1	33.7	7446	1463	35	7420	1458	35.3	8868	1466
2	34.1	10092	1899	35.6	10094	1894	36.6	11540	1900
3	35.7	13066	2375	37.6	12834	2333	38.4	14120	2310
4	36.8	15856	2835	39	15634	2792	40.3	16872	2737
5	39.3	20468	3624	42.6	19958	3538	43.8	21384	3441
6	41.8	24722	4368	45	22842	4046	47.7	27284	4378
7	43.1	27164	4794	49	29208	5150	49.4	29838	4796
8	45.6	30286	5337	51.3	32400	5687	52.2	33242	5342
9	47.3	33532	5895	53.1	36332	6347	53.9	37182	5973
10	52.6	44012	7619	61	47428	8194	57.2	41538	6667
11	59.9	57160	9798	65.5	53062	9134	60.1	45982	7387
12	68.6	73640	12529	69.8	59836	10259	63.2	50908	8163
13	73	80634	13715	74.5	66298	11326	67.7	56548	9074
14	85.1	103500	17513	79.5	74308	12653	71.2	62752	10055
15	91.1	115004	19417	85.9	82404	14011	75.8	69216	11066
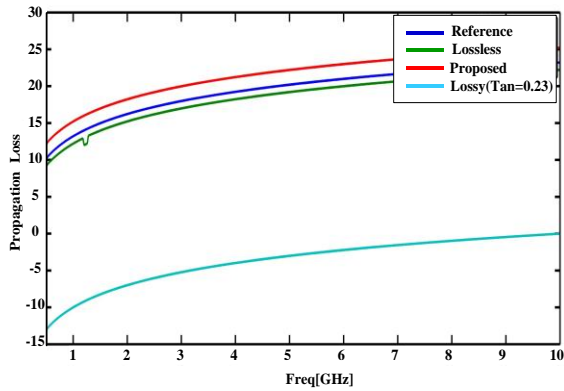
Fig. 8. Comparison of normalized propagation loss.
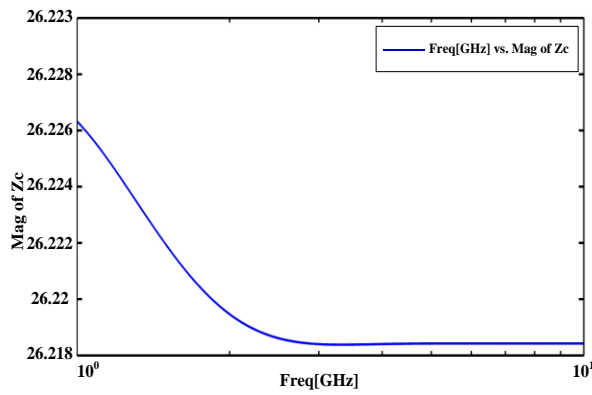

Fig. 9. The Magnitude of Zc versus freuquency.
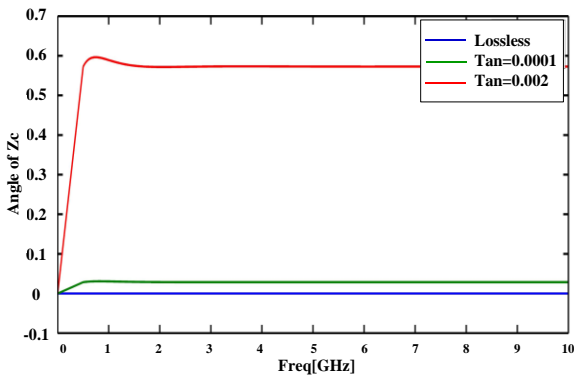
Fig. 10. The angle of Zc versus frequency.

C. Active matching techniques

In this subsection, active impedance matching of MTL is disscued. For this purpose, FET transistor CGH40006P based active matching technique is used. The datasheet of FET transistor CGH40006P is given [24]. The complex source and load impedances are 3.54-j*14.86 and 9.44+j*11.68 respectively at 4 GHz. The S-parameter is obtained from ANSYS HFSS

environment, which is based on ACA approach. This S-parameter is exported into ADS software and circuit is designed in ADS environment.

To match the source impedance and load impedance of the MTL at 50 ohms, the acting impedance matching technique is used to optimize S-parameters matrix result. First set the goal which is mag(S(1,1)) linearly, to get optimized matching. The condition for the magnitude of S-matrix is to set the value nearly equal to zero. Furthermore, to achieve the goal, set the random type of optimization which is based on the Min/Max continuous value. In the circuit, the open TL stub is also used to tune the minimum and maximum value. In the impedance matching, two matching methods are adopted. The smith chart and transmission matching by active matching techniques are shown in Fig. 11 and Fig. 12.
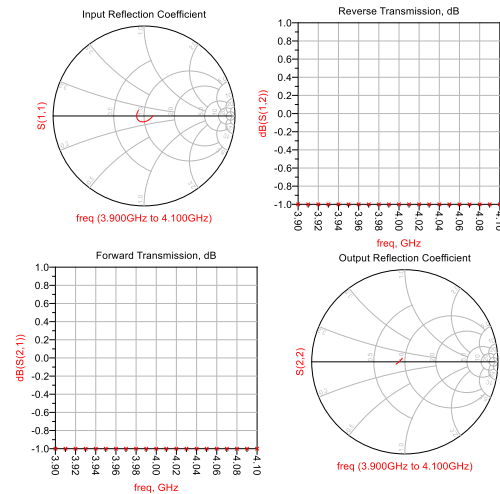

Fig. 11. Impedance matching with Smith chart.
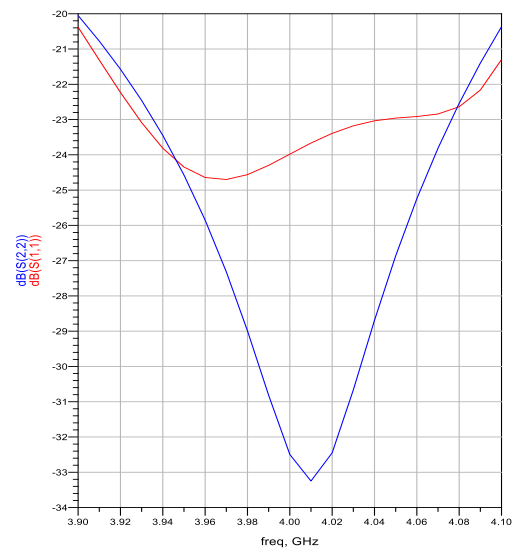
Fig. 12. Impedance matching with the transmission line.

V. CONCLUSION

In this article, the performance parameters of lossy MTL is discussed. The frequency dependent losses such as characteristic impedance, propagation loss and dielectric loss are calculated based on the ACA approach. The ACA algorithm is reliable that provides an efficient compression quality and simple procedure of compression. Moreover, ACA is a useful and efficient algorithm, which is capable to reduce the computation time, set-up time, and required less memory.

ACKNOWLEDGMENT

REFERENCES

[1] Y. Zhao and Y. Y. Wang, "A new finite-element solution for parameter extraction of multilayer and multiconductor interconnects," *IEEE Microwave and Guided Wave Letters*, vol. 7, no. 6, pp. 156-158, 1997.

[2] D. Topchishvili, R. Jobava, F. Bogdanov, B. Chikhradze, and S. Frei, "A hybrid MTL/MOM approach for investigation of radiation problems in EMC," *In Proceedings of the 9th International Seminar/Workshop on Direct and Inverse Problems of Electromagnetic and Acoustic Wave Theory*, pp. 65-68, Oct. 2004.

[3] J. M. Jin, .*The Finite Element Method in Electromagnetics*. John Wiley & Sons, 2015.

[4] Y. Zhao, K. Y. See, S. J. Li, N. Q. Jiang, Q. Wang, Y. Cao, and X. H. Wu, "Current probe method applied in conductive electromagnetic compatibility (EMC)," *International Conference on Microwave and Millimeter Wave Technology*, vol. 3, pp. 1442-1445, Apr. 2008.

[5] W. C . Chew, E. Michielssen, J. M. Song, and J. M. Jin, *Fast and Efficient Algorithms in Computational Electromagnetics*. Artech House, Inc., 2001.

[6] C. R. Paul, *Analysis of Multiconductor Transmission Lines*. John Wiley & Sons, 2008.

[7] H. W. Gao, Z. Peng, and X. Q. Sheng, "A coarse-grained integral equation method for multiscale electromagnetic analysis," *IEEE Transactions on Antennas and Propagation*, vol. 66, no. 3, pp. 1607-1612.

[8] P. Li and L. J. Jiang, "A rigorous approach for the radiated emission characterization based on the spherical magnetic field scanning," *IEEE Transactions on Electromagnetic Compatibility*, vol. 56, no. 3, pp. 683-690, 2014.

[9] A. Mahmoud, S. Kahourzade, and R. K. Lalwani, "Computation of cable ampacity by finite element method under voluntary conditions," *Australian Journal of Basic and Applied Sciences*, vol. 5, no. 5, pp. 135-146, 2011.

[10] F. S. H. Lori, M. S. Hosen, A. Menshov, M. Shafieipour, and V. Okhmatovski, "Accurate transmission lines characterization via higher order moment method solution of novel single-source integral equation," In *2017 IEEE MTT-S International Microwave Symposium (IMS)*, pp. 694-696, June 2017.

[11] C. Jiao, Z. Xia, and W. N. Fu, "A generalized multiconductor transmission line model and optimized method for the solution of the MTL equations," *International Journal of Antennas and Propagation*, 2012.

[12] A. J. Gruodis and C. S. Chang, "Coupled lossy transmission line characterization and simulation," *IBM Journal of Research and Development*, vol. 25, no. 1, pp. 25-41, 1981.

[13] M. Saih, H. Rouijaa, and A. Ghammaz, "Computation of multiconductor transmission line capacitance using method of moment," In *IEEE Proceedings of 2014 Mediterranean Microwave Symposium (MMS2014)*, pp. 1-6, Dec. 2014.

[14] G. Schmidlin, U. Fischer, Z. Andjelič, and C. Schwab, "Preconditioning of the second-kind boundary integral equations for 3D eddy current problems," *International Journal for Numerical Methods in Engineering*, vol. 51, no. 9, pp. 1009-1031, 2001.

[15] S. Chabane, P. Besnier, and M. Klingler, "Enhanced transmission line theory: Frequency-dependent line parameters and their insertion in a classical transmission line equation solver," *In IEEE International Symposium on Electromagnetic Compatibility*, pp. 326-331, Sep. 2013.

[16] R. F. Harrington, *Field Computation by Moment Methods*. Wiley-IEEE Press, 1993.

[17] M. Bebendorf, "Approximation of boundary element matrices," *Numerische Mathematik*, vol. 86, no. 4, pp. 565-589, 2000.

[18] J. M. Rius, J. Parron, A. Heldring, J. M. Tamayo, and E. Ubeda, "Fast iterative solution of integral equations with method of moments and matrix decomposition algorithm–singular value decomposition," *IEEE Transactions on Antennas and Propagation*, vol. 56, no. 8, pp. 2314-2324, 2008.

[19] M. Bebendorf and S. Kunis, "Recompression techniques for adaptive cross approximation," *The Journal of Integral Equations and Applications*, pp. 331-357, 2009.

[20] S. Kurz, O. Rain, and S. Rjasanow, "The adaptive cross-approximation technique for the 3D boundary-element method," *IEEE Transactions on Magnetics*, vol. 38, no. 2, pp. 421-424, 2002.

[21] A. Heldring, J. M. Rius, J. M. Tamayo, J. Parrón, and E. Ubeda, "Multiscale compressed block decomposition for fast direct solution of method of moments linear system," *IEEE Transactions on Antennas and Propagation*, vol. 59, no. 2, pp. 526-536, 2010.

[22] H. Zhao, Y. Zhang, J. Hu, and E. P. Li, "Iteration-free-phase retrieval for directive radiators using field amplitudes on two closely separated observation planes," *IEEE Transactions on Electromagnetic Compatibility*, vol. 58, no. 2, pp. 607-610, 2016.

[23] M. Bebendorf and S. Rjasanow, "Adaptive low-rank approximation of collocation matrices," *Computing*, vol. 70, no. 1, pp. 1-24, 2003.

[24] https://www.mouser.com/ds/2/90/gh40006p876367.pdf

[25] ANSYS, High Frequency Structure Simulation (HFSS), ver. 18, SAS IP, USA, 2018.

[26] N. Ranjkesh, M. Shahabadi, and D. Busuioc, "Effect of dielectric losses on the propagation characteristics of the substrate integrated waveguide," *Asia-Pacific Microwave Conference Proceedings, IEEE*, vol. 3, Dec. 2005.

Zhao Yang received his B.E., M.E., and Ph.D. degree all in Power Electronic Technology from Nanjing University of Aeronautics and Astronautics, Nanjing, China, in 1989, 1992, and 1995, respectively. He is currently the Professor with Nanjing Normal University. His research interests are in the areas of electromagnetic compatibility, power electronics and automotive electronics.

Wei Yan is a Doctor & Assoc. Professor from Nanjing Normal University. He obtained the Physics and Electronics Ph.D. and Electrical Engineering M.S. from Nanjing Normal University in 2014 and 2011. He is the Senior Member of China Electrical Technology Association and the Evaluation Expert of the Electromagnetic Compatibility Calibration Specification of China.

Abdul Mueed was born in Bhakkar, Pakistan. He received the Master degree in Electrical Engineering from the University of Engineering and Technology, Taxila, Pakistan in 2015. From 2009 to 2017, he worked as a Lecturer in Electrical Engineering at the Dr. A. Q. Khan Institute of Technology, Mianwali, Pakistan. He is currently working as a Research Scholar at Nanjing Normal University, Nanjing, China. His primary research interests include electromagnetic compatibility problems, computational electromagnetics, power system transients, and application of artificial intelligent in power systems.

Rotary Coupling Magnetic Field Characteristics of a Two-Degree-of-Freedom Direct Drive Induction Motor

Haichao Feng [1], Jikai Si [2,1], Zhiping Cheng [2], Caixia Gao [1], and Wenping Cao [3]

[1] School of Electrical Engineering and Automation
Henan Polytechnic University, Jiaozuo, 454000, China
fhc@hpu.edu.cn, gcx@hpu.edu.cn

[2] College of Electric Engineering
Zheng Zhou University, Zhengzhou, 450001, China
sijikai527@126.com, zpcheng@zzu.edu.cn

[3] School of Engineering and Applied Science
Aston University, Birmingham, B47ET, UK
w.p.cao@aston.ac.uk

Abstract ─ A two-degree-of-freedom direct drive induction motor is investigated in this study. Owing to its special structure and motion forms, coupling magnetic fields are generated inside the motor, which links with the main magnetic field and results in low speeds and high fluctuations. In this paper, a three-dimensional finite element model of the two-degree-of-freedom direct drive induction motor is developed to determine the rotary coupling magnetic field and its effect on the motor. The distribution of the rotary coupling magnetic field is calculated qualitatively based on a simplified model, and its variation law is investigated based on the changes of the induced voltages in a special coupling model. Moreover, the relationship between the rotary coupling magnetic field and the motor speed is determined by the rotary coupling coefficient. A test platform is applied to verify the coupling model and its results.

Index Terms ─ Coupling magnetic field, induced voltages, three-dimensional finite element model, two-degree-of-freedom.

I. INTRODUCTION

The combination of rotary and linear motions on the same axis is often required in robot arms, diverse industrial and vehicles applications [1-2]. These proposed two-degrees-of-freedom motors (2DoFMs), which are capable of rotary, linear and helical motions through the use of single motors, seems to be an excellent solution.

2DoFMs with different structures have been proposed and investigated in recent years due to their advantages of integrated structures, small volume, and high reliability. To realize special motion forms,

2DoFMs adopt special structures [3-6], such as Halbach structure, multi-stators, and multi-windings. Amiri et al. [5] investigated a two-armature rotary-linear induction motor, which adopted a rotary armature connecting with a linear armature in series to achieve helical motion. Li et al. [7] investigated a decoupled 2DoF in the linear and rotary directions of a motor based on switched reluctance principle. Szabó et al. [8] proposed a rotary-linear switched reluctance motor, in which the armature was constructed with a rotor stack of six common poles mounted on a common shaft. A Halbach magnet array and multi-windings were adopted in a permanent magnetic rotary-linear motor, in which the motion forms were determined by the power supply [9]. However, their major structures and magnetic fields were more complicated than the traditional single-degree-of-freedom motors. Previously, the rotary torque and efficiency of the two-armature rotary-linear induction motor could be weakened to some extent by the linear end magnetic field and motion [10-11]. For the magnetic field modeling and the motor characteristic analysis, the severe magnetic saturation should be accurately predicted [12]. Furthermore, by considering the weakening effect in the form of additional magnetomotive force, the computational accuracy of its equivalent circuit model could be improved, and verified by the finite element results [13]. References [14] presented a three-dimensional (3D) finite element analysis (FEA) applicable to all forms of sheet rotor, cylindrical, linear induction motor, as well as, helical motion induction motor. The linear thrust of the rotary-linear switched reluctance motor with multi rotary stators, which is dependent on the power supply mode, could be generated by the coupling among the stators [15]. For the permanent magnetic rotary-linear motor with Halbach

magnet array, its circular magnetic field was linked to its axial magnetic field and verified by the static magnetic field solved via the FEA [6]. Furthermore, the interval between two successive magnets in the axial direction could affect the rotary and linear magnetic flux densities [16]. Thus, the special coupling phenomenon, by which the magnetic fields of different degrees of freedom interact with each other, is common in 2DoFMs.

A two-degree-of-freedom direct drive induction motor (2DoFDDIM) was proposed and designed to realize the three motion forms, namely rotary, linear and helical [17]. Owing to the special structure and assembly form of 2DoFDDIM stators, the presence of coupling magnetic fields lead to distinctive features, such as 'super-synchronization' and the static coupling effect, which have been analyzed in references [18] and [19], respectively. The characteristics of the helical motion of the two-degree-of-freedom induction motor were investigated, and a set of torque and force equations of the helical motion were deduced in references [20]. However, these studies do not focus on the origin of these phenomena, and the coupling magnetic field, which should be fully investigated and considered in the design and control system of the motors.

The coupling magnetic fields and their effect on the performances of 2DoFDDIM are determined via a 3D finite element model of the motor. Two forms of coupling magnetic fields exist inside 2DoFDDIM, namely the rotary coupling magnetic field (RCMF) and linear coupling magnetic field (LCMF). In this paper, only the RCMF was mainly investigated. The equation for RCMF was calculated qualitatively based on a simplified model, and its variation law was determined based on the changes of induced voltages in a special coupling model, which was validated via experiments on a prototype coupling motor.

II. STRUCTURE AND COUPLING MAGNETIC FIELD OF 2DoFDDIM

A. Structure and characteristics of 2DoFDDIM

Figure 1 shows the 2DoFDDIM structure, which contains a rotary arc armature in the rotary part, a linear arc armature in the linear part, and a solid copper-coated mover shared by the two parts. Table 1 lists the main parameters of 2DoFDDIM.

On the basis of the power supply mode, 2DoFDDIM produces different forms of air gap magnetic fields, which generate the corresponding electromagnetic force on the mover surface to drive it directly and perform the rotary, linear, or helical motion.


(a) Rotary arc-armature   (b) Linear arc-armature

(c) Mover   (d) Assembly
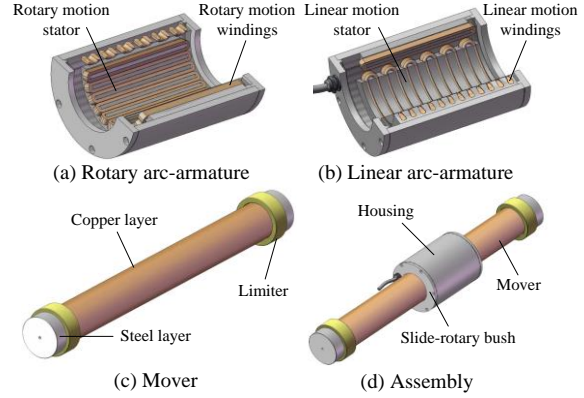
Fig. 1. 2DoFDDIM structure.

Table 1: Main parameters of 2DoFDDIM

Item	Values/Dimension	
	Rotary Part	Linear Part
Rated power (P_N)	1.1 kW	1.1 kW
Rated voltage (U_N)	220 V (Y)	220 V (Y)
Rated current	9 A	12 A
Frequency (f)	50 Hz	50 Hz
Pole pair (p)	2	2
Stator inner diameter	98 mm	98 mm
Stator outer diameter	155 mm	155 mm
Stator axial length	135 mm	135 mm
Slots	12	12
Air-gap length	2 mm	2 mm
Mover length	655 mm	
Copper layer thickness of mover	1 mm	
Steel layer thickness of mover	7 mm	

According to the 2DoFDDIM structure shown in Fig. 1 and its working principle, the 3D finite element model of 2DoFDDIM is established in *Magnet*, as shown in Fig. 2.
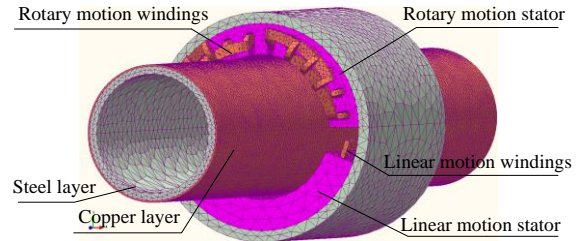

Fig. 2. 3D finite element model of 2DoFDDIM.

Figure 3 shows the torque-slip ratio S_r and force-slip ratio S_l curves of 2DoFDDIM, where S_r and S_l denote the slip ratios in the rotary and linear motions, respectively. Figure 3 (a) presents the torque-S_r curve indicating the mechanical characteristics of the 2D rotary motion of 2DoFDDIM. Rotating torque increased monotonously with the increase in S_r, which was similar to that of the traditional solid-rotor rotary induction motor. Figure 3 (b) shows the force-S_l characteristic of the linear motion of 2DoFDDIM. The increase in S_l increased the force.


(a) Torque-S_r (Rotary motion)

(b) Force-S_l (Linear motion)
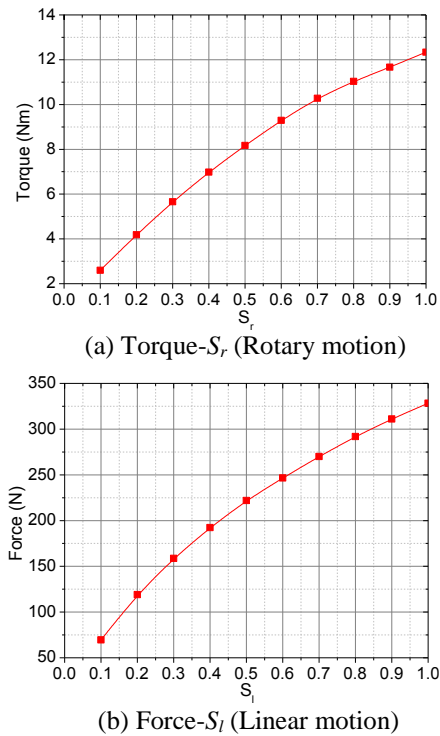
Fig. 3. (a) The torque-slip ratio S_r and (b) force-slip ratio S_l characteristics of 2DoFDDIM.

B. Coupling magnetic field of 2DoFDDIM

According to the special structure and the installation mode of the armature of the 2DoFDDIM, when the rotary part or linear part is energized independently, the distribution of the magnetic field is shown in Fig. 4. Figure 4 presents that the 0°-180° area in the circumference belongs to the rotary part, and the other belongs to the linear part according to the 2DoFDDIM structure.

It can be seen from Fig. 4 (a) that the rotary magnetic field will affect the linear part, when only the rotary part of the motor is powered. As shown in Fig. 4 (b), when the motor is only doing linear motion (only linear part is powered), the traveling wave magnetic field in the linear part has an impact on the rotary part.

The magnetic field generated by the rotary part stator and crosslinking in the linear part stator (induced magnetic field in linear part) is defined as rotary coupling magnetic field (RCMF). Similarly, the magnetic field generated by the linear stator and crosslinking in the rotary part stator (induced magnetic field in rotary part) is called the linear coupling magnetic field (LCMF).

Figure 4 illustrates the parts of the magnetic field when 2DoFDDIM performs the single degree of freedom motion as follows:

1) Effective magnetic field, by which the mover is driven to perform a rotary or linear motion.

2) Coupling magnetic field, produced by the rotary or linear part and then links with the relative part.

The comparison of Figs. 4 (a) and 4 (b) indicated that the coupling magnetic fields of the rotary and linear parts were different. The upper and lower sides of the RCMF were almost symmetrical, whereas the left and right sides of the LCMF were almost symmetrical because the RCMF and LCMF were generated by the longitudinal end effect of the rotary part and the end windings of the linear part, respectively.


(a) Rotary motion magnetic field
(Only rotary part is powered)

(b) Linear motion magnetic field
(Only linear part is powered)
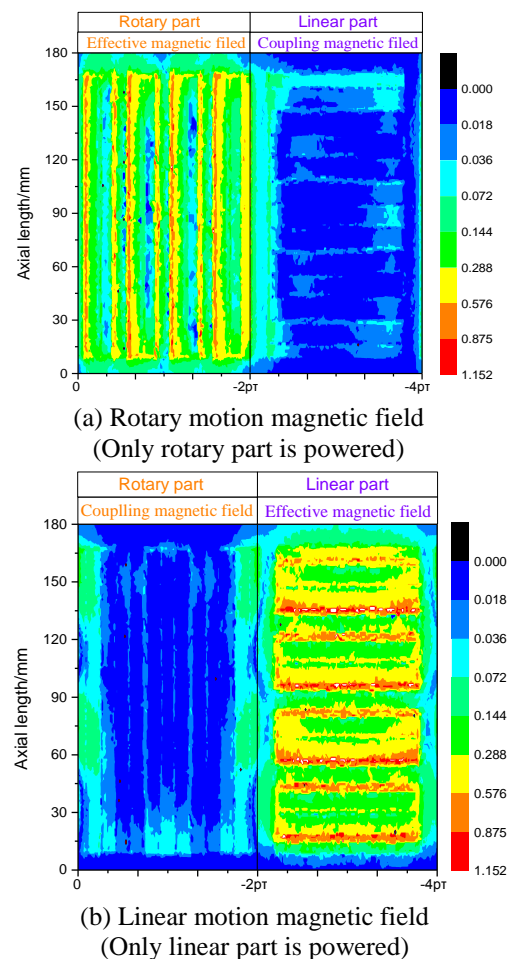
Fig. 4. Distribution of the air-gap magnetic field of 2DoFDDIM.

C. The effect of coupling magnetic field

Both the rotary and linear parts of 2DoFDDIM can produce the coupling magnetic fields (Fig. 4), which are determined by the cut-off structure of the armature stator cores in the rotary and linear parts and their 2DoFDDIM installation mode. When 2DoFDDIM is under helical motion, coupling magnetic fields still exist and link with the effective magnetic fields. Then, the linear effective magnetic field is taken as an example, and Fig. 5 shows the difference between the linear effective magnetic field with and without the rotary coupling magnetic field.

The comparison of Figs. 5 (a) and 5 (b) indicated that the distribution of the effective magnetic field in the linear part changed in the presence of RCMF. Similarly, the coupling magnetic field in the linear part can also affect the distribution of the effective magnetic field in the rotary part. As the bridge in the conversion of electric to mechanical energy in motors, the effective magnetic field changes will lead to the change in motor performance.

(a) Without rotary coupling magnetic field

(b) With rotary coupling magnetic field
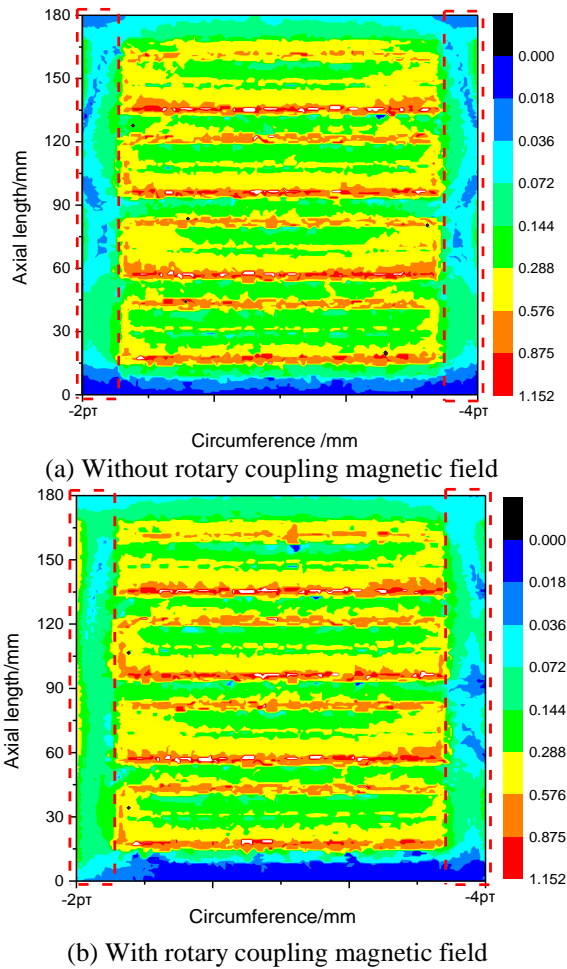
Fig. 5. Distribution of effective magnetic field in the linear part.

According to the equations in the reference [20], Fig. 6, and Tables 2 and 3 show the influence of the coupling magnetic fields on the output characteristics of the motor based on the 3D finite element model of 2DoFDDIM.
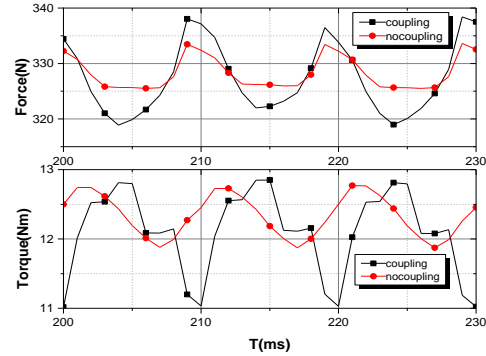
(a) Waveforms of the linear force and rotary torque
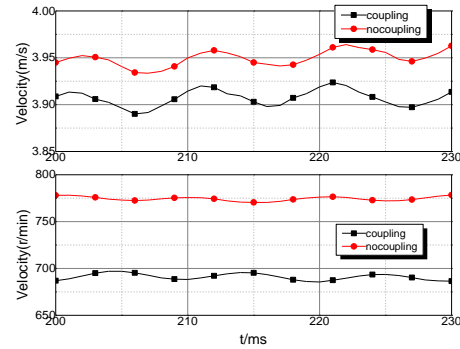
(b) Waveforms of the linear and rotary velocity

Fig. 6. Influence of the coupling magnetic field.

Table 2: Influence of the coupling magnetic field on the linear force and rotary torque

Items		With Coupling	Without Coupling
Rotary part torque	Average (Nm)	12.09	12.34
	Fluctuation(Nm)	0.61	0.30
	Ripple (%)	5.05%	2.43%
Linear part force	Average (N)	327.3	328.3
	Fluctuation (N)	6.236	2.903
	Ripple (%)	1.91	0.88

Table 3: Influence of the coupling magnetic field on the linear and rotary velocity

Items		With Coupling	Without Coupling
Rotary part velocity	Average (r/min)	691	775
	Fluctuation(r/min)	3.35	2.22
	Ripple (%)	0.48	0.29
Linear part velocity	Average (m/s)	3.907	3.949
	Fluctuation (m/s)	0.0086	0.0080
	Ripple (%)	0.22	0.20

Figure 6 (a) and Tables 2 and 3 show that the locked mover torque reduces by 2.03% and the torque fluctuation increases by 104% under the effect of LCMF of 2DoFDDIM. Figure 6 (b) and Table 2 present that the rotary speed reduces by 10.7% and the speed fluctuation increases by 50.9% when compared with that without LCMF. Similarly, similar changes were observed in the performance of the linear part.

Such changes caused by the coupling effect illustrate that the motor performance can be affected by the coupling magnetic field. In general, the effect of the coupling magnetic field will lead to low electromagnetic forces and speeds and high motor fluctuations.

III. THE COUPLING MAGNETIC FIELD IN THE ROTARY PART

At present, the effect of the coupling magnetic field on the motor's performance has been simply verified by the previous section. The characteristics of the coupling magnetic field should be examined in depth to determine the details on such effect.

In this study, only the RCMF was selected as the research project, whereas the LCMF will be investigated in a corresponding study.

To calculate the rotary coupling magnetic field of 2DoFDDIM, the rotary part was converted into a simplified model (Fig. 7) with the following assumptions.

1) Relative permeability, μ_r, of the arc armature core in the 2DoFDDIM rotary part was infinitely great, and conductivity, γ_r, was infinitely small. Hence, $\mu_r = \infty$, $\gamma_r = 0$.

2) The impact of the linear stator core and slot was ignored, and the magnetic field was deemed uniformly distributed along the axial length. Therefore, such impact had no relation with the Z coordinates while analyzing the coupling magnetic field in the rotary part.

3) The stator and the mover were spread; thus, the armature and mover curvature were ignored, respectively.

4) The three-phase symmetrical sinusoidal current was connected to the armature winding, and all the electromagnetic volumes were characterized by sinusoidal variation.
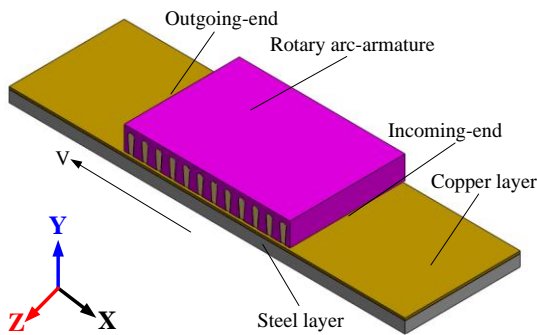

Fig. 7. Equivalent coupling magnetic field model.

The following equations define the vector magnetic potential:

$$\begin{cases} \nabla^2 \dot{A}_{mx} - j\mu_0\gamma\omega_1\dot{A}_{mx} = -\mu_0\dot{J}_{mx} \\ \nabla^2 \dot{A}_{my} - j\mu_0\gamma\omega_1\dot{A}_{my} - \mu_0\gamma v\left(\dfrac{\partial A_{my}}{\partial x} - \dfrac{\partial A_{mx}}{\partial y}\right) = -\mu_0\dot{J}_{my} \\ \nabla^2 \dot{A}_{mz} - j\mu_0\gamma\omega_1\dot{A}_{mz} - \mu_0\gamma v\left(\dfrac{\partial A_{mz}}{\partial x} - \dfrac{\partial A_{mx}}{\partial z}\right) = -\mu_0\dot{J}_{mz} \end{cases} \quad (1)$$

where $\dot{A}_{mx}, \dot{A}_{my}, \dot{A}_{mz}$ denote the complex amplitude of the vector magnetic potential in the x, y, and z directions, respectively, and $1_x\dot{A}_{mx} + 1_y\dot{A}_{my} + 1_z\dot{A}_{mz} = \dot{A}_m$; $\dot{J}_{mx}$, $\dot{J}_{my}$, $\dot{J}_{mz}$ refer to the electrical current density $\dot{J}_m$ in the x, y, and z directions, respectively; μ_0 indicates the vacuum permeability; γ represents the relative electrical conductivity of the mover; ω_1 refers to the angular frequency; and v denotes the rotary speed of the mover.

The above coupling magnetic field model and assumed conditions indicated that $\dot{A}_{mx} = \dot{A}_{mz} = 0$ and $\dot{A}_m = \dot{A}_{my}$. When only the rotary part was powered in the system, electrical current density in the coupling magnetic field will be $\dot{J}_m = 0$. When they are substituted into the equation set of the vector magnetic potential (1), the vector magnetic potential in the coupling magnetic field region can be derived as:

$$\frac{d^2 \dot{A}_m}{d^2 x^2} - j\mu_0\gamma\omega_1\dot{A}_m - \mu_0\gamma v\frac{d\dot{A}_m}{dx} = 0. \quad (2)$$

The general solution of Equation (2) is:

$$\dot{A}_m = \dot{C}_1 e^{(\lambda_2+\eta_2)\alpha x} + \dot{C}_2 e^{-(\lambda_2-\eta_2)\alpha x}, \quad (3)$$

$$\begin{cases} \eta_2 = (\mu_0\gamma v)/\alpha \\ \lambda_2 = \sqrt{\eta_2^2 + jG}\dot{A}_m, \\ G = \mu_0\gamma\omega_1\alpha^2 \\ \gamma = \gamma_2\Delta/\delta \end{cases} \quad (4)$$

where $\dot{C}_1$ and $\dot{C}_2$ denote the complex constants of the integrals to be confirmed, $\alpha = \pi/\tau$, τ refers to the equivalent pole pitch of the rotating part, γ_2 represents the conductivity of the mover, δ indicates the equivalent electromagnetic air gap, and Δ denotes the thickness of the conductor plant of the mover.

According to the vector magnetic potential in the region of the outgoing-end of the mover, $\dot{A}_{mo}\big|_{x=\infty} = 0$, it can be obtained that:

$$\begin{cases} \dot{C}_1 = 0 \\ \dot{A}_{mo} = \dot{C}_2 e^{-\left(\sqrt{\eta_2^2+jG}-\eta_2\right)\alpha x} \end{cases}, \quad (5)$$

where $0 \le x \le 2p\tau$.

According to the vector magnetic potential in the region of the incoming-end of the mover, $\dot{A}_{mi}\big|_{x=-\infty} = 0$, it

can be obtained that:

$$\begin{cases} \dot{C}_2 = 0 \\ \dot{A}_{mi} = \dot{C}_1 e^{-\left(\sqrt{\eta_2^2 + jG} + \eta_2\right)\alpha x} \end{cases}, \qquad (6)$$

where $-4p\tau \leq x \leq -2p\tau$.

Given that the simplified model was obtained by using an equivalent plate model of the 2DoFDDIM, the vector magnetic potential in the coupling magnetic field was the superposition of the vector magnetic potential in the outgoing and incoming ends. Thus, the complex amplitude of the vector magnetic potential in the coupling magnetic field can be expressed as follows:

$$\begin{aligned} \dot{A}_m &= \dot{A}_{mi} + \dot{A}_{mo} \\ &= \dot{C}_1 e^{\left(\sqrt{\eta_2^2 + jG} + \eta_2\right)\alpha(x - 4p\tau)} + \dot{C}_2 e^{\left(\sqrt{\eta_2^2 + jG} - \eta_2\right)\alpha x}, \end{aligned} \qquad (7)$$

where $0 \leq x \leq 2p\tau$.

Therefore, the magnetic flux density of the coupling magnetic field B_m can be calculated according to $B_m = \partial \dot{A}_m / \partial x$, as shown in Equation (6):

$$B_m = \dot{C}_1 m_1 e^{m_1(x - 4p\tau)} - \dot{C}_2 m_2 e^{-m_2 x}, \qquad (8)$$

where:

$$\begin{cases} m_1 = \sqrt{\mu_0^2 \gamma^2 v^2 + j\dfrac{\mu_0 \omega_1 \gamma_2 \Delta}{\delta}} + \mu_0 \gamma v \\ m_2 = \sqrt{\mu_0^2 \gamma^2 v^2 + j\dfrac{\mu_0 \omega_1 \gamma_2 \Delta}{\delta}} - \mu_0 \gamma v \end{cases}.$$

Replace x to θ through coordinate conversion, and the equation becomes:

$$B_m = \dot{C}_1 m_1 e^{m_1(\theta - 2\pi)} - \dot{C}_2 m_2 e^{-m_2 \theta}, \qquad (9)$$

where $0 \leq \theta \leq \pi$.

Equation (9) shows that the rotary coupling magnetic field of 2DoFDDIM is a complicated function related to the position θ, velocity of the mover v, and equivalent electromagnetic air gap δ.

Given that the above equation was derived based on certain assumptions, its computational accuracy was not as high as that of FEA. However, this equation can provide guidance for the research on the variation law of RCMF.

IV. CHARACTERISTICS OF THE COUPLING MAGNETIC FIELD

RCMF also needs specialized magnetic measuring methods combined with the guidance of the equation for accurate measurement. The magnetic field can be measured by using the superconducting magnetic measurement, induction coil, fluxgate, and Hall device [21]. The induction coil is a simple method to measure the magnetic field based on Friday's law of electromagnetic induction. Induction coil exposed to alternating magnetic fields will generate the induced voltage between both of its ends. If the parameters of the

induction coil are constant, then the large induced voltage strengthens the magnetic field. In addition, induction coil and the magnetic field can be modeled and simulated through finite element software *Magnet*. Therefore, a special coupling model was proposed and designed in *Magnet* to measure the RCMF by using the induction coil.

A. The coupling model

The special coupling model was established in *Magnet* to calculate the variation of the rotary coupling magnetic field of 2DoFDDIM (Fig. 8 (a)). Figure 8 (b) shows the structure and distribution of the coupling model coils. The coupling model consisted of a rotary arc armature, a solid rotor, and a magnetic field measuring device. The magnetic field measurement device was composed of an iron core and six sets of induction coils with the same structural parameters. Accordingly, the value of the induction voltage at both ends of the induction coils could reflect the intensity of the coupling magnetic field at the coil position, and the change of the induced voltage at both ends of the same induction coil could indicate the variation of the intensity of the coupling magnetic field in this position.

(a) Finite element model

(b) Structure and distribution of coils of the coupling model
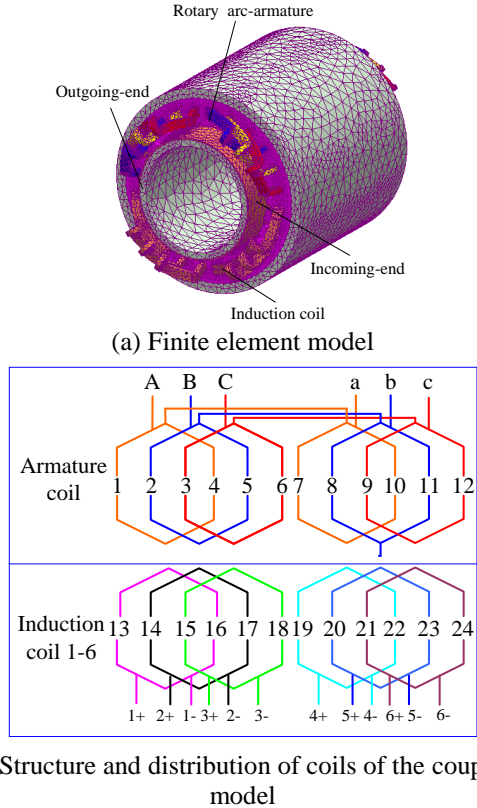
Fig. 8. Finite element model and structure of the analysis on the coupling magnetic field.

B. Finite element analysis

To output the same magnetomotive force and reduce the impact on the variables, the coupling model was driven by a current source. When a three-phase sinusoidal alternating current of 14 A was connected with the rotary arc armature of the coupling model, induced voltages could be obtained in the induction coils (Fig. 9).

Figure 9 (a) shows that the induced voltages possess the same frequency as the coupling magnetic field and power source. Furthermore, the induced voltages of induction coils (from coils 1 to 6) decreased first and then increased (Fig. 9 (b)), and the induced voltage of coil 1 was higher than that of coil 6. The above phenomenon illustrated that the RCMF decreased first and then increased from the outgoing end to the incoming end, and the magnetic field in the outgoing end as stronger than that in the incoming end. This phenomenon was consistent with the distribution of the coupling magnetic field in the region from 180°-360° shown in Fig. 4.

(a) Curves of induced voltages


(b) Effective value of induced voltages
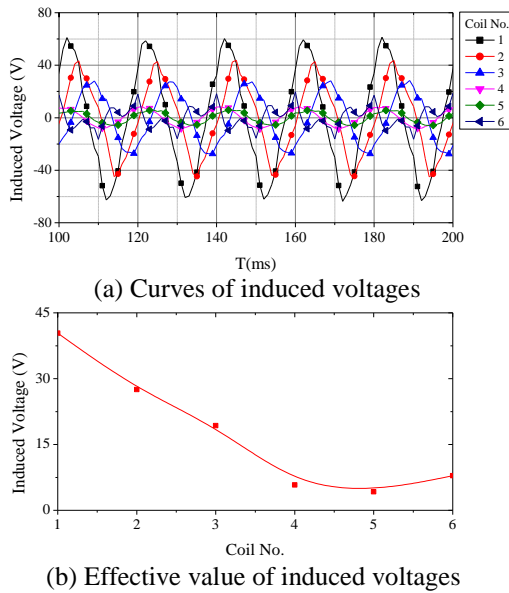
Fig. 9. Induced voltages in the induction coils.

RCMF was affected by the rotary speed and the equivalent electromagnetic air gap, and the equivalent electromagnetic air gap was determined by the thickness of the physical air gap and the conductor plate (Fig. 10).

Figure 10 (a) presents the variation of the induced voltages along with the rotary slip. Figures 10 (b) and 10 (c) illustrate the variation of induced voltages under different thickness of the physical air gap and the conductor plate, respectively.

The induced voltages from coils 1 to 6 decreased first and then increased (Fig. 10), thereby indicating that the RCMF decreased first and then increased from the outgoing to the incoming end, and the magnetic field in

the outgoing end was stronger than that in the incoming end, which can be considered a general characteristic of the RCMF. Furthermore, the induced voltages decreased generally along with the rotary slip, air gap, and conductor plate thickness, thereby reflecting the general intensity of the decreasing RCMF with the increase in these factors. Moreover, RCMF in the outgoing end reduced more than that in the incoming end with these factors.

(a) Induced voltages *vs.* rotary slip ratio S_r

(b) Induced voltages *vs.* air-gap

(c) Induced voltages *vs.* conductor plate
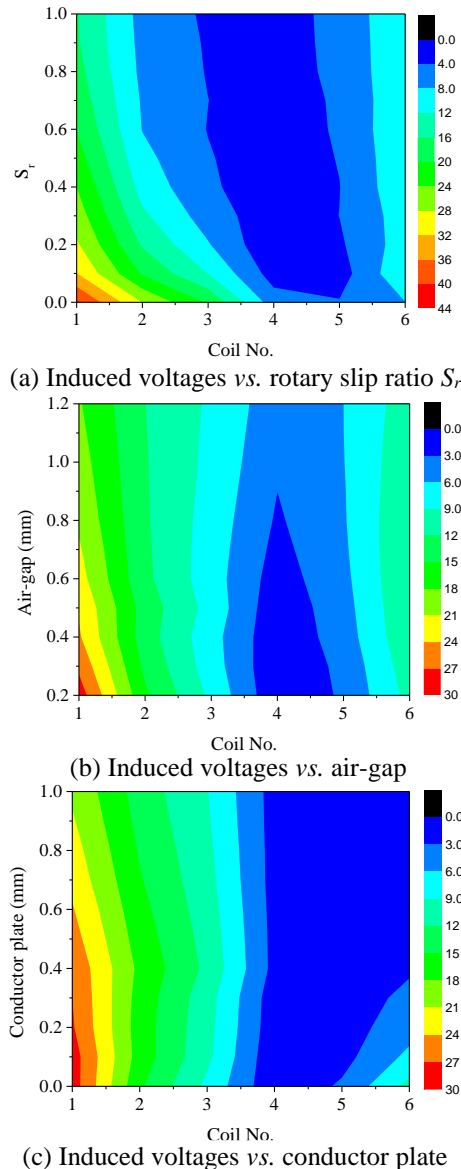
Fig. 10. Variations of the induced voltages.

However, RCMF varied along with the rotary slip, air gap, and conductor plate thickness. The comparison of the induced voltage changes of coil 1 in the three figures indicated that its variation along with the rotary slip was higher than that of the other factors. This finding

shows that the coupling magnetic field was significantly affected by the rotary slip.

Both the increase in air gap and conductor plate thickness can change the equivalent electromagnetic air gap and lead to high reluctance. However, the induced voltages of coils 1-3 were decreasing faster than the conductor plate with the increase in air gap. Moreover, the induced voltages of coils 4-6 slowly increased with the increase in air gap but decreased with the increase in conductor plate. Therefore, the corresponding coupling magnetic field demonstrated a similar changing trend with the induced voltages.

C. Rotary coupling coefficient

Section II-C presents that coupling magnetic field has a decreased effect on the motor speed. Additionally, RCMF is variable with the rotary speed, which can be concluded from Section IV-B. To measure the effect of RCMF on linear speed, the following rotary coupling coefficient, K_{rcm}, was introduced:

$$K_{rcm} = V_{lm} / V_{lcm}, \qquad (10)$$

where V_{lcm} and V_{lm} express the linear speed of 2DoFDDIM with or without the effect of RCMF, respectively.

Based on the finite element model of 2DoFDDIM shown in Fig. 2, the linear speeds in the presence and absence of RCMF were first measured. Then, the rotary coupling coefficient was calculated and its variation along with rotary slip was shown in Fig. 11.
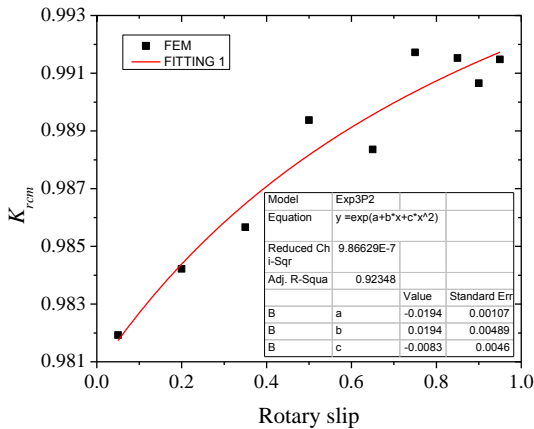

Fig. 11. Fitting curve of rotation coupling coefficient.

By applying curve fitting, the relationship between the rotary coupling coefficient and slip can be obtained as follows:

$$K_{rcm} = e^{-0.0194+0.01943S-0.00838S^2}. \qquad (11)$$

From the finite element results in Fig. 11 and Equation (11), the rotary coupling coefficient gradually became close to 1 with increasing rotary slip. This result shows that the effect of RCMF on motor performance

decreased with the increase in rotary slip. Section IV-B demonstrates that the general RCMF weakens with the increase in rotary slip. Hence, the effect of coupling magnetic field on motor performance was proportional to its intensity.

Future works include the mathematical model and control system, in which the rotary coupling coefficient should be considered to enhance their precision.

V. EXPERIMENTAL VERIFICATION

To verify the FEA of the rotary coupling magnetic field carried out above, a prototype was manufactured and its main parameters were listed in Table 4. Figure 12 shows the test platform for coupling model prototype.

Table 4: Main parameters of the experimental prototype

Item		Values
Stator inner diameter		98 mm
Stator outer diameter		155 mm
Axial length		135 mm
Slots		24
Armature coil	Phase	3
	Turns	90
Induction coil	Number	6
	Turns	90
Air-gap length		2 mm
Copper layer thickness of mover		1 mm
Steel layer thickness of mover		7 mm
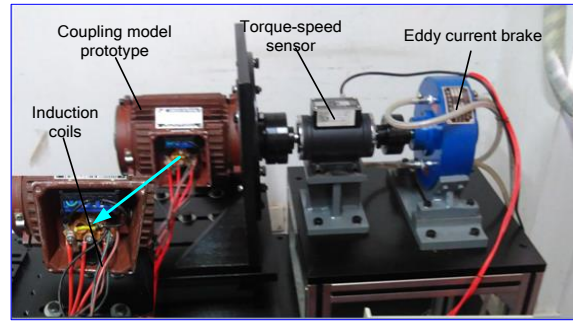
(a) Prototype of the coupling model
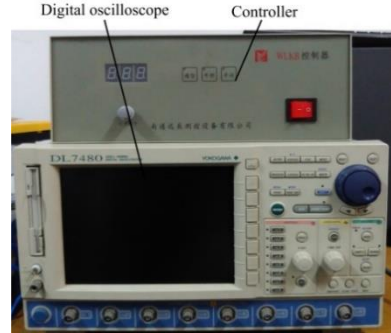

(b) Peripheral equipment

Fig. 12. Platforms and equipment used to conduct prototype experiment of the coupling model.

The test platform for the coupling model prototype included the following: coupling model prototype, torque-speed sensor, eddy current brake, controller, upper computer, and digital oscilloscope. The structure of the coupling model prototype and the distribution of the coils were the same as the coupling model in *Magnet.* The windings were charged with the three-phase AC source, and then the induced voltages could be measured by the digital oscilloscope from the induction coils.

The controller could adjust the output load of the eddy current break by controlling the input current. Then, the speed of the prototype could be controlled by adjusting the load supply and acquired from the upper computer through the torque-speed sensor. The variation of induced voltages along with speed could be measured. Considering safety in the experiment, the slip of the coupling model prototype was set between 0 and 0.5. The induced voltage waveforms measured by the digital oscilloscope are shown in Fig. 13 (a). At the same time, the comparison of finite element and experimental results are shown in Fig. 13 (b).
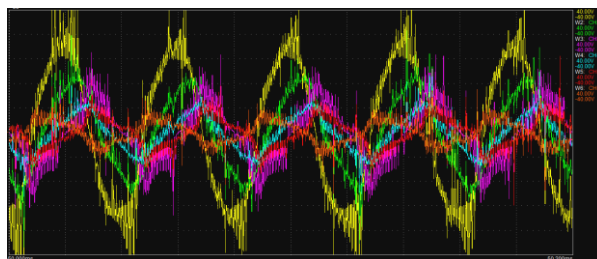
(a) Induced voltage waveform
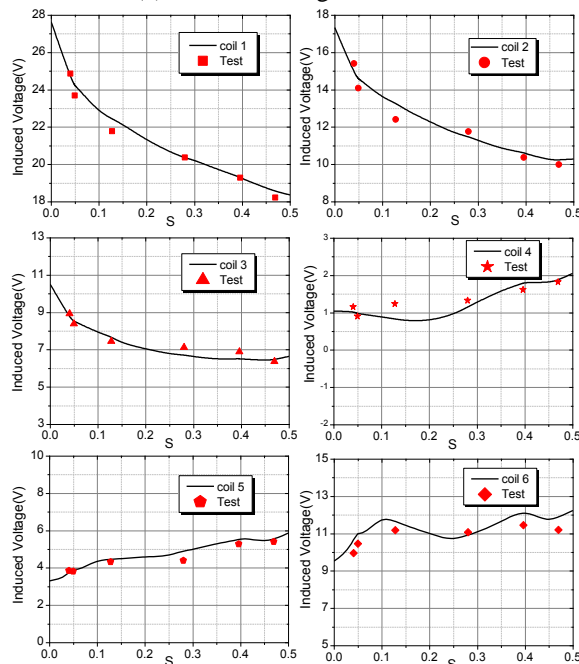
(b) Experimental and finite element results

Fig. 13. Comparison of experiment and FEA results.

The induced voltage waveforms in Fig. 13 (a) were roughly the same as that in Fig. 9 (a). Figure 13 (b) shows that the finite element results are basically the same as the induced voltages measured by the experiment and the variation of the induced voltage as the speed changes. This finding verified the feasibility and correctness of the coupling model of the rotary part. Furthermore, the application of the induced voltage in analyzing the variation of the coupling magnetic field was also validated.

VI. CONCLUSION

As part of the origin of the coupling effect in 2DoFDDIM, the rotary coupling magnetic field is mainly explored and investigated. Through a simplified model of the rotary part, the equation for calculating the RCMF is derived to provide guidance for research on its characteristics. Its variation law with the rotary slip, air gap, and conductor plate thickness is determined based on the special coupling model in *Magnet*. The results show that 2DoFDDIM has the following features:

1) The coupled magnetic field of 2DoFDDIM is caused by the breaking of stator cores in the rotary and linear parts and the mounting method of the stator. The rotary and linear coupling magnetic fields re caused by the longitudinal end effect of the rotating part and the transverse end effect and end winding, respectively.

2) From the view of the rotary coupling magnetic field, the coupling magnetic field in the outgoing end is stronger than that in the incoming end but weakened as the distance between the longitudinal ends of the stator increases.

3) The rotary coupled magnetic field will increase with the increase in velocity and decrease in air gap thickness, which is greatly affected by velocity and minimally affected by air gap thickness.

This research will be considered in future studies that include the development of the precise control of the helical motion and the construction of a mathematical model for the entire motor in the study.

REFERENCES

[1] Y. Sato, "Development of a 2-degree-of-freedom rotational/linear switched reluctance motor," *IEEE Transactions on Magnetics*, vol. 43, no. 6, pp. 2564-2566, June 2007.

[2] S. Y. Li and K. WE. Cheng, "A new two-degree of freedom switched reluctance motor for electric vessel," *In Proceedings of 2015 6th International Conference on Power Electronics Systems and*

Applications (PESA), Hong Kong, pp. 1-6, Dec. 2015.

[3] P. Bolognesi, O. Bruno, F. Papini, V. Biagini, and L. Taponecco, "A low-complexity rotary-linear motor useable for actuation of active wheels," *In Proceedings of 2010 International Symposium on Power Electronics, Electrical Drives, Automation and Motion (SPEEDAM)*, Pisa, Italy, pp. 331-338, June 2010.

[4] M. M. Nezamabadi, E. Afjei, and H. Torkaman, "Design and electromagnetic analysis of new rotary-linear switched reluctance motor in static mode," *Applied Computational Electromagnetics Society Journal*, vol. 31, no. 2, pp. 171-179, Feb. 2016.

[5] E. Amiri, P. Gottipati, and E. A. Mendrela, "3-D space modeling of rotary-linear induction motor with twin-armature," *In Proceedings of 2011 1st International Conference on Electrical Energy Systems (ICEES)*, Tamilnadu, India, pp. 203-206, Jan. 2011.

[6] P. Jin, Y. Yuan, and G. Jian, "Static characteristics of novel air-cored linear and rotary halbach permanent magnet actuator," *IEEE Transactions on Magnetics*, vol. 50, no. 2, pp. 977-980, Feb. 2014.

[7] S. Y. Li, K. W. Cheng, N. Cheung, and Y. Zou, "Design and control of a decoupled rotary-linear switched reluctance motor," *IEEE Transactions on Energy Conversion*, vol. 33, no. 3, pp. 1363-1371, Sep. 2018.

[8] L. Szabó, I. Benţia, and M. Ruba, "A rotary-linear switched reluctance motor for automotive applications," *In Proceedings of 2012 20th International Conference on Electrical Machines (ICEM)*, Marseille, France, pp. 2615-2621, Sep. 2012.

[9] P. Jin, H. Lin, and S. Fang, "Decoupling control of linear and rotary permanent magnet actuator using two-directional d-q transformation," *IEEE Transactions on Magnetics*, vol. 48, no. 10, pp. 2585-2591, Oct. 2012.

[10] O. Dobzhanskyi, E. Amiri, and R. Gouws, "Comparison analysis of electric motors with two degrees of mechanical freedom: PM synchronous motor vs induction motor," *In Proceedings of 2016 2nd International Young Scientists Forum on Applied Physics and Engineering (YSF)*, Kharkiv, Ukraine, pp. 14-17, Oct. 2016.

[11] E. Amiri, M. Jagiela, O. Dobzhanski, and E. Mendrela, "Modeling dynamic end effects in rotary armature of rotary-linear induction motor," *In Proceedings of 2013 IEEE International Electric Machines and Drives Conference (IEMDC)*, Chicago, IL, United States, pp. 1088-1091, May 2013.

[12] S. L. Hu and S. G. Zuo, "Analytical modeling of magnetic field considering the saturation in switched reluctance motor," *Applied Computational Electromagnetics Society Journal*, vol. 33, no. 12, pp. 1467-1474, Dec. 2018.

[13] E. Amiri, "Circuit modeling of double-armature rotary-linear induction motor," *In Proceedings of 2014 40th Annual Conference of the IEEE Industrial Electronics Society (IECON)*, pp. 431-436, Feb. 2014.

[14] J. H. Alwash and L. J. Qaseer, "Three-dimension finite element analysis of a helical motion induction motor," *Applied Computational Electromagnetics Society Journal*, vol. 25, no. 8, pp. 703-712, Aug. 2010.

[15] I. Benţia, M. Ruba, and L. Szabó, "On the control of a rotary-linear switched reluctance motor," *In Proceedings of 2011 5th International Symposium on Computational Intelligence and Intelligent Informatics (ISCIII)*, Floriana, Malta, pp. 41-46, Sep. 2011.

[16] S. Tanaka, T. Shimono, and Y. Fujimoto, "Optimal design of length factor for cross-coupled 2-DOF motor with halbach magnet array," *In Proceedings of 2015 IEEE International Conference on Mechatronics (ICM)*, Nagoya, Japan, pp. 529-534, Mar. 2015.

[17] J. K. Si, H. C. Feng, and L. W. Ai, "Design and analysis of a 2-DOF split-stator induction motor," *IEEE Transactions on Energy Conversion*, vol. 30, no. 3, pp.1200-1208, Sep. 2015.

[18] J. K. Si, L. J. Xie, and X. Z. Xu, "Static coupling effect of a two-degree-of-freedom direct drive induction motor," *IET Electric Power Applications*, vol. 11, no. 4, pp. 532-539, 2017.

[19] J. K. Si, L. W. Ai, and J. B. Han, "Characteristic analysis of no-load speed of linear induction motor," *Dianji yu Kongzhi Xuebao/Electric Machines and Control*, vol. 18, no. 7, pp. 37-43, July 2014.

[20] L. J. Xie, J. K. Si, Y. H. Hu, and H. C. Feng, "Helical motion analysis of the 2-degree-of-freedom split-stator induction motor," *IEEE Transactions on Magnetics*, vol. 55, no. 6, Article Sequence Number: 8103705, June 2019.

[21] Q. J. Pan, W. M. Ma, and Z. H. Zhao, "Development and application of measurement method for magnetic field," *Diangong Jishu Xuebao/ Transactions of China Electrotechnical Society*, vol. 20, no. 3, pp. 1-3, Mar. 2005.

Haichao Feng was born in China in 1983. He received B.S. and M.S. degrees in Electrical Engineering and Automation, Control Theory and Control Engineering from School of Electrical Engineering and Automation, Henan Polytechnic University, China, in 2005 and 2008, respectively. He is currently an Associate Professor and Doctor of Philosophy in Henan Polytechnic University. His research interests are the optimization design of linear and rotary machines, power electronics, and their controls.

Jikai Si received the B.S. degree in Electrical Engineering and Auto-mation from the Jiaozuo Institute of Technology, Jiaozuo, China, in 1998; the M.S. degree in Electrical Engineering from Henan Polytechnic University, Jiaozuo, China, in 2005; and the Ph.D. degree in 2008 from the School of Information and Electrical Engineering, China University of Mining and Technology, Xuzhou, China, in 2008. He is currently a Distinguished Professor at Zhengzhou University. His main research interests include the theory, application, and control of special motor. He has authored and co-authored over 100 technical papers in these areas. Dr. Si is a Member of the Institute of Linear Electric Machine and Drives, Henan Province, China.

Zhiping Cheng was born in China in 1974. He received M.S. degree in Control Theory and Control Engineer from School of Electrical Engineering and Automation, Henan Polytechnical University, China, in 2003. He is currently an Associate Professor in Zhengzhou University, China. His research interests are linear motor and its control.

Caixia Gao was born in China in 1981. She received B.S. and M.S. degrees in Electrical Engineering and Automation, Control Theory and Control Engineering from the School of Electrical Engineering and Automation, Henan Polytechnic University, China, in 2003 and 2008, respectively. She is currently an Associate Professor with Henan Polytechnic University. Her research interests are electrical automation, artificial intelligence and industrial process control.

Wenping Cao received the B.Eng. degree in Electrical Engineering from Beijing Jiao-tong University, China, in 1991, and the Ph.D. degree in Electrical Machines and Drives from the University of Nottingham, U.K., in 2004. He is currently a Professor with Aston University, U.K. His research interests include thermal performance of electric machines, drives and power electronics.